Experimental and Numerical Modelling of Walking Locomotion on Vertically Vibrating Low-Frequency Structures

by

Hiệp Vũ Đặng

A thesis submitted in partial fulfilment of the requirements for the degree of Doctor of Philosophy in Civil Engineering

University of Warwick, School of Engineering

June 2014

Table of Contents

List of Tables

List of Figures

Notations

$\mathrm{DLF}_{1,\mathrm{mr}}$	Dynamic load factor of first harmonic measured on the rigid surface
$\mathrm{DLF}_{1,\mathrm{sr}}$	Dynamic load factor of first harmonic simulated on the rigid surface
F_{p}	Vertical ground reaction force induced by pedestrian
$F_{\mathrm{p},i}$	Vertical ground reaction force induced by the i^{th} leg
F_{s}	Force induced by the shaker
G	Body weight
I_n	Impulse applied at the end of the n^{th} step
L	Span length of a simply supported bridge
L_{a}	Anatomical leg length
L_{e}	Pendulum length of an inverted pendulum model equivalent to a rocker foot model
R	Pearson's correlation coefficient
R^2	Coefficient of determination
T	Kinetic energy
T_{p}	Period of a step cycle generated by a pedestrian
V	Potential energy

a_{CT}	Acceleration of complaint threshold
a_{ppc}	Peak-per-cycle acceleration
$a_{\mathrm{ppc,m}}$	Measured peak-per-cycle acceleration
$a_{\mathrm{ppc,s}}$	Simulated peak-per-cycle acceleration
a_{s}	Acceleration of the moving mass of a shaker
c	Damping constant of walking models with dampers
c_{b}	Damping constant of a structure
d	Step length
f_{n}	Fundamental frequency of a structure
f_{p}	Pacing rate
$\tilde{f}_{\mathrm{p}}$	Pacing rate normalised to structural frequency
$f_{\mathrm{p,ml}}$	Pacing rate measured on the lively surface
$f_{\mathrm{p,mr}}$	Pacing rate measured on the rigid surface
$f_{\mathrm{p,r}}$	Pacing rate produced on the rigid surface
$\tilde{f}_{\mathrm{p,r}}$	Pacing rate produced on the rigid surface and normalised to structural frequency
$f_{\mathrm{p,sr}}$	Pacing rate simulated on the lively surface
$\tilde{f}_{\mathrm{p,sr}}$	Pacing rate simulated on the rigid surface and normalised to structural frequency
f_{s}	Stamping frequency
g	Acceleration of gravity
k	Spring stiffness of compliant legs
k_{b}	Modal stiffness of a structure

l	Pendulum length of inverted pendulum model or the length of the leg part of the rocker foot model
$\dot{l}$	First derivative of l
l_0	Leg length at rest of walking models with compliant legs
$l_{0,i}$	Initial length at beginning of a walking phase of the i^{th} leg
$\dot{l}_{0,i}$	First derivative of $l_{0,i}$
$l_{\text{e},2}$	Leg length of the second leg at the end of a walking step
$\dot{l}_{\text{e},2}$	First derivative of $l_{\text{e},2}$
l_i	Leg length of the i^{th} leg
$\dot{l}_i$	First derivative of l_i
$\ddot{l}_i$	Second derivative of l_i
m_{i}	Mass of the i^{th} body segment
m_{p}	Body mass
m_{s}	The mass of a shaker that moves to generate force
r	Rocker radius
t	Time variable
v	Walking velocity
v_{mr}	Walking velocity measured on the rigid surface
v_{sr}	Walking velocity simulated on the rigid surface
w	Step width
$\dot{x}_0$	Initial forward speed at the beginning of a step
$\dot{x}_{0,n+1}$	Forward speed at beginning of step $(n+1)$
x_{Ankle}	Coordinate of ankle marker in forward direction
x_{BCoM}	Coordinate of body centre of mass in forward direction

x_{Toe}	Coordinate of toe marker in forward direction
$\dot{y}_0$	Initial vertical speed at the beginning of a step
y_{b}	Modal displacement of a bridge
$\dot{y}_{\text{b}}$	Modal velocity of a bridge
$\ddot{y}_{\text{b}}$	Modal acceleration of a bridge
$\dot{y}_{\text{e},n}$	Vertical speed of pedestrian mass by the end of step n
z	Modal displacement of the structure
z_{Ankle}	Coordinate of ankle marker in vertical direction
z_{BCoM}	Coordinate of body centre of mass in vertical direction
$\ddot{z}_{\text{BCoM}}$	Second derivative of z_{BCoM}
z_{Toe}	Coordinate of toe marker in vertical direction
$\ddot{z}_i$	Second derivative of vertical displacement of centre of mass of the i^{th} body segment
ϕ_{s}	Mode shape ordinate at location of the shaker
ϕ_x	Mode shape ordinate at location x
ρ	Roll factor represents the increase of leg length of a rocker foot model when compared to the equivalent inverted pendulum model
θ	Angle made by the leg and the ground
$\dot{\theta}$	First derivative of θ
$\ddot{\theta}$	Second derivative of θ
θ_0	Attack angle
$\dot{\theta}_0$	Initial angular speed
$\theta_{0,i}$	Initial angle at beginning of a walking phase of the i^{th} leg

$\dot{\theta}_{0,i}$	First derivative of $\theta_{0,i}$
θ_i	Angle made by the i^{th} leg and the ground
$\dot{\theta}_i$	First derivative of θ_i
$\ddot{\theta}_i$	Second derivative of θ_i
θ_{e}	End-of-step angle
$\theta_{\text{e},2}$	End-of-step angle of the second leg
$\dot{\theta}_{\text{e},2}$	First derivative of $\theta_{\text{e},2}$
θ_{tr}	Trunk angle
φ_i	Phase shift of the i^{th} harmonic
ζ	Damping ratio of the structure
Δ_{DLF_1}	Percentage errors of DLF_1 between measured data and reconstructed results
Δ_{Peak}	Percentage error of peak acceleration between simulations using measured and reconstructed forces
ΔC	Added damping coefficient
ΔCoV	Discrepancy in coefficient of variation of a gait parameter
ΔDLF_1	Discrepancy in DLF_1
Δa_{ppc}	Discrepancy in average peak-per-cycle acceleration
Δd	Discrepancy in average step length
Δf	Frequency shift of inverted pendulum model in simulations on the lively surface
Δf_{p}	Discrepancy in average pacing rate
Δv	Discrepancy in average walking speed
Δw	Discrepancy in average step width

$\Delta\dot{y}_{\mathrm{b,n}}$	Instantaneous deduction of the modal velocity at the end of step n of the interactive model
$\Delta\theta_0$	Discrepancy in average attack angle
$\Delta\theta_{\mathrm{e}}$	Discrepancy in average end-of-step angle
$\Delta\theta_{\mathrm{tr}}$	Discrepancy in average trunk angle
$\Delta\theta^{\mathrm{tr}}$	Maximum variation of the trunk angle within a step

Abbreviations

2D	Two–dimensional
3D	Three–dimensional
BCoM	Body's centre of mass
BSP	Body segment parameter
CDF	Cumulative density function
CoP	Centre of pressure
CoV	Coefficient of variation
DLF_i	Dynamic load factor of the i^{th} harmonic
DSP	Double support phase
GC	Gait cycle
GRF	Ground reaction force
HAT	Head, arms and trunk
IC	Initial contact
IFMT	Instrumented force measuring treadmill
IM	Interactive model
IPM	Inverted pendulum model
LR	Loading response
MCS	Motion capture system

MHM	Moving harmonic model
MSD	Mass-spring-damper
MSt	Midstance
NR	Non-randomisation
PDF	Probability density function
PS	Pre-swing
PSDI	Pedestrian–structure dynamic interaction
RFM	Rocker foot model
SCoM	Segment's centre of mass
SDoF	Single degree-of-freedom
SEF	Self-excited factor
SMDM	Spring mass with damper
SMM	Spring mass model
SMRFDM	Spring mass with rocker foot and damper model
SMRFM	Spring mass with rocker foot model
SSP	Single support phase
TFF	Total force factor
TP	Test point
TS	Test subject
TSt	Terminal stance
WB	Warwick Bridge
WB1	Warwick Bridge with span length of 16.2 m
WB2	Warwick Bridge with span length of 17.4 m
WR	With randomisation

Acknowledgements

This thesis has been completed with Dr Stana Živanović as main supervisor and Dr Michael Chappell as co-supervisor. I gratefully acknowledge their supports. My deepest gratitude goes to Dr Živanović for the considerate guidance, valuable suggestions and dedicated time throughout this project.

The research work was supported by the UK Engineering and Physical Sciences Research Council (grant number EP/I03839X/1: Pedestrian Interaction with Lively Low-Frequency Structures). I am also indebted with the support of the Warwick Postgraduate Research Scholarship and School of Engineering, the University of Warwick.

I want to thank all technician members of the Civil Research Group at the University of Warwick for the constant supports in this project. Special acknowledgement is dedicated to Mr Colin Banks and Mr Ian Baylis for their tremendous contributions.

I would like to thank Birmingham Science City and Advantage West Midlands for the access to the Gait Laboratory. I am also grateful to Prof. Adrian Wilson and Dr Tung Fai Yu for their useful suggestions in the application of the Vicon system.

All experimental studies in this thesis have been performed with volunteering help of members of School of Engineering, the University of Warwick.

I want to thank my brother Sơn B. Đặng for the vital participation in the experimental study and my parents for their loving supports. This work is especially dedicated to my wife Trang T.H. Phùng and our little angel Chi K. Đặng. Thank you for being with me all the way.

Declaration

This thesis is submitted to the University of Warwick in support of my application for the degree of Doctor of Philosophy. It has been composed by myself and has not been submitted in any previous application for any degree.

The work presented (including data generated and data analysis) was carried out by the author.

Parts of this thesis have been published by the author:

- Dang, H.V. and Živanović, S. Modelling Pedestrian Interaction with Perceptibly Vibrating Footbridges. *FME Transactions*, 41 (4), 271-278, 2013.

- Dang, H.V. and Živanović, S. Investigation of Human-Structure Dynamic Interaction using Biomechanical Model. In *Expert Scientific Meeting*, Department of Health Science and Technology, Aalborg University, Denmark, 1 - 4 August, 2012.

Abstract

Vibration serviceability is a governing factor in the design of low-frequency structures, which are sensitive to human-induced loads. To achieve reliable vibration estimates, structural engineers need to model the combined pedestrian-structure system as close to reality as possible. The most uncertain aspect in the modelling is accounting for pedestrian interaction with perceptibly vibrating structure. To improve understanding of this aspect, the thesis aims to provide experimental and numerical modelling of walking locomotion on lively structures in the vertical direction.

Experimental programmes were conducted to provide characteristics of walking gait on both rigid and lively surfaces, where the former was used as benchmark for comparison. Both kinematic and kinetic parameters were measured using a motion capture system. Discrepancies of the gait parameters between data collected on imperceptibly and perceptibly vibrating surfaces, as consequences of the pedestrian-structure dynamic interaction, were quantified. The unique database provided in this thesis contributes to the understanding of locomotion on the vibrating surface and, therefore, can be used for calibration of pedestrian models intended for civil engineering applications.

An interactive model was developed, using a biomechanical model to represent the pedestrian. The novel feature of this model is to account for two-way interaction between the pedestrian and the structure. A sensitivity analysis and validations of the proposed model against experimental data were also provided. Results of the modelling work inform designers detailed evaluations of performance of the model on both virtual and as-built structures.

Chapter 1

Introduction

Use of light high-strength materials is increasingly popular in design of modern structures, often resulting in structures having low natural frequencies and being more sensitive to dynamic excitation induced by human activities. As a result, vibration serviceability becomes a governing factor in the design of these structures.

Humans, being intelligent and adaptable dynamic systems, tend to interact with perceptibly vibrating structures and alter their vibration behaviour. This interaction, however, is still not well understood. As a consequence, it is neglected in the design guidelines, which often results in inaccurate vibration estimates. The lack of understanding of this phenomenon is due to inadequate research, especially about interaction in the vertical direction. This thesis aims to enhance understanding of the subject through providing experimental and numerical modelling of walking locomotion on structures that are lively in the vertical direction.

This introductory chapter begins with the background information. Next, a summary of up-to-date work is presented, along with gaps of knowledge in

the research subject. Main aims of the thesis are then stated. Finally, an outline for the remainder of the thesis is provided.

1.1 Vibration serviceability of low-frequency structures

Vibration serviceability problems due to human-induced loads have been reported for different types of structures, such as footbridges, grandstands and open-plan floors (Racic et al., 2009). This type of loads is induced from different human activities (e.g. jumping, bouncing and walking), where the focus of this thesis is on the load generated during walking. The situation of vibration serviceability problems arises due to inconvenient dynamic properties often encountered in modern structures made of light high-strength materials. These potentially problematic properties are low mass and damping as well as natural frequencies coinciding with the typical range of frequencies that can be generated by human walking. As a result, vibration serviceability often governs designs and it inspires academic research in determining reliable methods for accurate estimation and control of structural vibration.

To have reliable vibration assessment, structural engineers need to model the combined pedestrian-structure system as close to reality as possible. While modelling structural dynamic properties and pedestrian-induced loads as separate entities advanced significantly over the last decade, it is still difficult to estimate the structural vibration response accurately. The most uncertain aspect in the modelling is accounting for pedestrian interaction with perceptibly

vibrating structure. Pedestrian–structure dynamic interaction (PSDI) occurs when pedestrians, who dynamically excite the structure, at the same time, perceive the vibrations induced and react to them. PSDI is more critical in low-frequency structures, where it is easier to generate perceptible vibration by normal walking.

To address PSDI, it is necessary to gain better understanding of walking locomotion and if/how it is affected by vibration of the supporting structure. This thesis aims to investigate both experimental and numerical modelling of walking locomotion on perceptibly vibrating surfaces. More information about PSDI and a summary of up-to-date research are provided in the next section.

1.2 Previous work in pedestrian-structure dynamic interaction

Best publicly known example of PSDI is excessive lateral vibration of the London Millennium Bridge on its opening day in 2000 (Dallard et al., 2001). The bridge (Figure 1.1) had to be closed shortly afterwards to be fitted with damping devices that reduced vibrations to acceptable levels. Since the problem of the London Millennium Bridge occurred, much research in PSDI in the lateral direction has been conducted resulting in development of sophisticated numerical models (Ingólfsson et al., 2011; Morbiato et al., 2011; Bocian et al., 2012). However, the investigation in the vertical direction is still under development. In current design guidelines (SETRA, 2006; ISO, 2007; BSI, 2008), the PSDI is neglected due to the lack of studies of walking on lively surfaces. This situa-

Figure 1.1: London Millennium Bridge.

tion is the motivation to conduct research of PSDI in the **vertical direction** in this thesis. In this section, a brief summary of experimental and numerical approaches to PSDI on the vertically vibrating surfaces, along with gaps of knowledge, are provided.

In experimental studies, occurrence of PSDI was often reported qualitatively through observations of changes either in dynamic properties of the human-structure system (Willford, 2002; Brownjohn et al., 2004a; Živanović et al., 2009) or in human-induced forces in comparison with walking on the rigid (i.e. non-perceptibly vibrating) surfaces (Pimentel et al., 2001; Živanović et al., 2005a). There is a lack of understanding of if/how gait parameters are influenced when walking on lively surfaces in comparison to those produced during walking on the rigid surface. It is generally believed that the alterations of kinematic and kinetic parameters occur and that they are the direct consequence of pedestrians being affected by perceptible vibration. Kinematic and kinetic parameters of human locomotion have been intensively studied in literature. However, to the best knowledge of the author, there exists no

information related to the walking gait on vibrating surfaces. The lack of experimental data for both kinematic and kinetic parameters under PSDI inspires the experimental work in this thesis.

As for numerical modelling, the number of studies attempting to model PSDI is steadily increasing. To model the interaction, different means are used, such as modelling the human body as a spring-mass-damper system (Alexander, 2006; Archbold et al., 2011), or a rigid bipedal system with controlled timing of individual steps (Bocian et al., 2013), or both (Qin et al., 2013). Among these developments, the model proposed by Bocian et al. (2013) has several advantages. In this model, a bipedal inverted pendulum is used to represent pedestrians walking on a surface that vibrates at a prescribed vibration level. Using such a biomechanical model enables the modelling of walking mechanism of human gait, and therefore the model features level of detail necessary for observing potential changes in walking gait on the lively surface. In addition, since inverted pendulum model is the simplest bipedal model, the incorporation of structural vibration into this model is also easier than the implementation of more complicated bipedal models. However, there are several shortcomings associated with this model. The model takes into account one-way interaction only, i.e. studying effects of the structural vibration on walking gait while disregarding influence of alterations in walking gait on the structural vibration. Furthermore, the inverted pendulum model is not studied in detail, e.g. its capability to represent different individuals in human population. Finally, firm experimental evidence in support of this model is not yet provided. In this thesis, Bocian et al.'s model has been improved to address these shortcomings.

1.3 Research aims

Given the current lack of understanding about PSDI, the aim of the research in this thesis is to provide experimental data and develop a numerical model for walking locomotion on structures that are lively in the vertical direction.

In the experimental work, a database of walking locomotion, consisting of kinematic and kinetic parameters, on both rigid and lively surfaces will be developed. A motion capture system will be used for this purpose. Since accuracy and a clear procedure for this measuring method are not available in literature, a study to test the suitability of this measuring method will be performed. The experimental data collected on rigid and lively surfaces will be compared to detect any alteration trends that are potentially due to PSDI.

In the modelling work, quantitative studies of several bipedal models will be performed to determine the most suitable bipedal to implement in the modelling of PSDI. Next, two-way interaction will be introduced into modelling PSDI. Performance of the proposed model will then be evaluated against collected experimental data.

1.4 Thesis outline

The thesis consists of seven chapters, which cover literature review, numerical modelling and experimental studies.

This introductory chapter is followed by an up-to-date literature review in Chapter 2. The review begins with recent development in the research of PSDI. Next, basic information of gait parameters, related to the study in

this thesis, typical for walking on the rigid surface were summarised. Then, six bipedal models used in biomechanics were critically evaluated, with the emphasis on their suitability for modelling human-structure interaction.

Among six models reviewed in Chapter 2, three representative models were chosen for more detailed evaluation in Chapter 3. For the investigation of each model, mathematical derivation and realistic ranges of input parameters were provided, followed by a parametric scan. These three models were critically evaluated and the inverted pendulum model was singled out for further study in this thesis.

Chapter 4 presents the experimental work involving ten test subjects walking on the rigid surface. In the first part of this chapter, suitability of use of motion capture systems to indirectly measure ground reaction force of pedestrians was investigated and its accuracy was quantified. A motion capture system was then used in the second part to characterise walking on the rigid surface, through quantifying inter- and intra-subject variability of gait parameters. Results on the rigid surface are used as benchmark data for later comparison.

In Chapter 5, an experimental programme of walking on a lively low-frequency structure was performed. Three test subjects were asked to perform nominally the same experiments as those conducted on the rigid surface to identify if/how humans alter their locomotion when walking on lively surfaces.

A numerical model consisting of the inverted pendulum model walking across a low-frequency structure was then developed in Chapter 6. The chapter includes a sensitivity analysis and validation of the model against experimental data.

Finally, Chapter 7 presents main conclusions and recommendations for further work.

All experimental work with human participants in this thesis was approved by the Biomedical and Scientific Research Ethics Committee at the University of Warwick (date of approval was 22 May 2012).

Chapter 2

Literature review

This chapter is divided into five parts. The first part explains basic terminology, while the second presents the current insight into pedestrian-structure dynamic interaction (PSDI). The third part provides background information on walking gait and the corresponding load induced on imperceptible vibrating surface. The fourth part identifies some bipedal walking models that have potential to be used for studying the PSDI. Major conclusions are provided in the fifth part.

2.1 Basic concepts and terminology

Throughout this chapter and the thesis, a number of terms are repeatedly used. Since these terms might have different meaning in other contexts, their definitions in the context of this thesis are explained as follows:

- **Low-frequency structures** (interchangeably called either wobbly, lively or flexible structures in this study) are structures that can easily be excited by human walking.
- **Rigid surface** is used to describe a walking surface that does not vibrate perceptibly under human-induced dynamic loads.

- **Gait** is the manner of walking (Racic et al., 2009). The focus of this thesis is on the non-pathological gait.

- **Reference planes** are three perpendicular planes shown in Figure 2.1a, which are used to divide human body into anatomical parts (Vaughan et al., 1999). While the sagittal plane separates the body into left and right and the frontal plane distinguishes the front and back parts, the transverse plane divides the body into upper and lower portions. The study in this thesis focuses on walking gait in the forward direction, where the sagittal plane is of interest.

- **Segment's centre of mass** (SCoM) is the spatial centre of mass of a body segment, which is conventionally defined by two endpoints. The segment's endpoints are often referred as proximal and distal points. The former is the point closer to the torso while the latter is the point further away (Racic et al., 2009). The mass distribution of different body segments can be visualised in Figure 2.1b (Drillis

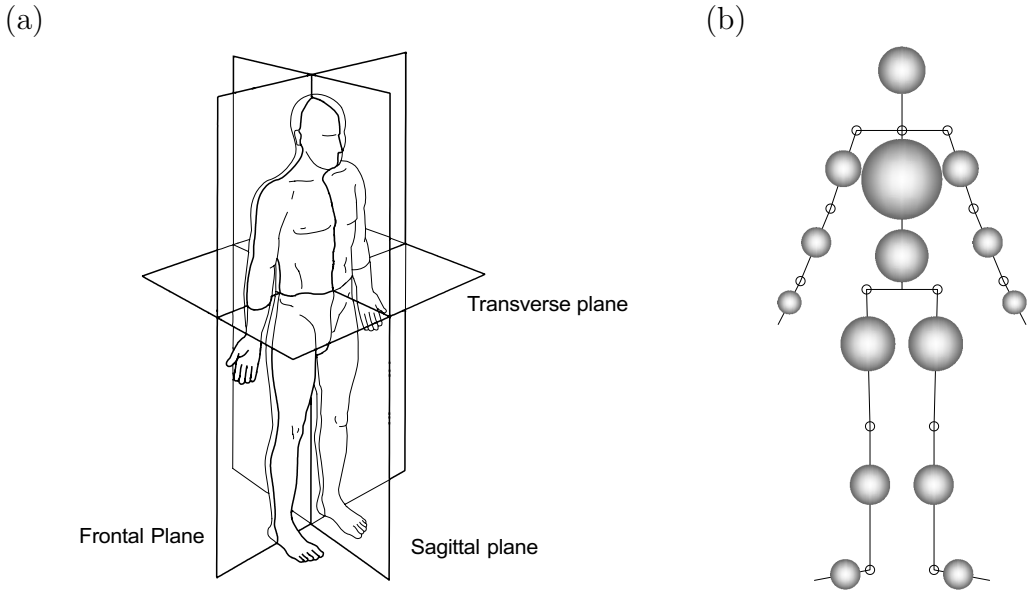

Figure 2.1: (a) Three reference planes (after Vaughan et al., 1999) and **(b)** a mass distribution model (after Drillis et al., 1964).

et al., 1964). Segment masses are proportional to the volumes of the spheres, while centres of the spheres indicate the SCoMs.

- **Body's centre of mass** (BCoM) is the point representing the centre of mass of the entire human body. In order to locate BCoM, information about positions of SCoMs and distribution of the mass throughout the body is normally used.

- **Human-induced load** is the dynamic load induced into the structure by human activities, such as running, walking, jumping and bouncing. This load is also frequently referred to as ground reaction force (GRF). This thesis focusses on pedestrian loading (i.e. walking-induced), and it will address other types of human activities only when necessary to help the study of walking. The human-induced load is composed of components acting in three perpendicular directions: anterior-posterior, lateral and vertical. Focus of this thesis is on the vertical component of the walking-induced force.

- **Harmonic** refers to one of the dominant frequencies in the amplitude spectrum of the walking-induced force. The dominant harmonics typically occur at the frequency of the pacing rate and its integer multiples.

- **Dynamic load factor** (DLF) represents the amplitude of a harmonic component of the human-induced force normalised by pedestrian's weight (Bachmann, 1995).

2.2 Pedestrian–structure dynamic interaction

This section first provides some observations of PSDI on full scale structures. Then the current approaches to the vibration assessment of structures exposed to pedestrian loadings and their shortcomings with regard to addressing PSDI

are presented. Finally, several recent developments in studying approaches into PSDI are reviewed and critically evaluated.

2.2.1 Observations of interaction on full-scale structures

Most studies on PSDI in the literature can be classified in two approaches. First approach looks at PSDI through changes in the dynamic properties with presence of humans compared with properties of the empty structure. On the second approach, PSDI was observed through the alterations in the dynamic load when pedestrians were exposed to perceptible vibrations.

In the first approach, it is known that the presence of passive (i.e. standing or sitting) humans tend to increase damping and decrease the natural frequency of the human-structure system (Brownjohn, 2001; Sachse et al., 2003). However, very few papers address the influence of active humans on dynamic properties of the structure. Ellis and Ji (1997) reported the unchanged dynamic characteristics of a beam exposed to walking and jumping by one test subject. However, the investigated structure had a relatively high fundamental frequency of 18.7 Hz. This frequency is well above the typical frequency range of walking, from 1.4 Hz to 2.4 Hz (Živanović, 2012), and jumping, from 1.0 Hz to 3.5 Hz (Yao et al., 2006). As a result, it is difficult to excite the beam by human-induced loads. This might be the reason why the change of dynamic properties was not detected. On the contrary, Willford (2002) reported analysis from experiments on the London Millennium Bridge claiming that the crowd traffic contributed to the increase of structural damping in the vertical direction. This result is in agreement with the study of a full-scaled

footbridge by Brownjohn et al. (2004a), where the damping ratio of the first torsional mode increased from 0.4 % of an empty structure to between 0.7 % and 1.0 % when the structure was occupied by a large group of pedestrians. More recently, Živanović et al. (2009) performed experiments with groups of people walking on a low-frequency (4.4 Hz) bridge in laboratory. The result showed that the damping ratio of the first bending mode increased from 0.72 % of an empty bridge to 2.86 % of the bridge with ten pedestrians.

In the second approach, Pimentel et al. (2001) and Živanović et al. (2005a) detected that the recorded response was significantly lower than the predicted. The attenuation of structural response was attributed to a drop in the DLF generated on the vibrating surface compared with that recorded on a rigid floor.

In much more detailed experimental studies of jumping and bouncing on a flexible platform, Yao et al. (2004; 2006) reported a significant reduction in DLF of the first forcing harmonic when the test subject was instructed to excite the resonance of the platform. The observations suggested that the source of reduction might be caused by excessive vibrations of the supporting platform. However, in another study on dynamic interaction of humans jumping on a grandstand-like deck, Comer et al. (2010) reported that the average DLF of a jumping group on a flexible deck was in the upper range of DLF of the same group observed on a rigid deck. The discrepancies in the two studies might come from the significant difference in the vibration level of the supporting structures. The flexible platform used in the experiments of Yao et al. was quite light (180 kg), which made the mass ratio of the test subject over the structure relatively high (i.e. about 0.41). Such a low mass

ratio induced excessive vibration of the platform during experiments. Yao et al. (2004; 2006) reported the maximum acceleration between 1.2–2.2 g (i.e. 11.8–21.6 $\mathrm{m/s^2}$). Such an excessive vibration contributed to the difficulty of test subject to maintain the instructed frequency, and consequently reduced the DLF. Although the total mass of the deck in Comer et al. (2010) was not reported, the peak displacement (8.8 mm) and acceleration (0.44 g, i.e. 4.3 $\mathrm{m/s^2}$) in their experiment were much lower than those in Yao et al.. In addition, Comer et al. (2010) reported a high level of coordination within the jumping group due to the popular songs played during the experiment. This remark might be the reason why the test subjects put more energy into the activity, and were consequently able to maintain the DLF as measured on the rigid deck.

Although scarce, most of the currently available studies indicate that the pedestrians are likely to influence dynamic properties of structures, and that perceptible vibrations could affect the human behaviour, and consequently influence the loads applied. However, more research is needed to improve the understanding of the PSDI phenomenon.

2.2.2 Current approaches used in vibration serviceability assessment

In the assessment of vibration serviceability of a structure under human-induced loads, it is required to estimate the vibration response of the structure accurately. Designers/engineers check the assessment result against limiting values in design guidelines, and make recommendation if the structure is ser-

viceable for a certain loading condition. To estimate the structural response, human-induced loads and dynamic properties of the structure are often considered as two sets of necessary input parameters.

The first set of input data is dynamic properties of structures. The developments in numerical (finite element) modelling of structures enable the estimation of the structural dynamic properties, such as natural frequencies, mode shapes and modal masses. While all these estimates contain inherent uncertainties, they, in conjunction with a sensitivity analysis, usually form a good basis for the evaluation of vibration performance of structures. For existing structures, dynamic properties can be experimentally evaluated with high level of accuracy, which is extremely important in understanding their vibration behaviour and learning about their damping levels.

The pedestrian-induced dynamic force is another input set required in the analysis. For walking over a rigid ground, early attempts to study the human loads were mostly limited to qualitative description of the pattern of plantar pressure (Racic et al., 2009). With the invention of a force plate, which is a platform instrumented with force transducers, GRF generated by a single step could be measured accurately. Use of a more advanced facility, in form of an instrumented treadmill, allowed investigators to record the dynamic forces in consecutive steps (Belli et al., 2001). The development of experimental facilities helped researchers to understand and quantify GRF in both time and frequency domains (Giakas and Baltzopoulos, 1997; Kerr, 1998). Figure 2.2a shows a recorded time history of GRF induced by each leg and the total GRF of a test subject. Assuming that walking is a periodic activity, the GRF in the time domain, $F_{\mathrm{p}}(t)$, can be approximated as the sum of body weight and

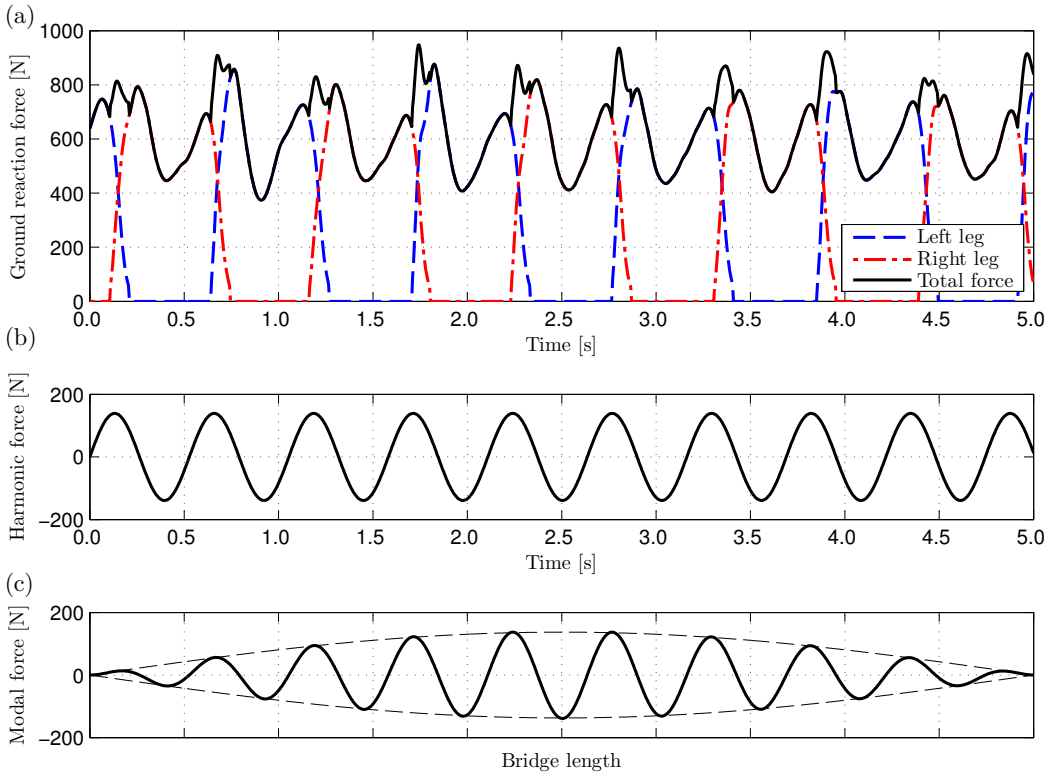

Figure 2.2: **(a)** Ground reaction force of a test subject weighted 650 N, **(b)** harmonic force and **(c)** modal force on a simply supported beam.

a number of Fourier harmonic components (Bachmann, 1995):

$$F_{\mathrm{p}}(t) = G + \sum_{i=1}^{n} G\ \mathrm{DLF}_i\ \sin(2\pi i f_{\mathrm{p}} t - \varphi_i) \tag{2.1}$$

where G is the walker's body weight of the walker (N), i indicates the i^{th} harmonic, n is the number of harmonics of interest, DLF is the dynamic load factor, f_{p} is the pacing rate (Hz), and φ is the phase shift (rad). Figure 2.2b shows the case when only the first harmonic is of interest, i.e. GRF is approximated as a sinusoidal function.

After the dynamic properties and the walking force were estimated, an-

other challenge for vibration assessors was to take into account the effect of mode shape and the limited duration the pedestrian needs to cross the structure. To solve this challenge, Rainer et al. (1988) introduced the modal walking force. Based on the assumption that the walking speed is constant, i.e. the position of the pedestrian on the structure at any point in time can be estimated, the modal force is calculated as the harmonic force multiplies with the mode shape. Figure 2.2c illustrates the modal force (solid line) for a beam with half-sine mode shape (dashed lines). This modal force is incorporated as the external force in the well-known equation of motion of structures (containing structural dynamic properties) to estimate the structural response. This approach is hereafter referred to as moving harmonic model (MHM).

Since the MHM neglects any interaction that might arise between pedestrians and the structure, the model cannot be used to explain the PSDI phenomenon. Nevertheless, current design guidelines are still based on the MHM approach despite the evidence of existence of PSDI described in Section 2.2.1 (SETRA, 2006; ISO, 2007; BSI, 2008). The negligence of PSDI can lead to significant under or overestimation of structural response. An example of the consequence of disregarding the interaction between a pedestrian and a 113–metre long cable-stayed bridge that exhibits high-level vibration in the vertical direction is shown in Figure 2.3 (Živanović et al., 2005a). A mismatch between the measured vibration response (black line) and the response calculated by the MHM approach (grey line) is significant. The peak value of the simulated response is almost four times larger than that of the measured response. It was concluded that the low vibration levels developed during first 35 s of the crossing were not significant enough to cause PSDI, hence almost perfect

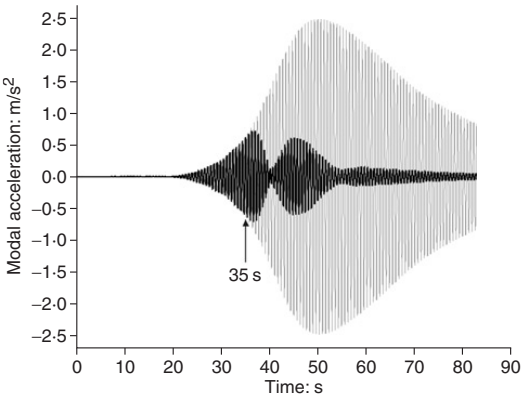

Figure 2.3: Calculated and measured responses of a cable-stayed footbridge (after Živanović et al., 2005a).

agreement between the two responses. After 35 s, the test subject seemed to react to vibrations, perhaps by slightly varying the pacing frequency, and as a consequence caused significant differences between the predicted and measured responses.

Not only neglecting PSDI, another shortcoming of the MHM approach is the periodicity assumption of the walking activity. As a result, MHM cannot reproduce the actual narrow band nature of the spectrum of the walking force (Živanović et al., 2005b). To rectify this shortcoming, researchers devoted significant effort by modelling imperfections in walking, i.e. slight changes in forcing magnitude and pacing frequency with each step. Some sophisticated models accounting for randomness of the walking parameters have been developed (Brownjohn et al., 2004b; Živanović et al., 2007; Racic and Brownjohn, 2011). While these models are genuine represents of time and/or frequency domain of walking forces induced by both individual and crowds, they are applicable only to structures on which PSDI does not take place.

So far, all the listed approaches treat the pedestrian and the structure

as two separate subjects. The evidence that these approaches are unable to anticipate the infamous sway of the London Millennium Bridge under crowd loading reveals the existence of the dynamic interaction between pedestrians and the structure. Such an interaction suggests that pedestrians and structures might need to be treated together in vibration serviceability assessment of structures. In the past, this interaction was normally neglected due to its small influence on vibration responses of traditional massive, heavy and high frequency structures. However with the development of more aesthetic designs and requirements for minimum use of materials, bulky and heavy structures were gradually replaced by more slender and light-weight structures. Consequently, the dynamic interaction has become more common and significant.

Overall, majority of the loading models and all of current design codes neglect PSDI, treating structure and pedestrian as two separate entities. Only recently, some models that do take into account PSDI started to emerge and they will be described in details in Section 2.2.3.1.

2.2.3 Developments in studying pedestrian-structure dynamic interaction

From the previous sections, it seems that neglecting PSDI could lead to significant discrepancies in the estimates of structural responses under human-induced loads. Also, modelling pedestrian and structure separately in the MHM cannot account for the PSDI. Even when the interaction is attributed to changes of structural dynamic properties or alteration of the human's forces, the aforementioned observations in Section 2.2.1 have not explained how the

PSDI phenomenon happens. As a result, new approaches must be derived to get more insight into PSDI. This section reviews some recent novel approaches that account for PSDI, followed by identifying key criteria required for successful modelling of the pedestrian-structure system.

2.2.3.1 Recent numerical models

There are at least two distinct approaches to model PSDI in the vertical direction that are currently being developed. They differ in the means used to describe the interaction. These means are either (1) dynamic properties of the human body (Alexander, 2006; Archbold et al., 2011) or (2) control of timing of individual steps (Bocian et al., 2013). The approach that combines the two is also emerging (Qin et al., 2013). It is worth noting that firm experimental evidence in support of any of the approaches is still not available.

Dynamic properties of the human body

Alexander (2006) and Archbold et al. (2011) attached a mass-spring-damper (MSD) model, representing the human body dynamics, to a virtual footbridge to simulate PSDI (Figure 2.4a). Although both studies used the same mechanical model of the body, the two models are distinctly different. Alexander (2006) used an actuator, acting against both the structure and pedestrian mass, to model the internal force generated by muscles during the locomotion process. Consequently the mass, spring and damper of the human body in his model represent the physical properties of the human.

Differently, Archbold et al. (2011) applied a harmonic force, as typically produced on rigid surfaces, to the structural mass only. This means that the

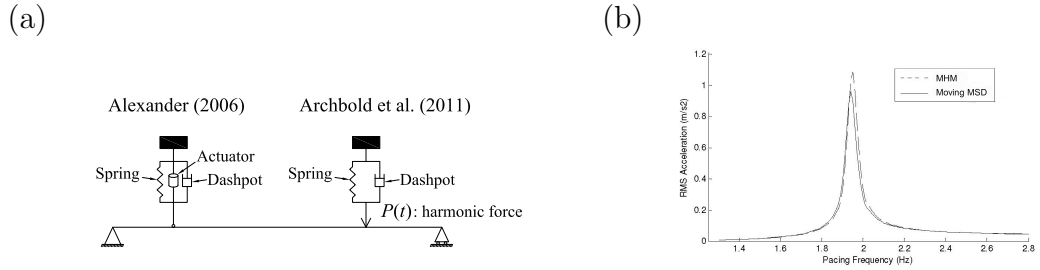

Figure 2.4: (a) Modelling pedestrian as a mass-spring-damper system and **(b)** comparison of structural response between moving single degree of freedom and moving harmonic approaches (after Archbold et al., 2011).

parameters of MSD model represent the increase/reduction in damping and stiffness of the human body due to walking on lively structure compared with walking on rigid surfaces. The virtual structure was a simply-supported beam with natural frequency at 1.94 Hz and the damping ratio was 0.5 %. As the pedestrian interacts with the structure, forces in the spring and damper alter the amplitude of the imposed sinusoidal force. The result of simulation was compared between the moving MSD and the MHM (i.e. neglecting PSDI) and shown in Figure 2.4b under a range of pacing frequencies (Archbold et al., 2011). The simulation found that there is a reduction in the response of the moving MSD model when the pacing rate was close to the bridge's natural frequency (around 1.94 Hz). The figure shows that the moving MSD model attenuates the bridge response compared with that obtained by MHM when the pacing rate is close to the bridge's natural frequency. It is likely that the interaction between pedestrian and structure contributes to this reduction.

In both models, the interaction is manifested through relative displacement and velocity between structural and human degree of freedom. The re-

maining challenge with these models is to calibrate them against experimental data, currently not readily available in the public domain.

Overall, the advantage of this approach is that it considers a human as a dynamic system, which interacts with dynamics of the structure. On the other hand, the two models do not attempt to model walking gait and therefore cannot explain the changes in human locomotion while walking on lively structures.

Control of timing of individual steps

The second approach to PSDI by controlling the timing of individual steps requires a model to capture the walking mechanism and its changes under the influence of PSDI. A promising method is to use bipedal models to represent pedestrians. Macdonald (2008) proposed such a model to investigate PSDI in the lateral direction. This approach was later developed to study the dynamic interaction in the vertical direction (Bocian et al., 2013). The pedestrian was modelled as an inverted pendulum with BCoM supported by rigid massless legs. The supporting structure was not modelled, but its displacement was predefined as a sinusoidal function $z(t)$. The combined system is illustrated in Figure 2.5a.

In the simulation on rigid ground, i.e. $z(t) = 0$, the GRF induced by the walking model is periodic. When the vertical displacement of the bridge is introduced, it is incorporated in the equation of motion of the inverted pendulum model. Under the influence of the bridge movement, the GRF loses its periodic nature. By dividing the vertical force into two components that are in phase with the modal velocity and acceleration, Bocian et al. (2013) attributed these

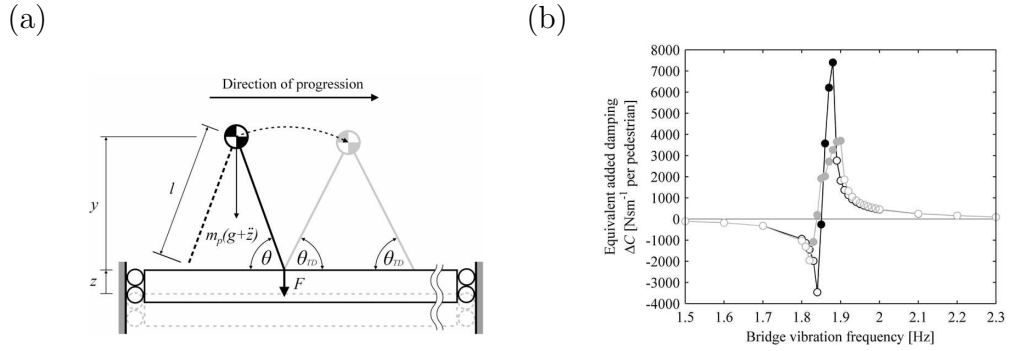

Figure 2.5: (a) Modelling pedestrian as an inverted pendulum model on a vertically oscillating surface and **(b)** quantification of the dynamic interaction as added damping coefficient (after Bocian et al., 2013).

two components to the added damping and mass of the bridge. Figure 2.5b illustrates the equivalent added damping coefficient, ΔC, for varying natural frequency of the supporting structure. Depending on the vibrating frequency (of the structure), ΔC can be either positive or negative, which results in beneficial or detrimental effect on the structural response.

This investigation opens a new approach of using a bipedal model in the study of vibration serviceability of lively structures. The key advantage of this approach is that it includes human walking mechanism and its interaction with the oscillating deck. Since Bocian et al. (2013) have not included the structural modal parameters into the model, the direct applicability of this approach in vibration assessment of real-life structures is not possible yet. However, it is a pioneering attempt to understand the nature of PSDI.

Combination of two aforementioned approaches

Recently, Qin et al. (2013) proposed a new model to combine the two previously described approaches. In their interactive model, the pedestrian was simulated as a bipedal spring-mass-damper model walking over a virtual

simply-supported beam (Figure 2.6a).

The equations of motion of the system of the pedestrian and the structure are coupled. Under given initial conditions, the interactive system was put into motion. The system's damping and stiffness matrices were time dependent due to the varying contribution of the bipedal model. As a result, the modal properties changed in every time instant. In turn, the displacement of the supporting structure affected the kinematic movement of the bipedal model, and consequently altered the walking force. The feedback loop between pedestrian and structure developed as the bipedal model crossed the structure. Because of the damping component in the pedestrian model, it was necessary to supply additional energy to the walking model throughout the simulation.

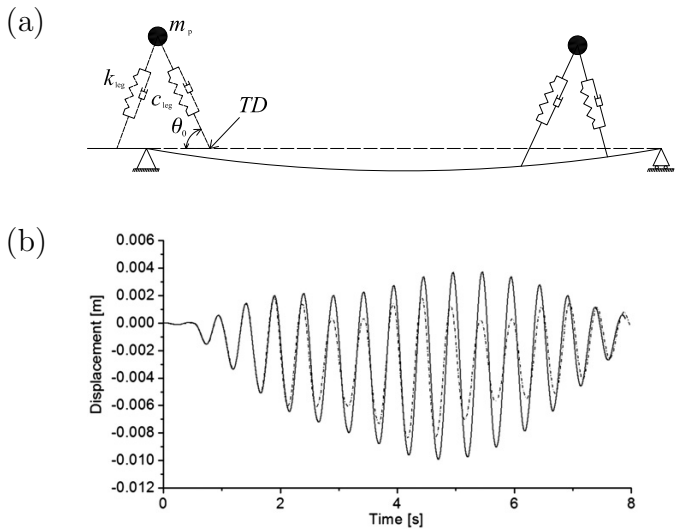

Figure 2.6: (a) Modelling pedestrian as a spring mass with damper model on a structure and **(b)** simulation results with (solid line) and without (dashed line) pedestrian-structure dynamic interaction (after Qin et al., 2013).

Simulation result of structural response on a flexible surface is shown in Figure 2.6b (after Qin et al., 2013). In this particular case, the response of the simulation with PSDI (i.e. the interactive model) was amplified when compared with the simulation without PSDI (i.e. the MHM). The authors concluded that the difference came from the dynamic interaction. However, the amplification of the simulation response has not been seen yet in experimental observations (Pimentel et al., 2001; Živanović et al., 2005a). A potential serious shortcoming of the simulations is that the period of simulation was very short (less than 10 s). It is unlikely that the interaction would develop over such a short period of time, and therefore simulations over short bridges have limited value.

2.2.3.2 Requirements for modelling pedestrian-structure dynamic interaction

The review of three recent models shows that modelling PSDI is still at the early stages and that more detailed insight into performance of the models and their validation against experimental data are required. Taking the advantages and disadvantages of the current approaches, this section will comment on requirements that, in the author's opinion, a future modelling should satisfy with respect to both pedestrian and structural features to successfully represent PSDI.

To account for PSDI, the structure and the pedestrian have to be modelled as a joint pedestrian-structure system. This requirement implies coupling between the two system components, i.e. accounting for the two-way interaction between them. An important aspect of understanding this interaction is to

analyse how structural movement influences the walking force and to study the phase between the applied force and the structural vibration. To achieve this goal, one needs to get insight into the walking mechanism and to understand how this mechanism develops on lively surfaces. In a truly interactive model, the GRF should be obtained as a result of the locomotion, rather than treated as an entity independent from the oscillation of the walking surface, as used in the MHM. Therefore, a way forward is to include the walking mechanism into the modelling.

While the locomotion over rigid surfaces has been studied for a long time (Saunders et al., 1953), the walking mechanism and contribution of different parts of the human body to the locomotion are relatively well known (Perry and Burnfield, 2010). Different models for replication of the walking process were proposed in various fields, such as medical science, robotics and biomechanics in the past. If these models can be used to genuinely represent walking over an oscillating surface then they are also likely to be successful in modelling the PSDI mechanism.

In summary, the structure and human should not be treated as two separate entities in the modelling of PSDI. An interactive model that account for their mutual influence is a promising approach for modelling of the PSDI phenomenon.

2.3 Background information of walking gait

Depending on the specific field of expertise, various bipedal models to replicate the walking gait of humans were proposed. Before the review of these models, it

is necessary to establish a firm understanding of the walking gait. This section first provides a detailed description of characteristics of human walking gait on a rigid ground (from Section 2.3.1 to 2.3.4). Then the criteria for the selection of models most suitable for studying PSDI are outlined in Section 2.3.5.

2.3.1 Gait cycle, trajectory of body centre of mass and time history of ground reaction force

Gait analysis is the systematic study of the walking locomotion (Whittle, 2002). This section explains main features of the gait relevant for structural engineering applications. In this context, the focus is placed on the role of different body parts in walking phases, the waveform of corresponding trajectory of BCoM, and, most importantly, the development of GRF throughout a typical gait cycle (GC).

During walking, the human body can be divided into two parts: passenger unit and locomotor unit (Perry and Burnfield, 2010). The passenger unit consists of the upper body segments, which include head, arms and trunk (HAT). This unit is carried by the lower body and it does not directly contribute to the walking process. It is the locomotor unit, containing thighs, shanks and feet, that plays an important role in the human movement. Therefore in a GC, all gait events are related to the movement of the lower body, especially the two feet. A GC can be defined as the duration between any two nominally similar gait events, such as the cycle starting with a heel strike of one foot and ending with a heel strike of the same foot. Therefore, a GC consists of two consecutive steps.

Each GC is separated into two distinct phases: stance and swing phases. Stance phase of one leg is defined as the duration of the leg contact with the ground, while the swing phase is the duration of the airborne phase of the same leg. Both stance and swing phases can be further subdivided into left and right ones. Besides stance and swing phases, a GC can also be divided into single support phase (SSP) and double support phase (DSP). The SSP is the duration when one foot is in contact with the ground and the other foot is in the swing phase, while the DSP happens when both feet make ground contact simultaneously. SSP and DSP occur consecutively in a GC, of which each phase appears twice. All walking phases, BCoM's trajectory and time history of GRF throughout a GC are illustrated in Figure 2.7 (based on Inman et al., 1989). The letters "R" and "L" in the figure indicate right and left legs, respectively.

Walking phases and functions of body segments' joints are detailed in Ayyappa (1997) and Perry and Burnfield (2010). Based on their work, description of a GC is summarised as follows. Considering the heel strike of the right leg as the starting event, the GC starts with the initial DSP and at the same time the right stance phase. The right foot makes initial contact (IC, lasting from 0 % to 2 % of the duration of the GC), during which the right knee is close to full extension and the leg is nearly straight. The abrupt drop of the foot to the ground generates a brief peak in the time history of GRF called the heel strike transient. Body weight starts transferring to the ground through the right heel.

After completion of the IC, the GRF time history enters the loading response (LR, 2–12 % of the GC) phase. During LR, the rapid transfer of

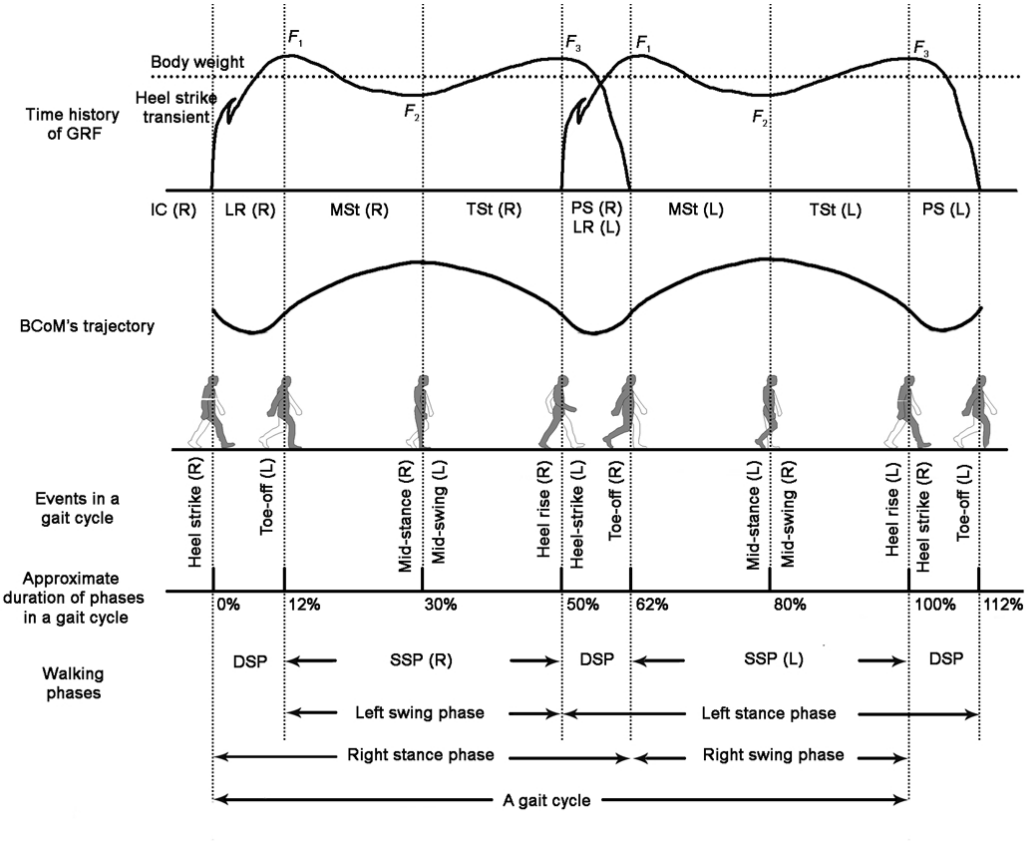

Figure 2.7: Ground reaction force, trajectory of body centre of mass and events of a gait cycle (based on Inman et al., 1989).

body weight to the right leg hinders the extended posture of the knee, which initiates knee flexion. As the result of this effect, BCoM starts descending and comes to the lowest point at approximately half way through the LR/DSP. The bony segment between the heel and the ankle joint of the right foot (also known as the heel rocker) acts as a lever arm, in which forward momentum of the leg drives the forefoot to the ground. The GRF builds up along with an increase of contact area of the right foot. On the contrary, the left foot prepares to lift off the ground, and it pushes against the ground to move the pedestrian forward. The push of the left foot contributes to the increase of

BCoM's elevation in the second half of the DSP. By the end of the LR, the GRF of the right leg reaches the first peak at F_1 while that force induced by the left leg decreases to zero, and BCoM is at nominally the same elevation as at the beginning of the DSP. Meanwhile, the right knee is at the maximum flexion and the right foot is approximately in full contact with the ground. The DSP ends with the toe-off event of the left leg and the GC enters the SSP.

In the SSP (approximately 40 % of a GC), only the right leg is in contact with the ground, while the left leg enters the swing phase. As soon as the left foot loses contact with the ground, the time history of GRF only consists of the right leg's reaction. The duration from the beginning to about the middle of a SSP is called the midstance (MSt, 12–31 % of the GC). During the MSt, the right foot is relatively stationary. Due to the momentum of forward advancement, the body moves from behind to in front of the ankle joint axis (often referred as the ankle rocker). At the same time, the knee-flexion keeps decreasing since the stability during stance phase is at its optimum when the knee is in extension. The swinging momentum of the left leg also plays a role in extending the right knee. As a consequence of the knee's extension, BCoM's elevation continues to increase. On the contrary, the amplitude of GRF decreases because of the upward momentum of the swinging leg. By the end of the MSt, the magnitude of GRF descends to its lowest point, F_2, in the SSP while BCoM reaches its maximum in a GC. While the right leg is at MSt, the left leg is in its swing phase, in which the knee flexion increases in the beginning of the phase. Once the left leg passes the right leg in the sagittal plane, there is a rapid knee extension so that the pedestrian can achieve a certain step length.

After the MSt, the GC enters the next stage called the terminal stance (TSt, 31–50 % of the GC). This phase completes the SSP of the right leg and the swing phase of the left leg. The event that initiates TSt is the heel rise of the right foot. The entire body makes a forward fall over the bony segment of the forefoot, acting as the forefoot rocker. In the meantime, the right knee reaches the state of full extension. It is the full extension of the knee that makes the falling-forward movement of BCoM relatively similar to the trajectory of an inverted pendulum. The TSt of the right leg is equivalent to the terminal swing of the left leg. To prepare for the stance phase of the left leg, the left knee is in full extension. By the end of the TSt, GRF of the right leg reaches the second peak at F_3. TSt ends when the swing leg makes first contact with the ground. The SSP ends and the GC enters the second DSP in a GC.

Right after TSt is the pre-swing (PS, 50–62 % of the GC) phase of the right leg. This phase is equivalent to the IC and the LR of the left leg, the BCoM, therefore, experiences the same trajectory pattern as explained earlier in relation to the right leg. The body weight is transferred from the right leg to the left leg, indicating in the rapid decrease and build up in GRF of the right and left legs, respectively. To prepare for the swing phase, the right knee experiences significant flexion. Meanwhile, the right foot pushes the ground through metatarsal heads and toes (known as toe rocker) to progress the limb forward. The PS phase ends with the toe-off event, which is also the terminal event of the stance phase of the right leg. The rest of the GC (62–100 %) is the SSP of the left leg (similar to that of the right leg) and the swing phase of the right leg (similar to that of the left leg). The GC ends with the heel strike event of the right foot.

Through the presentation of all walking phases in a GC, three important aspects of a walking gait can be summarised. First, the movement of BCoM can be approximately described as continuous arcs (Figure 2.7). This approximation is relatively good during the SSP, which is the reason why the walking gait is often modelled as an inverted pendulum. However, under the influences of knee and ankle flexion, the transition from one arc to another is smoother than the movement of the pendulum model (Saunders et al., 1953). The total vertical excursion, calculated as difference between maximum and minimum elevations of BCoM, is reported by different researchers to be 2–6 cm (Whittle, 1997; Gard et al., 2004). Second, during the stance phase of one leg, the foot acts with four functional rockers: heel, ankle, forefoot and toe rocker. These rockers not only maintain the stability of the gait, but also assist the forward progression of the limb (Perry and Burnfield, 2010). Third, the time history of the force generated by one leg follows the M-shape with two peaks occurring approximately at the beginning and at the end of the SSP. At the normal walking speed, the peaks are about 110 % of the body weight while the trough, approximately at the middle of the SSP, is about 80 % of the body weight (Perry and Burnfield, 2010).

All of these observations are important components in the development of a walking model that can genuinely replicate the key features of the human gait.

2.3.2 Spectrum of ground reaction force

It is often beneficial to convert the time history of GRF into the frequency domain, especially when assessing vibration serviceability of footbridges. A comprehensive study of DLF recorded approximately 1,000 footfall (Kerr, 1998). The study shows that DLF of the first harmonic tends to increase with an increase in the pacing rate (Figure 2.8a). Depending on the pacing rate, it is able to achieve the first DLF up to about 0.65. DLF_1 can also be estimated using the empirical equation as follows (Kerr, 1998):

$$\mathrm{DLF}_1 = -0.265 f_\mathrm{p}^3 + 1.321 f_\mathrm{p}^2 - 1.760 f_\mathrm{p} + 0.761 \tag{2.2}$$

where f_p is the pacing rate.

An example of spectrum of GRF generated by walking at 1.95 Hz is shown in Figure 2.8b. The data show that the first harmonic is dominant and there is dissipation of energy around main harmonics. This energy dissipation reflects the narrow-band nature of the walking process (Živanović et al., 2005b).

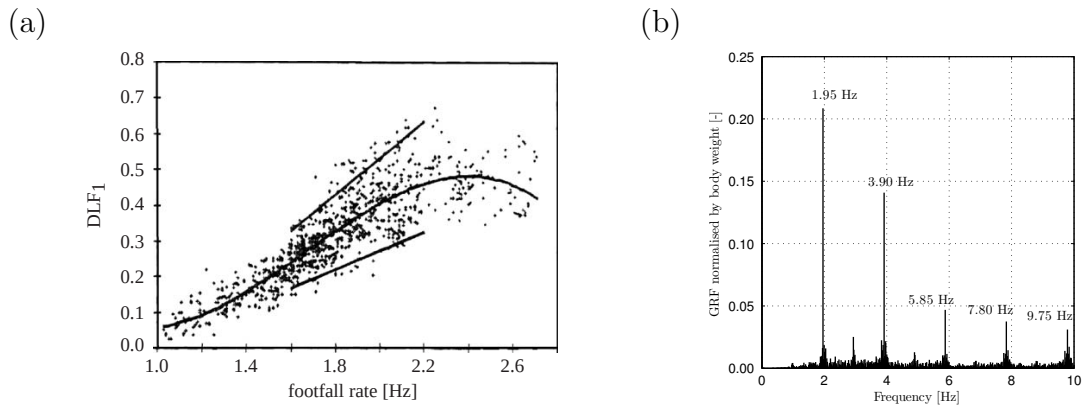

Figure 2.8: (a) Dynamic loading factor of first harmonic of walking (after Kerr, 1998) and **(b)** a spectrum of ground reaction force.

2.3.3 Energy in walking gait

As the human body progresses forward, BCoM moves up and down. The total energy of a person during walking can be split into potential and kinetic energy. The potential energy is stored in the elevation of BCoM and also in the body parts being lengthened and shortened during locomotion. On the other hand, the kinetic energy is the energy of BCoM with respect to its motion.

During a GC, BCoM has the lowest forward velocity when reaching the highest position at around midstance (Gard and Childress, 2001). On the contrary, BCoM achieves the maximum forward velocity when descending to the lowest position during the DSP. In this fluctuation of BCoM, potential and kinetic energies are continuously interchanged.

If the human body is an efficient machine, the kinetic and potential energy would be converted to each other and the total energy would be conserved (Saunders et al., 1953). However, as humans dissipate energy during locomotion, part of this total energy is lost throughout the process. Cavagna et al. (1976) introduced recovery level as the percentage of energy restored after a walking step. During normal walking (velocity around 5.0 km/hour, i.e. 1.4 m/s), the level of recovery was found to be about 50–70 %. The energy lost must be compensated by "external" work that the muscle generates to maintain a stable walking gait (Cavagna et al., 1976).

2.3.4 Gait parameters

Gait parameters can be divided into spatial and temporal parameters. Spatial parameters are the left and right step lengths and the step width, while

temporal parameters are all parameters related to time, such as walking speed and cadence (Vaughan et al., 1999).

Spatial parameters are illustrated in Figure 2.9. A stride length is the distance that a person travels during a GC. Similar to the definition of a GC, the stride length can be measured as the distance between any two nominally similar gait events, such as the distance between the location of heel strike of one foot to that of the same foot (Vaughan et al., 1999). Another spatial parameter is the step length, d, which is the distance between two identical events of different legs. When the gait is assumed to be symmetrical, it can be said that a step length is equal to half of a stride length.

Walking speed v is a temporal parameter indicating the distance travelled in a given time. When the direction of walking is known, the term walking velocity is often used (Whittle, 2002). Often in literature, the term free-walking is used to describe the most comfortable walking speed for a particular person, while slow and fast walking describe walking at speeds that are lower or greater than the comfortable speed, respectively. Another temporal parameter is cadence, which is a number of steps in given time, commonly presented as steps per minute. To be compatible to the Sistemé International units, cadence is

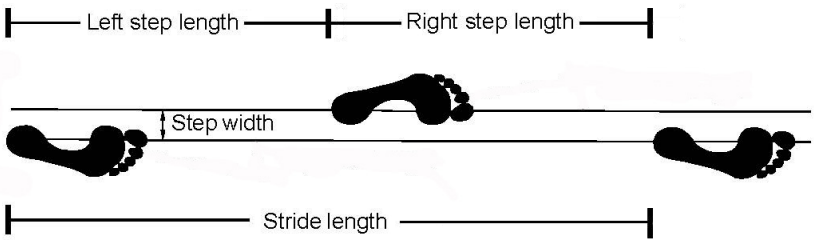

Figure 2.9: Spatial parameters in a gait cycle (after Vaughan et al., 1999).

often expressed as number of cycles per second (or Hertz, Hz), and it is also known as pacing rate or walking frequency, f_{p}. The pacing rate, walking speed and step length are interrelated by the relationship: $v = f_{\mathrm{p}}d$.

In a recent study, pacing rate, walking speed and step length for over 2,000 people was monitored on a footbridge (Živanović, 2012). It was found that the normal distribution seems to be a good approximation for all three parameters (shown in Figure 2.10). The means ± standard deviation for these distributions are 1.87 ± 0.19 Hz for pacing rate, 1.39 ± 0.20 m/s for walking speed and 0.74 ± 0.08 m for step length. With regard to step width, Owings and Grabiner (2004) reported the mean ± standard deviation as 10.2 ± 2.7 cm.

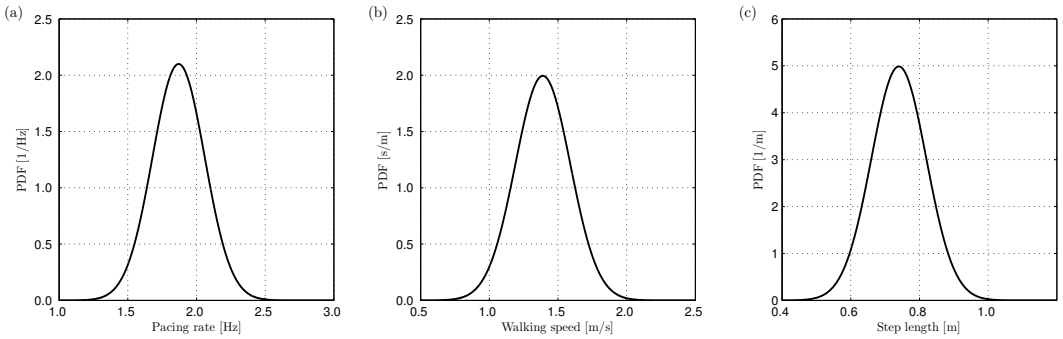

Figure 2.10: Probability density functions (PDF) for **(a)** pacing rate, **(b)** walking speed and **(c)** step length (after Živanović, 2012).

2.3.5 Criteria for a walking model to simulate pedestrian-structure dynamic interaction

The information about non-pathological gait typical for walking on a rigid surface provided so far will be used to evaluate different walking models for studying PSDI. For a model to be selected for PSDI studies, three criteria (hereafter referred to as Criterion 1, 2 and 3) need to be satisfied. These criteria are:

- **Criterion 1**: the model should be able to replicate the normal walking gait of a pedestrian, i.e. it should produce the walking phases and trajectory of BCoM which are in accordance with the literature.
- **Criterion 2**: the model should be able to generate the realistic range of kinematic parameters, e.g. pacing rate and walking speed.
- **Criterion 3**: the model should produce a genuine form of GRF on rigid surface in terms of both the shape of the time domain waveform and the amplitude of the frequency spectrum.

2.4 Review of bipedal walking models

The research on locomotion was motivated partly by the curiosity about its mechanic (McGeer, 1990). Throughout the history, many walking models were developed to replicate the walking mechanism. Most of the existing models are based on the observations of major determinants of walking gait: (1) pelvic rotation, (2) pelvic tilt, (3) knee flexion, (4) foot mechanism, (5) knee mechanisms and (6) lateral displacement of pelvis (Saunders et al., 1953). Since this study is limited to the investigation of walking gait in the sagittal plane, the first and sixth determinants can be neglected.

Bipedal walking models were firstly developed to distinguish between the normal and pathological gait for the medical purpose (Saunders et al., 1953). Later, the walking locomotion has been studied in various fields, such as biomechanics, animated image processing and robotics. The following sections review six bipedal models in order of increased complexity level as shown in Figure 2.11. The reviews in this chapter are related to descriptions of general

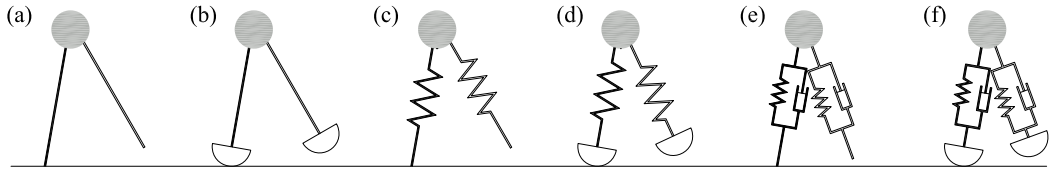

Figure 2.11: Bipedal walking models: **(a)** inverted pendulum (after Saunders et al., 1953), **(b)** rocker foot (after Gard and Childress, 2001), **(c)** spring mass (after Geyer, 2005), **(d)** spring mass with rocker foot (after Whittington and Thelen, 2009), **(e)** spring mass with damper (after Qin et al., 2013), **(f)** spring mass with rocker foot and damper (after Kim and Park, 2011).

features. Detailed simulations and evaluations of some representative models against criteria listed in Section 2.3.5 are performed in Chapter 3.

2.4.1 Inverted pendulum model

Inverted pendulum model (IPM) is the simplest bipedal walking model in literature, which was firstly introduced by Saunders et al. (1953). The model consists of a point mass representing BCoM and two legs that are rigid, straight and massless (Figure 2.12).

The development of the IPM is based on a number of simplifications of the walking gait. First, the mass of all body segments is lumped to BCoM, m_{p}. As a result, the human locomotion can be represented by the movement of a single point. In this way, the contribution of the upper body to the pedestrian kinematics is neglected since it is the passenger unit (Perry and Burnfield, 2010). Second, the human body is assumed to be symmetrical thus the properties of two legs are identical, which is reasonable for the study of non-pathological gait. Third, the human foot is represented as a point foot, i.e. the whole geometry of the foot is lumped into a single point. Fourth, the

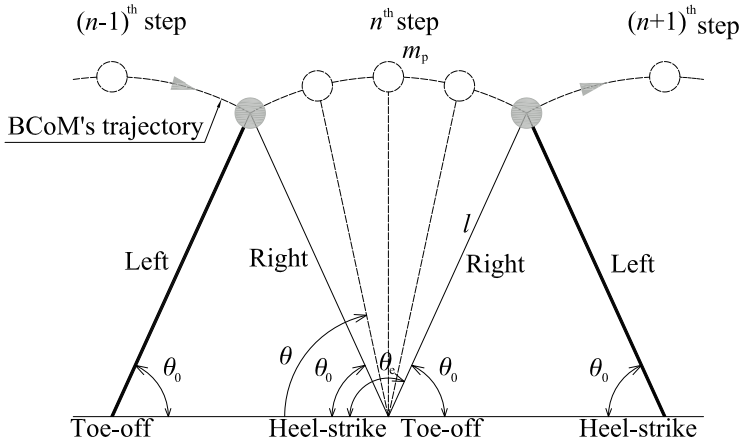

Figure 2.12: Inverted pendulum model.

point foot does not slip during contact with the ground.

A walking cycle of the IPM starts when one leg touches the ground and it is characterised by initial conditions in the form of attack angle θ_0 (Figure 2.12) and initial angular speed $\dot{\theta_0}$. As a consequence, mass m_p vaults over the ground about the point of foot placement.

By the end of each step, there are two assumptions for the step transition process. First, the swinging leg is directed to the new position with the attack angle θ_0. From the geometry constrains it follows that the angle marking the toe-off event at the end of a step is: $\theta_\mathrm{e} = \pi - \theta_0$ (Figure 2.12). Second, a mechanism must be provided to redirect the BCoM, having the momentum of falling downwards at the end of each step, to the next step. One option to address this issue is to provide m_p with an upward impulse to imitate the effect of a heel strike (Bocian et al., 2013). An alternative method of maintaining the walking cycle is to place the model on a downhill slope, in which case gravity and inertia forces can generate a stable locomotion pattern without addition of external energy (McGeer, 1990). However, this option is not suitable for

structural engineering applications since the walking surface could be either flat or tilted in either directions.

Because of the simplifications of the model, the trajectory of BCoM forms a perfect arc with the radius equal to the leg length (Figure 2.12), which is not corresponding with data shown in Figure 2.7. Consequently, the IPM overestimates the total vertical excursion of BCoM in a step (Lee and Farley, 1998). Despite this shortcoming, the IPM can depict quite well the pattern of BCoM's movement in the single stance phase. The IPM is, however, not capable of modelling the double support phase, during which the human weight is transferred from one leg to another.

Within any step, potential and kinetic energies are continuously interchanged. Because there is no friction or loss of energy, the total energy of BCoM is conserved.

Overall, the simplicity of the IPM contains both advantages and disadvantages. While it is evident that the model cannot genuinely replicate all features of the human locomotion, the model might still be a good candidate for the investigation of PSDI due to its simplicity. Besides, studying the IPM can also help understanding the evolution of bipedal models.

2.4.2 Rocker foot model

It was shown in Section 2.4.1 that the IPM overestimates the vertical excursion of BCoM and cannot accurately replicate the human-like gait. The shortcomings are due to the negligence of several determinants of the walking gait (Saunders et al., 1953). To address this issue, the IPM must be upgraded

to accommodate more gait determinants. It was found that pelvic tilt and knee flexion (the second and third determinants) have little or no effects in the reduction of the total vertical excursion of BCoM (Gard and Childress, 1997, 1999). On the other hand, foot and ankle mechanisms (the fourth and fifth determinants) seems to be more important, suggesting that the assumption of point foot of the IPM is not appropriate. Based on this observation, Hansen et al. (2000) developed the rocker foot model (RFM) shown in Figure 2.13.

A new feature that the RFM introduces is the non-deformable rocker foot with radius r (Figure 2.13). The presence of the rocker leads to several improvements compared with the IPM. The introduction of the rocker is equivalent to lengthening the physical length of the leg in the IPM (Hansen et al., 2000). Although the trajectory of BCoM in the RFM still follows the pattern of continuous arcs, the effective lengthening of the RFM decreases the total excursion of BCoM when compared to the IPM (with comparable parameters). In addition, the introduction of the rocker reflects the walking

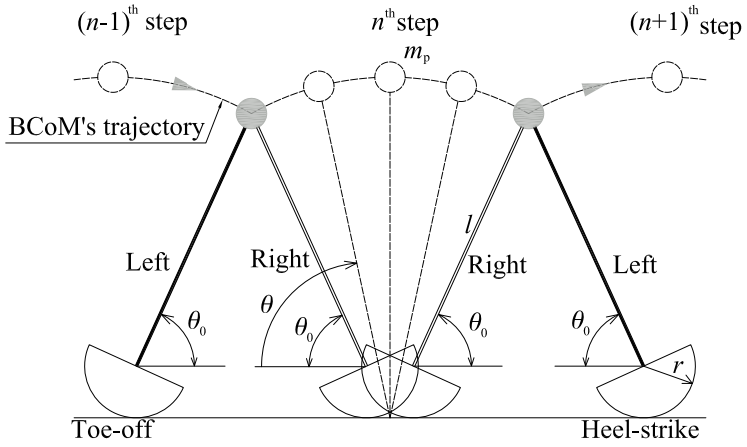

Figure 2.13: Rocker foot model.

mechanism during stance phase more accurately. As described in Section 2.3.1, the foot rockers assist humans in progressing forward. The design of the rocker in the RFM in form of one arc is an approximation of the actual foot rocker. Finally, while the centre of pressure (CoP) in the IPM is unnaturally fixed to one point, there is a more natural transition of CoP during the walking cycle in the RFM. The position of CoP progresses from "heel" to "toe" as the foot rolls forward. This CoP progression contributes to the reduction of BCoM's excursion in comparison with that of the IPM (Lee and Farley, 1998).

Apart from these improvements, the RFM inherits the remaining features of the IPM. It should be noticed that the RFM was initially developed for medical purpose to match the excursion of BCoM with experimental data (Hansen et al., 2000). Therefore, it was not developed to address all the shortcomings of the IPM. Some remaining drawbacks are: the model represents the single support phase only, the BCoM's trajectory deviates from the experimentally observed data, and the model requires an external source of power to maintain stable walking cycle.

In summary, the RFM is a slight upgrade of the IPM which opens new opportunities for the development of other bipedal models.

2.4.3 Spring mass model

From the observation that the vertical excursion of BCoM in the IPM overestimates the actual excursion observed in experiments, it is recognised that the leg does not stay rigid during the stance phase (Lee and Farley, 1998). Therefore, to simulate more realistic walking gait, flexibility of the leg has

to be accommodated. For this purpose, the spring mass model (SMM) was introduced. The model was initially used to simulate running and hopping activities (Blicknan, 1989). Later, it was found that the SMM can also be applied for modelling the walking gait, unifying both walking and running gait patterns into a simple model (Geyer, 2005).

The SMM is illustrated in Figure 2.14. The SMM consists of a mass m_{p} on top of massless legs, acting as two identical springs with constant stiffness k. The springs are released to the full length, l_0, in the swing phase and compressed during the stance phase.

It is assumed that a walking step of the SMM starts when BCoM is at the apex of, say, left leg's stance phase (Figure 2.14a). This leg is compressed and has the length $l_1 < l_0$. At the same time, the right leg is in the swing phase, preparing to hit the ground with the attack angle θ_0. As the right leg makes contact with the ground (Figure 2.14b), the SMM enters the double support phase. During this phase, the load of BCoM starts transferring from the left to

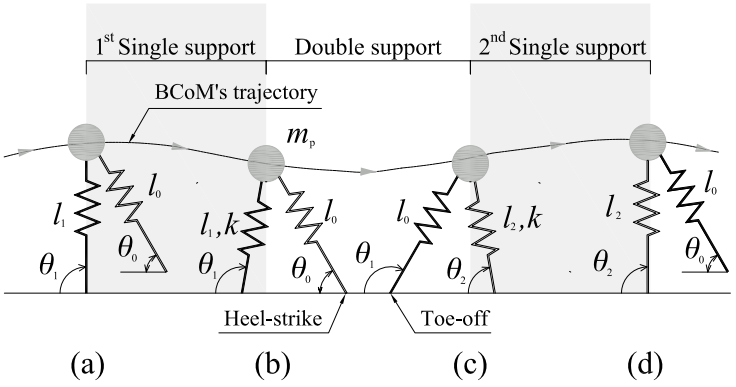

Figure 2.14: Spring mass model (after Geyer, 2005). **(a)** Start of simulation, **(b)** heel-strike event of the leading leg, **(c)** toe-off event of the trailing leg and **(d)** end of a walking step.

the right leg. As a result, the right leg is gradually compressed, while the left leg is gradually unloaded. By the end of the double support phase, the left leg returns to the full length l_0 and prepares for its swing phase (Figure 2.14c). At the time instant when the left leg lifts off the ground (toe-off event), the SMM enters the single support phase of the right leg. The next step cycle starts again when BCoM reaches its apex (Figure 2.14d). Overall, the description of one walking step shows that the SMM has the capability of representing all phases of the walking gait.

The novel feature of the SMM is the introduction of spring-like legs. The springs not only account for actual changes of leg lengths during walking, but they also absorb energy throughout the walking cycle. The total energy of this model is the sum of potential energy (consisting of energy defined by BCoM's elevation and restoring energy in the springs) and kinetic energy (related to BCoM's motion). With the availability of the springs, the two types of energy are continuously interchanged, keeping the total energy of the system conserved. Unlike the IPM and the RFM, the SMM, once exposed to initial conditions, is set into motion without the need of any external power source.

Figure 2.15 shows two examples of GRF of one leg generated by the SMM (Geyer, 2005), where the typical M-shape of GRF can be produced. The ability of the SMM to reproduce the frequency content of the GRF accurately was beyond the scope of Geyer's study and therefore was not discussed. This feature of the model will be elaborated on Chapter 3.

Overall, the SMM still inherits a shortcoming from the IPM in the form of a point foot. Although this assumption makes calculations simpler, it does

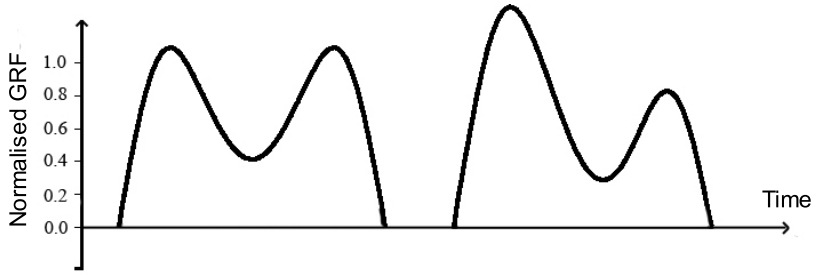

Figure 2.15: Two ground reaction force patterns produced by the spring mass model (after Geyer, 2005).

not replicate the true walking mechanism of humans as commented in the review of the RFM (Section 2.4.2).

2.4.4 Spring mass with rocker foot model

As the RFM fails to provide a correct force pattern due to the rigid leg assumption and the SMM still inherits the shortcoming of point foot, introducing a new model that combines the RFM and SMM might be a desired solution. The spring mass with rocker foot model (SMRFM) has all the characteristics and assumptions as the SMM except that instead of point foot, the base of each leg is modelled using a massless rocker foot (Whittington and Thelen, 2009). It is this new feature that allows the CoP to progress during the stance phase, and therefore to overcome the shortcoming of the SMM. Similar to the RFM, the rocker foot has a certain radius r, as shown in Figure 2.16.

Similar to the SMM, the SMRFM can be used to describe the three phases of a walking step, illustrated in Figure 2.16. Each step cycle starts from the upright position of one limb (say, the left leg), while the right leg has a predefined attack angle θ_0. Both limbs have an equal stiffness k. The model comes to the next phase when the trailing right limb hits the ground, and

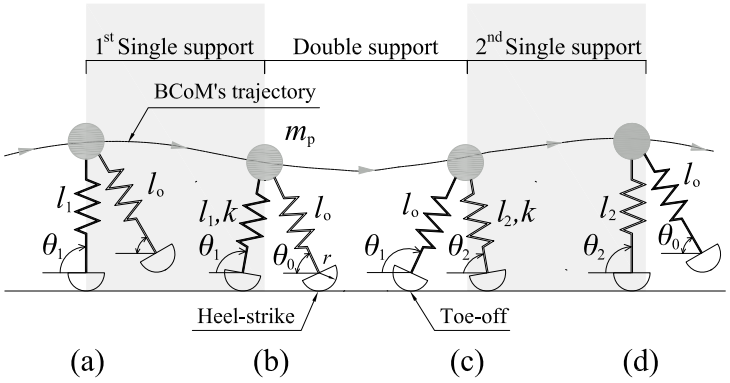

Figure 2.16: Spring mass with rocker foot model (after Whittington and Thelen, 2009). **(a)** Start of simulation, **(b)** heel-strike event of the leading leg, **(c)** toe-off event of the trailing leg and **(d)** end of a walking step.

shifts to the last phase when the left leg takes off. A step cycle is considered finished when the right limb reaches the upright position. Possessing the same advantages as the SMM, this model can explain well the kinematics of walking of BCoM. Also, the SMRFM can operate without the need for an external power source.

It can be shown that by varying the model parameters (θ_0 and k), the SMRFM can represent people walking with different step length, walking speed and pacing rate, as well as generate different GRF patterns (Whittington and Thelen, 2009). Selection of suitable combinations of parameters gives opportunity to reproduce range of walking gait with characteristics seen in experimental data.

Similar to the RFM, use of the rocker allows for progression of CoP during simulation in the SMRFM. This progression, expressed in terms of CoP excursion, has an almost linear dependency on the radius of rocker (Figure 2.17a, after Whittington and Thelen, 2009). Although increasing computa-

tional efforts, the rocker feature of the SMRFM reflects closely the walking pattern of humans. It should also be noticed that the rocker radius is within a reasonable range of human foot lengths. Moreover, the progression of CoP reduces the peaks in walking forces, making them comparable with experimental data. Figure 2.17b shows different shapes of GRF generated by one leg under a range of rocker radii (Whittington and Thelen, 2009). When the radius ranges from 0.2 m to 0.3 m, the shapes replicate quite well the GRF induced by humans in the time domain. Similar to SMM, the quality of GRF in the frequency domain of the SMRFM is not investigated in the literature.

Overall, the SMRFM is a bipedal model that combines positive features from the RFM and the SMM. The downside is that the model requires significant computational effort, due to double and single support phases being characterised by different set of equations and the incorporation of the rocker feet.

(a) (b)

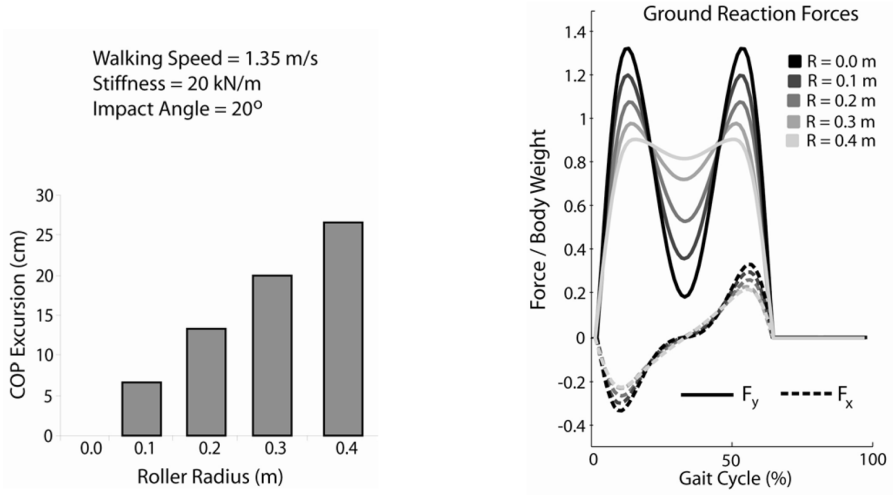

Figure 2.17: Effects of rocker in **(a)** centre of pressure progression and **(b)** ground reaction forces (after Whittington and Thelen, 2009).

2.4.5 Bipedal walking models with dampers

Since the SMM and the SMRFM have compliant (i.e. spring) legs, they do not require a continuous power supply. However, this feature is in contrast with the finding of Cavagna et al. (1976), who stated that "external" work must be done to compensate for the energy lost during locomotion. Their research suggests that there must be a damping mechanism in the human body. It is, therefore, reasonable to introduce dampers in a bipedal model. Recently, two bipedal models of this kind emerged: spring mass with damper model (SMDM, Qin et al., 2013) and spring mass with rocker foot and damper model (SMRFDM, Kim and Park, 2011). The two models are shown in Figure 2.18.

Both SMDM and SMRFDM represent the damping potential of each leg by damping constant c. Both models seem to be able to replicate realistic patterns of GRF forces (Kim and Park, 2011; Qin et al., 2013). Detailed parametric study of the SMDM was not available, while a database of the stiffness and damping parameters that can replicate realistic walking gait of humans was provided by Kim and Park (2011). Figure 2.19 shows the dependency of these parameters on the walking speed. The spring stiffness normalised by weight to height ratio was 50–75, while the damping ratio for each leg was

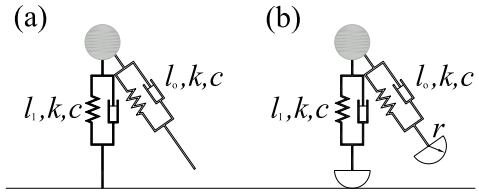

Figure 2.18: **(a)** Spring mass with damper model (after Qin et al., 2013) and **(b)** spring mass with rocker foot and damper model (after Kim and Park, 2011).

found to be 2–7 %. For an average person has body weight of 760 N and height of 1.68 m (NHS, 2010), the spring constant was in the range from 22 kN/m to 34 kN/m, while the damping coefficient was 50–230 Ns/m.

For a small damping constant, the two models can still produce relatively steady-state walking gait. To achieve stable solutions in long simulations, both models must be continuously provided with a power supply, which imitates the positive work of muscles. A method, which was suggested by Kim and Park (2011) and later developed by Qin et al. (2013), is to apply a time-dependent control force that acts on the system so that the total energy remains constant.

In general, the introduction of dampers makes the SMDM and the SM-RFDM seem to be able to replicate the walking mechanism seen in humans. Both models show that realistic walking parameters can be achieved with suitable combination of model parameters. However, it should be noted that the increased level of complexity makes these models more computationally demanding, and their advantages, if any, over the simpler bipedal models are still to be identified.

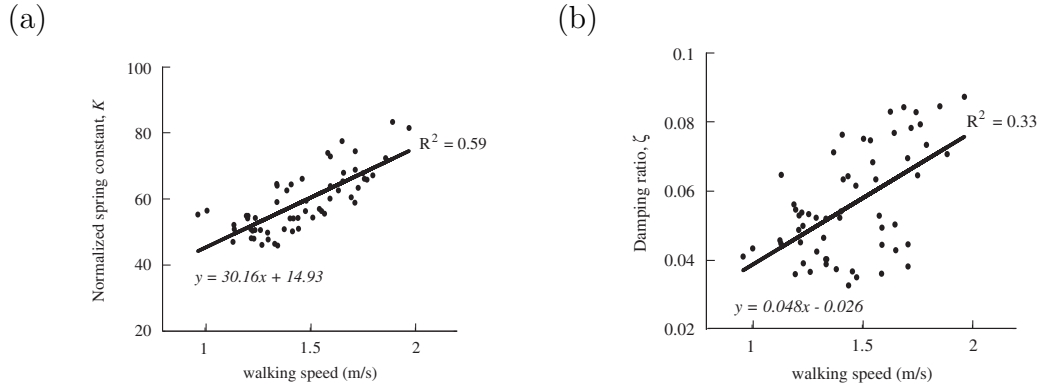

Figure 2.19: (a) Normalised spring constant and **(b)** damping ratio of the spring mass with rocker foot and damper model (after Kim and Park, 2011).

2.5 Conclusions

This chapter reviewed the current knowledge of PSDI in literature. In some experimental observations, the PSDI was seen either through the changes in dynamic properties of structures or alteration in the walking forces. It was usually commented that the existence of PSDI in the vertical direction could lead to significant errors in estimation of the vibration response of the structure. However, these observations were incomplete and usually of qualitative nature.

The pedestrian loading models used in current design practice neglect PSDI. To address this shortcoming, a novel approach of establishing an interactive model between the pedestrian and the structure is needed. This chapter reviewed three recent approaches for modelling PSDI. It was found that representing a pedestrian as a bipedal model has the potential to replicate key features of the human walking mechanism.

Before addressing PSDI, it is crucial to have a firm understanding of the human walking gait. This chapter reviewed the important properties of the walking gait. Phases in the gait cycle, BCoM's trajectory, GRF in the time and frequency domains and gait parameters have been reviewed and their ranges have been presented. These details will be required in the evaluation of simulations of different bipedal walking models in Chapter 3.

Identifying bipedal walking models as most suitable for PSDI studies, six models were described in Section 2.4, ranging from the simplest (inverted pendulum) to the most complex model (spring mass with rocker foot and damper). Each model has its own advantages and disadvantages. The IPM is the most

primitive model that can replicate relatively well the single stance phase of walking locomotion. Studying the IPM is helpful for understanding of more complex models, despite the tendency to overestimate the vertical excursion of BCoM. To address this shortcoming, the rocker-foot feature is introduced in the RFM. However, this model maintains the assumption of rigid legs, and therefore it is unable to replicate actual kinematics of the walking process. For this issue, the introduction of spring-like legs is a natural step forward. This feature is introduced in both the SMM and the SMRFM. The latter model has benefits of more genuine representation of the BCoM excursion and progression of the CoP during walking due to the presence of the rockers. To account for the damping effect of the legs, SMDM and SMRFDM are developed. The capacity to describe loss of energy during walking cycle, however, does not justify use of these models when their advantages over other simpler bipedal models are not yet clear.

It should be noted that the reviewed models in this chapter are taken from various fields. As a result, not all the information relevant to applications in structural engineering was available. It is, therefore, not possible at this stage to fully evaluate suitability of the bipedal models for the study of PSDI. The next chapter will present quantitative calculations of three representative models, and it will critically evaluate them against the criteria identified in Section 2.3.5. The selection of a model for further study will inevitably be a trade-off between ability of the model to reproduce experimental data and the required computational effort.

Chapter 3

Performance of bipedal models on rigid surface

3.1 Introduction

In Chapter 2, six bipedal walking models were reviewed qualitatively. However, not all information relevant for the applications of structural engineering was properly addressed in literature. This chapter, therefore, will review three bipedal walking models in detail. These are the inverted pendulum model, the rocker foot model and the spring mass model. These three models are chosen due to their simplicity and expectation that understanding these model better would facilitate future developments of pedestrian modelling in structure engineering.

Description and ranges of input parameters for each model are provided first, followed by examples of simulation results and parametric study. Finally, the suitability of each model for representing interaction between pedestrian and structure is critically evaluated and discussed using three criteria presented in Section 2.3.5.

3.2 Inverted pendulum model

Inverted pendulum model (IPM) is the simplest bipedal model reviewed in Chapter 2. The analysis of this model not only helps to evaluate suitability of the model for structural engineering purposes but also sets foundations for analysing other bipedal models.

3.2.1 Model description

The IPM is shown in Figure 3.1. Using the Lagrangian approach (Goldstein, 1980), the equation of motion of the model can be written as follows (Appendix A.1):

$$\ddot{\theta} = \frac{\cos\theta}{l} g \tag{3.1}$$

where θ is the angle between the leg and the ground, $\ddot{\theta}$ is the second derivative of θ, l is the distance from the pedestrian mass m_{p} to the foot, hereafter referred to as the pendulum length (Figure 3.1), and g is the acceleration of gravity

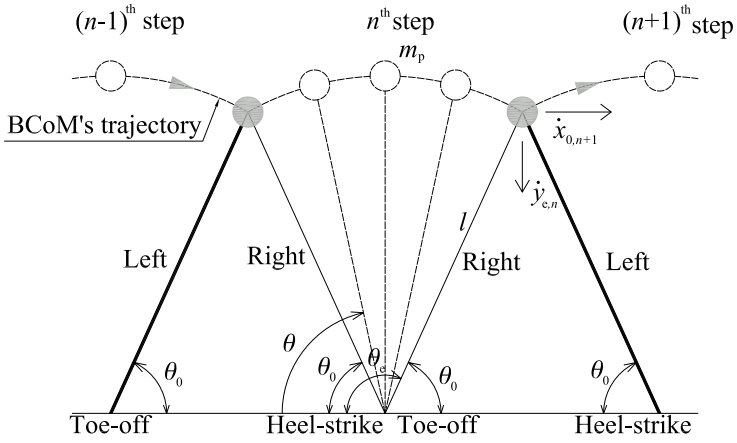

Figure 3.1: Parameters of inverted pendulum model.

($g = -9.81\,\mathrm{m/s^2}$). Equation 3.1 describes the stance phase of one leg only since the IPM neglects the double support phase (Chapter 2). All derivatives in this chapter are calculated with respect to time.

Within a step, the GRF generated by the IPM is:

$$F_\mathrm{p} = -m_\mathrm{p}(g\sin^2\theta + l\dot{\theta}^2\sin\theta) \tag{3.2}$$

where $\dot{\theta}$ is the first derivative of θ.

At the beginning of the next step, the swinging leg touches the ground at an angle called the attack angle θ_0. From the geometry constrain of the model, it follows that angle θ_e marking the toe-off event at the end of the previous step is (Figure 3.1):

$$\theta_\mathrm{e} = \pi - \theta_0 \tag{3.3}$$

At the end of each step, m_p has the momentum of falling downwards. To start the next step, an upward impulse can be provided to m_p. The amplitude of this vertical upward impulse at the end of the n^th step, I_n, is (Bocian et al., 2013):

$$I_n = -m_\mathrm{p}\dot{y}_{\mathrm{e},n} + m_\mathrm{p}\dot{x}_{0,n+1}\cot\theta_0 \tag{3.4}$$

where $\dot{y}_{\mathrm{e},n}$ is the vertical speed of m_p by the end of the n^th step while $\dot{x}_{0,n+1}$ is the forward speed at the beginning of the $(n+1)^\mathrm{th}$ step (Figure 3.1).

3.2.2 Input parameters

To perform simulations of the IPM, two sets of input parameters are required: model parameters and initial conditions. The model parameters of the IPM consist of pedestrian mass and the pendulum length. The body mass of 77.5±17.2 kg (mean ± standard deviation) and height of 1.676±0.097 m of an average person are chosen as representative values in this chapter (NHS, 2010). The body height can be used to calculate the physical leg length, in this case being 0.864±0.050 m (Pheasant, 1982). This value is increased by 20 % to estimate the pendulum length of 1.037±0.060 m (Hof et al., 2005).

Initial conditions required by the model are θ_0 and $\dot{\theta}_0$. The attack angle θ_0 is chosen between 65° and 80°, which covers the measured range reported by Geyer (2005). On the other hand, $\dot{\theta}_0$ can be replaced by the initial forward speed $\dot{x}_0$ via the relationship:

$$\dot{\theta}_0 = \frac{\dot{x}_0}{l \sin \theta_0} \tag{3.5}$$

The range of initial forward speed $\dot{x}_0$ is set between 1.0 m/s and 2.5 m/s. The parametric scan in Section 3.2.4 will investigate if this chosen range of $\dot{x}_0$, together with the range of θ_0 (65–80°), can provide realistic ranges of gait parameters.

In normal conditions, walking can be considered as a repetitive activity. As a result, it is assumed that the initial conditions of the IPM are the same at the beginning of each step. This assumption will be revisited later in this thesis. The assumption of repetitive initial conditions applies to simulations of all other bipedal models reviewed in this chapter.

3.2.3 Simulation results

Solver *ode45*, from MATLAB library that utilises the Runge-Kutta integration method with variable step size (Mathworks Inc., 2010), is used to solve Equation 3.1. The maximum time step of the solver is set at 10^{-3} s while the absolute and relative error tolerances are set at 10^{-6}.

An example of the GRF generated by the model for input values of $m_\mathrm{p} = 77.5\,\mathrm{kg}$, $l = 1.037\,\mathrm{m}$, $\theta_0 = 69°$ and $\dot{x}_0 = 1.61\,\mathrm{m/s}$ is shown in Figure 3.2a. The input parameters of the model are chosen so that it results in the pacing rate of 1.87 Hz and the average walking speed of 1.39 m/s, which correspond to mean values measured on an as-built bridge (Živanović, 2012). The arches in the figure represent the inertia force due to pedestrian mass m_p while the vertical lines represent the externally applied impulses. Duration of each impulse in the simulation is chosen to be about 1 % of the step duration, which is similar to the duration of the initial contact phase of the walking locomotion (Perry and Burnfield, 2010).

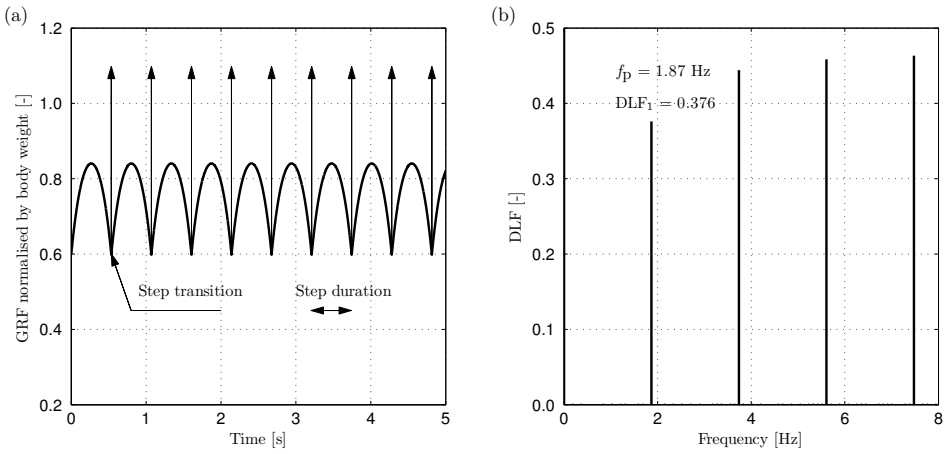

Figure 3.2: (a) Ground reaction force generated by the inverted pendulum model in time domain and **(b)** DLFs in frequency domain.

Figure 3.2b shows the amplitude spectrum of the GRF normalised by the body weight. Each line represents a dynamic load factor (DLF) for the relevant forcing harmonic. The interplay between the arch-like shapes and the impulses produces a spectrum in which only the amplitude of the first harmonic, denoted as DLF_1, is comparable with that experimentally measured (Kerr, 1998). The model significantly overestimates the higher harmonics due to contribution of the impulses.

3.2.4 Parametric scan

In the parametric scan, the initial forward speed varies from 1.0 m/s to 2.5 m/s, the attack angle is between 65° and 80° while the pendulum length is first fixed at 1.037 m. Figures 3.3a–c shows the domains for the three parameters of interest, which are the pacing rate, DLF_1 and walking speed. Figure 3.3a shows that there are ranges of the initial forward speed and attack angle (hereafter called Subset 1, bounded by two dashed lines) that provide pacing rate in the realistic range of 1.4–2.4 Hz (Živanović, 2012). Using the reported range of DLF_1 corresponding to the pacing rate of 1.4–2.4 Hz (Kerr, 1998), Subset 1 is further narrowed to Subset 2, representing by all values within the dashed boundary in Figure 3.3b. Subset 2 is then drawn on Figure 3.3c, in which the average walking speed is between 1.0 m/s and 1.8 m/s. The parametric scan results show that the IPM can provide full realistic range when investigating each walking parameter independently.

Using one value of pendulum length (i.e. 1.037 m), the realistic ranges of gait parameters are presented in Figures 3.3a–c. One potential method to

achieve different ranges of the gait parameters in the model is to adjust the pendulum length. Two pendulum lengths of 0.9 m and 1.2 m (as represents of the mean ± two standard deviations of pendulum length calculated in Section 3.2.2) are used to demonstrate this possibility. Parametric studies for pendulum length of 0.9 m and 1.2 m are shown in Figures 3.3d–f and Figures 3.3g–j, respectively. The range of initial conditions providing realistic ranges of gait parameters (determined in the same way as the ranges in Figures 3.3a–

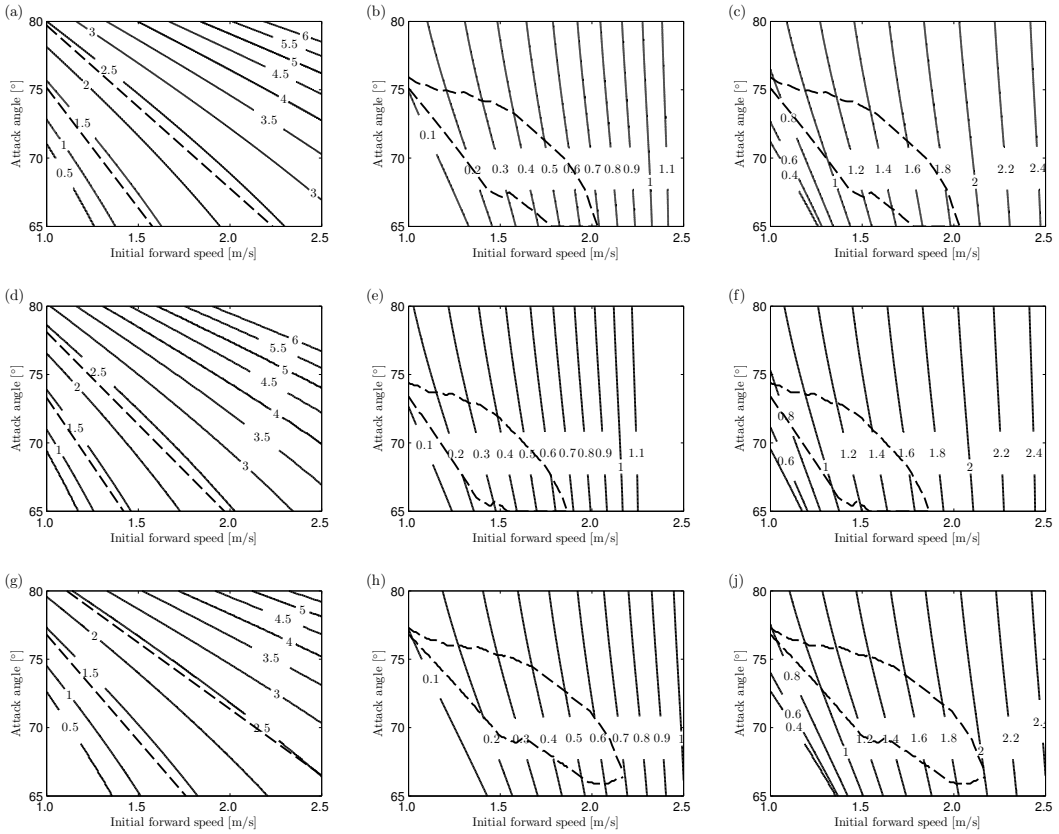

Figure 3.3: Parametric scan of the inverted pendulum model. Top, middle and bottom rows represent parametric scan for pendulum length of 1.037, 0.900 and 1.200 m, respectively. First, second and third columns represent the scan of pacing rate, DLF_1 and walking speed, respectively.

c) changes depending on the pendulum length. Therefore, utilising different pendulum lengths allows more flexibility in modelling different individuals in human population.

3.3 Rocker foot model

In Chapter 2, it was discussed that the IPM overestimates the vertical excursion of m_{p} and that the rocker foot model (RFM) can be used to better represent this quantity. This model is analysed in more detail in this section.

3.3.1 Model description

The RFM is shown in Figure 3.4. A rigid stick with length l and the rocker with radius r form, hereafter referred to as, the leg of the RFM.

Using the Lagrangian approach, the equation of motion can be written

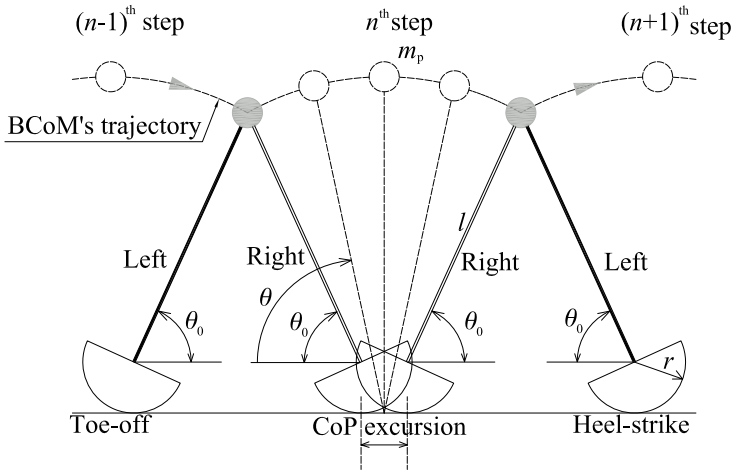

Figure 3.4: Parameters of rocker foot model.

as (Appendix A.2):

$$\ddot{\theta} = \frac{l\cos\theta(g - r\dot{\theta}^2)}{r^2 + l^2 + 2rl\sin\theta} \tag{3.6}$$

Within a step, the GRF generated by the RFM is:

$$F_{\mathrm{p}} = -m_{\mathrm{p}}\left[g + l\dot{\theta}^2\sin\theta - \frac{l^2\cos^2\theta(g + 2r\dot{\theta}^2)}{r^2 + l^2 + 2rl\sin\theta}\right] \tag{3.7}$$

The end-of-step condition and the amplitude of applied impulses are calculated using Equations 3.3 and 3.4, respectively.

3.3.2 Input parameters

Model parameters (mass m_{p} and leg length $l + r$) and initial conditions (θ_0 and $\dot{\theta}_0$) are the same as those used in the IPM. The only new feature in this model is addition of the rocker. Morawski and Wojcieszak (1977) provided a formula to convert the leg length of the RFM into an equivalent IPM with a lengthened leg as follows:

$$L_{\mathrm{e}} = \frac{L_{\mathrm{a}}^2}{L_{\mathrm{a}} - r} = L_{\mathrm{a}}\left(\frac{L_{\mathrm{a}}}{L_{\mathrm{a}} - r}\right) = L_{\mathrm{a}}\rho \tag{3.8}$$

where L_{e} is the pendulum length of the equivalent IPM, L_{a} is the anatomical leg length, and ρ is a dimensionless quantity called the "roll factor". ρ stands for the increase of leg length of a RFM when compared to the equivalent IPM. Hansen et al. (2000) claimed that ρ is approximately 1.8 for normal walking gait. Using this estimation for an adult person whose height in the range of 1.48–1.87 m (mean ± two standard deviations, NHS, 2010), the rocker radius is calculated as 0.34–0.43 m.

3.3.3 Simulation results

Figure 3.5a shows a comparison of simulated trajectories of m_p produced by the RFM and the IPM. The input parameters are chosen so that both models generate nominally similar pacing rate and average walking speed. Although the arc-shaped motion of the m_p is still preserved in the RFM, the excursion of m_p in the RFM is reduced due to the presence of rockers.

In addition, while the centre of pressure (CoP) is lumped into a single point in the IPM, there is a more natural transition of CoP in the RFM. Namely, the position of the CoP progresses from "heel" to "toe" as the foot rolls forward. This progression is denoted as the CoP excursion in Figure 3.4. Figure 3.5b shows the pacing rate and the CoP excursion as functions of the rocker radius (ranging from 0.00 m to 0.45 m). The input values of the simulation are $m_\mathrm{p} = 77.5\,\mathrm{kg}$, $l + r = 1.037$ m, $\theta_0 = 69°$ and $\dot{x}_0 = 1.61\,\mathrm{m/s}$. When $r = 0$, the RFM is equivalent to the IPM with the corresponding parame-

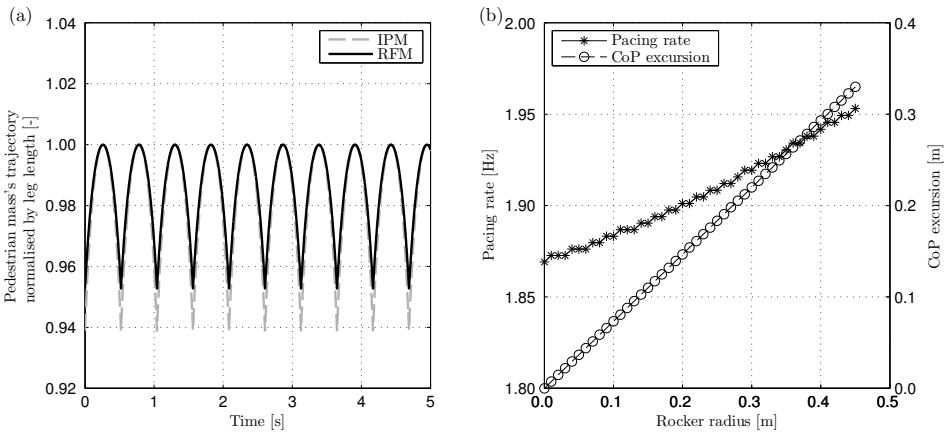

Figure 3.5: (a) Comparison of the trajectory of pedestrian mass between the inverted pendulum model and the rocker foot model and **(b)** dependency of pacing rate and centre of pressure excursion on rocker radius.

ters. As the rocker radius increases, both pacing rate and the CoP excursion increase. In the latter case, this increase is almost linear.

Due to the contribution of impulses, the GRF generated by the RFM has the same shortcoming as the GRF produced by the IPM, i.e. DLFs for the second and higher harmonics are overestimated (Figure 3.2b).

3.3.4 Parametric scan

The parametric scan of the RFM is shown in Figure 3.6. The rocker radius is set at 0.4 m while the leg length $l + r$ is kept constant at 1.037 m. The initial forward speed ranges from 1.0 m/s to 2.5 m/s, and the attack angle is between 65° and 80°. Dashed lines in Figure 3.6a show the range of parameters that can generate pacing rate from 1.4 Hz to 2.4 Hz. Figures 3.6b and 3.6c narrow this range based on the reported range of DLF_1 corresponding to the pacing rate of 1.4–2.4 Hz reported by Kerr (1998) (all data points within the dashed boundary). The scan shows that similar to the IPM, the RFM can produce wide realistic range of walking parameters. Also, the RFM has the same

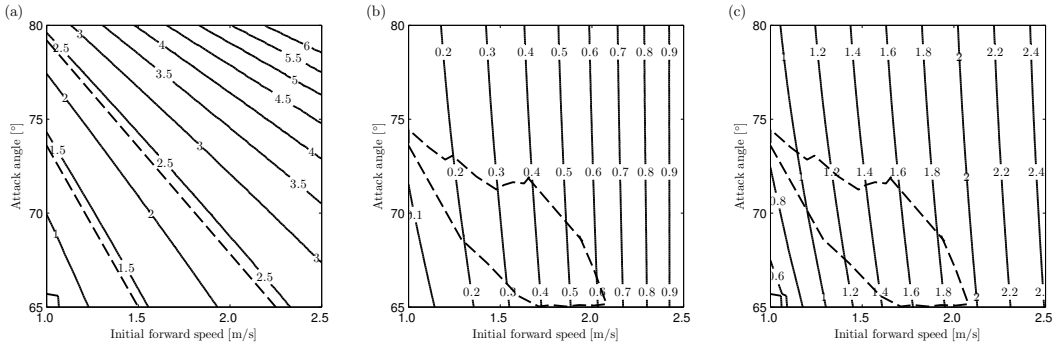

Figure 3.6: Parametric scan of rocker foot model: **(a)** pacing rate, **(b)** DLF_1 and **(c)** average walking speed.

issue of being difficult to produce all realistic combinations of gait parameters. Potential methods to improve the ranges of parameter combinations of the RFM (not presented in this thesis) are to adjust either the rocker radius, leg length or both.

3.4 Spring mass model

As shown in Chapter 2, the assumption of rigid leg used in the IPM and the RFM cannot explain the compliant feature of the leg in human gait. In addition, the two models require provision of external energy (in form of artificially applied impulses) to generate continuous walking. The spring mass model (SMM) was introduced to address these shortcomings (Geyer, 2005).

3.4.1 Model description

A walking step in the SMM constitutes of the pedestrian mass m_{p} travelling from one apex, i.e. highest elevation, to another (Figure 3.7). As a result, each walking step contains two single support phases and one double support phase.

Using the Lagrangian approach, the equations of motion for the first single support phase are (Appendix A.3.1):

$$\ddot{\theta}_1 = \frac{1}{l_1}(g\cos\theta_1 - 2\dot{l}_1\dot{\theta}_1) \tag{3.9}$$

$$\ddot{l}_1 = l_1\dot{\theta}_1^2 + g\sin\theta_1 + \frac{k}{m_{\mathrm{p}}}(l_0 - l_1) \tag{3.10}$$

where l_0 is the leg length at rest, l_1 is the compressed length of the first leg

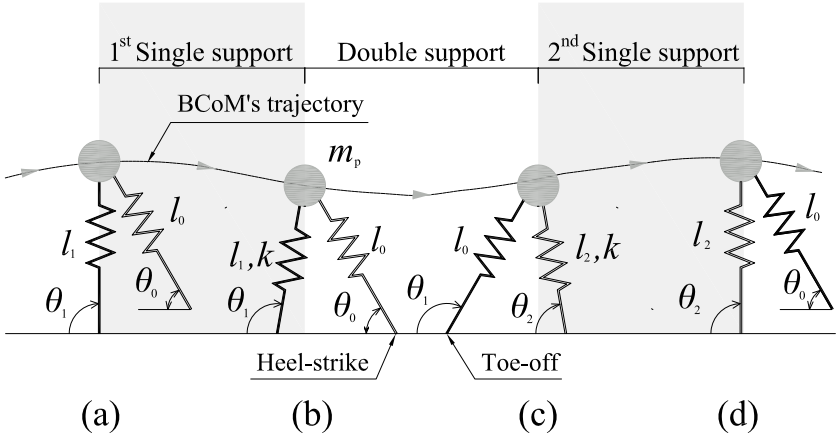

Figure 3.7: Parameters of spring mass model (after Geyer, 2005). **(a)** Start of simulation, **(b)** heel-strike event of the leading leg, **(c)** toe-off event of the trailing leg and **(d)** end of a walking step.

and k is the stiffness of the spring representing the leg. $\ddot{\theta}_1$ and $\ddot{l}_1$ are second derivatives of θ_1 and l_1, respectively. Both legs are assumed to have the same values of k and l_0. The leg of the SMM is referred to as the spring connecting m_p to the foot in the context of this chapter.

In simulations, the first single support phase stops when the second leg touches the ground. The condition for this event is that the elevation of m_p is equal to $l_0 \sin\theta_0$, where θ_0 is the attack angle (Figure 3.7b). The simulation continues with a new set of equations of motion for the double support phase (Appendix A.3.2):

$$\ddot{\theta}_1 = \frac{1}{l_1}\left[g\cos\theta_1 - 2\dot{l}_1\dot{\theta}_1 - \frac{k}{m_\mathrm{p}}(l_0 - l_2)\sin(\theta_1 - \theta_2)\right] \tag{3.11}$$

$$\ddot{l}_1 = l_1\dot{\theta}_1^2 + g\sin\theta_1 + \frac{k}{m_\mathrm{p}}(l_0 - l_1) + \frac{k}{m_\mathrm{p}}(l_0 - l_2)\cos(\theta_1 - \theta_2) \tag{3.12}$$

$$\dot{\theta}_2 = \frac{1}{l_2}\left[\dot{l}_1\sin(\theta_1 - \theta_2) + l_1\dot{\theta}_1\cos(\theta_1 - \theta_2)\right] \tag{3.13}$$

$$\dot{l}_2 = \dot{l}_1\cos(\theta_1 - \theta_2) - l_1\dot{\theta}_1\sin(\theta_1 - \theta_2) \tag{3.14}$$

where l_2 is compressed length of the second leg while θ_1 and θ_2 are the angles made by the ground and the first and second legs, respectively (Figure 3.7). $\dot{\theta}_2$ and $\dot{l}_2$ are first derivatives of θ_2 and l_2, respectively.

Equations 3.11 and 3.12 determine the motion of the first leg, while Equations 3.13 and 3.14 are the interrelation between the two legs due to geometry constraints. Simulation of the double support phase stops when the length of the first leg l_1 returns to the rest length l_0 (Figure 3.7c).

After completion of the double support phase, the SMM enters the single support phase of the second leg while the first leg is in the swinging phase and its motion is not accounted for in the simulation. Equations of motion in this phase are the same as Equations 3.9 and 3.10, after accounting that subscript "1" should be substituted by "2". A walking step ends when m_p reaches its apex (Figure 3.7d). Overall, the simulation of the SMM, unlike the IPM and the RFM, reproduces all walking phases in a step cycle of the human gait.

The GRF generated by the i^{th} leg ($i = 1$ or 2) is calculated as:

$$F_{\mathrm{p},i} = k(l_0 - l_i)\cos\left(\theta_i - \frac{\pi}{2}\right) \tag{3.15}$$

The total energy of the system is the sum of kinetic energy T and potential energy V, which are calculated as:

$$T = \frac{1}{2}m_\mathrm{p}\left(\dot{l}_1^2 + l_1^2\dot{\theta}_1^2\right) \tag{3.16}$$

$$V = -m_\mathrm{p}gl_1\sin\theta_1 + \frac{1}{2}k\left(l_0 - l_1\right)^2 + \frac{1}{2}k\left(l_0 - l_2\right)^2 \tag{3.17}$$

The two types of energy are continuously interchanged as the elevation

of m_p and spring lengths vary while the total energy remains constant. As a result, the SMM can operate without an external power supply.

3.4.2 Input parameters

The model parameters consist of the pedestrian mass, leg length at rest and spring constant. Similar to the IPM and the RFM, m_p is selected as 77.5 kg while l_0 is set at 1.037 m. To estimate the spring constant k, Geyer (2005) did a series of experiments on an instrumented treadmill. The speed of the treadmill during the experiments was from 0.6 m/s to 3.6 m/s. The normalised spring constant was identified as the mean value of stiffness of the, say, first leg during contact with the ground from the measured $F_{\mathrm{p},1}$, l_1 and θ_1 using Equation 3.15. For $m_\mathrm{p} = 77.5\,\mathrm{kg}$ and $l_0 = 1.037\,\mathrm{m}$, the spring constant from the study by Geyer (2005) can be presented as a function of the walking speed in Figure 3.8a. The data show that k and its variation tends to decrease when

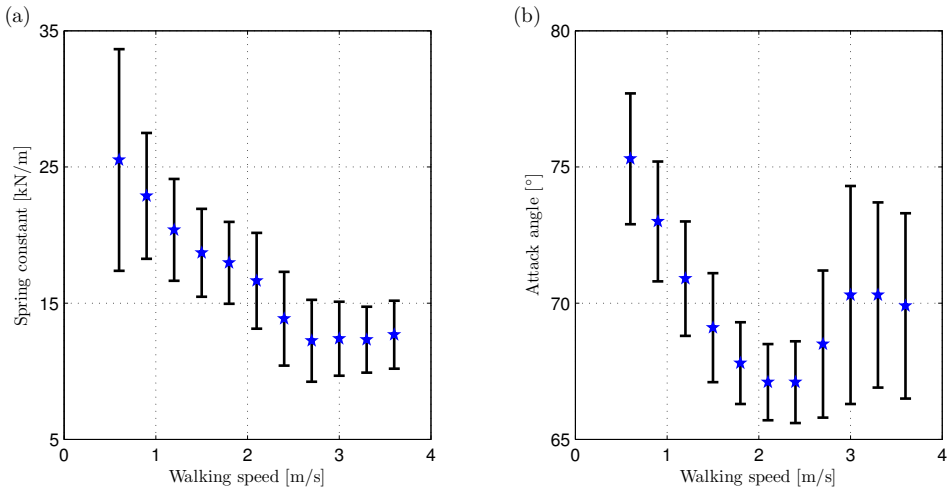

Figure 3.8: Spring constant and attack angle measured in experiments (after Geyer, 2005). Stars and vertical lines represent the mean and ± standard deviation range, respectively.

the walking speed increases. The mean k is from 12.2 kN/m to 25.5 kN/m while the standard deviation is 2.4–8.1 kN/m.

Apart from the initial conditions containing angular information of the leg (i.e. $\theta_{0,i}$ and $\dot{\theta}_{0,i}$, $i = 1$ or 2 representing first or second leg), the SMM also requires additional initial conditions that represent the longitudinal length of the i^{th} leg (i.e. $l_{0,i}$ and its rate of change $\dot{l}_{0,i}$). The initial conditions for each of three support phases shown in Figure 3.7 are as follows:

- The first single support phase requires initial conditions for the first leg only.
  - $\theta_{0,1}$ is the angle made between the first leg and the ground when m_{p} is at its apex. It is assumed that $\theta_{0,1}$ is 90°.
  - $l_{0,1}$ is the length of the first leg at the apex. Saunders et al. (1953) noticed that the maximum vertical elevation of m_{p} during walking is lower than that during standing for about half an inch (i.e. about 0.013 m). Similar observation was also reported in the experiments by Murray et al. (1985). When the upper body is considered as rigid, this reduction can be solely attributed to the compression of the leg at the apex during walking. For the leg length of 1.037 m and taking into account the shortening of the leg is up to 0.013 m, the ratio $l_{0,1}/l_0$ ranges from 0.985 to 1.000.
  - $\dot{\theta}_{0,1}$ and $\dot{l}_{0,1}$ are the angular and longitudinal velocities of the first leg, respectively. These initial conditions can be expressed via the vertical and horizontal speeds of m_{p} (i.e. $\dot{x}_0$ and $\dot{y}_0$):

$$\dot{\theta}_{0,1} = \frac{\dot{x}_0}{l_{0,1} \sin \theta_{0,1}} \tag{3.18}$$

$$\dot{l}_{0.1} = \frac{\dot{y}_0}{\sin \theta_{0,1}} \tag{3.19}$$

The range of initial forward speed $\dot{x}_0$ is chosen here to range from 0.7 m/s to 2.0 m/s. This range is lower than that used in the IPM (i.e. 1.0–2.5 m/s) because in simulations of the SMM, it is assumed that the simulation starts from the apex, where the horizontal speed is at its minimum. It is assumed that $\dot{l}_{0,1}$ is equal to zero.

- The double support phase requires initial conditions for both legs.
  - All the initial conditions related to the first leg (i.e. $\theta_{0,1}$, $\dot{\theta}_{0,1}$, $l_{0,1}$ and $\dot{l}_{0,1}$) are taken from the last instant in the simulation of the first single support phase.
  - $\theta_{0,2}$ is equal to θ_0. $\theta_{0,2}$ was determined from kinematic data and plotted as a function of the walking speed in Figure 3.8b (after Geyer, 2005). The mean attack angle ranged from 67.1° to 75.3 ° while the standard deviation was 1.4–4.0 °.
  - $l_{0,2}$ is the initial length of the second leg. $l_{0,2}$ is equal to l_0 due to the observation that the leg at the first instant of its stance phase is not compressed (Chapter 2).
- The second single support phase requires initial conditions for the second leg only (starting at Figure 3.7c and ending at Figure 3.7d). All initial conditions (i.e. $\theta_{0,2}$, $\dot{\theta}_{0,2}$, $l_{0,2}$ and $\dot{l}_{0,2}$) are taken from the last instant in the simulation of the double support phase. At the end of this phase (also the end of a walking step), the values of four variables are hereafter called $\theta_{\mathrm{e},2}$, $\dot{\theta}_{\mathrm{e},2}$, $l_{\mathrm{e},2}$ and $\dot{l}_{\mathrm{e},2}$.

Since the simulation of the SMM is governed by three sets of equations with different conditions stipulating the end/beginning of each support phase, the state of m_{p} in the beginning ($\theta_{0,1}$, $\dot{\theta}_{0,1}$, $l_{0,1}$ and $\dot{l}_{0,1}$) and the end ($\theta_{\mathrm{e},2}$, $\dot{\theta}_{\mathrm{e},2}$, $l_{\mathrm{e},2}$ and $\dot{l}_{\mathrm{e},2}$) of a walking step is usually not the same. Therefore, simulations often results in unstable solutions, e.g. m_{p} jumps off the ground or

falls downwards. To address this issue, Geyer (2005) determined ranges of initial conditions that can provide stable solutions of the SMM. Such a study requires rigorous mathematical derivations to find stable solutions of differential equations. Derivation of the required stability conditions is beyond the scope of this thesis. Instead, the assumption of repetitive initial conditions will be used for this model, preventing occurrence of instabilities. The simulation in a walking step is paused when $\theta_{e,2} = \theta_{0,1}$. For the continuity of the simulation result, a solution is hereafter considered stable when the maximum discrepancy percentage of the other three variables ($\dot{\theta}$, l and $\dot{l}$) at the beginning and the end of a walking step is less than 1 %. All other solutions, deemed unstable, are disregarded in this chapter. To achieve a stricter criterion, i.e. lower percentage discrepancies, a more careful procedure to select parameter combinations should be applied.

3.4.3 Simulation results

Figure 3.9 shows an example of the trajectory of m_p generated by the SMM ($m_p = 77.5\,\text{kg}$, $l_0 = 1.037\,\text{m}$, $k = 23\,\text{kN/m}$, $l_{0,1}/l_0 = 0.985$, $\theta_{0,1} = 90.0°$, $\theta_0 = 69.1°$ and $\dot{x}_0 = 1.02\,\text{m/s}$). This combination of input parameters results in the pacing rate of 1.87 Hz and average walking speed of 1.15 m/s. Comparing to simulation results from the IPM and the RFM given in Figure 3.5a, the trajectory of m_p in the SMM is smoother and qualitatively in agreement to that seen in measured data (Figure 2.7). The improvement stems from the spring-leg feature of the SMM, which provides the capability of modelling the double support phase.

Figure 3.10 shows the GRF generated by the SMM in time and frequency domains. The time history of GRF induced by one leg has the M-shape pattern (Figure 3.10a), which qualitatively agrees with the experimental data (Figure 2.2a). In the frequency domain, the DLFs generated by the SMM, differently from IPM (Figure 3.2b), qualitatively agree with experimental data even for higher harmonics (Figure 3.10b).

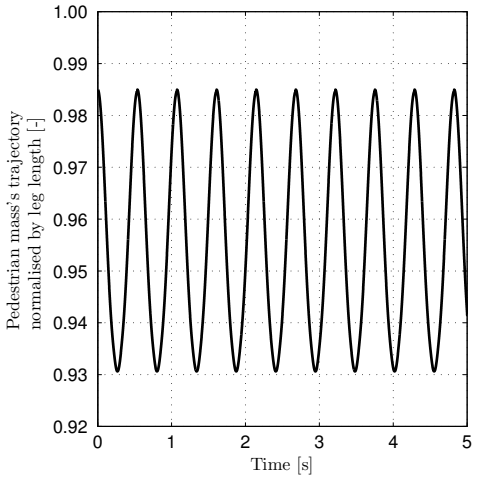

Figure 3.9: Trajectory of pedestrian mass in the spring mass model.

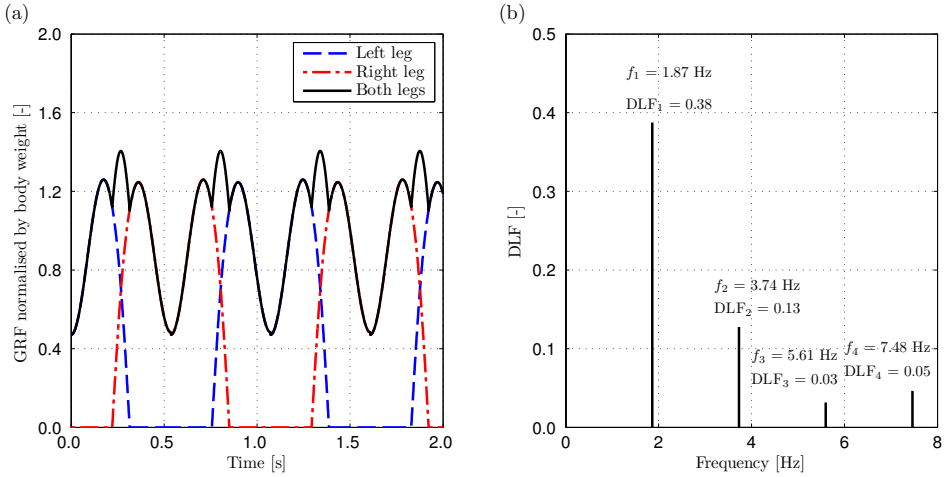

Figure 3.10: Ground reaction force generated by the spring mass model in **(a)** time and **(b)** frequency domains.

3.4.4 Parametric scan

k, θ_0, $\dot{x}_0$, $l_{0,1}/l_0$ and l_0 in the SMM are varied to generate different gait parameters. Realistic ranges of the first four parameters are stated in Section 3.4.2 while l_0 is initially set at 1.037 m. These values are used in the parametric scan. All resulting solutions that overestimate values of DLFs for first four harmonics reported by Kerr (1998) are considered unrealistic, and are consequently disregarded.

Figure 3.11 shows ranges of walking speed, pacing rate and DLFs that the SMM can produce in a subset of parametric space when θ_0 is 65°, 70° and 75° (top, middle and bottom rows, respectively). The parametric scan includes the attack angle of 80° but results are not presented since only a small number of stable solutions can be found. The horizontal colour bar indicates the magnitude of the system's total energy in Joules. This total energy is presented as the combination of $\dot{x}_0$ and $l_{0,1}/l_0$ in the first column in Figure 3.11. The second column shows the pacing rate f_p as a function of the spring constant. The SMM can provide the full realistic range of 1.4–2.4 Hz and the increase in the attack angle results in the increase of the range of f_p. Walking speed is presented in the third column. The maximum walking speed that the SMM can produce is from 0.6 m/s to 1.4 m/s, which is in the lower range of human walking speed. This finding is in line with the results reported by Geyer (2005). DLFs of the first four harmonics are presented from fourth to seventh columns, respectively. DLFs produced by the SMM fall within the ranges found in experimental data (Kerr, 1998).

Simulated DLF_1 is shown as a function of the pacing rate in Figure

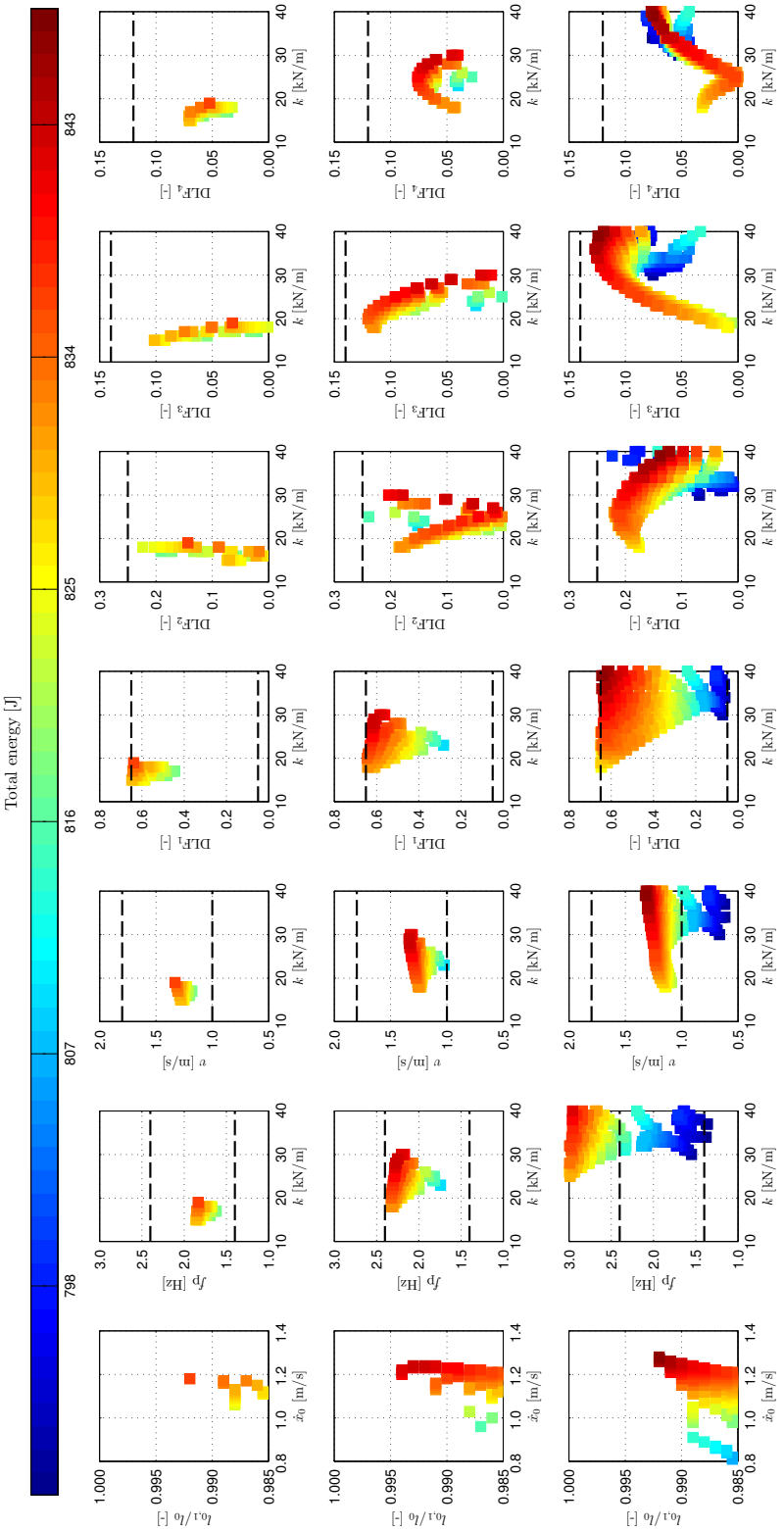

Figure 3.11: Parametric scan of the spring mass model with $l_0 = 1.037\,\mathrm{m}$. Dashed lines indicate boundaries of the realistic ranges of each parameter. For DLF_2–DLF_4, upper boundary is presented only. Top, middle and bottom rows represent the scan for θ_0 of 65°, 70° and 75°, respectively.

3.12a, along with the experimental data reported by Kerr (1998). Besides the leg length of 1.037 m (grey-filled), simulation results of two pendulum lengths of 0.900 m (unfilled) and 1.200 m (black-filled) are also presented. These additional lengths cover the range of mean ± two standard deviations calculated for the leg length (i.e. $1.037 \pm 2 \times 0.060$). Squares, circles and triangles represent the attack angle of 65°, 70° and 75°, respectively. For θ_0 of 70°, the resulting DLF_1 is within the realistic range, while the attack angle of 65° and 75° over- and underestimate the experimental DLF_1, respectively. In the case of $\theta_0 = 70°$, different leg lengths help to populate the realistic range of DLF_1. To investigate the range of attack angle in the vicinity of 70°, Figure 3.12b shows the achieved range of DLF_1 when varying θ_0 around 70°, i.e. from 67° to 73° (1° increment). For the pacing rate greater than 1.7 Hz, it is possible to find numerous parameter combinations that result in DLF_1 within the range

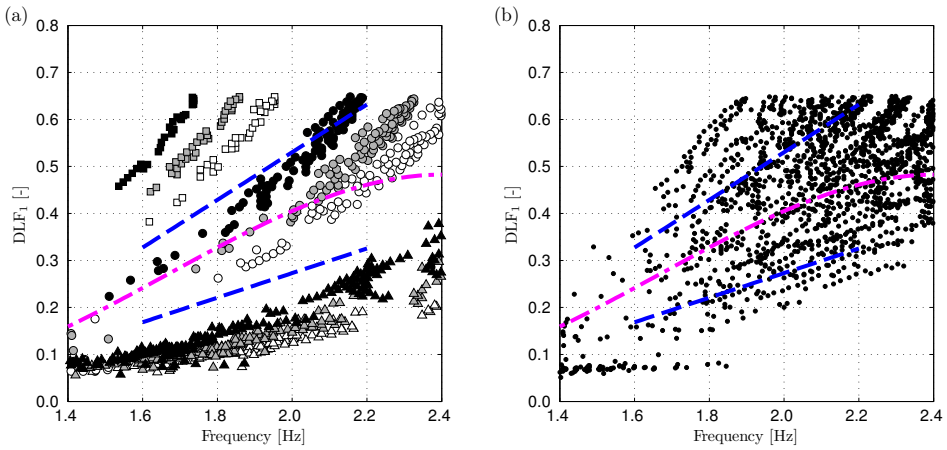

Figure 3.12: DLF_1 generated by the spring mass model when l_0 is 0.900, 1.037 and 1.200 m. **(a)** θ_0 is either 65° (squares), 70° (circles) or 75° (triangles) and **(b)** θ_0 ranges from 67° to 73°. Dash-dotted and dashed lines represent the mean and ± standard deviation of experimental data reported by Kerr (1998).

reported by Kerr (1998) while the number of these combinations decreases for the pacing rate between 1.4 Hz to 1.7 Hz. To populate this range of pacing rate, the scan will require extremely fine resolution for the initial conditions, which is unrealistic given limited precision in measuring walking parameters. This observation suggests the difficulty in choosing initial conditions to result in DLF_1 at low pacing rate.

3.5 Discussion and conclusions

Three bipedal models (IPM, RFM and SMM) were quantitatively reviewed in this chapter. In the analysis of each model, ranges of input parameters and parametric scan were provided. To assess the applicability of the models for modelling pedestrian-structure dynamic interaction (PSDI), each model is evaluated against three criteria defined in Section 2.3.5 and the results are summarised in Table 3.1. Three criteria are repeated as follows:

- **Criterion 1**: the model should be able to replicate the walking phases and trajectory of BCoM (i.e. m_{p}) which are in accordance with the literature.
- **Criterion 2**: the model should be able to generate the realistic range of kinematic parameters, e.g. pacing rate and walking speed.
- **Criterion 3**: the model should produce a genuine form of GRF on rigid surface in terms of both the shape of the time domain waveform and the amplitude of the frequency spectrum.

As the simplest model reviewed, IPM cannot accurately reproduce all phases of walking gait or the trajectory of the BCoM. However, it does provide a good approximation of human walking gait in the single stance phase, which

Table 3.1: Evaluation of bipedal models against criteria for PSDI study.

Models	Criterion 1	Criterion 2	Criterion 3
IPM	✓	✓	✓
RFM	✓	✓	✓
SMM	✓	-	-

represents 80 % of a gait cycle (Chapter 2). As a result, it can be considered that the IPM satisfies, at least partially, Criterion 1. The parametric scan shows that a wide range of walking parameters seen in experimental data can be reproduced. IPM can be used to represent different walking gaits of human population and can be said to satisfy Criterion 2. Finally, the model produces a realistic range of DLF_1, which is sufficient for modelling human walking of low-frequency structures (i.e. natural frequency below 2.5 Hz). Thus, the IPM satisfies Criterion 3.

The introduction of the rocker foot feature in the RFM leads to reduced, i.e. more realistic, excursion of BCoM when compared to the IPM. Moreover, the rocker feature contributes to more genuine representation of the CoP progression. As a result, the RFM is deemed satisfactory for Criterion 1. The parametric scan suggests that the RFM can produce a wide range of walking parameters and therefore it is considered to meet Criteria 2 and 3. Overall, the RFM possesses a number of improvements when compared to the IPM. However, as only a minor upgrade from the IPM, the RFM still has limitations that are inherited from the IPM (e.g. neglects the double support phase and provides unrealistic DLFs for second and higher harmonics). Thus, it is unlikely that utilising the RFM can provide significant improvements in PSDI modelling when compared with the application of the IPM.

Among the three models reviewed, the SMM is capable of best replicating the trajectory of BCoM. Therefore, the SMM satisfies Criterion 1. The parametric scan shows that the SMM has difficulties in covering range of human walking speed and, therefore, only partly satisfies Criterion 2. In addition, the spring-like legs contribute to the qualitatively accurate replication of the typical M-shaped GRF pattern. DLFs of the higher harmonics are in realistic ranges, which is a significant improvement when compared to simulations using the IPM and the RFM. Unfortunately, the parametric scan only found limited number of stable solutions that have realistic DLF_1 in the low range of pacing rate (1.4–1.7 Hz). This feature prevents the SMM from fully meeting Criterion 3. In summary, the SMM does not fully satisfy Criteria 2 and 3. These limitations, along with the complexity in selecting initial conditions to result in stable solutions, indicate that the SMM is not the best choice for further investigation of PSDI.

To conclude, the analysis in this chapter shows that the IPM, despite its limitations, has potential to be used in the study of PSDI. The IPM is, therefore, chosen for modelling PSDI in this thesis. After completing an experimental programme to determine characterisation of walking on the rigid surface (Chapter 4) and the lively surface (Chapter 5), the IPM will be utilised for modelling human locomotion on vibrating surfaces in Chapter 6.

Chapter 4

Experimental characterisation of walking on rigid surface

4.1 Introduction

To establish a model of pedestrian-structure dynamic interaction (PSDI), it is necessary to gain experimental insight into structural and human behaviour when structure vibrates perceptibly. Therefore, the next step in the study is to develop an understanding of the PSDI phenomenon through controlled experiments. The ultimate aim of the experimental work is to verify/correct assumptions made in numerical modelling, and to increase the reliability of the model and resulting vibration estimates.

To understand PSDI, it is also crucial to continuously monitor pedestrian behaviour while walking over perceptibly vibrating surfaces and observe any potential changes in human walking. In addition, it is important to compare the observed parameters to those recorded when walking on rigid surface. As a result, the experimental programme started with measurements on the rigid surface, and the results are reported in this chapter. These results will be

used as a benchmark in the analysis of experimental data acquired on a lively structure that will be reported in Chapter 5.

To quantify PSDI, knowledge about the pedestrian-induced dynamic force and pedestrian kinematics are required. In the context of this thesis, the first aim is to accurately quantify force in both time and frequency domains to allow structural engineers to use the information in vibration prediction. The second aim of monitoring the kinematic data is to improve understanding of variations in key walking parameters during PSDI (such as pacing rate, step length, step width etc.).

To study variations of the dynamic force and walking parameters during PSDI, it is necessary to monitor pedestrians over multiple steps. Since walking is an activity in which the pedestrian's position in space changes with time, capturing consecutive steps is not a straightforward task. Section 4.2 of this chapter provides a short background information of ground reaction force (GRF) measurement. Among a number of methods to monitor the dynamic loads, a motion capture system for indirect measurement of the force was at the author's disposal, and is described in the same section. The precision of this method has not been fully documented in literature. For this reason, Section 4.3 quantifies the accuracy of the method with respect to force measurement and propagation of the measurement error into the structural vibration estimate. In Section 4.4, the kinematic and kinetic data of pedestrians are investigated. To the best knowledge of the author, this is the most comprehensive study investigating kinematic and kinetic data (while walking) relevant for civil engineering applications. Section 4.5 at the end of the chapter provides summary of main findings.

All experiments in this thesis were approved by the Biomedical and Scientific Research Ethics Committee at the University of Warwick. Before commencing experiments, test subjects (TSs) signed a consent form, acknowledging their awareness of the test protocol and associated risks. In addition, each TS was asked to answer questions about their health status. Only TSs in good health condition were allowed to take part in the experiments. Both the consent and the questionnaire forms can be found in Appendix B.

4.2 Measurement of ground reaction force

This section first reviews most frequently used techniques for measuring GRF. Then the usage of a motion capture system for this application is described in detail, followed by a description of the system used for experiments in this chapter.

4.2.1 Measurement techniques

Methods used to record GRF are often classified into two categories: direct and indirect (Racic et al., 2013). In the direct methods, the measurement is the force/pressure-induced. In the indirect methods, the GRF is derived from other measurements such as kinematics of human body or video data.

Facilities for direct measurement of GRF are force plate, instrumented treadmill and foot pressure insoles. Each facility has its own merits as well as disadvantages. Force plate is probably the most popular facility used in majority of gait laboratories. Although the working principle of a force plate depends on the type of built-in force transducers, the general concept in every

force plate is to sense the load applied by monitoring electrical charge/voltage in transducers, and then convert the electrical quantity to the corresponding loads, usually using specialised software (Racic et al., 2013). A force plate can only be used to record one single step at a time when studying walking or running. This limitation makes the use of a force plate inappropriate for studying PSDI. An improved set-up includes multiple force plates (Figure 4.1a). In this case, the TSs are asked to walk over a predefined pathway and to target the force plates' surfaces. The targeting action inevitably influences the subject's gait to some degree and it would be difficult to separate this influence on the gait from that caused by PSDI on lively surfaces. Another limitation of the system is that the covered walking distance is confined to, usually small, the combined length of multiple force plates only.

In order to increase the number of monitored steps, an instrumented force measuring treadmill (IFMT) can be used for studying both running (Kram et al., 1998) and walking (Belli et al., 2001). An IFMT has features of an ordinary treadmill, with addition of being equipped with force sensors. When a person walks on an instrumented treadmill, the total GRF is recorded. With

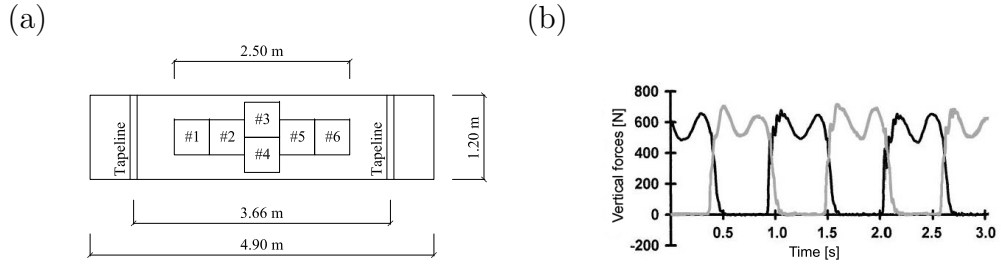

Figure 4.1: (a) Set-up of multiple force plates (after Gard et al., 2004). **(b)** Ground reaction force of right foot (dark lines) and left foot (grey lines) recorded on an instrumented treadmill (after Belli et al., 2001).

the double belt design (Belli et al., 2001), it is possible to record the GRF induced by the left and right feet separately (Figure 4.1b). With an adequate accommodation period, walking data on treadmills were found to be a good representation of walking over level ground (Matsas et al., 2000).

Another direct method for load measurements is to use pressure sensors, built-in the insoles of the shoes. Pressures at the contact between the foot and the insole are measured continuously. Time history of the total GRF can then be obtained by integration of measured pressure over the corresponding areas. Although this facility is able to record multiple steps, and it does not significantly impede natural movement of TS, the accuracy in measuring force amplitude is inadequate in comparison to force plate and IFMT facilities (Racic et al., 2013). To quantify the accuracy of this method, Cordero et al. (2004) compared the GRF reconstructed by insoles sensors with that measured by force plates. Combining the measured pressure and kinematic data, the authors developed a method to convert the pressures from local coordinates of the insoles to global coordinates, calculating the vertical component of the GRF in the process. It was found that the root mean square discrepancies of the measured vertical GRF by the two methods were less than 10 % in the time domain. In this publication, no information was given for the frequency domain.

Apart from the direct measurement methods, the GRF can also be found indirectly using a motion capture system (MCS). This system consists of a series of video cameras to capture movement of markers that are attached to human anatomical landmarks. In this way, it is possible to acquire relevant kinematic data of body segments. Kinematic data have been reportedly used

to reconstruct GRF induced during walking (Racic et al., 2010a), running (Bobbert et al., 1991) and bouncing and jumping (Racic et al., 2010b). The key advantage of MCS is that it can record consecutive walking steps and allow a TS to move in a natural way, making it suitable for the study of PSDI. With the availability of a MCS named Vicon (Oxford Metrics Group, 2007) in the Gait Laboratory at the University of Warwick, the author decided to utilise this system for the experimental work.

4.2.2 Use of motion capture system

If the entire mass of the human body is lumped into the body's centre of mass (BCoM), the movement of the pedestrian can be represented by the motion of this single point (Saunders et al., 1953). Applying Newton's second law of motion to this point, the total vertical component of GRF, F_{p}, induced at foot contact is equivalent to the force acting on BCoM, which is calculated as (Bobbert et al., 1991):

$$F_{\mathrm{p}} = m_{\mathrm{p}}(\ddot{z}_{\mathrm{BCoM}} - g) \tag{4.1}$$

where m_{p} is the body mass of the pedestrian, $\ddot{z}_{\mathrm{BCoM}}$ is the vertical component of the acceleration at BCoM and g is the acceleration of gravity ($g = -9.81\,\mathrm{m/s^2}$; definition of positive direction is upward).

BCoM is normally a point inside the human body and therefore it cannot be directly monitored. Instead, some approximate methods to determine the movement of BCoM have been developed. A method, called the sacral method, considers BCoM movement to be the same as movement of a point on the back near the centre of the pelvis (Thirunarayan et al., 1996; Eames

et al., 1999). To validate this method, Gard et al. (2004) performed experiments at four walking speeds (0.8, 1.2, 1.6 and 2.0 m/s) and measured the BCoM's excursion using the sacral method and double integration method of force plate data. The latter is commonly used to measure the trajectory of BCoM (Thirunarayan et al., 1996). The result showed that the two methods provided similar measurements at the slow speed of 0.8 m/s, while the sacral method became worse (i.e. overestimating) the BCoM's excursion as the speed increased. A potential reason for the overestimation is that the sacral method disregards the movement of all other body segments, e.g. arms and legs, and relies on a single point.

Although the sacral method is time-efficient, its inability to accurately quantify the kinematics of BCoM makes the method unreliable for the use in GRF reconstruction. To tackle the shortcoming of the sacral method, location of BCoM should be identified more accurately. A method to achieve this goal is to divide the body into a number of segments. In this way, Equation 4.1 can be written as (Bobbert et al., 1991):

$$F_{\mathrm{p}} = \sum_{i=1}^{n} m_i(\ddot{z}_i - g) \tag{4.2}$$

where m_i and $\ddot{z}_i$ are the mass of the i^{th} segment and the corresponding vertical acceleration of segment's centre of mass (SCoM), respectively, while n is the number of segments.

This method, called the segmental method, assumes that the human body consists of rigid chained segments. These segments are head, upper arms, forearms, hands, trunk, thighs, shanks and feet. This assumption is

not always valid during experiments due to the problem known as soft tissue artifact, in which markers move relatively to the underlying bones (Leardini et al., 2005). There are a number of methods to minimise the detrimental effect of this problem such as using a cluster of markers to represent one segment's location or fixing markers on plates attached to the body. These methods are both time-consuming and cumbersome for TSs induced in the experiments. Besides, Racic et al. (2010a and 2010b) did not use any mitigation methods and they still reported good-quality results. It can be concluded that for the low frequency range of interest, soft tissue artifact does not have significant influence on the quality of results, which makes the MCS a convenient method to use in this study.

Using the rigid segment assumption, Equation 4.2 indicates that each body segment contributes to the GRF. Therefore instead of directly measuring the force at the ground contact, kinematic data of body segments are used to reconstruct GRF.

To apply Equation 4.2, the data on body segment parameters (BSPs) are needed. BSPs in this particular application are the mass of body segments and locations of SCoMs. A segment's mass can be presented as a percentage of the body mass, while the location of a SCoM can be defined as a percentage of the segmental length measured from the proximal end-point. Proximal end-points are defined as the upper point for trunk parts and the points closer to the trunk for other body segments. For decades, regression equations generated from human cadaver data have been widely used to determine BSPs (Dempster, 1955; Clauser et al., 1969; Chandler et al., 1975). For living TSs, the immersion method for measuring the segment's volume and the reaction board method

for estimating the segment's mass (based on moment of the reaction force measured in two postures of a segment) were developed (Drillis et al., 1964). Development of radioisotope technology led to determining BSPs by scanning TSs' bodies (Zatsiorsky et al., 1990). In this method, the intensity of the gamma-radiation beam becomes weaker after passing through a material layer, such as a body segment. This information is used to calculate the density of body segments and, together with segment's volume, to estimate BSPs. A limitation of this study is that the authors used bony landmarks, some of which are not close to the centres of the neighbouring joints, as reference points to define segment length and SCoM. As a consequence, the estimates of SCoMs are inaccurate, especially when the TSs flex their joints. De Leva 1996 suggested adjusting Zatsiorsky et al.'s BSPs by shifting the end-points of segments to joint centres.

The BSPs for male TSs, as reported in two representative publications, are shown in Table 4.1. The values from the two studies are not comparable because of different definitions of segment end-points. In addition, TSs in the study of Clauser et al. (1969) were cadavers with mixed origins of Caucasian and African American, while those in de Leva (1996) were all living Caucasian people.

BSPs defined by de Leva (1996) are chosen for this study due to a number of reasons. In the first place, de Leva's study includes 100 TSs (as opposed to 13 cadavers studied by Clauser et al., 1969) and, this number provides a statistical sample of a reasonable size. In addition, the sample's average age of 23.8 years is relatively similar to that of human participants in the author's study. Finally, all segment end-points are clearly reported in the publication.

Table 4.1: Body segment parameters, mean (standard deviation if available).

	Clauser et al. (1969)		de Leva (1996)	
Number of TSs	13		100	
Age (years)	49.3 (13.9)		23.8 (6.2)	
Height (cm)	172.7 (5.9)		174.1 (6.2)	
Mass (kg)	66.5 (8.7)		73.0 (9.1)	
Body segments	Mass (%)	SCoM (%)	Mass (%)	SCoM (%)
Head	7.3 (0.6)	40.0 (3.0)	6.9	40.2
Trunk	50.7 (2.1)	38.0 (1.6)	43.5	44.9
Upper arm	2.6 (0.2)	51.3 (2.7)	2.7	57.7
Forearm	1.6 (0.2)	39.0 (2.1)	1.6	45.7
Hand	0.7 (0.1)	82.0	0.6	79.0
Thigh	10.3 (0.8)	37.2 (1.7)	14.2	41.0
Shank	4.3 (0.4)	37.1 (1.3)	4.3	44.6
Foot	1.5 (0.1)	44.9 (1.6)	1.4	44.2
Upper trunk	-	-	16.0	30.0
Middle trunk	-	-	16.3	45.0
Lower trunk	-	-	11.2	61.2

This advantage allows for designing the experiments in an appropriate way so that the BSPs data can be utilised. Despite these considerations, it should be noted that no matter how extensive and statistically reliable the BSPs data are, using literature data to calculate BSPs (for any particular TS) inevitably leads to a certain level of uncertainty error. The error could be significant if BSPs of the actual TS are significantly different from the average characteristics of TSs presented in Table 4.1.

Once the BSPs are known, the MCS can be used to reconstruct GRF through Equation 4.2. To prove the reliability of the segmental method, some researchers compared BCoM's trajectory estimated by the segmental method with that derived by the double integration method (Thirunarayan et al., 1996; Eames et al., 1999; Gard et al., 2004). It was found that the two methods

produced close estimates of BCoM's excursion during walking.

In the study of human-induced loads, the method was applied for different human activities (Bobbert et al., 1991; Racic et al., 2010a,b). The most successful application of MCSs is in the measurement of bouncing and jumping forces (Racic et al., 2010b). This is expected since these activities are simpler forms of human movement compared with walking and running. During bouncing and jumping, it can be considered that the trunk, in which BCoM is located, moves up and down as a rigid mass. Moreover, the left and right halves of the body usually exhibit similar pattern of movement, preserving the body symmetry. This is the reason why kinematic data of only half of the human body was recorded (Racic et al., 2010b). On the contrary, walking is considered a more complex activity, during which the two legs could generate different forces (Chapter 2). Therefore, it would be beneficial if a full-body model is employed in the study of walking. To the best knowledge of the author, only one previous study conducted by Racic et al. (2010a) looked into evaluating the pedestrian force measured by a MCS by comparing it against benchmark data recorded using an IFMT. They showed that the two sets of data agreed well in both time and frequency domains when inspected visually. However, no quantitative analysis for verification of the MCS method was provided. Besides, the study was limited to experiments with a single TS only.

To use MCS for GRF measurement, accuracy of the method as well as a practically achievable instrumentation of the human body by markers (e.g. using minimum number of markers and defining their exact locations) have to be investigated. Unfortunately, the literature does not provide recommendations

on these issues. As a result, one objective of the investigation in this chapter is to identify a marker model that produces reliable and relevant GRFs, preferably in both time and frequency domains.

With the availability of a single force plate (AMTI, 2007) and Vicon MCS in the Gait Laboratory at the University of Warwick, continuous walking could not be investigated. The author opted to compare the two methods with a stamping activity instead. Stamping is similar to walking in that it consists of single and double support phases, with a difference that because it is performed on the spot it can be recorded directly by a force plate. However, it should be noted that the trunk is more passive during stamping. Consequently, the stamping activity is likely to generate a lower GRF than walking. The author's hypothesis is that if the MCS can be used to measure the GRF generated by stamping, and given that it has already been proven to work in cases of highly energetic activities such as jumping and bouncing (Racic et al., 2010b), then it is likely that MCS can be used for monitoring the walking activity as well.

4.2.3 Facilities in Gait Laboratory

Gait Laboratory contains the Vicon system, a video-based optoelectronic system (Oxford Metrics Group, 2007). The capture room and camera layout are illustrated in Figures 4.2a and b, respectively. There are 12 Vicon cameras, MX1 to MX12, and one force plate, model OR6-7 (AMTI, 2007). The surface of the force platform is at the same elevation with the surrounding floor tiles, leaving a horizontal gap of 3 mm. This set-up aims to prevent occurrence of both mental and physical obstructions that may arise while the TS is

performing the stamping activity during an experiment.

The MCS consists of high speed and low latency cameras to allow for capturing real-time motion. Each camera records 200 two–dimensional (2D) frames in every second. The cameras are equipped with wide angle lenses. The aperture setting (in the range of 1.4–16) is set at 2.8 to control the amount of light passing through each lens. This parameter also stipulates the depth of field, i.e. the range of distances from objects to the camera lens that remains in sharpness, a requirement for the system to recognise markers. The capture volume, also known as the field of view, during experiments described in this chapter is $2 \times 3 \times 2.2\,\text{m}$ (width, length, and height, respectively, indicated as

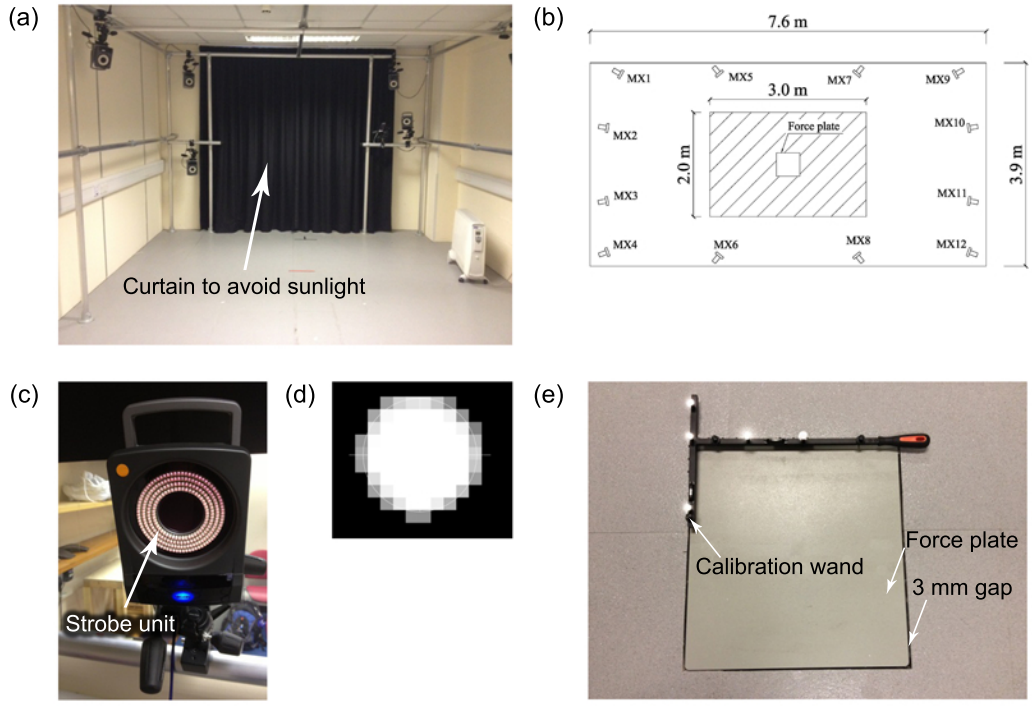

Figure 4.2: Gait Laboratory at the University of Warwick: **(a)** capture room, **(b)** camera layout, **(c)** camera with a strobe unit, **(d)** view of a marker in Vicon Nexus and **(e)** calibration wand and force plate.

shaded area in plan in Figure 4.2b).

The Vicon system uses passive markers, i.e. markers that reflect the light. The system is different from the alternative active markers system, in which markers emit the light. The advantage of the passive markers is that the TS is not required to wear wires and batteries to power the markers during trials. The use of the system, however, still faces challenges. Since the markers do not have unique identifiers, the anatomical landmarks on which they are placed are not recognised automatically. The post-processing of the acquired data requires manual labelling of each marker in Vicon Nexus, a specialised software used for capturing and analysing the data (Oxford Metrics Group, 2008). This step entails assigning each marker on the TS to a corresponding point on the body. This operation results in creating a TS's body model within the software, which can be used as a marker template. To apply this predefined template to a different TS, a procedure named "Subject calibration process" is employed (Oxford Metrics Group, 2008). In this step, all markers are captured while the TS is in a stationary (standing) posture. Afterwards, markers are labelled and the marker layout representing the body shape of the particular TS is fitted to the model template. Moreover, distances between labelled markers are measured and can be used later for automatic labelling.

The marker used in this study is 14 mm in diameter and is coated with a highly retro-reflective material. Each marker has the negligible mass of about 2 grams. To illuminate markers, the front of each Vicon camera contains a strobe unit (Figure 4.2c) configured with light-emitting diodes. When markers are visible inside the view range of a specific camera, rays of light from the strobe hit the markers and are reflected back to the camera lens. To optimize

the system's performance, each lens is fitted with an optical filter so that only the reflected light having similar wavelength with the one generated by the strobe unit can pass into the camera lens. The image from each camera is processed by the system, in which centroid-fitting algorithms are used to determine which objects are most likely to represent markers (Figure 4.2d). This process results in reconstructing the three–dimensional (3D) coordinates of markers within the capture space.

The light from light bulbs inside the capture room does not interfere with normal working conditions of the system. Any strong light sources have to be removed from the capture room (e.g. the lab window is covered by curtains to prevent passage of sunlight, Figure 4.2a). Although, the Gait Laboratory is designed in accordance with recommendations from Vicon user manual, there are still non-marker reflection points inside the capture volume. To avoid the possibility that the system might recognise them as markers, these points are removed within the software by a process called "Masking MX Cameras" (Oxford Metrics Group, 2008). The 3D space inside the capture volume is established through a dynamic calibration process. The system records the movement of a calibration wand with five fixed marker points until a sufficient number of frames are captured by all cameras. Based on these reference frames and known geometry of the wand, the system calculates the relative distances between cameras and their projections. By placing the wand on the floor and levelling it (Figure 4.2e), the horizontal plane of the 3D space is defined by the two perpendicular axes of the wand. After this step, the system is capable of using data from multiple cameras to reconstruct the 3D space inside the capture volume (Hasan et al., 1996). If a marker can be recognised by at least

two cameras, its spatial coordinates can be determined.

In static condition, the background noise of spatial data can be checked by monitoring stationary markers located within the capture volume for 30 s (Hasan et al., 1996). In the Gait Laboratory, the maximum 1 s RMS of the background noise was found to be less than 0.05 mm, which is considered acceptable for the current study.

4.3 Experiments of stamping activity

This section describes experiments involving TSs stamping on the top of the force plate and evaluates the accuracy of the GRF derived from kinematic data recorded using MCS at a sampling rate of 200 Hz. The force plate data are recorded at 1,000 Hz. Both force plate and camera data are recorded using Vicon Nexus. Data from the two systems are synchronised, making it possible to compare the GRF obtained from the two systems in the time domain.

The aim of the experimental programme is to identify best marker model that can be utilised for indirect measuring of the GRF. The strategy to achieve this aim consists of the following steps:

- Instrument a TS with a large number of markers, which can be combined in different ways to reconstruct the GRF, as per suggestions in literature and own ideas.
- Quantify the discrepancies in GRFs measured using the MCS (hereafter referred to as reconstructed force) and the force plate (hereafter referred to as directly measured force). Only first harmonic of the force in form of its dynamic load factor, called DLF_1, will be considered. The force signal measured using the force plate is

considered as a benchmark. Any discrepancies between the reconstructed and directly measured forces are considered to be errors caused by using the MCS. This assumption is not strictly correct, but it is considered as sufficient for the type of analysis performed in this section.

- Apply the reconstructed and directly measured forces as dynamic loads on a virtual structure, compare the structural responses and quantify the propagation of errors from the force measurement to the response estimation.

4.3.1 Methodology

Ten male TSs with no history of gait issues volunteered to participate in the experiments in Gait Laboratory. General information about TSs is summarised in Table 4.2. The data show that the characteristics of TSs in this study, expressed via a mean value and a standard deviation are not significantly different from those in the study of de Leva (1996) reported in Table 4.1.

Table 4.2: Characteristics of test subjects for experiments of stamping.

Test subject (TS)	Age (years)	Height (cm)	Mass (kg)
TS1	21	180	66.0
TS2	28	172	67.8
TS3	21	178	84.2
TS4	27	168	61.5
TS5	23	182	77.5
TS6	21	182	77.4
TS7	22	184	66.2
TS8	22	181	66.9
TS9	22	178	62.4
TS10	20	170	63.2
Mean ± standard deviation	22.7 ± 2.7	177.5 ± 5.6	69.3 ± 7.7

Prior to experiments, the test procedure and associated health and safety issues were explained to the TSs. TSs were requested to stay topless and to wear a pair of black tight running shorts to maximize the number of markers placed directly on the skin. TSs were asked to remove all objects that could reflect light, e.g. watches and spectacles, to avoid these objects to be identified as potential markers in Vicon. Markers were attached to the TS's body using double-sided tapes.

There were 34 markers used to instrument a TS, 15 of which were positioned on either half of the body. The remaining four markers (No. 9, 10, 11 and 14) were located approximately in the sagittal plane. The exact anatomical positions of all markers are explained in Table 4.3, while all markers are shown in Figure 4.3. Most of marker positions were chosen to match those from publications related to research on balance during standing (Lafond et al., 2004), gait's measurement (Bell et al., 1989; Kadaba et al., 1990; Whittle, 1997; Eames et al., 1999; Gard et al., 2004), and GRF reconstruction (Racic et al., 2010a).

Out of 34 markers, four candidate marker models consisting of one to 27 markers were chosen for the purpose of force reconstruction. The models are denoted as A, B, C and D in Table 4.3, and the markers associated with them are shown in Figure 4.4. Detailed descriptions of the four models are as follows:

Table 4.3: Positions of markers for experiments of stamping.

Body segment	Marker No.	Anatomy position	Model
Head	1,21	Cheek bone	B, C, D
Arms	2,22	Bony prominence on top of the shoulder joint	D
	3,23	Upper arm at the same longitudinal elevation with shoulder joints	B, C
	4,24	Bony prominence on the outside of the elbow joint	B, D
	5,25	On biceps tendon at the location of elbow joint	C
	6,26	Radial styloid process at wrist joint	C, D
	7,27	Ulnar styloid process at wrist joint	B, D
	8,28	Just below the middle knuckle on the hand	D
Trunk	9	Top of the breast bone	C, D
	10	Base of the breast bone	D
	11	On top of the navel fixed in position by using a wrap band	D
	12,13	Anterior superior iliac spine	C, D
	14	Midpoint of the two posterior superior iliac spines	A
Legs	15,29	Greater trochanter	B, C, D
	16,30	On knee cap, at the elevation of the knee joint centre	B, C, D
	17,31	Lateral malleolus	B, D
	18,32	On the extensor hallucis longus muscle, at the elevation of ankle joint centre	C
	19,33	Tip of the big toe	B, C, D
	20,34	On the back of the foot, at the elevation of toe markers	B, D

- **Model A** is an one-marker model. The purpose of this model is to test the hypothesis if one marker in the proximity of BCoM can be used to reconstruct GRF. Based on a number of studies of the sacral method (Eames et al., 1999; Gard et al., 2004), marker No. 14 is selected for this purpose.

- **Model B** comprises of 18 markers on two sides of the body. This

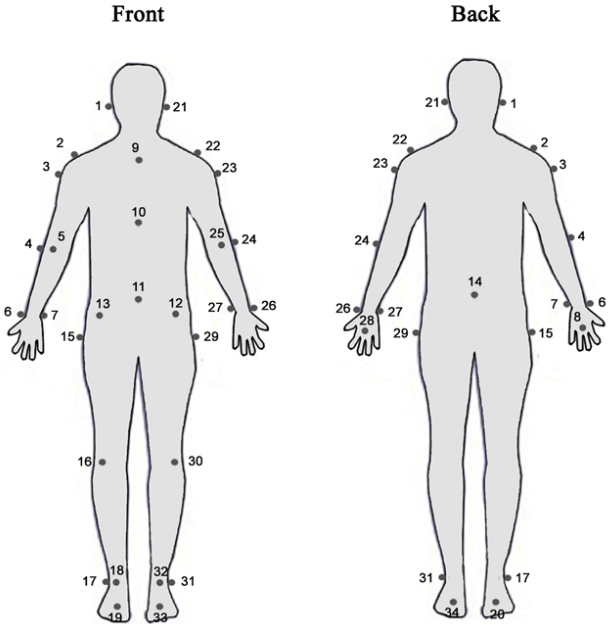

Figure 4.3: Positions of 34 markers attached to a test subject.

is the model used in a recent study of walking force reconstruction (Racic et al., 2010a). One outstanding issue that might be a shortcoming of Model B is that movement of the trunk is interpolated from markers on shoulders and hips, i.e. no markers are placed on the trunk for direct measurement. This interpolation might result in higher error associated with calculation of the inertia force of the trunk and potentially high influence of this error on the total GRF due to the trunk having the largest mass among body segments (Table 4.1). Besides, hands are not monitored in this model, of which masses are included in the corresponding forearm. This assumption is acceptable since the two hands possess only around 1.2 % of the body mass, and they are unlikely to have significant influence on the quality of the GRF reconstruction.

- **Model C** is a model involving 19 markers on the frontal part of the body only. This set-up was motivated by the fact that if all cameras are aimed at the front of the body, the number of cameras used in experiments can be reduced, making experiments more cost effective. Compared to Model B, a significant improvement

of Model C is the monitoring of the trunk by using markers No. 9, 12 and 13. On the downside, placing all markers on the frontal part of the body results in the ankle and elbow markers not being attached to the bony landmarks, which is likely to induce soft tissue artifact errors during measurements. Also, SCoMs of the two feet are measured using ankle and toe markers only, neglecting the heel parts. However, it is expected that this simplification does not significantly affect the force estimate. As in Model B, kinematics of hands are neglected.

- **Model D** is the most comprehensive model in this study, consisting of 27 markers. While the trunk is considered as one section in Models B and C, it is split into three parts in Model D, called upper, middle and lower trunks. The purpose is to track movements of different parts of the trunk and investigate if more detailed measurements can lead to better quality of GRF. The objective originates from the speculation that due to its high mass, inaccuracies in measuring kinematics of the trunk might be a source of large error. Differently from the previous models, hand movement is recorded in Model D.

Apart from layouts of markers in the four models, Figure 4.4 also shows individual body segments, the SCoMs and the BCoM. The locations of SCoMs and BCoM are calculated using data from de Leva (1996).

Before starting experiments of stamping, TSs were instructed to quietly stand on the force plate for 30 s. The average of the vertical component of recorded force plate data was then divided by the gravity acceleration to determine the body mass.

After measurement of body mass, a TS was requested to stamp on the force plate at eleven frequencies ranging from 1.5 to 2.5 Hz (0.1 Hz frequency step) with the assistance of a metronome. The order of stamping frequencies

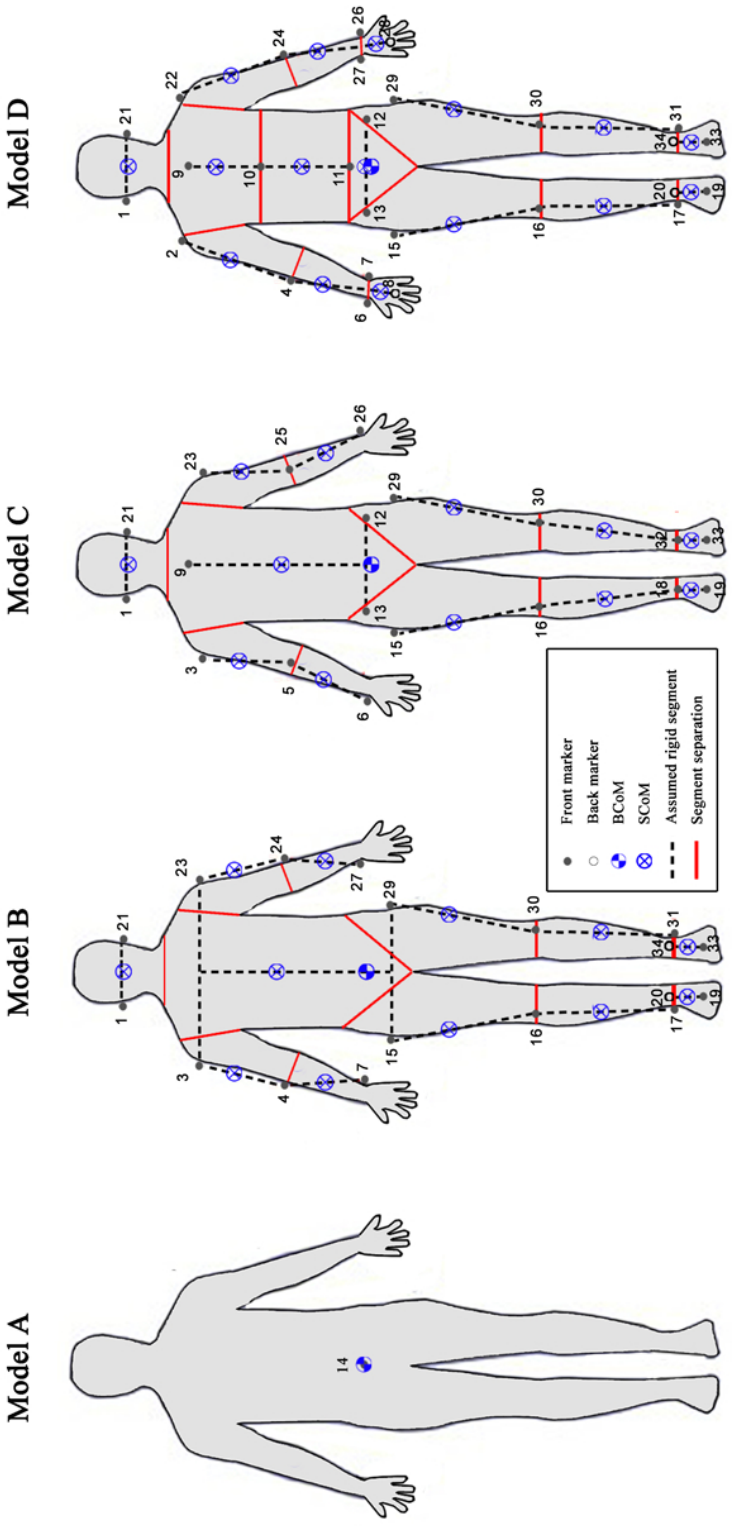

Figure 4.4: Frontal view of body segments in four marker models, and locations of the segment's and body's centre of mass.

during experiments for all TSs was 1.7, 2.0, 1.8, 2.3, 1.6, 2.1, 2.5, 1.9, 2.4, 1.5 and 2.2 Hz. The randomised order was chosen to avoid possible psychological bias associated with using exclusively either increasing or decreasing frequency order. Each TS completed three consecutive trials at any particular frequency before moving on to another frequency. In each trial, data capturing was started after the TS felt comfortable with synchronising the stamping pace with the metronome beat. The duration of each recorded trial was 60 s to ensure good frequency-resolution when transferring the data from the time to the frequency domain. After three trials at a single frequency, there was a short break of 30 s. During this break, the attachment of the markers to the body was checked. If a loose marker was detected, the last three trials were repeated. Overall, each TS completed 33 trials that qualified for the analysis. This process was completed in a test session lasting between 1.5 and 2.5 hours.

While stamping on the force platform, the TS might unconsciously step out of the force plate. To avoid this scenario, the TS was notified whenever he was close to the edge of the force plate. All trials when TSs stepped out of the force plate were repeated. In addition, a video camera aiming at the force plate operated in all trials for quality assurance.

4.3.2 Analysis of experimental data

For each marker model defined in Section 4.3.1, the GRF can be calculated. This section starts with description of data pre-processing, followed by some remarks about the stamping activity. Then accuracy of the reconstructed GRF across the four models is compared and quantified.

4.3.2.1 Data pre-processing

Raw kinematic data recorded using Vicon contain noise from different sources, e.g. electrical noise in the optoelectronic system (Winter, 2009) and soft tissue artifact (Racic et al., 2009). To remove the high frequency noise, both marker and force plate data were filtered by a low-pass Butterworth fourth-order zero-phase-shift filter with the cut-off frequency of 10 Hz (Mathworks Inc., 2010). Then force plate data were down-sampled to 200 Hz to make the signal directly comparable to Vicon data.

Occasionally during experiments, the camera's view of some markers was blocked by the moving parts of the TS's body (e.g. arms). As a result, the trajectories of these markers were lost for several fractions of a second. To rectify this, a procedure called "Fill gaps" was applied in Vicon Nexus software (Oxford Metrics Group, 2008). In this procedure, the data that precede and follow the missing portion were curve fitted and used as a basis for interpolation of the lost data. All trials with gaps of missing data greater than 0.1 s were repeated.

For the reliable vibration serviceability assessment of low-frequency structures under pedestrian excitation, the reconstructed force is required to have accurate frequency content around the first harmonic. To isolate the first harmonic, the reconstructed and measured forces were filtered by a band-pass filter with bandwidth between $0.75f_{\mathrm{s}}$ and $1.25f_{\mathrm{s}}$, where f_{s} is the stamping frequency. These filtered forces are used for the analysis in the rest of this chapter.

4.3.2.2 Key features of stamping activity

In every test session, each TS completed three trials at 11 frequencies. Even with the help of a metronome, there existed some variation in the achieved stamping frequency f_s. The stamping frequency of each step was found as a reciprocal value of the period of the step extracted from the time history of the filtered force. Figure 4.5a shows coefficient of variations (CoVs) of all TSs against stamping frequency. Each data point represents the average of three trials performed by a single TS at a particular frequency. Most trials exhibit a low CoV (up to 4 %) regardless of the stamping frequency, which is in line with findings of Brownjohn et al. (2004b) in relation to the walking activity.

DLF_1 is calculated as average of amplitudes of the reconstructed force in the time domain. Figure 4.5b shows the range of DLF_1 averaged across the trials for each TS. The data show that DLF_1 is less than 0.2 for all trials. As expected, DLF_1 for stamping is lower than that for walking. The latter, based on findings by Kerr (1998), is presented for comparison in Figure 4.5b.

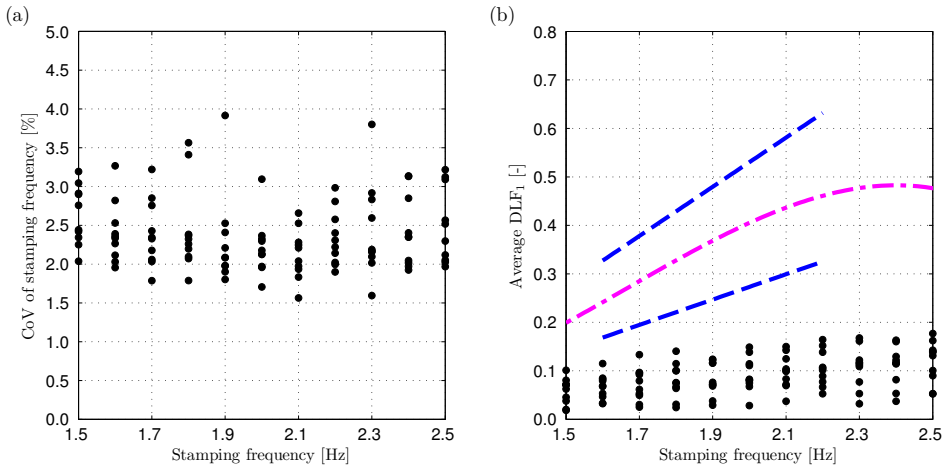

Figure 4.5: **(a)** Coefficient of variation of stamping frequency. **(b)** average DLF_1 in all trials, dash-dotted and dashed lines represent the mean and ± standard deviation of DLF_1 reported by Kerr (1998).

4.3.2.3 Reconstruction of ground reaction force

An example of the comparison between the reconstructed force (Model C) and the directly measured force is shown in Figure 4.6. The correlations between reconstructed and directly measured forces in the time domain are quantified by the coefficient of determination (R^2, where $R^2 = 1$ indicates perfect correlation). R^2 in this particular trial is 0.98. In the frequency domain, the frequency contents of the two measurements are quite close around the vicinity of the first harmonic (Figure 4.6b), with the discrepancy between the peaks being 13 % in this trial. The illustrated example is one of the least accurate measurements by the MCS when utilising Model C.

The R^2 coefficients, averaged across the three trials for each stamping frequency and each TS, are plotted in Figure 4.7. Model A results in the widest range of R^2 (from 0.2 up to nearly 1.0) while Models B, C and D have much narrower ranges (all above 0.83). Models C and D result in highest values of R^2, with vast majority of trials having $R^2 \geq 0.98$.

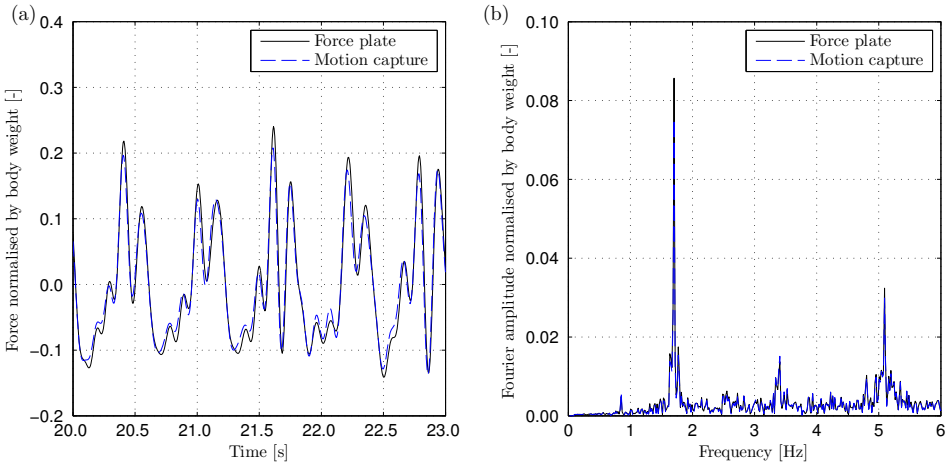

Figure 4.6: An example of reconstructed and directly measured ground reaction forces in **(a)** time domain and **(b)** frequency domain.

The percentage errors of DLF_1 (Δ_{DLF_1}) is calculated as follows:

$$\Delta = \frac{X - Y}{Y} 100\ [\%] \tag{4.3}$$

where Δ, X and Y represent Δ_{DLF_1}, reconstructed DLF_1 and directly measured DLF_1, respectively.

The percentage errors for all trials are shown in Figure 4.8. Each data point in the figure is the average error over the three trials by a TS at a particular frequency. While Model A significantly underestimates the directly measured DLF_1, Model B experiences a wide range of errors (from $-10\,\%$ to

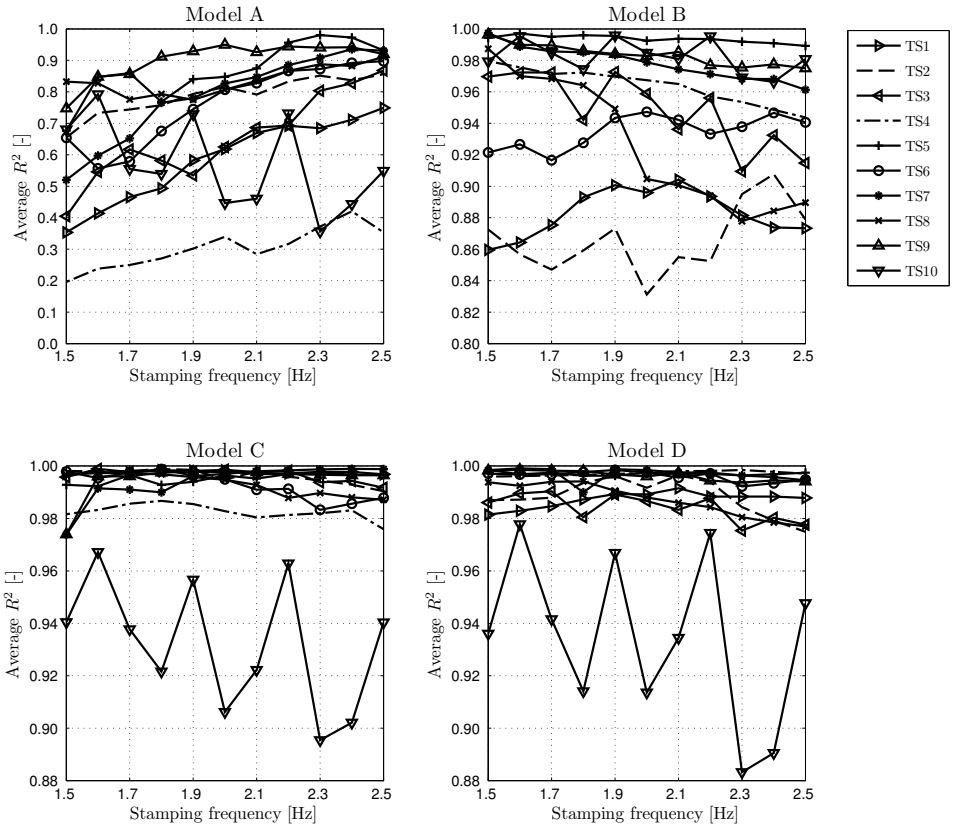

Figure 4.7: Average coefficient of determination of four models.

40 %). Similar to the result of R^2, Models C and D provide best estimates to DLF_1. In particular, 90 % of TSs have trials with the absolute percentage errors less than 15 %. It is noted that reconstructed forces in trials of TS10 have highest absolute errors in Models C and D. Results in Figures 4.7 and 4.8 show that Models C and D provide best GRF estimates.

Figure 4.9 shows the correlation between average R^2 of GRF in the time domain and the average error in DLF_1 for these two models. When R^2 is greater than 0.98 (dashed line in Figure 4.9), the absolute error in DLF_1 is less than 15 % (data points within two dash-dotted lines).

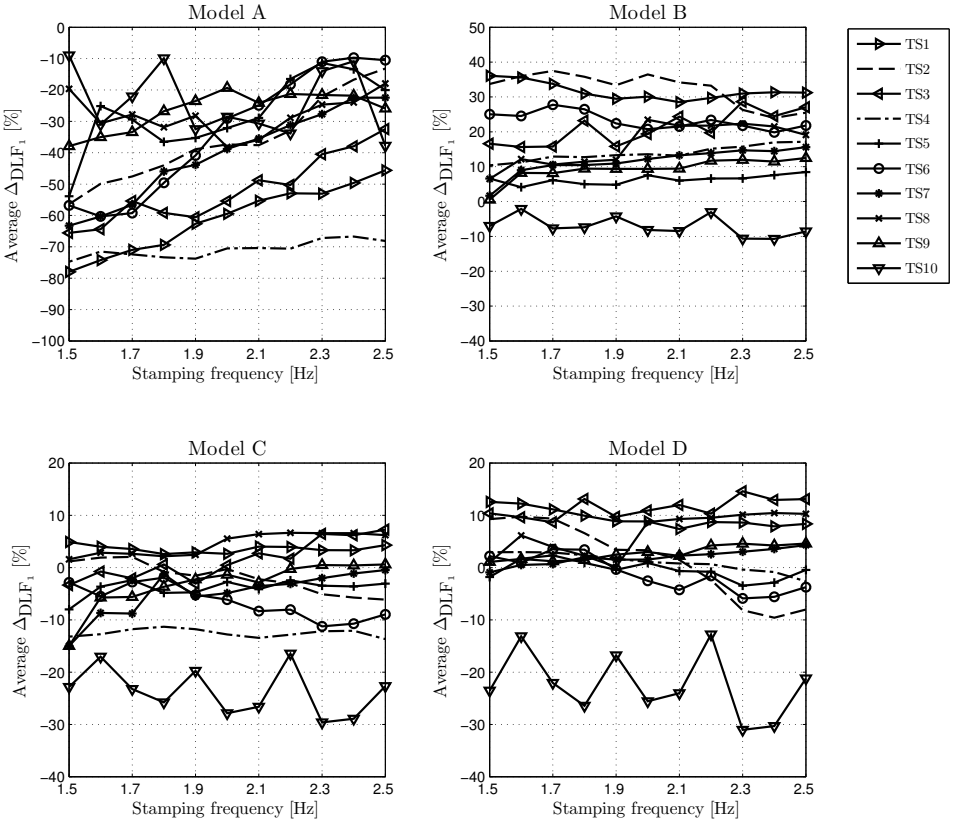

Figure 4.8: Percentage error of reconstructed DLF_1 of four models.

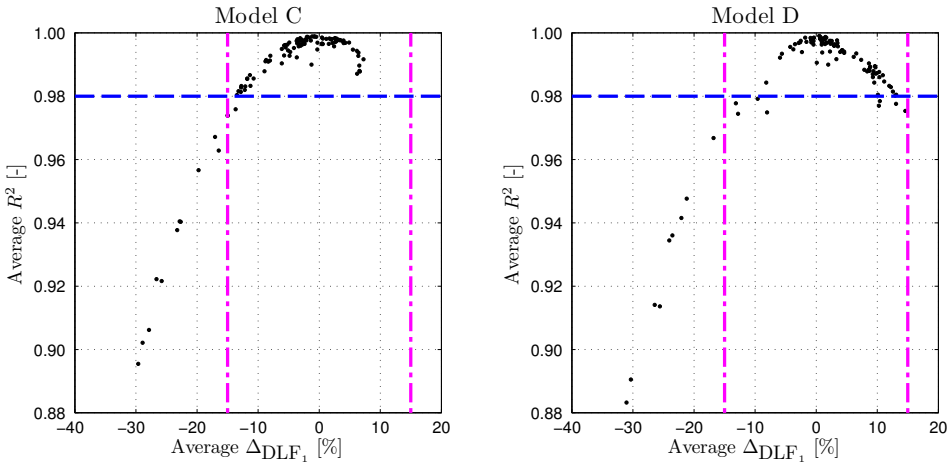

Figure 4.9: Correlation between average Δ_{DLF_1} and average R^2.

4.3.2.4 Simulation of structural responses

To test the performance of the four marker models, the reconstructed force and the directly measured force are used in simulations of vibration responses of a virtual structure. The purpose of this simulation is to quantify the error propagating from the reconstructed DLF_1 to the estimated structural response.

The structure is represented by a single degree-of-freedom (SDoF) system. The system has the modal mass of 10,000 kg. The damping ratio of the system ζ is selected at 0.3 %, which is at the lower end of the damping ratios seen in slender footbridges (Živanović et al., 2005b). The SDoF system is chosen to have a natural frequency varied in the range of 1–3 Hz (covering the range of stamping frequency 1.5–2.5 Hz), with 0.01 Hz frequency increment. The simulation time is chosen as the length of the reconstructed force signal in each trial, i.e. 60 s. This duration is expected to be sufficient for the build-up of structural vibration.

Simulations of structural responses induced by the reconstructed and directly measured forces in a resonant case are shown in Figure 4.10a. By varying the natural frequency of the SDoF, the peak responses obtained for the four reconstructed forces in a trial at 1.9 Hz are recorded and plotted in Figure 4.10b. In this particular case, Model A underestimates the structural response compared with that induced by the directly measured force (shaded area in Figure 4.10) while Model B overestimate the response. Similar to previous observations of performances of four marker models, Models C and D provide the best results, with Model C performing slightly better.

Similar simulations were carried out for all trials and all ten TSs. The discrepancy of peak response at resonant cases between the reconstructed and measured force simulations is quantified using percentage error Δ_{Peak} (calculated in the same manner as Δ_{DLF_1} from Equation 4.3). The errors across

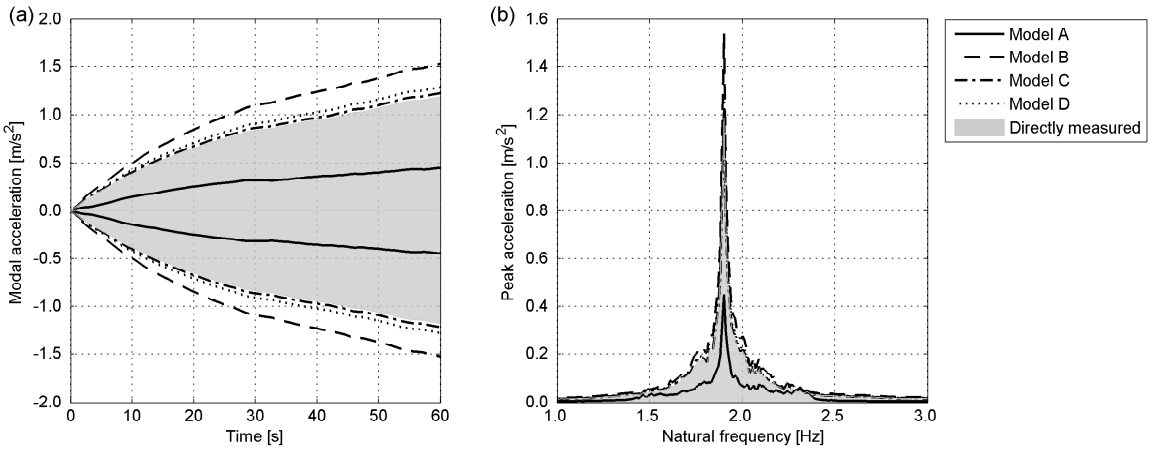

Figure 4.10: **(a)** Structural response of single degree-of-freedom system under reconstructed and directly measured forces in a resonant case and **(b)** peak acceleration as a function of natural frequency of single degree-of-freedom system. The force used is the trial of TS1 stamping at 1.9 Hz.

three trials (performed by a TS at a particular stamping frequency) are averaged and plotted in Figure 4.11. The range of the error for Models C and D is much narrower than that for Models A and B. For Models C and D, 90 % of TSs have all trials with the absolute percentage errors below 15 %. Similar to the average errors of DLF_1, absolute errors in trials by TS10 are greatest.

Figure 4.12a presents the correlation between the error in DLF_1 and the error in the peak response at resonance for all trials. The results show that the relation is almost linear. This observation is confirmed by the Pearson's linear correlation coefficient being close to 1 (Figure 4.12b). It is noted that

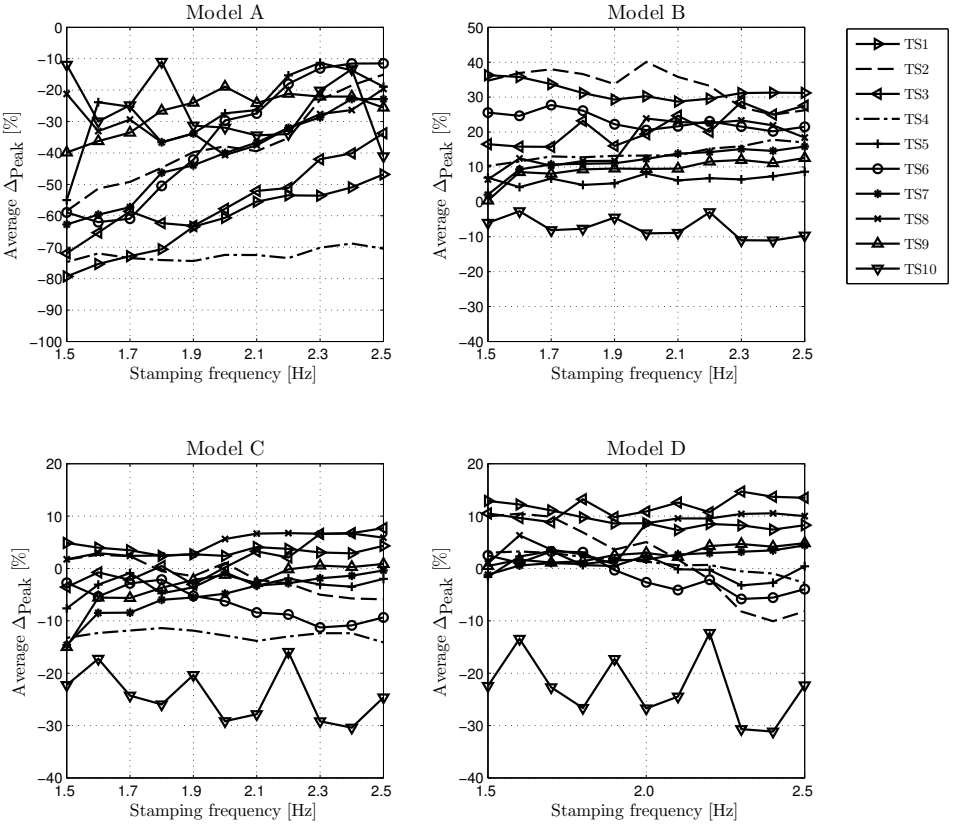

Figure 4.11: Percentage error of peak responses of single degree-of-freedom system for excitation in resonance.

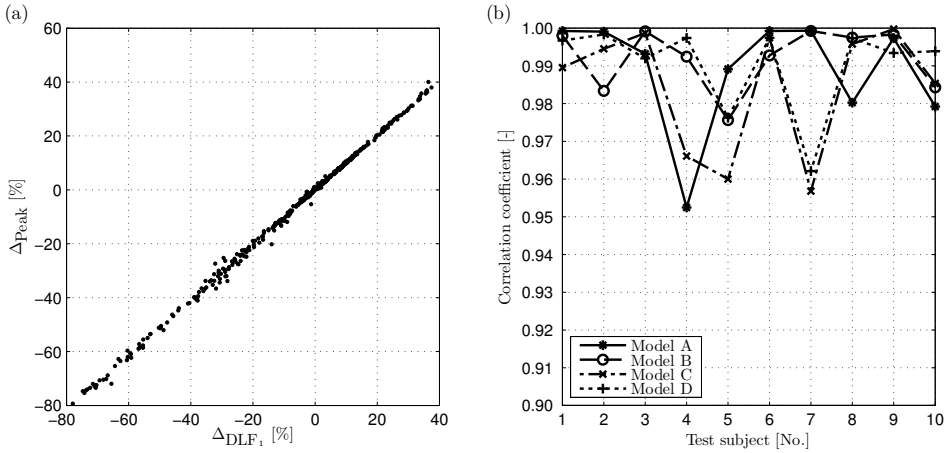

Figure 4.12: (a) Average error in the structural response as a function of average error in DLF_1 for all trials. **(b)** Pearson's linear correlation coefficient.

each data point in Figure 4.12b shows the correlation coefficient averaged across all 33 trials performed by a TS. Good correlation is expected due to the narrow-band nature of the first forcing harmonic. Small amount of energy dissipation around this harmonic means that the dominant frequency line has major influence on the vibration response at resonance. Higher the error in estimation of the amplitude of this harmonic leads to a higher error in the estimation of the vibration response.

4.3.3 Discussion

Four marker models taken from various studies in literature were used to reconstruct GRF generated by stamping. The reliability of each model for assessing vibration of low-frequency structures was quantified to identify the best model to be used for further experiments of walking activity on the rigid surface (Section 4.4) and the lively surface (Chapter 5).

Though it is desirable to use a single marker to represent the pedestrian force, the study shows that using only the sacral marker (Model A) is not a reliable method. The reconstructed GRF does not correlate well with the measured force in either time or frequency domain. The errors in DLF_1 and peak acceleration response are also excessive. As a result, Model A is not used further in this study. It is noted that there may be other points on the body that can be better suited to reconstruct the GRF from measurement using a single marker. It is, however, beyond the scope of this thesis to determine/investigate locations of such points.

Model B was selected for evaluation since it was the only model available in literature (Racic et al., 2010a), where it was used for GRF reconstruction during walking. The reconstructed force seems to be in qualitative agreement with the directly measured force. However, comparisons of DLF_1 and peak acceleration response show that the accuracy of this model is not satisfactory, in which absolute errors were greater than 15 % for 50 % of TSs. The likely reason for higher errors in this study compared with that of Racic et al. (2010a) is that this study used experimental data from ten TSs while Racic et al. (2010a) only used a single TS. As a result, this study is more comprehensive and able to capture cases of high errors in Model B that the previous study might have missed.

The analysis shows that Models C and D provide best reliability with respect to GRF reconstruction. Although Model D is a more comprehensive model (the trunk is composed of three parts, hand and heel markers are instrumented, ankle and elbow markers are placed at bony landmarks), the difference between the two models has been shown to be insignificant. In both models,

the percentage error of reconstructed DLF_1 and peak simulated response (in most trials) are less than 15 %.

It should be noted that even when using Models C and D, the reconstructed GRF exhibit errors, which are most excessive for TS10. In general, there are two probable sources of the errors. The first source originates from the application of BSP data available in literature to the TSs in this study. The variations in terms of body shape result in different BSP data for each individual. In some cases when the individual data is too different from the BSP data in literature, the estimations of SCoMs and BCoM (and consequently reconstructed GRF) are prone to errors. The highest error in the reconstructed force is for TS10, who is from Chinese Asian ethnic origin. He is shorter and lighter than the average TS in the study of Zatsiorsky et al. (1990), from which the BSP data used in this study originate. This discrepancy is most likely the main cause of the error in GRF reconstruction. The second source of errors is the assumption of rigid segments. Due to the inherent errors of soft tissue artifact, this assumption is not strictly correct. When markers move relatively to the underlying bones, measurements of movements of the assumed segment end-points contain errors. This type of error propagates to the estimation of SCoMs and, again, subsequently affects the accuracy of the reconstructed GRF.

It was found in the review in Chapter 2 that PSDI might influence frequency content of dynamic forces. The changes could be reflected in the variations of the pacing rate and amplitude of averaged DLF_1 when compared to walking on the rigid ground. It is, therefore, crucial that the measurement method proposed in this chapter is able to capture these potential changes.

During the analysis, it was found that the DLF_1 for reconstructed and directly measured forces always had peaks at the same frequency. This observation gives confidence that the MCS can be used to accurately determine the actual frequency of the performed activity. In addition, the maximum percentage errors of DLF_1 and peak responses using Models C and D are $\pm 15\,\%$ (if data from TS10 are discarded), with majority of trials (about $65\,\%$) exhibiting errors up to $\pm 10\,\%$. This uncertainty level is believed to be lower than the expected discrepancy between the forces recorded in the presence and in the absence of PSDI. As a result, it is believed that using MCS is an acceptable method for the GRF reconstruction provided Model C or D is implemented. Due to the fewer number of required markers and cameras, Model C is chosen for GRF reconstruction in further studies.

4.4 Experiments of walking activity

This section investigates the kinematic and kinetic aspects of walking on the rigid surface using the MCS. The result will later be compared with those acquired on the lively surface (Chapter 5) and used to establish a numerical model (Chapter 6). To capture walking gait over multiple steps in a confined space like the Gait Laboratory, a treadmill was used in the experiments. This section begins with a description of the treadmill, followed by the experimental methodology. Then a detailed analysis of gait parameters is provided along with the discussion how characterised parameters could inform experimental modelling. At the end of the section, a critical evaluation of the findings in the context of use of the inverted pendulum model is made. Ten TSs participating

in the study of the "walking activity" are not the same TSs that took part in the study of the "stamping activity". Therefore, the code names from TS1 to TS10 used in the two sets of tests are not linked.

4.4.1 Treadmill

A treadmill, model F63 (Fuel Fitness, 2013), was installed in the Gait Laboratory to allow for monitoring of the walking gait over multiple steps. The treadmill is located approximately in the centre of the capture room. Positive directions of X, Y and Z axes of the global coordinate system used for data capture by Vicon are displayed in Figure 4.13a.

The treadmill can withstand walker with the maximum body mass of 130 kg. The belt speed ranges from 1 km/h to 18 km/h (i.e. from 0.28 m/s to 5.00 m/s), covering the speed range of interest (0.8–2.0 m/s) typical for walking (Živanović, 2012). The treadmill has the speed adjustment step of 0.1 km/h (i.e. 0.028 m/s). The circumference of the walking belt is measured and has the length of 3.01 m. Users can select a particular walking speed

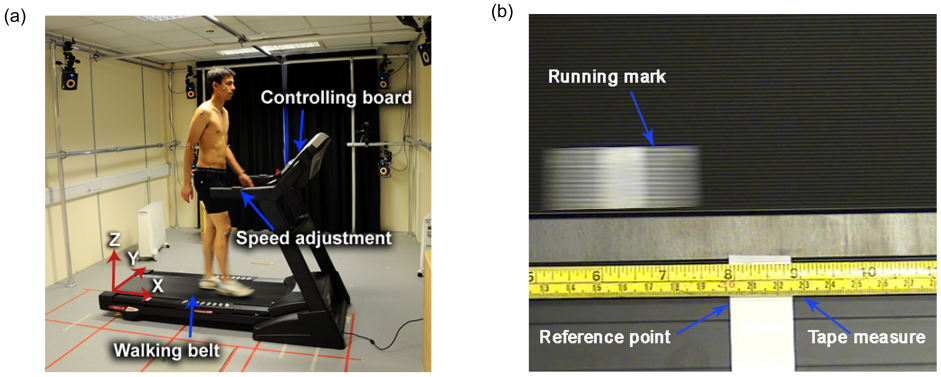

Figure 4.13: (a) Treadmill used in experiments of walking and **(b)** verification of treadmill speed.

on the controlling board and use the speed adjustment buttons (increase or decrease) to refine the speed selection (Figure 4.13a). The speed shown on the display of the controlling board is hereafter referred to as the displayed speed. The displayed speed was verified by monitoring a mark (Figure 4.13b) on the walking belt by a video camera. Measuring time needed for the running mark to make 50 laps and knowing the belt circumference, the actual belt speed could be calculated. The result of this check shows that the displayed speed underestimates the actual speed from 3 % to 5 % across the speed range of interest (0.8 m/s to 2.0 m/s). The displayed speed was used to instruct TSs during experiments while the speed used in the analysis was increased by 4 % to compensate for the error.

4.4.2 Methodology

Ten young and healthy male TSs volunteered to participate in the experiments. Their characteristics are summarised in Table 4.4. Having shown that the MCS could produce sufficiently accurate GRF when used in conjunction with marker Model C (Section 4.3), this marker model was used in the walking experiments to reconstruct the GRF.

Prior to the experiments, each TS was given a 15-minute session on the treadmill at a number of speeds of personal-choice, ranging from 0.8 m/s to 2.0 m/s. The purpose of this warm-up exercise was to help TS familiarise himself with walking on treadmill, so that this study can be considered equivalent to walking on rigid surface (Matsas et al., 2000).

During experiments, TSs were required to stay topless and wear a black

Table 4.4: Characteristics of test subjects for experiments of walking on rigid surface.

Test Subject	Age (years)	Height (cm)	Mass (kg)
TS1	21	180	62.4
TS2	28	172	72.7
TS3	21	181	68.7
TS4	23	178	64.4
TS5	24	184	75.4
TS6	24	177	86.0
TS7	25	177	63.0
TS8	28	181	82.0
TS9	29	172	86.0
TS10	27	166	63.2
Mean ± standard deviation	25.0 ± 2.9	176.8 ± 5.4	72.4 ± 9.6

tight shorts (as in the experiments of stamping activity). Then, 21 markers were attached to the TS's body, of which 19 markers were chosen so to represent Model C (Figure 4.4). The additional two markers were placed one on each heel.

In each trial, TS was instructed to select a particular displayed speed. Data capturing started 30 s after speed selection so that the treadmill could reach the targeted speed and TS could achieve a stable walking gait. A minimum of 450 steps was captured in every trial. The choice of 450 steps was made to ensure acquiring statistically reliable data on gait parameters, in accordance with suggestion by Owings and Grabiner (2003) that at least 400 steps should be measured.

There was a one-minute break between two consecutive trials. In one test session (lasting about two hours), a TS completed 13 trials with different speeds in the range from 0.8 m/s to 2.1 m/s (approximately 0.1 m/s speed

step). This speed range covers the mean (1.39 m/s) ± three standard deviation (0.2 m/s) of experimentally acquired walking speed (Živanović, 2012). The order of the walking speed in a session was 1.15, 1.56, 1.36, 1.88, 1.67, 2.08, 1.76, 1.04, 1.24, 0.84, 0.93, 1.97 and 1.45 m/s. This randomised order was used to avoid psychological bias that could appear in experiments with increasing or decreasing speed values.

At the end of each trial, the TS was asked to categorise the speed as either slow, normal or fast. A summary of answers of TSs is shown in Figure 4.14. The boundary between two neighbouring categories (represented by solid lines) is calculated as the mean of two neighbouring speeds which lie in different categories. Answers of the TSs show that the range of speeds in the experiments covers the three categories of walking speeds for all TSs. The boundaries between slow and normal speeds and between normal and fast speeds vary among TSs, which is the result of the inter-subject variability in the speed perception. The variability might stem from the different level

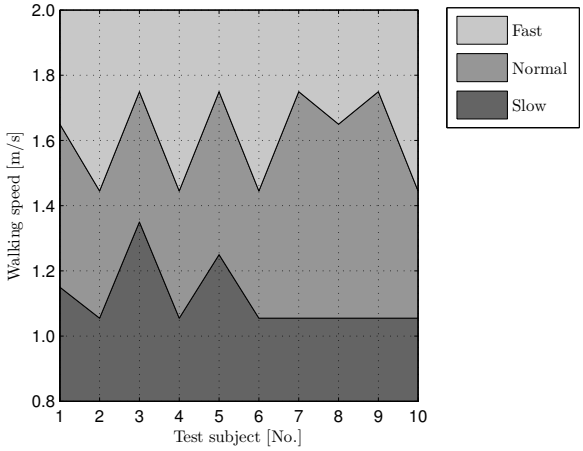

Figure 4.14: Walking speed perception for ten test subjects.

of fitness between TSs and differences in their body configurations. All TSs with high upper limit of normal walking speed (1.6 m/s and above) acknowledged their weekly participation in sport activities (running, squash, tennis or football).

4.4.3 Analysis of experimental data

Similar to the analysis of stamping activity, the post-processing of the data acquired during walking consists of filtering and gap-filling (when needed). This section presents statistical characterisation of experimentally monitored gait parameters and quantification of the inter- and intra-subject variabilities. Pacing rate, which is the key temporal parameter, is first analysed. Next, two spatial parameters (step length and step width) are presented. Angular positions of legs and the trunk during walking are then investigated. Finally, the reconstructed GRF is presented. The analysis in this section includes all the steps captured in each trial, i.e. approximately 450 steps.

In this section, average value of a parameter in a trial is hereafter referred to as "the average value". Mean value of the averages across all TSs (walking at a particular speed) is referred to as "the mean value".

4.4.3.1 Pacing rate

Pacing rate f_{p} is calculated as the reciprocal value of the duration of the walking step. The duration can be measured as time elapsed from the heel-strike event of one foot to the heel-strike event of the other foot. To detect these events, a method proposed by Zeni et al. (2008) is used. The method is

based on the observation that the X coordinate of the heel marker (solid line in Figure 4.15) changes from moving in the positive X direction to a negative X direction at the heel-strike event (coordinate system is in Figure 4.13a). As a result, the time instant at which the X component of the velocity vector changes from a positive to a negative value can be regarded as the heel-strike event (circles in Figure 4.15). When this time instant occurs between two consecutive data points, linear interpolation of the two neighbouring frames was used to determine the timing of the heel-strike event. As a result, the period (denoted as T_p in Figure 4.15), and eventually pacing rate, can be calculated on a step-by-step basis.

Examples of the pacing rate induced by left and right feet for four TSs on a step-by-step basis are presented in the left side of Figure 4.16. The data show that the pacing rate exhibit large variations. The average and average ± standard deviation of the pacing rate are shown as dashed and dash-dotted

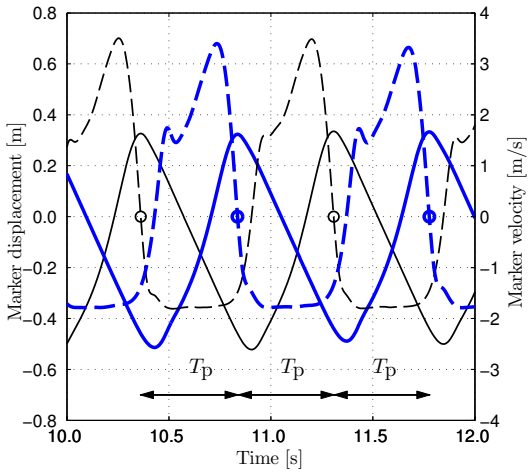

Figure 4.15: Displacement (solid line) and velocity (dashed line) of heel marker in X direction. Thick and thin lines represent the right and left legs, respectively.

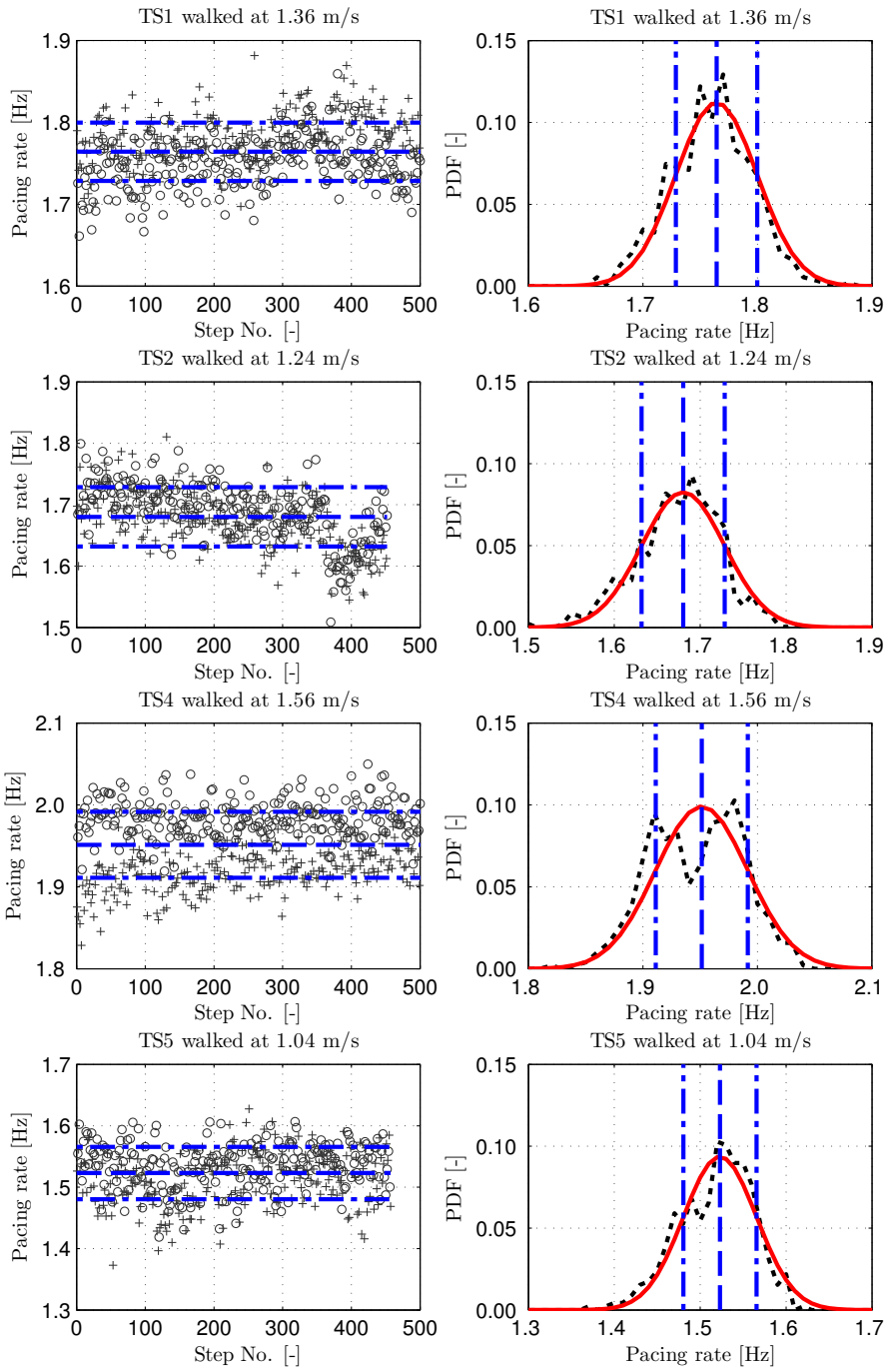

Figure 4.16: Pacing rate and its distribution in four trials. Left side: crosses and circles are pacing rate induced by left and right legs, respectively. Right side: distribution of the measured pacing rate (dotted line) and the corresponding normal distribution model (solid line). Dashed and dash-dotted lines represent the average and ± standard deviation of the pacing rate, respectively.

lines, respectively. These statistical values are used to define the normal distribution model shown in the right side of Figure 4.16, along with the probability density functions (PDFs) of the experimental data. Judged visually, the two distributions are quite similar in many trials. Based on this observation, a hypothesis that the experimental data follow normal distribution was made. To test the hypothesis, the Kolmogorov-Smirnov goodness-of-fit test is used (Massey, 1951). One of the test statistics, p-value, indicates the plausibility of the hypothesis, i.e. high p-value supports the hypothesis while lower value casts doubt on the hypothesis. The cumulative distribution function (CDF) of p-value calculated for all trials is plotted in Figure 4.17a. For the significance level of 5 % (dashed line in Figure 4.17a), around 90 % of the trials fail to re-

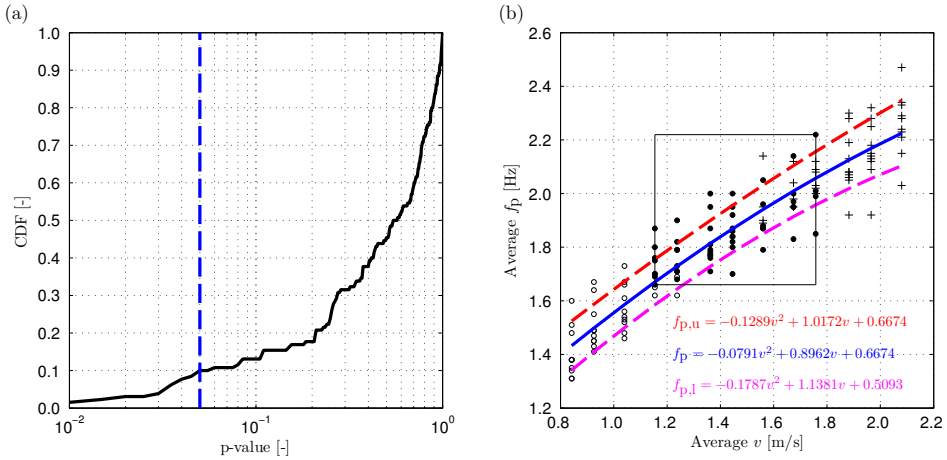

Figure 4.17: **(a)** Cumulative distribution function of p-value in Kolmogorov-Smirnov test (solid line) and the significance level of 5 % (dashed line). **(b)** Average pacing rate as a function of average walking speed. Unfilled circles, filled circles and crosses represent slow, normal and fast walking speeds, respectively; the rectangular box contains all data points for normal walking speed; solid and dashed lines represent best fits of mean values and the corresponding standard deviation band (calculated at individual speeds), respectively.

ject the hypothesis. The top two rows in Figure 4.16 are examples of the trials that failed to reject the hypothesis of normal distribution, while the bottom two rows represent two trials in which the hypothesis was rejected. Since the majority of the trials fail to reject the normal distribution hypothesis, it is highly probable that the pacing rate on the rigid surface might be modelled as normally distributed.

Figure 4.17b illustrates the relation between the average pacing rate f_{p} and the average walking speed v. Each data point was calculated as the average of recorded pacing rates on a trial-by-trial basis. The inter-subject variation in pacing rate can be attributed to the individual's natural walking style and physical features, e.g. leg length. Results in Figure 4.17b show that the average pacing rate increases at higher walking speeds. Best least square second-order polynomial fit of the mean value (solid lines) and standard deviation boundaries (dashed lines) across the TS population are also shown. The best fit polynomial functions are also written in the figure and they appear in the same order as the best fit lines in the graphic representation. Subscripts "u" and "l" refer to the upper and lower boundaries of the standard deviation band.

Figure 4.17b also conveys information about the TS's perception of the walking speed. Unfilled circles represent slow speed, filled circles are related to normal speed, while crosses represent fast speed. The rectangular area in the figure is a subset that includes all trials in which the speed was classified as normal (1.15–1.76 m/s). The average pacing rate over the normal speed range is between 1.66 Hz and 2.22 Hz.

The CoV of pacing rate was calculated for each trial and it is plotted as a function of the average walking speed and the average pacing rate in Figure

4.18. The result shows that the CoV is highest at lowest speed and pacing rate. This observation is expected since at low speeds (and also low pacing rates), the duration of each step is unnaturally long and pedestrians find it difficult to walk in a consistent way. In comparison, TSs exhibited less variation at higher speeds. It is interesting that least variation occurs approximately at the boundary between the normal and fast walking categories. For all trials at normal walking speed, the CoV is between 1.1 and 2.9 % (the data points inside the rectangle in Figure 4.18a). In Figure 4.18b, the CoV is between 1.1 % and 5.1 % across the recorded pacing rate range (1.31–2.47 Hz). This is a refined finding compared with the study by Brownjohn et al. (2004b), which states that the CoV is about 3 % (without specifying the pacing rates). It should be noted that their results are based on data from three TSs only.

Statistical characterisation of the pacing rate shown in Figures 4.17 and 4.18 is used as a template for presentation of data related to other locomotion parameters in the remainder of Section 4.4.3.

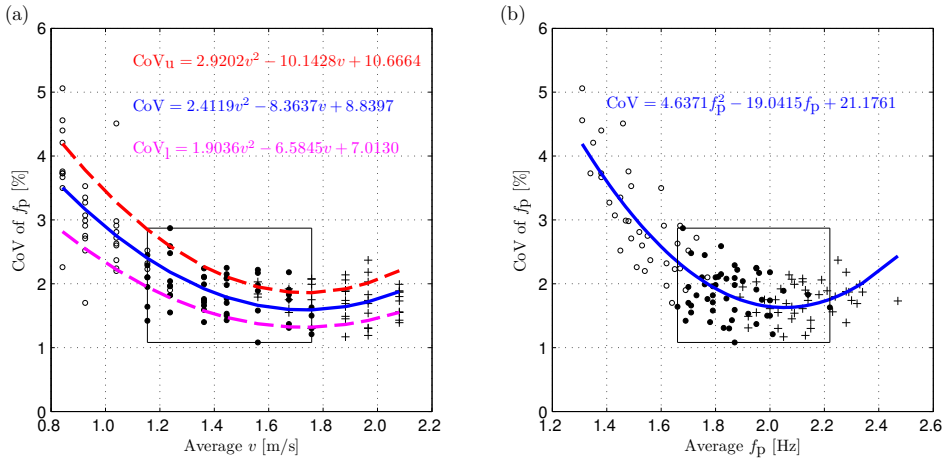

Figure 4.18: Coefficient of variation of pacing rate as a function of **(a)** average walking speed and **(b)** average pacing rate. Lines and symbol explanations are the same as in Figure 4.17b.

4.4.3.2 Step length

Step length d can be calculated as the distance the pedestrian travels between two successive heel-strikes. Because the walking belt keeps rolling during experiments, the calculation of step length on the treadmill is more difficult than that on the ground. Instead of measuring the distance between two consecutive heel-strikes, the measurement can be simplified by calculating the distance between the two heel markers at the heel-strike event of the leading leg. For a particular trial, these time instants are represented as circles while the calculated step lengths are shown as dash-dotted lines in Figure 4.19a. A limitation of this method is that at the heel-strike of the leading leg, the trailing leg's heel is not in contact with the ground, i.e. the heel is airborne (Figure 4.19b). Through engaging in upward movement, this heel marker starts progressing

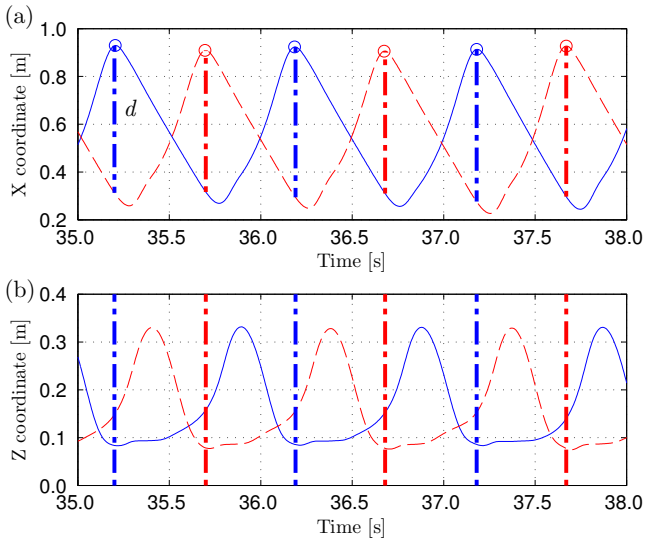

Figure 4.19: Trajectories of left (solid) and right (dashed) heel markers in **(a)** forward and **(b)** vertical directions. Data presented belong to the trials of TS7 walking at 1.45 m/s.

forward (to the positive direction of the X axis) shortly after the heel-strike event of the leading leg (Figure 4.19a). Therefore, the error between the calculated and actual step length is expected to be small.

Figure 4.20a shows the distribution of step length in a typical trial (TS3 walking at 1.45 m/s), in which the distribution is close to the normal distribution. In Figure 4.20b, CDF of p-value from the Kolmogorov-Smirnov test shows that 90 % of the trials fail to reject the hypothesis of normal distribution for step length. Similar to the analysis of pacing rate, it is highly possible that step length can be modelled as normally distributed.

Figures 4.20c and 4.20d show the plots of average step length as a function of the average walking speed and the average pacing rate. The step length tends to increase with an increase in walking speed and pacing rate. For normal walking speeds, the range of step length is between 0.56 m and 0.84 m.

CoV of step length was calculated for every trial and plotted against walking speed and pacing rate in Figures 4.20e and 4.20f. The CoV seems to be at minimum at the walking speeds around the boundary between normal and fast walking. For normal walking speed, the CoV is between 1.3 % and 4.7 %.

4.4.3.3 Step width

Bauby and Kuo (2000) defined the step width w as the distance between the centres of the two feet in the lateral direction (i.e. Y direction in Figure 4.13a). In this study, the centre of each foot is approximated as the midpoint between the toe and the heel markers. The step width for each step is then calculated as the lateral distance between these centres at heel-strike of the leading leg.

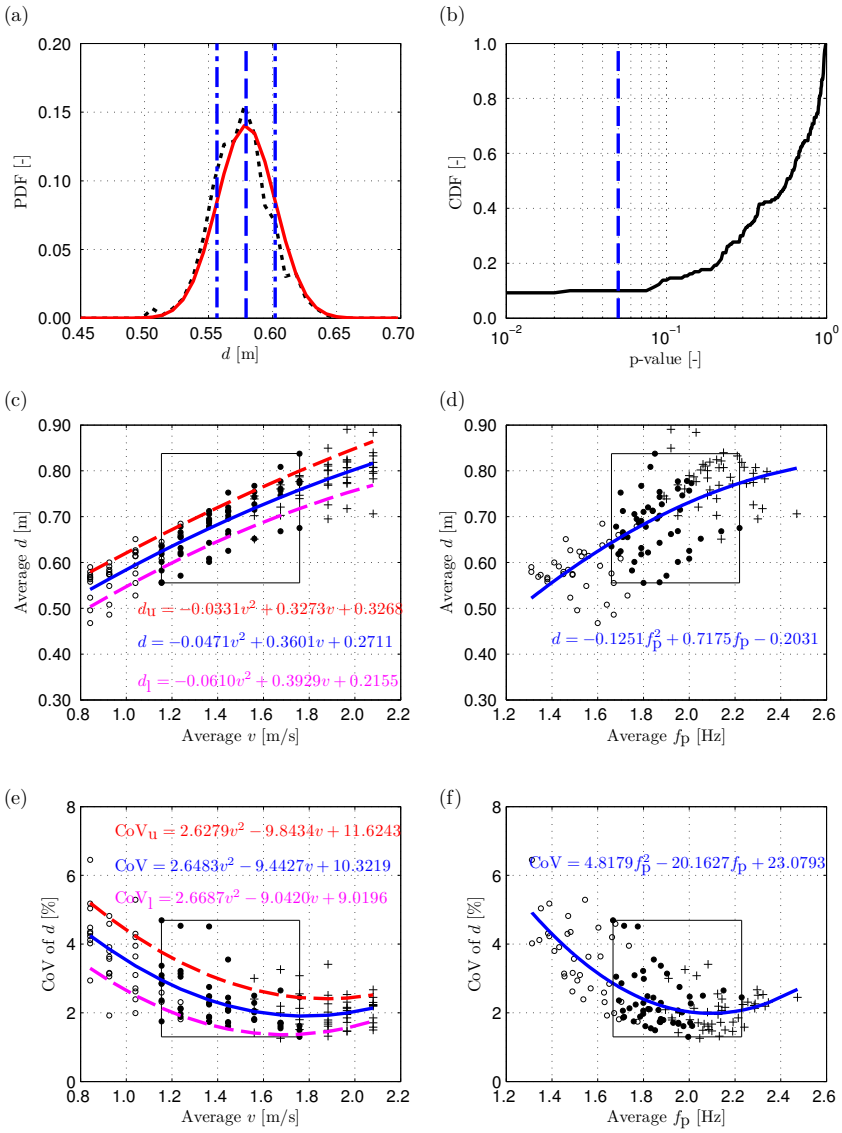

Figure 4.20: **(a)** Distribution of step length (dotted line), average step length (dashed line), average ± standard deviation (dash-dotted line) and the corresponding normal distribution model (solid line). **(b)** Cumulative distribution function of p-value of Kolmogorov-Smirnov test (solid line) and the 5 % significance level (dashed line). Average step length versus **(c)** average walking speed and **(d)** average pacing rate. Coefficient of variation of step length versus **(e)** average walking speed and **(f)** average pacing rate. From figures **(c)** to **(e)**: unfilled circles, filled circles and crosses represent slow, normal and fast walking speeds, respectively; rectangular boxes contain all of data points for normal walking speed; solid lines and dashed lines represent best fit of mean values and the corresponding standard deviation band (calculated at individual speeds), respectively.

Figure 4.21a shows the distribution of w measured on a step-by-step basis in a single trial (TS7 walking at 1.45 m/s). Kolmogorov-Smirnov test of normal distribution is used to calculate the p-value, of which CDF for all trials is plotted in Figure 4.21b. The result shows that 99 % of the trials fail to reject the hypothesis of normal distribution.

Figures 4.21c and 4.21d show the average step width as a function of the average walking speed and the average pacing rate. The results show that w seems to be independent from either walking speed or pacing rate. The mean step width for ten TSs is approximately 100 mm across the investigated speed range. The result is in line with the preferred step width of about 120 mm reported by Donelan et al. (2001). For normal walking speeds, the step width ranges from 60 mm to 143 mm.

The CoV of step width as a function of the average walking speed and the average pacing rate is shown in Figures 4.21e and 4.21f, respectively. It seems that the CoV is not strongly dependent on either the average walking speed or the average pacing rate. For normal walking speed, the CoV is between 13.4 % and 39.2 %. This variation is significantly larger than the variation of step length. It can be concluded that the spatial parameter exhibits much smaller variation in the superior-anterior direction than in the lateral direction. This observation is in line with findings by Bauby and Kuo (2000).

4.4.3.4 Other kinematic parameters of interest

This section describes three angular parameters during walking, which are of interest in modelling walking gait. These parameters are attack angle, end-of-step angle and trunk angle.

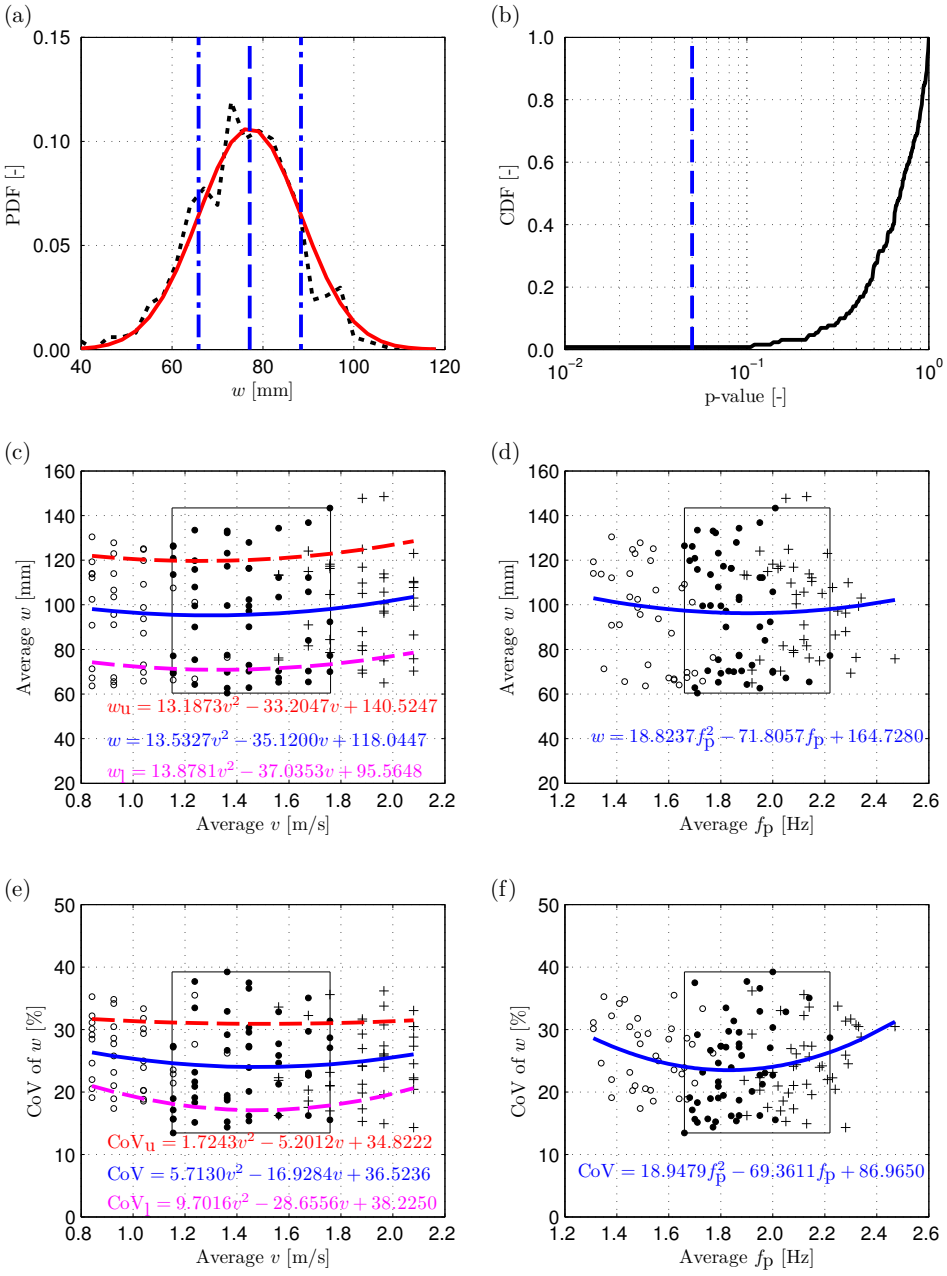

Figure 4.21: **(a)** Distribution of step width and the corresponding normal distribution model. **(b)** Cumulative distribution function of p-value of Kolmogorov-Smirnov test. Average step width versus **(c)** average walking speed and **(d)** average pacing rate. Coefficient of variation of step width versus **(e)** average walking speed and **(f)** average pacing rate. Line and symbol explanations are the same as in Figure 4.20.

Attack and end-of-step angles

Two key parameters used to formulate bipedal models of walking locomotion are the attack angle θ_0 and end-of-step angle θ_e, characterising the beginning and the end of the stance phase, respectively (Figure 4.22).

To measure θ_0, Geyer (2005) approximated the leg as a line connecting the BCoM and the foot. The BCoM was estimated as the midpoint between the two hip markers while the foot was represented by the midpoint between the toe and the ankle markers. In another attempt to measure the attack angle, Kim and Park (2011) approximated the BCoM by the sacral marker while the foot was represented using the ankle marker. The shortcoming in the two studies of not correctly defining the position of the BCoM is overcome in this thesis by determining the BCoM using the segmental method (Model C in Section 4.3).

With regard to the measurement of θ_0, the foot position is defined by the

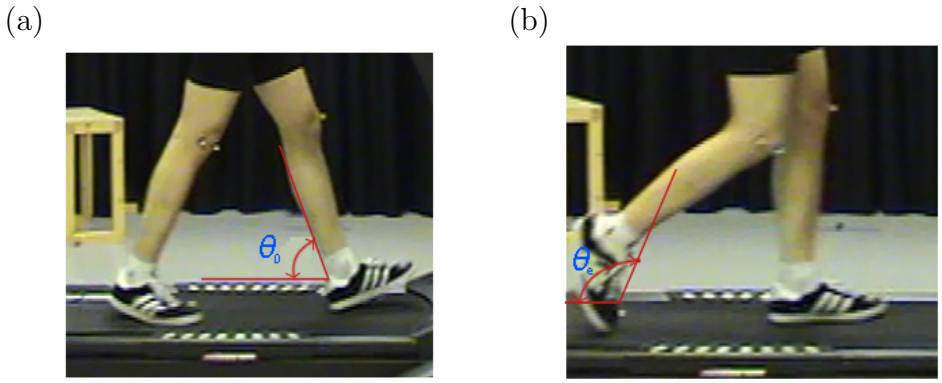

Figure 4.22: Measurement of **(a)** attack angle and **(b)** end-of-step angle.

ankle marker. The attack angle for every step is calculated as:

$$\theta_0 = \arctan\left(\frac{z_{\text{BCoM}} - z_{\text{Ankle}}}{x_{\text{Ankle}} - x_{\text{BCoM}}}\right) \tag{4.4}$$

where x and z represent the coordinates in the X and Z directions, respectively.

Figure 4.23a shows the distribution of attack angle in a trial (TS4 walking at 1.45 m/s). Kolmogorov-Smirnov test is again used to test the hypothesis of normal distribution, where CDF of p-value is shown in Figure 4.23b. For 5 % significance level, 97 % of the trials fail to reject the normal distribution hypothesis.

Average attack angle is shown as a function of the average walking speed and the average pacing rate in Figures 4.23c and 4.23d, respectively. The mean attack angle measured by Geyer (2005) is plotted in Figure 4.23c for comparison (dotted line). The discrepancies in the results of the two studies stem from different calculation methods used. However, both sets of results show that θ_0 tends to decrease with an increase of walking speed. The attack angle ranges from 69.1° to 77.3° at normal walking speed.

The CoV of attack angle is plotted versus the average walking speed and the average pacing rate in Figures 4.23e and 4.23f. It seems that the CoV is minimum at the boundary of normal and fast walking speeds. Within the normal walking speeds, the CoV is between 0.6 % and 2.1 %.

In the measurement of the end-of-step angle θ_{e}, the toe-off event needs to be determined for every step in the experiments. The methodology used to recognise this gait event is explained by Zeni et al. (2008). The event is detected when the toe marker starts moving from the negative to the positive

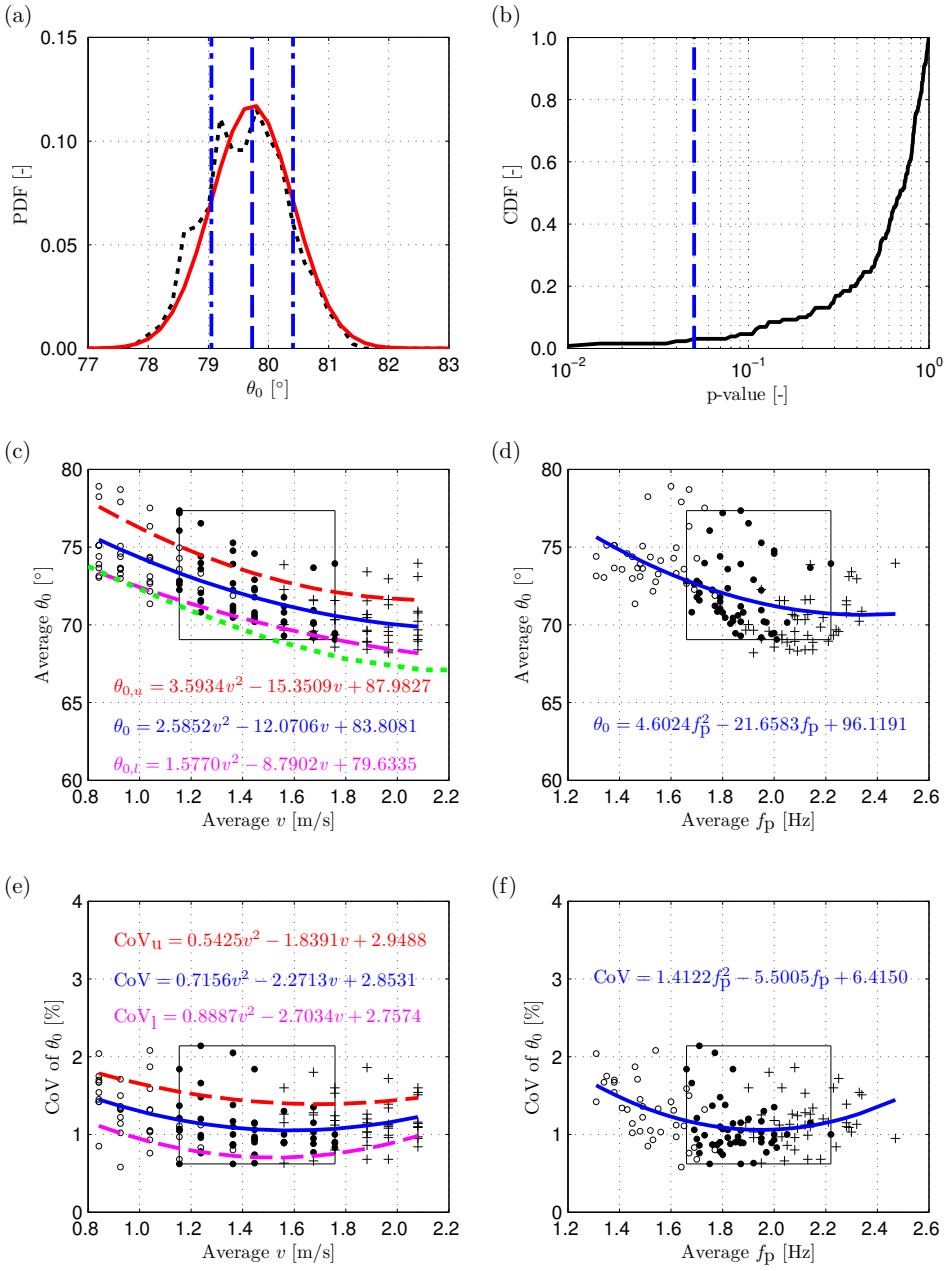

Figure 4.23: **(a)** Distribution of attack angle and the corresponding normal distribution model. **(b)** Cumulative distribution function of p-value of Kolmogorov-Smirnov test. Average attack angle versus **(c)** average walking speed and **(d)** average pacing rate. Coefficient of variation of attack angle versus **(e)** average walking speed and **(f)** average pacing rate. Line and symbol explanations are the same as in Figure 4.20.

of X axis direction (Figure 4.13a). Using BCoM measured by the segmental method and the point foot defined as the toe marker, θ_e is calculated as:

$$\theta_e = 180^\circ - \arctan\left(\frac{z_{\text{BCoM}} - z_{\text{Toe}}}{x_{\text{BCoM}} - x_{\text{Toe}}}\right) \tag{4.5}$$

Figure 4.24a shows the distribution of the end-of-step angle in a trial (TS6 walking at 1.45 m/s). CDF of p-value from Kolmogorov-Smirnov test is plotted in Figure 4.24b. At the 5 % significance level, 98 % of the trials fail to reject the normal distribution hypothesis for the end-of-step angle.

The average end-of-step angle versus the average walking speed and the average pacing rate is shown in Figures 4.24c and 4.24d. In the range of normal walking speeds, the end-of-step angle ranges from 107.8° to 119.2°. The CoV of end-of-step angle is plotted as a function of the average walking speed and the average pacing rate in Figures 4.24e and 4.24f. The CoV seems to reach the minimum range when walking speed changes from normal to fast. Within the normal walking speeds, the CoV ranges from 0.3 % to 1.0 %.

The sum of attack angle and end-of-step angle is often assumed as 180° in the simulation of inverted pendulum model (Bocian et al., 2013). Summing up the best fit functions for the two parameters shows that the deviation increases linearly with speed v [m/s]:

$$\theta_0 + \theta_e = 4.99v + 180.07 \tag{4.6}$$

This information might need to be included in advanced bipedal models.

Trunk movement

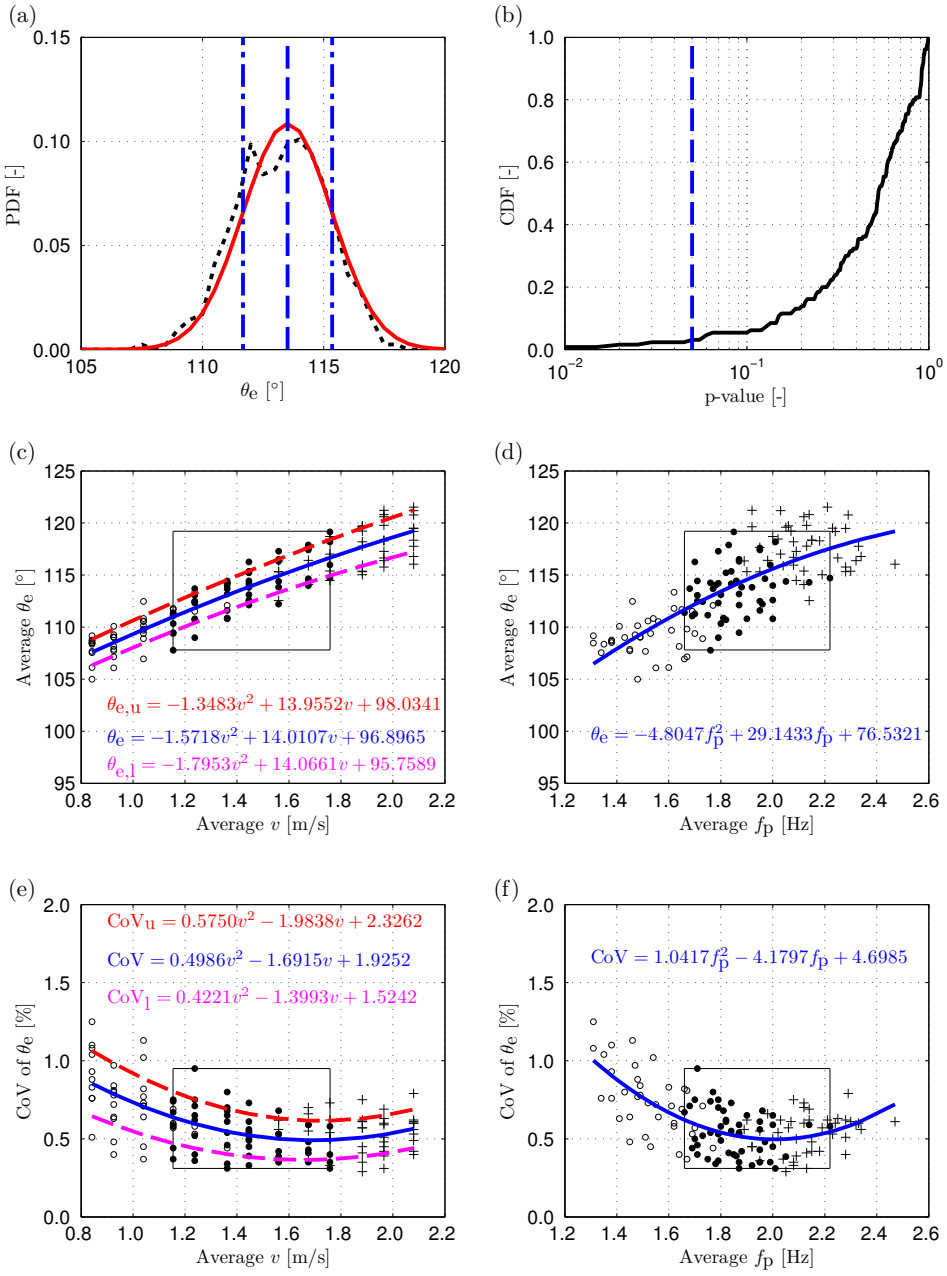

Figure 4.24: **(a)** Distribution of end-of-step angle and the corresponding normal distribution model. **(b)** Cumulative distribution function of p-value of Kolmogorov-Smirnov test. Average end-of-step angle versus **(c)** average walking speed and **(d)** average pacing rate. Coefficient of variation of end-of-step angle versus **(e)** average walking speed and **(f)** average pacing rate. Line and symbol explanations are the same as in Figure 4.20.

Trunk is the biggest body segment, making around 72 % mass of the upper body (de Leva, 1996). Thus, monitoring movement of the trunk is important for quantifying kinematics of the upper body. The trunk in this study is approximated as a line connecting the sternum marker and the midpoint of two hip markers (Figure 4.4, Model C), hereafter referred to as top trunk and bottom trunk, respectively. The angle between this line and the X axis is called the trunk angle θ_{tr} (Figure 4.25) and it can be calculated as:

$$\theta_{\text{tr}} = 90^\circ + \arctan\left(\frac{x_{\text{ top trunk}} - x_{\text{ bottom trunk}}}{z_{\text{ top trunk}} - z_{\text{ bottom trunk}}}\right) \tag{4.7}$$

θ_{tr} is calculated at the heel-strike event of each step. The distribution of θ_{tr} in a trial is shown in Figure 4.26a (TS8 walking at 1.45 m/s). Result from the Kolmogorov-Smirnov test shows that 93 % of the trials fail to reject the normal distribution hypothesis at 5 % significance level (Figure 4.26b).

The average trunk angle is plotted as a function of the average walking

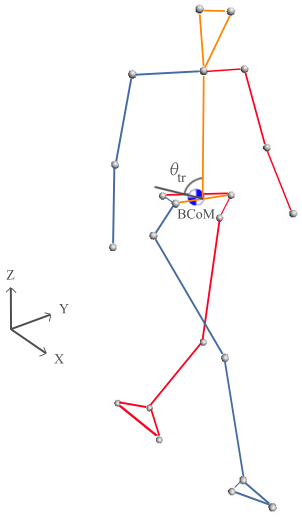

Figure 4.25: Measurement of trunk angle.

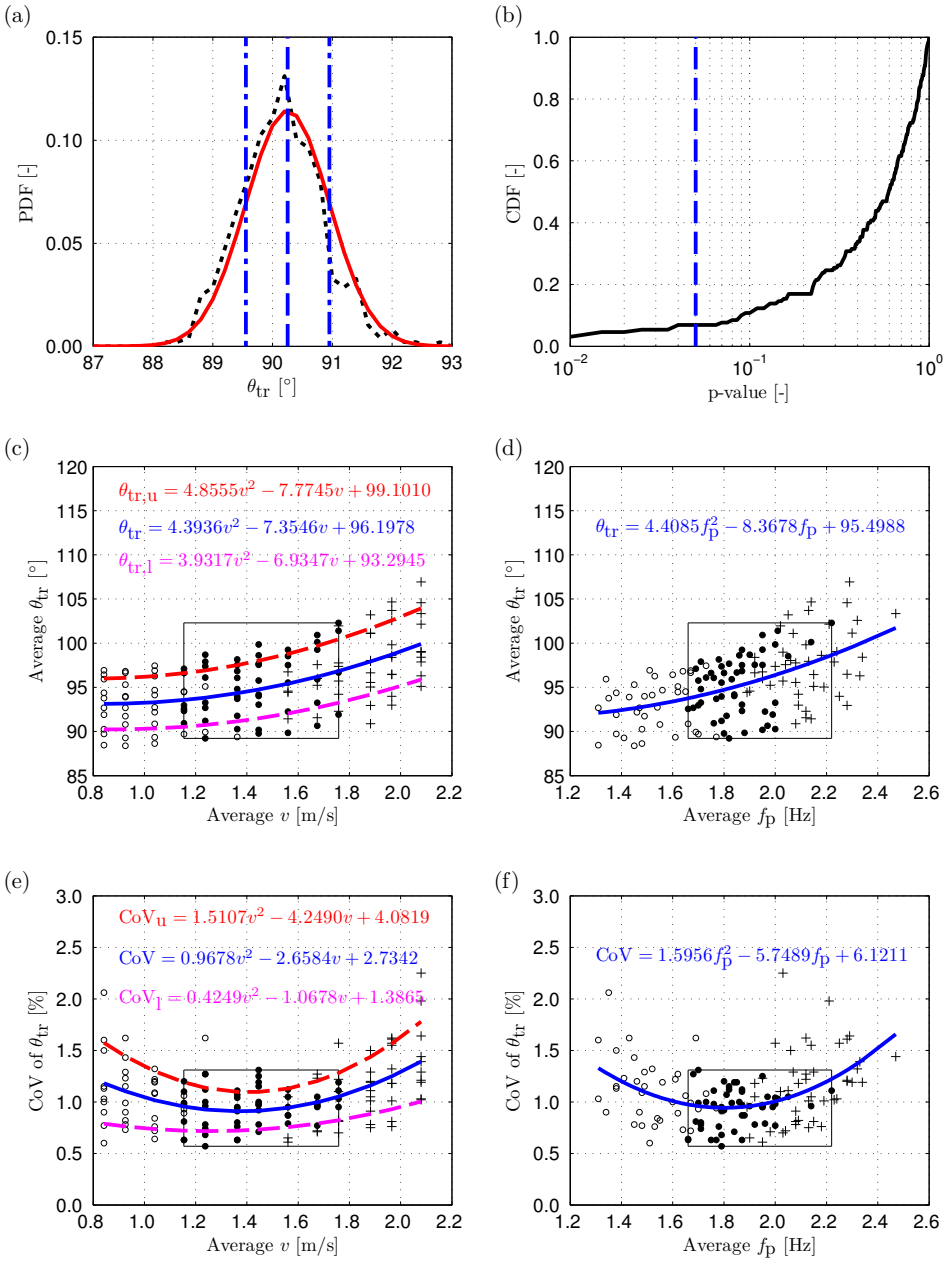

Figure 4.26: **(a)** Distribution of trunk angle and the corresponding normal distribution model. **(b)** Cumulative distribution function of p-value of Kolmogorov-Smirnov test. Average trunk angle versus **(c)** average walking speed and **(d)** average pacing rate. Coefficient of variation versus **(e)** average walking speed and **(f)** average pacing rate. Line and symbol explanations are the same as in Figure 4.20.

speed and the average pacing rate in Figures 4.26c and 4.26d. For slow speed, the trunk is relatively vertical, i.e. θ_{tr} is close to 90°. As the speed increases, θ_{tr} also increases, indicating that TSs tend to lean forward at higher speeds. For normal walking speeds, the trunk angle ranges from 89.2° to 102.3°.

The CoV of θ_{tr} is shown as a function of the average walking speed and the average pacing rate in Figures 4.26e and 4.26f. Within the normal walking speeds, the CoV ranges from 0.6 % to 1.3 %.

The results provided so far are for θ_{tr} at heel-strike events. When the trunk angle is continuously calculated, the $\Delta\theta^{\text{tr}}$ defined as the maximum variation of the trunk angle within a step can be extracted. The average $\Delta\theta^{\text{tr}}$ in every trial is plotted against the walking speed in Figure 4.27a. For normal walking speed, the mean $\Delta\theta^{\text{tr}}$ ranges from 1.6° to 3.5°. This result confirms the finding by Winter (1995) that the trunk rotation is small within any particular step. In Figure 4.27b, the CDF of p-value in Kolmogorov-Smirnov test for $\Delta\theta^{\text{tr}}$ shows that 74 % of the trials fail to reject the hypothesis.

A further analysis of θ_{tr} at all time instants during trials shows that the CoV of θ_{tr} ranges between 0.6 % and 2.3 %. This range of CoV indicates that the trunk orientation is quite stationary during walking.

4.4.3.5 Ground reaction force

The GRF generated during walking on treadmill can be reconstructed using Model C in Section 4.3. Time history of GRF reconstructed over several steps in a trial (TS1 walking at 1.45 m/s) is plotted in Figure 4.28a while its spectrum calculated using the force recorded in 50 steps is shown in Figure 4.28b. The TS slightly changes the pacing rate on a step-by-step basis, causing the spread

of energy around the dominant harmonics, reflecting the narrow-band nature of the force.

For the Fourier series analysis of GRF, the force history must be truncated to avoid the leakage problem (Shin and Hammond, 2008). The truncation was applied so that the force record (after removing body weight) in time domain begins downwards from zero and ends downwards approaching

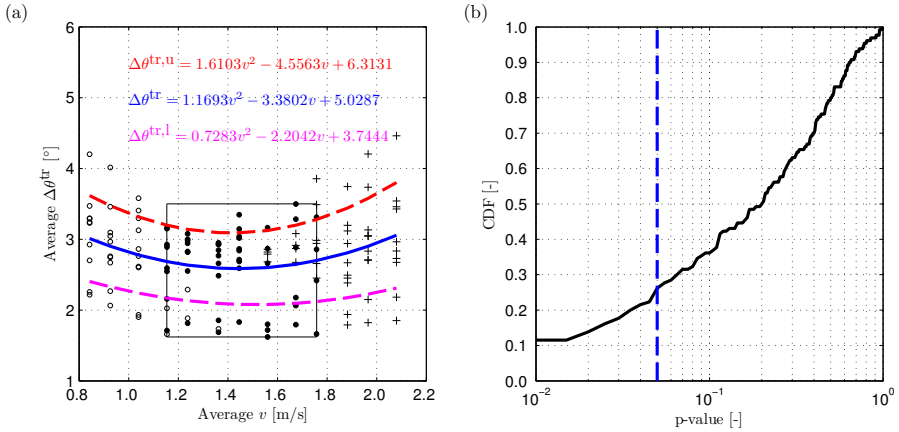

Figure 4.27: **(a)** Average trunk angle variation versus average walking speed and **(b)** Cumulative distribution function of p-value of Kolmogorov-Smirnov test. Line and symbol explanations are the same as in Figure 4.20.

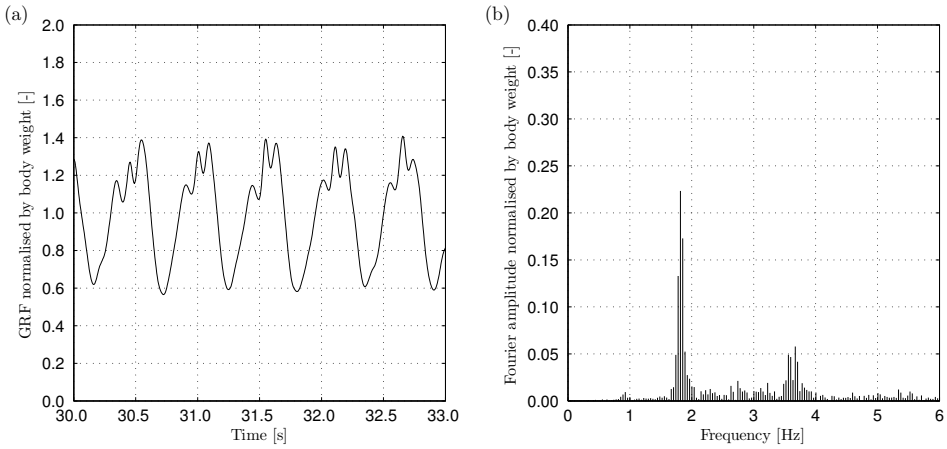

Figure 4.28: Measured ground reaction force in **(a)** time and **(b)** frequency domains.

zero. To determine the DLF_1 on a step-by-step basis, the truncated GRF is band-pass filtered using Butterworth filter (bandwidth: $0.75f_p$–$1.25f_p$, where f_p is the pacing rate). Cycle-by-cycle amplitude of the filtered force in the time domain is extracted across the whole trial. The distribution of DLF_1 in a trial is plotted in Figure 4.29a. For the Kolmogorov-Smirnov test, the result (solid line) shows that only 93 % of the trials fail to reject the normal distribution hypothesis at 5 % significance level (Figure 4.29b).

The average DLF_1 for each trial is calculated as the mean of amplitudes of the filtered force. Average DLF_1 is plotted in Figure 4.29c and Figure 4.29d against the average walking speed and the average pacing rate, respectively. DLF_1 tends to increase with an increase in walking speed and pacing rate. In the range of normal walking speeds, DLF_1 ranges from 0.11 to 0.50. The average DLF_1 in this study is consistently lower than that in the study by Kerr (dotted line in Figure 4.29d), up to the pacing rate of 2.2 Hz, with differences being more pronounced at slower pacing rates. The differences in the mean values are expected for different populations of TSs.

The CoV of DLF_1 is plotted against the average walking speed and the average pacing rate in Figure 4.29e and Figure 4.29f, respectively. The CoV is lowest when walking speeds are close to boundary between normal and fast walking. In the normal walking speed, the range of CoV is 3.1–12.8 %.

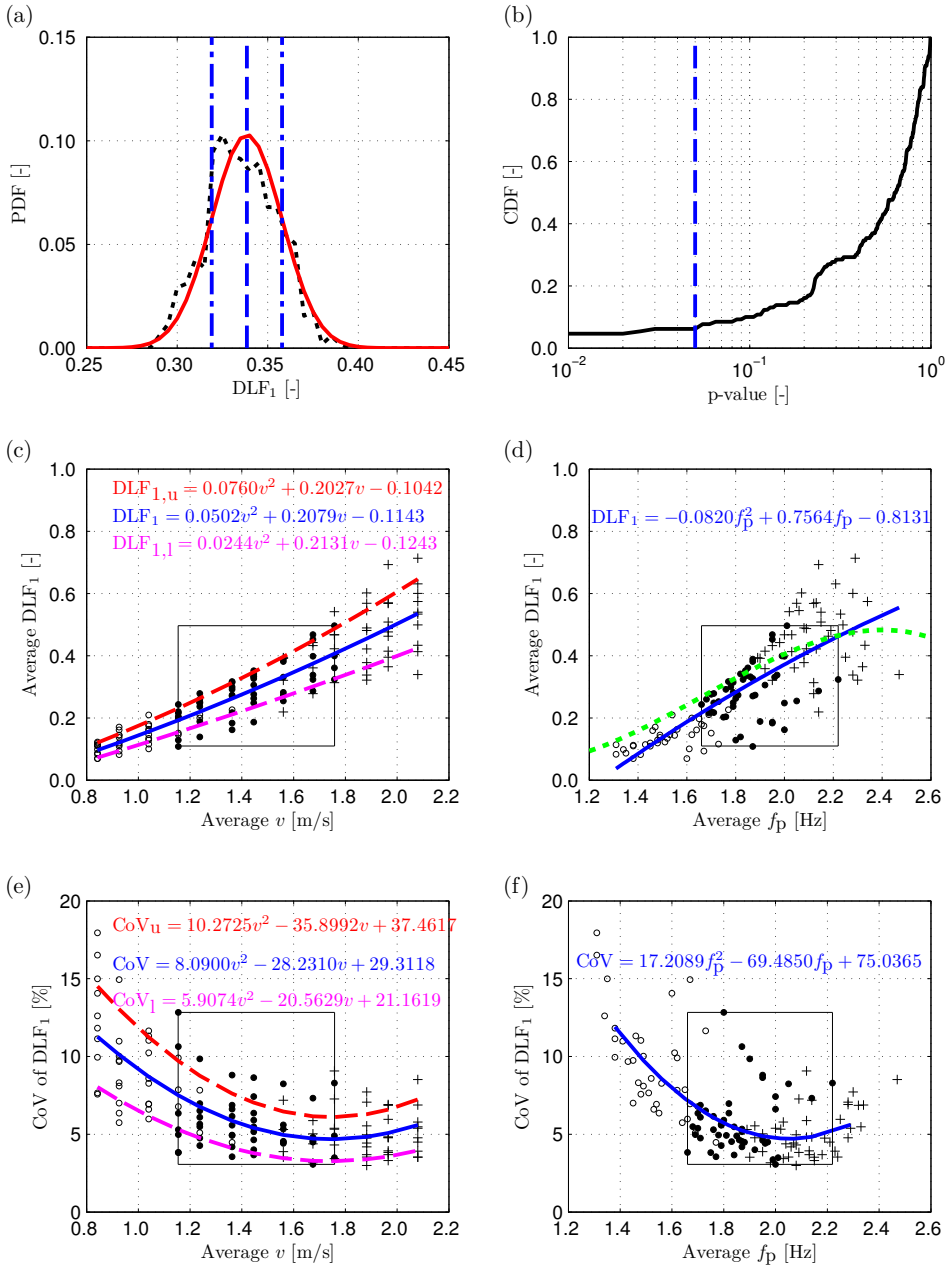

Figure 4.29: **(a)** Distribution of DLF_1 and the corresponding normal distribution model. **(b)** Cumulative distribution function of p-value of Kolmogorov-Smirnov test. Average DLF_1 versus **(c)** average walking speed and **(d)** average pacing rate. Coefficient of variation of DLF_1 versus **(e)** average walking speed and **(f)** average pacing rate. Line and symbol explanations are the same as in Figure 4.20.

4.4.4 Critical evaluations of assumptions used in inverted pendulum model

A number of assumptions are used in the inverted pendulum model (IPM) described in Chapter 2 and developed in Chapter 3. It is interesting to check how well these assumptions agree with the actual properties of the walking gait. Results of experiments obtained from Section 4.4.3 are used to evaluate these assumptions.

The pacing rate f_{p} of pedestrians experience small variations during walking, where the CoV ranges from 1.1 % to 5.1 % (Figure 4.18a). Given high sensitivity of structural vibration to the pacing rate (Pedersen and Frier, 2010), it would be useful if the variation is included in the IPM. Periodic force resulting from IPM (Chapter 3) is due to the repetition of initial conditions at the beginning of each step, i.e. initial forward speed and attack angle θ_0. The analysis of the attack angle shows that this angle has variation during walking, where the mean CoV ranges from 1.0 % to 1.6 %. As a result, the assumption of fixed attack angle is incorrect. If this intra-subject variability in the attack angle is built-in in the IPM, it will cause variability of f_{p} and eventually the walking force.

The analysis of trunk angle θ_{tr} shows that the TS experiences small variations in posture throughout the walking process, with the CoV for θ_{tr} ranging from 0.6 % to 2.3 %. The low values of CoV suggest that the trunk orientation is quite stable. This result is in line with the observation that the trunk, and in general the upper body, is considered as the passenger unit during walking (Perry and Burnfield, 2010). This observation justifies removing the

upper body from the IPM.

4.5 Conclusions

A motion capture system Vicon was utilised in this chapter for monitoring of walking locomotion parameters. Although use of Vicon and similar systems in civil engineering research is growing, there exists no recommendation for marker layout that can provide good accuracy of the measured force. Performance of four marker models, including two models proposed by the author (called Models C and D), was investigated in this study. It was found that Models C and D, consisting of 19 and 27 markers, respectively, provide acceptable absolute error in DLF_1 of up to 15 % in 90 % of trials. Both models can therefore be recommended for future studies. The 19-marker model has two advantages: 1) it utilises fewer number of markers, and 2) all markers are positioned on the frontal part of the body, allowing a reduced number of cameras to be used.

Ten test subjects, walking on a treadmill positioned inside the Gait Laboratory, were instrumented using marker layout from Model C and monitored using motion capture system Vicon. Seven locomotion parameters were then measured: pacing rate, step length, step width, attack angle, end-of-step angle, trunk angle and DLF_1. All parameters were studied in relation to 13 walking speeds (ranging from 0.8 m/s to 2.1 m/s). About 450 steps were recorded in each trial. In total, 130 trials were conducted, consisting of about 60,000 recorded steps.

The average value and CoV of each parameter on a step-by-step basis

were calculated for each person at each treadmill speed. The mean value of both quantities as well as their standard deviation bands were then calculated across the population of ten test subjects. Within the investigated population, walking speed range subjectively perceived as comfortable was between 1.15 m/s and 1.76 m/s. The ranges of values for other parameters recorded when walking at normal speeds were found to be: 1.66–2.22 Hz for pacing rate, 0.56–0.84 m for step length, 60–143 mm for step width, 69.1–77.3° for attack angle, 111.0–125.0° for end-of-step angle, 89.2–102.3° for trunk angle, and 0.11–0.50 for DLF_1. The CoV over normal speed range was less than 5 % for most parameters. The only exceptions were DLF_1 (CoV=3.1–12.8 %) and a large variation for step width (CoV=13.4-39.2 %). It is interesting to note that the CoV for all parameters, apart from the step width and trunk angle, tended to reach minimum value at walking speeds at the boundary between normal and fast walking. This observation indicates that test subjects achieved the most consistent (i.e. least variable) walking pattern at this boundary. The results provided in this chapter represent the most comprehensive description of locomotion parameters, with particularly detailed characterisation of variability on a step-by-step basis.

Statistical information about all parameters studied in this chapter is presented as a function of walking speed. Assuming that a distribution of the speed is known or can be assumed for a particular site, the mean and standard deviation for any parameter at a particular speed can be extracted and used for modelling of inter-subject variability. Although this study includes a small population subset (ten young and healthy males) the suggested statistics can be used in preliminary design, especially in those (frequently encountered)

cases when more detailed information about the features of the population in question is not available. As for modelling the variation on step-by-step basis, detailed statistics presented in this study can be utilised. Variations in all parameters can be assumed to follow normal distribution.

Chapter 5

Experimental characterisation of walking on lively surface

5.1 Introduction

In Chapter 3, three models that could potentially be used for studying pedestrian-structure dynamic interaction (PSDI) were reviewed. However, none of the existing models have been validated through experiments. In Chapter 4, a methodology for capturing kinematic and kinetic data of walking over multiple steps was developed. A series of experiments on the rigid surface was conducted to quantify walking parameters in absence of PSDI. In this chapter, the experiments were repeated on a lively structure. The aim of this chapter was to quantify human gait parameters (kinematic and kinetic) when the test subject (TS) was exposed to vibration and to compare them with benchmark parameters collected on the rigid surface. To allow for comparison, the experiments on the lively surface were performed in nominally the same manner as the experiments on the rigid surface. The findings will be utilised when developing a numerical model in Chapter 6.

Some previous studies have investigated the PSDI phenomenon while bouncing and jumping (Yao et al., 2004, 2006) and walking on laterally vibrating surface (Ingólfsson et al., 2011). In the former study, the mass ratio of the test subject over the supporting platform was high (0.41), which led to the excessive peak vibration between 1.2–2.2 g (i.e. 11.8–21.6 $\mathrm{m/s^2}$) during experiments. In the latter study, the authors performed experiments on an instrumented treadmill exposed to controlled lateral vibration. These studies represent pioneering work towards understanding and modelling PSDI. The author of this thesis builds on the previous work by performing experiments on a full-scale structure for the first time. Three test subjects participated in the experimental programme, each walking over the structure vibrating at a range of frequencies and vibration amplitudes. The study in this chapter aims to form the first database of experimentally characterised human behaviour when walking on vertically oscillating surfaces and to quantify effects of PSDI on the walking gait.

This chapter first presents description of a lively structure, followed by details of the experimental programme. Then test subjects' perceptions of speed and vibration are investigated. Analysis of characteristics of walking gait on the lively surface is then performed and compared with the benchmark data recorded on the rigid surface. At the end, major findings are presented.

5.2 Lively structure

A lively bridge was constructed in the Structures Laboratory at the University of Warwick, hereafter referred to as the Warwick Bridge (WB). Detailed in-

formation of the design, construction and post-construction monitoring of the WB can be found in a paper by Živanović et al. (2013). This section provides a brief description of the WB and measurements of its dynamic properties.

5.2.1 Description of Warwick Bridge

The bridge (Figure 5.1a) was designed to be lively under human walking, i.e. to have the natural frequency between 1.4 Hz and 2.4 Hz, which is a range typical for normal walking (Živanović, 2012).

The WB has a deck that is 2 m wide and 19.9 m long. The total mass is about 16,500 kg. To achieve such a low natural frequency, the bridge is extremely slender. The composite cross section (Figure 5.1b) consists of two I-profiles (UC 203x203x52) and 150 mm thick reinforced concrete deck. The deck and the steel beams are connected by shear studs welded on the top flanges of the beams (Figure 5.1c). The concrete deck has two layers of reinforcement mesh (Figure 5.1d). Polypropylene fibres (Figure 5.1e) were added to the concrete mix (class 40/50) for the purpose of crack control.

The WB has a tunable frequency, by means of altering the span length. This can be achieved by moving an end support to a chosen location (Figure 5.1f and Appendix C, Section C.1.1).

5.2.2 Measuring structural dynamic characteristics

For the experiments in this chapter, two span lengths at 16.2 m and 17.4 m, hereafter referred to as WB1 and WB2 respectively, were investigated. For modal test on WB1, the test grid consisting of 42 test points (TPs) is shown

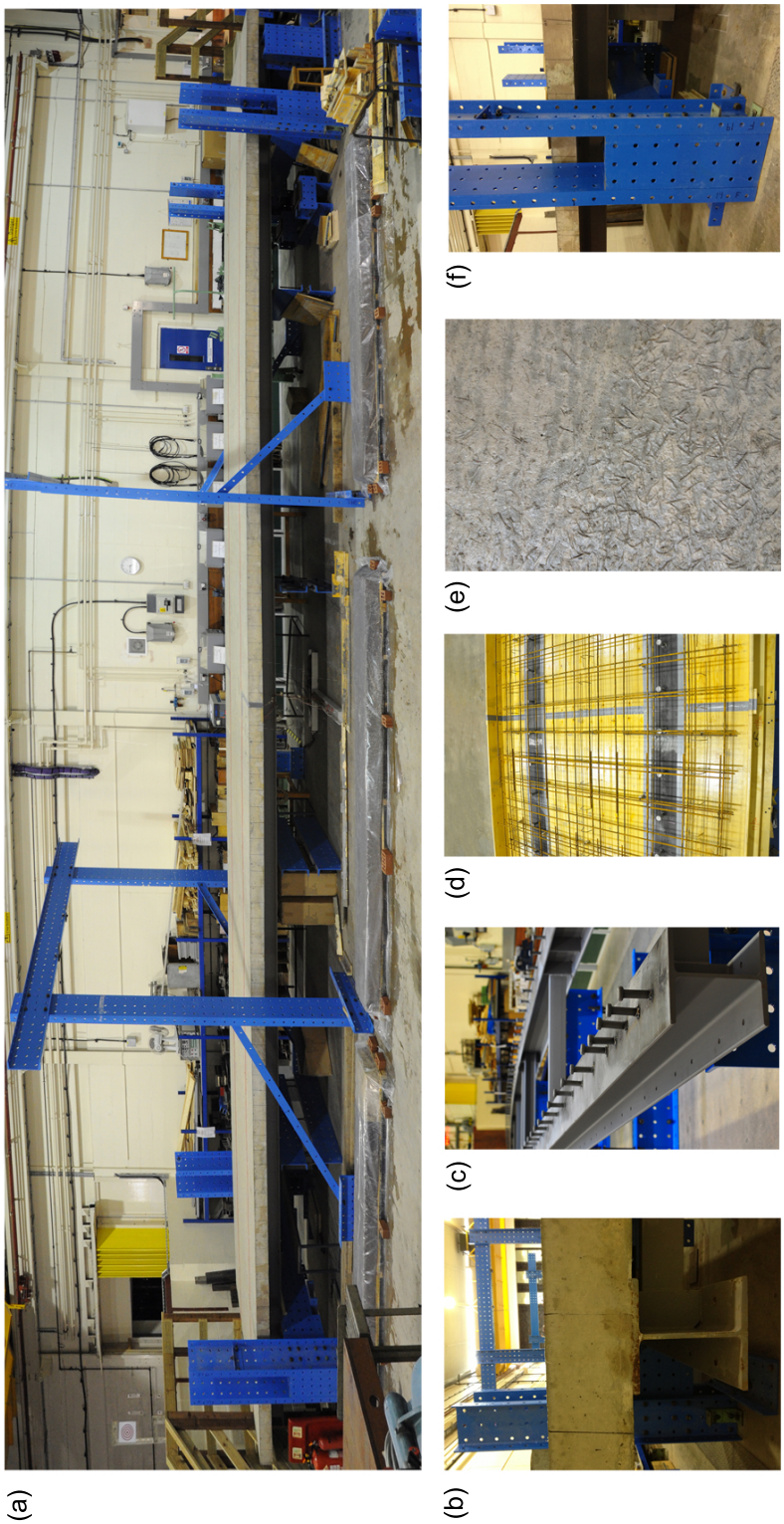

Figure 5.1: Warwick Bridge: **(a)** panoramic view (image is distorted), **(b)** part of composite cross section, **(c)** studs welded on the top flanges of I-profiled steel beams, **(d)** formwork and reinforcement mesh for the concrete deck, **(e)** finished surface of concrete mixed with polypropylene fibres and **(f)** one support.

in Figure 5.2a. A four-channel data acquisition system (National Instruments, 2013) was utilised and only the responses were acquired (at sampling frequency of 1651.61 Hz). To find the structural mode shapes, impact tests were performed using an impulse hammer. By trial and error, it has been found that applying impacts at TP57 could excite all vibration modes in the frequency range up to 25 Hz. During the impact tests, one accelerometer was kept at TP57 as the reference point while three other accelerometers formed different combinations of test points until all points in the test grid were covered. Nominal sensitivity of all accelerometers was 500 mV/g (Dytran Instrument Inc., 2003). Spectra of responses recorded on WB1 at TP11, TP13 and TP15 are shown in Figure 5.2b, where each peak represents a mode of vibration. The peaks correspond to frequencies at 2.44, 7.78, 9.15, 11.28, 18.18 and 23.75 Hz.

(a)

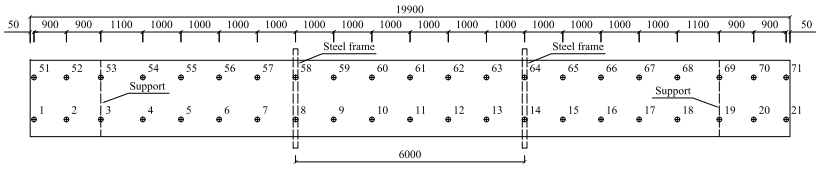

(b)

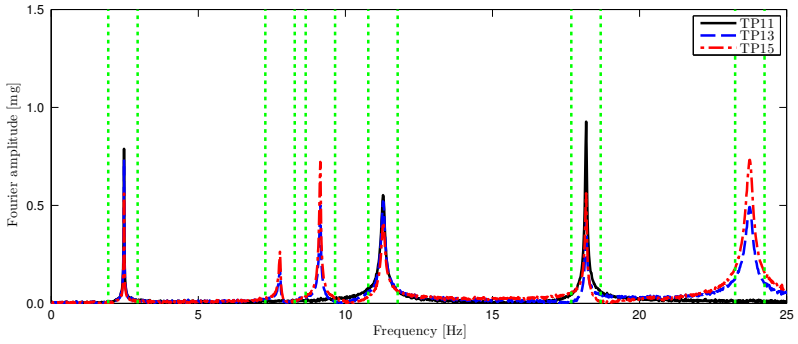

Figure 5.2: (a) Test grid for modal test of WB1. **(b)** Fourier spectra for responses measured on WB1 under hammer impact at TP57.

To determine mode shapes, time-histories of responses at each TP were band-pass filtered (bandwidth of ±0.5 Hz around the frequency of interest is shown in Figure 5.2b for each mode). Cycle-by-cycle amplitudes of the responses were normalised to the corresponding amplitudes at the reference point and then averaged. This process resulted in determination of the scaling factor at each point (compared with the reference point), leading to identification of mode shapes. Since span lengths of WB1 and WB2 are only slightly different, the shapes of the vibration modes of these two bridges are qualitatively the same. The six peaks in Figure 5.2b represent first four vertical bending modes and two torsional modes, which are presented in Figure 5.3. Mode 1 (Figure 5.3a) is the first vertical bending mode with the half-sine shape, which is expected for a simply supported structure. Modes 2 and 3 (Figures 5.3b and 5.3c) have relatively similar shapes with nodal line in the midspan. Modes 4 and 6 (Figures 5.3d and 5.3f) are torsional modes with natural frequencies above 10 Hz. Mode 5 (Figure 5.3e) is the forth vertical bending mode with maximum amplitude at around midspan of the bridge.

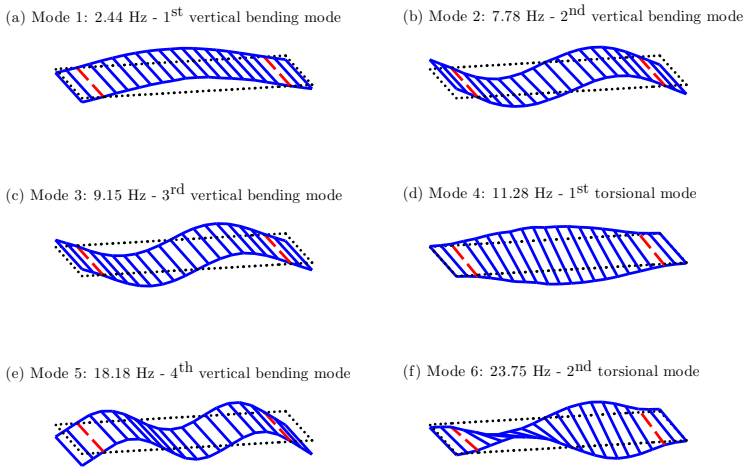

Figure 5.3: Mode shapes of WB1 (solid lines), stationary position of the bridge (dotted lines) and two supports (dashed lines). Figures **(a–f)** represent Modes 1–6, respectively.

To check the amplitude-dependency of natural frequency f_n and damping ratio ζ of the first mode, these modal properties were extracted from free decay vibration measured after a person walked across the bridge at the pacing rate matching f_n. The measured response was band-pass filtered with bandwidth of 1–5 Hz. Then, f_n was calculated as the reciprocal value of the duration of a vibration cycle (determined by two consecutive downward zero-crossings in the acceleration record), while the damping ζ was extracted using the logarithmic decrement method (Maia et al., 1997). The values of f_n and ζ calculated from every four consecutive cycles are plotted as functions of vibration amplitude in Figure 5.4. The measured data were fitted by third-order polynomial functions using least squares method. With the increase in the vibration amplitude, the natural frequency decreases while the damping ratio increases. The maximum measured ζ (0.52 %) is still quite low, ensuring the desired lively behaviour of the first mode.

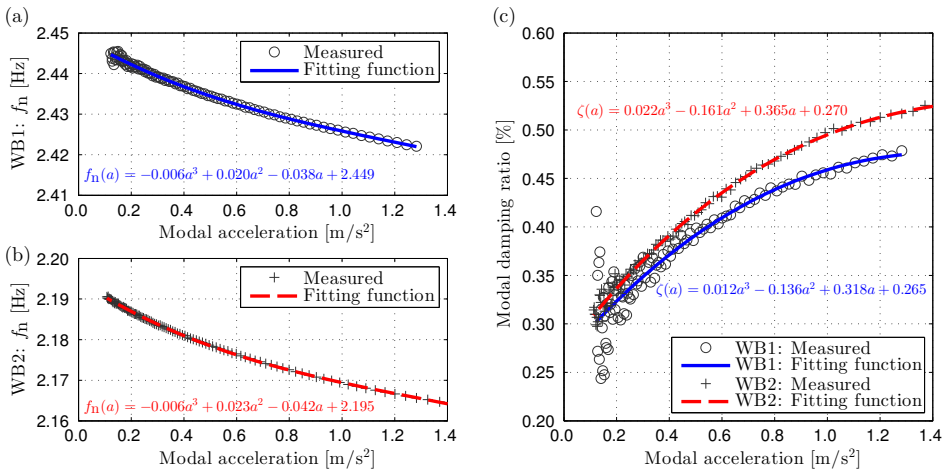

Figure 5.4: Vibration amplitude dependency of **(a)** natural frequency of WB1, **(b)** natural frequency of WB2 and **(c)** damping ratio of WB1 and WB2.

To measure the modal mass, a method proposed by Brownjohn and Pavic (2007) was partly applied. A shaker, model ELECTRO-SEIS APS 400 (APS Dynamics, 2011), located at TP57 (Figure 5.2a) was used as the source of excitation. The shaker induced resonant vibration of the bridge. The response at TP61 was recorded. The shaker-induced force and previously measured dynamic properties of the first vibration mode were used as inputs for a single degree-of-freedom (SDoF) simulation. By trial and error, it was found that when using only 10 cycles around the initial resonance build-up, the influence of damping ratio was negligible. The dynamic properties of the SDoF system were assumed to be constant: natural frequency of 2.44 Hz for WB1 and 2.18 Hz for WB2, while damping ratio of 0.35 % and an assumed modal mass of 1,000 kg were used for simulations for both bridges. By finding the average ratio of simulated to measured peak-per-cycle, the modal mass was estimated at 7,700 kg for WB1 and 8,200 kg for WB2. Figure 5.5 demonstrates good agreement between the simulated and measured responses in the resonance build-up for WB1 achieved when using the estimated modal mass of 7,700 kg. These estimated values are used in the simulations later in this thesis.

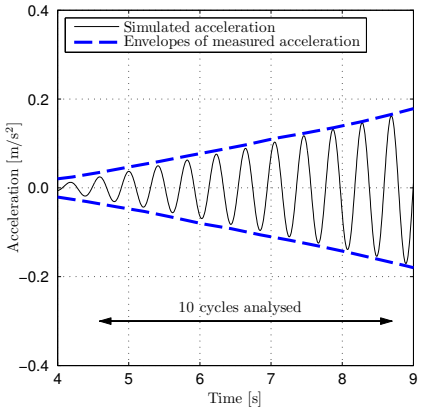

Figure 5.5: Comparison between simulated and measured accelerations in a shaker-induced resonant case for WB1.

5.3 Methodology

This section begins with information about the TSs who participated in the experiments, followed by descriptions of experimental facilities and test set-up. Then detailed information about the experimental programme is presented along with a description of data pre-processing.

5.3.1 Test subjects

Three TSs participated in the experiments on the lively bridge. Their characteristics are shown in Table 5.1. All TSs are healthy male, declaring no history of leg/foot injuries at the time of experiments. Before the experiments, TSs provided a written consent and were declared as eligible for the experiments after answering a physical readiness questionnaire (both forms are available in Appendix B).

Table 5.1: Characteristics of test subjects for experiments of walking on Warwick Bridge.

Test subject	Age (years)	Height (cm)	Mass (kg)
TS1	22	180	62.4
TS2	55	178	70.0
TS3	28	172	72.7

TS1 and TS3 participated in the walking activities reported in Chapter 4. As for TS2, he had to complete experiments on the rigid surface first. These experiments were conducted in the same way as reported in Chapter 4 for other TSs. The experimental data on the rigid surface for the three TSs are used as benchmark data for evaluation of data collected on the lively surface. It is noted that any discrepancy between trials on rigid and lively surfaces (in

nominally same conditions) can be attributed to the effects of PSDI only if the intra-subject variability of gait parameters of TSs on different days is small. This issue will be commented in the analysis of experimental data.

In Chapter 4, the indirect measurement of GRF using a motion capture system has been proposed. It has been found that the method is reliable for the reconstruction of GRF for majority of TSs for two marker layouts: Model C and Model D. Model C is utilised in experiments in this chapter. For the three TSs, the discrepancies between the directly measured DLF_1 using a force plate and the indirectly measured DLF_1 using the motion capture system when performing stamping activity (as described in Chapter 4) are plotted in Figure 5.6. The percentage discrepancies Δ_{DLF_1} for these three TSs are all below 10 % except in one trial. In the experiments reported by Pimentel et al. (2001) and Živanović et al. (2005a), the measured response was around 50 % of the simulated response using carefully chosen DLF_1 when pedestrians tried to excite structures to resonance. This discrepancy was partly attributed to the reduction of DLF_1 caused by PSDI. As a result, it is expected that the

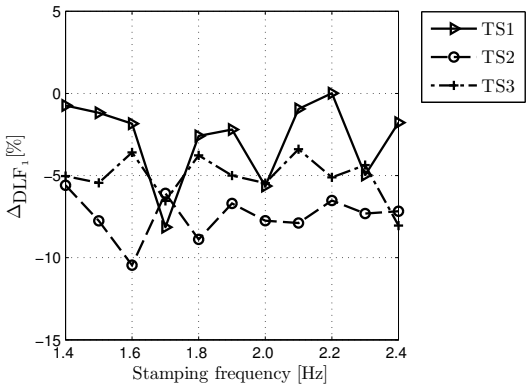

Figure 5.6: Percentage errors of reconstructed DLF_1 in experiments of stamping for three test subjects.

discrepancy in DLF_1 caused by PSDI is likely to be higher than the maximum 10 % discrepancy exhibited in the measurement method. The analysis of GRF measured on vibrating surface in Section 5.5.7 will provide more information to justify the use of the motion capture system in the study of PSDI.

5.3.2 Experimental set-up

The aim of the experiments is to simultaneously monitor gait of the pedestrian and vibration of the supporting structure. Apart from the bridge, a number of other facilities were needed. Figure 5.7a shows the layout of the equipment.

Six Vicon cameras (described in Chapter 4) were mounted on two steel

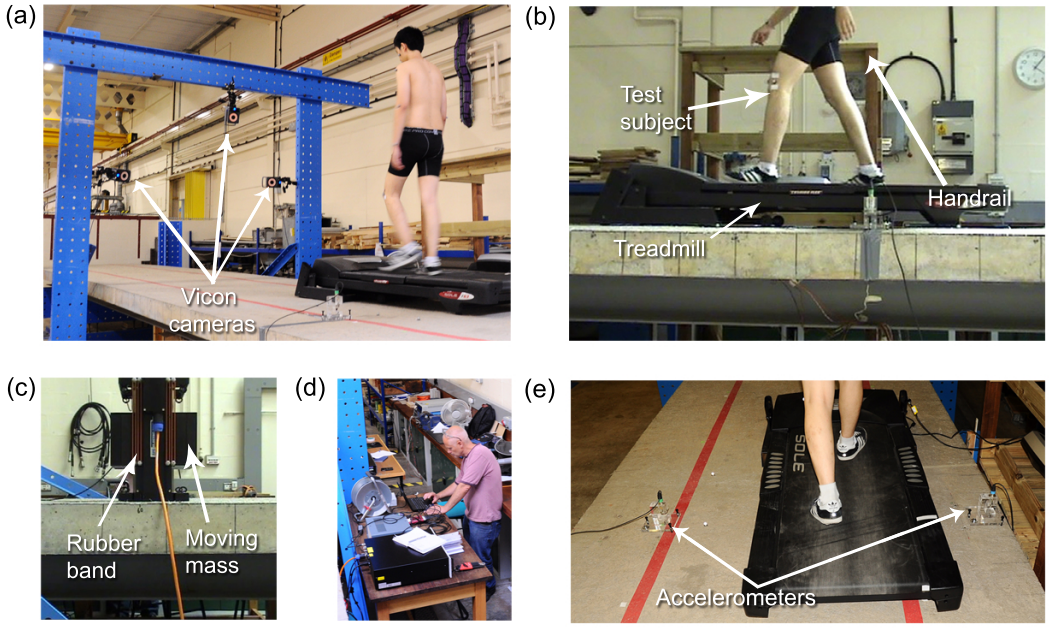

Figure 5.7: **(a)** Vicon cameras mounted on a steel frame, **(b)** a test subject walking on treadmill, **(c)** an electrodynamic shaker used to excite the bridge, **(d)** data acquisition centre aside the bridge and **(e)** two accelerometers at the midspan.

frames built around the bridge. The two frames were located at the structural cross section at TP58 and TP64 (Figure 5.2a). The cameras were used to monitor the kinematic data of TSs. Each TS was instrumented with 21 reflective markers. This marker layout covers 19 markers of Model C and one marker on each heel (markers No. 20 and 34 in Figure 4.3). To monitor the structural displacements, three markers were placed on the bridge surface at TP60–62 (Figure 5.2a). Three cameras monitored the frontal part of the TS's body (sufficient for force reconstruction) while the other three captured the back (to provide kinematic data for heel markers). Vicon Nexus (Oxford Metrics Group, 2008) was used to acquire data at the sampling rate of 200 Hz. It was found that the ambient light inside the lab did not adversely affect normal working conditions of the cameras.

The treadmill used in Chapter 4 (Fuel Fitness, 2013) was utilised for experiments in this chapter (Figure 5.7b). The mass of the treadmill is 86 kg. Since the natural frequency of the WB is low, the first bending mode is easily excited by fast walking on WB1 (2.44 Hz) and normal to fast walking on WB2 (2.18 Hz). Given that the first bending mode has the biggest amplitude at midspan (TP11 and TP61), it was decided to position the treadmill at the midspan (i.e. about TP10–TP12) so that the vibration the TS perceived is also the maximum vibration observed on the bridge during the trials in which the resonance was excited. A handrail was placed next to the bridge as a safety measure to prevent the TSs from falling off the structure (Figure 5.7b).

A shaker was used to generate required vibration levels (APS Dynamics, 2011). The shaker, having the total mass of 106.5 kg, was located at TP57 (Figure 5.2a), at which mode shape amplitude in Mode 1 was significantly

large (i.e. 70 % and 82 % of the amplitude at the midspan for WB1 and WB2, respectively) so that this mode can be excited, as required. A data acquisition system Quattro SignalCalc (Data Physics, 2011) was used to record the excitation and response signals. The system accommodates four input channels (acceleration responses) and one output channel (signal sent to the shaker). When the shaker is in operation, the mass of 30.8 kg hung by rubber bands (Figure 5.7c) moves vertically inducing force to the bridge. At the data-acquisition centre (Figure 5.7d), the shaker activity, the structural response, treadmill speed and TS behaviour were closely monitored.

An accelerometer, model QA-750 with nominal sensitivity of 1.32 V/g (Honeywell Sensing & Control, 2005), was placed on top of the moving mass m_s of the shaker to record its acceleration a_s. Using Newton's second law, the vertical force generated by the shaker was calculated as $F_s = m_s a_s$. Another three accelerometers were placed at TP11, TP57 and TP61. Accelerometer at TP57 was used to monitor the structural vibration at the shaker location. Accelerometers at TP11 and TP61 recorded the structural response at the midspan (Figure 5.7e). Acceleration at TP61 is adopted as the acceleration perceived by the TS in the analysis. The signal from TP11 was split between Vicon and SignalCalc systems and used to synchronise data. Acceleration and force data were acquired at the sampling rate of 200 Hz.

5.3.3 Experimental programme

Two span lengths of 16.2 m and 17.4 m were utilised in the experiments. Each TS completed one test session on each bridge on a different day.

At the beginning of a test session, the TS was given a 15-minute warm up on treadmill placed on the rigid surface. Then, the treadmill was placed on the bridge. First, experiments were performed while the shaker was switched off, i.e. TS walking on the treadmill was the only excitation source of bridge vibration. In the next stage, vibrations were induced by the shaker to replicate a real life scenario of a person crossing a bridge excited by other pedestrians, and therefore being exposed to perceptible vibration levels. Sinusoidal force was generated by the shaker to excite the bridge at resonance. Depending on the generated force amplitude, different steady-state vibration amplitudes were achieved.

The selection of vibration levels for the experiments was informed by current standards of practice. ISO (2007) defines the boundary between unacceptable and acceptable vibrations. For the vibration frequencies relevant for this study (2.18 Hz and 2.44 Hz), this boundary in form of 1 s RMS is between $0.36\,\mathrm{m/s^2}$ and $0.42\,\mathrm{m/s^2}$, which (assuming sinusoidal vibration) is equivalent to the peak acceleration between $0.51\,\mathrm{m/s^2}$ and $0.59\,\mathrm{m/s^2}$. SETRA (2006) provides vibration limits for different levels of vibration comforts. Structures exhibiting vibration up to $0.5\,\mathrm{m/s^2}$ are considered to provide maximum comfort, those with vibration of 0.5–$1.0\,\mathrm{m/s^2}$ and 1.0–$2.5\,\mathrm{m/s^2}$ are mean and minimum comforts, respectively, while vibration levels above $2.5\,\mathrm{m/s^2}$ are not allowed. To cover a range of vibration levels, including one within minimum comfort rating, three steady-state vibration levels of the bridge are to be induced by the shaker: $0.50\,\mathrm{m/s^2}$, $1.20\,\mathrm{m/s^2}$ and $0.85\,\mathrm{m/s^2}$. The experiments on the bridge were performed in this order. The order was influenced by the decision not to induce the largest vibration level of $1.20\,\mathrm{m/s^2}$ in the first series of experiments

to prevent the TS from being surprised by such a strong vibration.

At every shaker-induced vibration level, the TS completed five to seven trials at different walking speeds. The speed range was chosen to be within the walking speed seen in reality, i.e. from 0.8 m/s to 2.1 m/s covering the range of mean (1.4 m/s) ± three standard deviation (0.2 m/s) reported by Živanović (2012). Due to the intensive amount of walking that each TS had to complete in a test session, it was decided to choose maximum of seven walking speeds for each vibration level in a test session (instead of 13 speeds completed in Chapter 4). The order of walking speeds for WB1 was 1.45, 1.15, 2.08, 1.76, 0.84, 1.59 and 1.30 m/s, while that for WB2 was 1.45, 1.88, 1.15, 2.08, 1.76, 0.84 and 1.97 m/s. These orders were chosen to avoid biased adaptation of TSs to a certain increased or decreased trend of walking speeds, and applied in each shaker-induced vibration level. Since WB1 has the natural frequency in the top range of pacing rate in walking (2.44 Hz), the purpose of speed selection was to spread from low to fast speeds. For WB2, TSs were well capable of walking at the pacing rate that matches the natural frequency of 2.18 Hz. Therefore in this case several test speeds (1.88, 1.97 and 2.08 m/s, which were equivalent to pacing rate of 2.1–2.3 Hz on the rigid surface, depending on TSs) were chosen to increase incidence of resonance.

Results described in Chapter 4 showed that when walking on the treadmill, each speed of the TS was equivalent to a certain average pacing rate. When the average pacing rate was in the vicinity of the natural frequency of the structure (±3 %), the trials are referred to as resonant walking trials. Out of 160 trials, there are 28 resonant trials. All the rest of the trials are called the non-resonant trials. The cut-off range was chosen based on the observa-

tion that the CoV of pacing rate on the rigid surface is 2–3 % in the range of natural frequency of WB. Overall, the experiments were designed so that the effect of structural vibration on human gait when walking in both resonant and non-resonant trials can be investigated.

In the trials with shaker-induced vibration, the TS was first instructed to stand still on the non-operational treadmill and then the shaker started. After achieving the predefined steady state vibration, the treadmill started and the TS began walking. Short time of 30 s was allowed so that the TS got used to walking on the lively surface and the treadmill reached the target speed. Then, the recording by the Vicon system started. A minimum of 400 steps was collected in each trial. Apart from the reason explained in Chapter 4, a large number of steps recorded in each trial is beneficial in the capturing of the potentially slow development of the PSDI phenomenon. Also, the long trial helps to minimise biased observations that could occur due to transient events in short recording. At the end of each trial, the Vicon system was stopped first, followed by the treadmill and finally the SignalCalc system. In the trials without the shaker operation, the experiment was performed in the same way apart from all procedures related to the shaker. A summary of risk assessment involved in the experiments is provided in Appendix C, Section C.2.2.

In summary, there were two test sessions (one for each bridge span) for every TS, lasting around four hours each. Three TSs completed 160 trials, making around 64,000 steps or equivalent to travelling approximately 45 km in total. To the best knowledge of the author, this experimental programme is the most comprehensive study performed on a surface that is lively in the vertical direction.

5.3.4 Data preparation

Displacement signals recorded in the Vicon system were filtered using a low-pass Butterworth fourth-order zero-phase-shift filter with the cut-off frequency of 10 Hz (Mathworks Inc., 2010). As described in Chapter 4, "Fill gaps" technique was applied to kinematic data having the maximum gap of 0.1 s (Oxford Metrics Group, 2008).

Acceleration signals were band-pass filtered to isolate the contribution of each mode when needed. The acceleration signal at TP11 that was split between Vicon and SignalCalc systems was used to manually synchronise data between the two systems. The numerical criterion for identifying the common reference time instant was defined as the time lag for which the coefficient of determination R^2 between the two signals is at its maximum. After establishing the common time reference, the kinematic data from Vicon system can be evaluated against the vibration perceived by the TSs.

5.4 Speed and vibration perceptions

For trials on the rigid surface, TSs were asked to categorise the walking speed as either slow, normal or fast. The normal speed ranges (determined as explained in Chapter 4) were 1.20–1.72 m/s for TS1 and 1.10–1.50 m/s for TS3. The speed values that are below/above these ranges are considered as slow/fast speeds. The boundary between slow and normal speeds for TS2 was 1.58 m/s. This TS classified all speeds above 1.58 m/s as normal, i.e. none of the speeds utilised in the experiments was considered as fast.

The acceleration at TP61 (Figure 5.2a) of the bridge is also the vibration perceived by the TSs. For further analysis, it is useful to know the contribution of each vibration mode to this perceived vibration. The energy contribution of the first bending mode can be determined as the ratio of the area of the energy-density spectrum between 1 Hz and 4 Hz over the area of the whole frequency range (Oppenheim et al., 1997). This energy contribution is shown as a function of the peak acceleration in Figure 5.8. Only 21 % of the trials have contribution of the first mode that is below 80 %. Figure 5.8 shows that most trials with less significant contribution of the first mode occurs in tests characterised by low vibration levels. In these trials (all non-resonant trials), the shaker was either inactive or operated at a low level (i.e. at $0.5\,\mathrm{m/s^2}$).

After each trial, the TS was asked to classify vibration into one of the following categories: did not perceive vibration (Category 1), the vibration was acceptable and had no effect on the walking style (Category 2), the vibration was acceptable and occasionally affected the walking (Category 3) and the

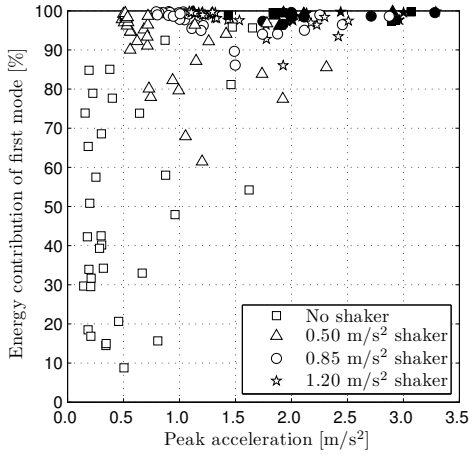

Figure 5.8: Energy contribution of first bending mode. Unfilled and filled symbols represent non-resonant and resonant trials, respectively.

vibration was strong/uncomfortable and affected the walking style most of the time (Category 4). It is noted that answers of test subjects were subjective, depending on the impression of the perceived vibration right after completing the trial.

To link subjective answers of the TSs to the vibration level, the peak acceleration in each trial is plotted as a function of the average pacing rate f_{p} in Figure 5.9. The data shown in Figure 5.9 are used to define a vibration threshold at which pedestrians start to be influenced by the perceived vibration, i.e. at which the classification shifted from Category 2 to Category 3 or 4. This vibration threshold is hereafter called the complaint threshold. There are only seven trials that were classified as Category 3, which is the reason to merge data in Categories 3 and 4. Best fitting functions (using the least square method) for Category 2 and Categories 3/4 are shown in Figure 5.9 as dashed and dash-dotted lines, respectively. The fitting function for the

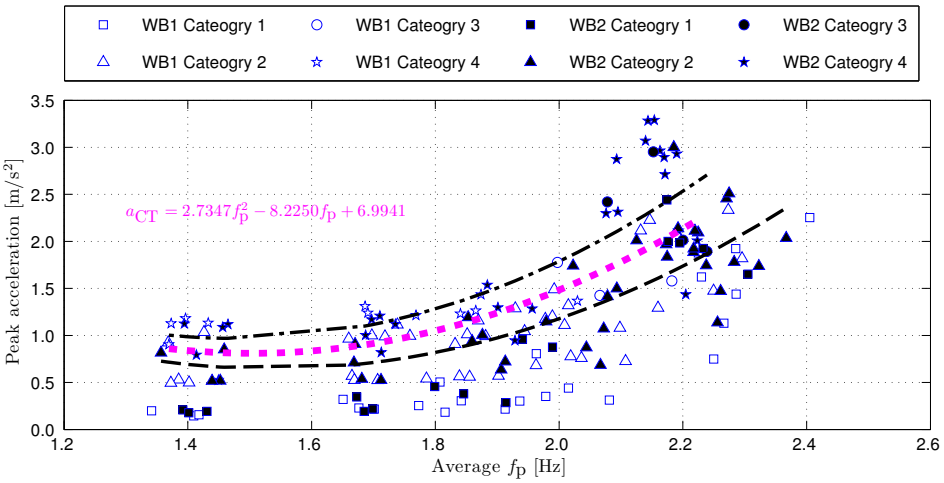

Figure 5.9: Vibration classification by test subjects. Best fitting functions of Category 2 (dashed line), Category 3/4 (dash-dotted line) and complaint threshold (dotted line).

complaint threshold of vibration perception a_{CT} (calculated as the average of fitting functions for the Categories 2 and 3/4) is also plotted in Figure 5.9 (dotted line). The threshold ranges from $0.86\,\mathrm{m/s^2}$ at the slow pacing rate of $1.37\,\mathrm{Hz}$ to $2.25\,\mathrm{m/s^2}$ at the fast pacing rate of $2.23\,\mathrm{Hz}$. Figure 5.9 shows that the threshold tends to increase when TSs walked at higher frequencies. Most likely reason for this observation is that at higher pacing rates the contact time (i.e. the duration while the feet is in contact with the ground) was reduced in comparison to slow pacing rates and, therefore, TSs were less likely to feel the vibration.

To compare the complaint threshold with vibration limits reported in literature, the range of 0.86–$2.25\,\mathrm{m/s^2}$ is within the range of mean and minimum comfort (i.e. 0.5–$2.5\,\mathrm{m/s^2}$) provided by SETRA (2006) while the minimum threshold is higher than vibration limits suggested by ISO (2007). The latter observation indicates that the limit recommended by ISO (2007) might be too conservative if a pedestrian is considered as a vibration receiver. Leonard (1966) and Smith (1969) are two rare studies investigating vibration perception of pedestrians. In these studies, pedestrians were interviewed about vibration perception when walking on vertically vibrating surfaces. Based on the answers, these researchers constructed the limiting vibration amplitude (separating unacceptable and acceptable vibrations), in which the limit was reported to decrease with an increase of vibrating frequency. However, information on the pacing rate was not provided in both studies. The results presented in this section are the first attempt known to the author to quantify human response to vibration in walking posture at a range of pacing rates.

5.5 Analysis of kinematic and kinetic characteristics of walking gait on lively surface

Seven gait parameters are presented in this chapter. These are six kinematic parameters (pacing rate, step length, step width, attack angle, end-of-step angle and trunk angle) and one kinetic parameter (walking force), measured in the same way described in Chapter 4. The following observations apply:

- The hypothesis of normal distribution tends to be assumed for each parameter whenever data are not available. In this chapter, the author wants to check if that assumption is correct for all parameters of interest. The hypothesis is evaluated using the Kolmogorov-Smirnov test, as presented in Chapter 4.
- The results/trials on rigid and lively surfaces are hereafter referred to as rigid and lively results/trials, respectively.
- The average value of one parameter throughout a trial is referred to as "the average". The mean of average values calculated for three TSs in the trials with the same walking speed is referred to as "the mean". The mean can be calculated for trials on each bridge span and on both bridges.
- 400 steps are used for analysis in both rigid and lively trials.
- Parameters extracted from the lively trials performed by a TS are compared with benchmark parameters acquired on the rigid surface at the same treadmill speed. The percentage discrepancy between two sets of data for each parameter is calculated using Equation 4.3, in which Δ, X and Y represent the discrepancy, average data measured on the lively surface and average data measured on the rigid surface, respectively.
- Measured gait parameters are presented as a function of one of the three variables: walking speed, pacing rate and acceleration level.

- Walking speed is used to effectively compare data for lively and rigid trials, since it was the key independent variable representing the treadmill speed in the experimental set-up.
- As for the pacing rate, it is commonly used as an independent variable in numerical modelling. The average pacing rate on the lively surface normalised to the structural natural frequency is denoted as $\tilde{f}_{\mathrm{p}} = f_{\mathrm{p}}/f_{\mathrm{n}}$. Subscript "r" will be used to denote the normalisation of the average pacing rate on the rigid surface ($\tilde{f}_{\mathrm{p,r}} = f_{\mathrm{p,r}}/f_{\mathrm{n}}$). For the purpose of the analysis, trials of a TS performed at nominally the same speed on rigid and lively surfaces will be considered to have the same pacing rate although small discrepancies between the average $f_{\mathrm{p,r}}$ and the average f_{p} exist.
- Finally, the acceleration is chosen due to the need to observe influence of structural vibration on the gait parameters. The average peak-per-cycle acceleration a_{ppc} is chosen instead of the peak, since the former is a better represent of those trials characterised by large variations in vibration response.

- First-order polynomial functions are used to identify best fit of the experimental data according to the least square method.

The following sub-sections present results for each measured parameter.

5.5.1 Pacing rate

Cumulative distribution function (CDF) of p-value in the Kolmogorov-Smirnov test for normal distribution hypothesis is shown in Figure 5.10. Results are first presented for each trial of individual TSs in Figures 5.10a–c. The purpose is to check if the parameter exhibits the same trend for different people. In Figures 5.10d and 5.10e, results are presented for each bridge to verify if the

vibration frequency has influence on any trend of data. Finally, the data are summarised for all trials in Figure 5.10f. For the significance level of 5 %, 88 % of all lively trials (average of lines indicating lively results in Figure 5.10f) fail to reject the normal distribution hypothesis while the corresponding number for rigid trials is 100 %. This observation indicates that while in majority of the lively trials the pacing rate is likely to be normally distributed, the presence of the structural vibration reduces the likelihood of this happening.

The pacing rate is plotted in Figure 5.11 as a function of the average walking speed. The logic behind the choice of the six graphs is the same as in Figure 5.10. In addition, the rectangle areas in Figures 5.11a–c contain all trials that were classified as normal walking speeds. The average values are used to describe the range of collected data for individual TSs (Figures 5.11a–c) while presentation in Figures 5.11d–f are for mean values to show trends across the TS population. Results of many trials without shaker, usually characterised by a low vibration level, are almost the same as the measurement from rigid trials (thin and thick solid lines, respectively, in Figures 5.11d–f). This observation suggests that the low vibration level has almost no effect on the average pacing rate, and interestingly, that the intra-subject variation in these experiments performed on different days is small. With the introduction of the pre-induced vibration level, the pacing rate becomes higher than the corresponding value in the rigid trials. The data suggest that TSs walk at a slightly higher pacing rate in lively trials. This increase becomes more pronounced with an increase of pre-induced vibration level (Figure 5.11f).

The discrepancy in the average pacing rate Δf_{p} for individual TSs is shown in Figure 5.12 as a function of the average $\tilde{f}_{\mathrm{p,r}}$ and the average a_{ppc}. The

ranges of Δf_p are from $-7.1\,\%$ to $6.1\,\%$ for TS1, from $-2.0\,\%$ to $8.2\,\%$ for TS2 and from $-2.6\,\%$ to $5.4\,\%$ for TS3. Pearson's correlation coefficient R is also calculated for each TS, denoted R_1 and R_2 for data collected on WB1 and WB2, respectively. Hereafter, the correlation is classified as weak/low for $R < 0.36$, moderate/medium for $0.36 \leq R \leq 0.67$ and strong/high for $R > 0.67$ (Taylor, 1990). Unfilled and filled symbols in Figure 5.12 represent non-resonant and resonant trials, respectively. The results show that the relationship between Δf_p and the average $\tilde{f}_\mathrm{p,r}$ is different for different TSs, with slight decrease in Δf_p for TS1 with an increase of the average $\tilde{f}_\mathrm{p,r}$, increase for TS3 and relatively independent value for TS2 (Figures 5.12a–c). With regard to the vibration level (Figures 5.12d–f), the correlation between Δf_p and the average a_ppc is generally weak, apart from trials of TS2 on WB1 and TS3 on WB2. These observations reflect the inter-subject variability of pedestrian's behaviour in responding to perceptible vibration.

CoV of pacing rate for each TS is plotted in Figure 5.13a–c as a function of the average speed. In most lively trials (84 %), the CoV is higher than in rigid trials. The discrepancy in the mean CoV also becomes larger when increasing the vibration level pre-induced by the shaker. This observation can be seen in data for individual bridge configuration (Figures 5.13d and 5.13e) and in the summary of all trials (Figure 5.13f).

The discrepancy of CoV for individual TSs ΔCoV is plotted in Figure 5.14. The ranges of ΔCoV are from $-23.3\,\%$ to $68.9\,\%$ for TS1, from $-13.4\,\%$ to $175.9\,\%$ for TS2 and from $-12.9\,\%$ to $99.9\,\%$ for TS3. These ranges are one order of magnitude higher than those related to the average pacing rate shown in Figure 5.12, which suggests that discrepancies of the intra-subject variability

within a trial are much higher than those of the average values. The results show that the level of linear dependence between ΔCoV and the average $\tilde{f}_{\mathrm{p,r}}$ as well as between ΔCoV and the average a_{ppc} are strongest for trials of TS2 (Figures 5.14b and 5.14e), while the same correlations for TS1 and TS3 are weaker (the rest of Figure 5.14). The general trend in lively trials is to increase the CoV of pacing rate though TSs respond to vibration in different ways.

Overview results for Δf_{p} and ΔCoV for all trials are plotted in Figures 5.15a and 5.15b as functions of the average $\tilde{f}_{\mathrm{p,r}}$. The purpose of these figures is to provide the mean and standard deviation of Δf_{p} and ΔCoV at different pacing rates. Since the average pacing rates at the same walking speed of different TSs are slightly different, the average $\tilde{f}_{\mathrm{p,r}}$ is allocated into 10 bins, whose centres are from 0.55 to 1.05 (there are no data points for the bin centre at 0.60). The bandwidth for each bin is 0.05 or equivalent to 0.11–0.12 Hz. Mean and standard deviation data point in Figures 5.15a and 5.15b are calculated from all the trials within a certain bin. The mean ranges from $-0.3\,\%$ to $3.1\,\%$ for Δf_{p} and from $9.3\,\%$ to $66.9\,\%$ for ΔCoV, while the standard deviation is 1.1–3.7 % and 13.9–56.7 %, respectively.

All data points for Δf_{p} and ΔCoV are presented with respect to the average a_{ppc} in Figures 5.15c and 5.15d, along with the best fitting functions. The correlations, calculated for all trials, between Δf_{p} and a_{ppc} as well as between ΔCoV and a_{ppc} are weak.

It is important to note that layouts of Figures 5.10–5.15 are used as templates for presentations of results for other kinematic parameters in Section 5.5. Only the most informative parts of each graph will be commented on while the rest of the graphs are presented for completeness and consistency.

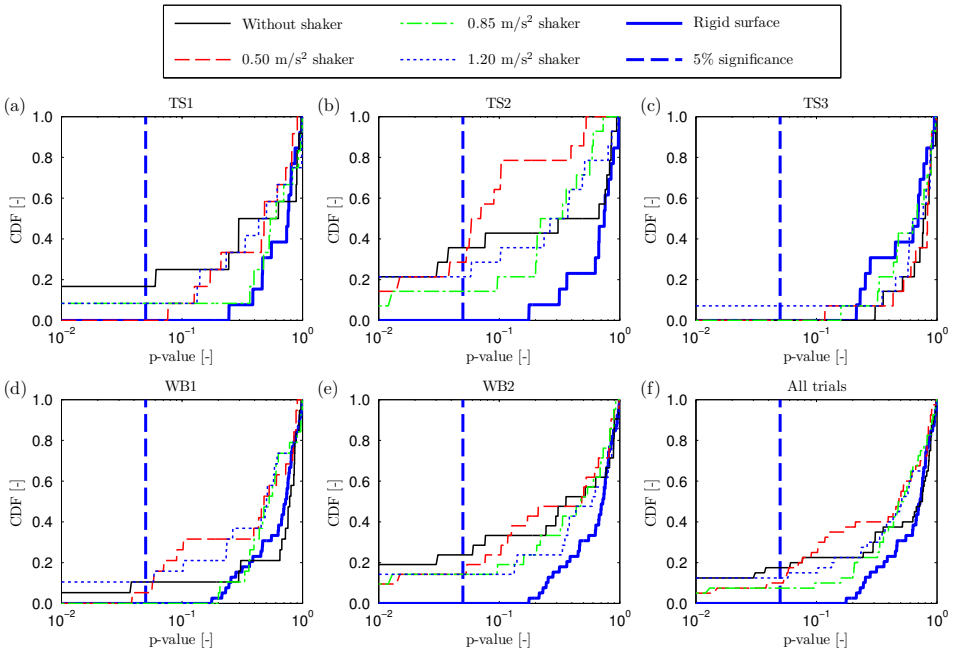

Figure 5.10: CDF of p-value of pacing rate in experiments **(a)** by TS1, **(b)** by TS2, **(c)** by TS3, **(d)** on WB1, **(e)** on WB2 and **(f)** in all trials.

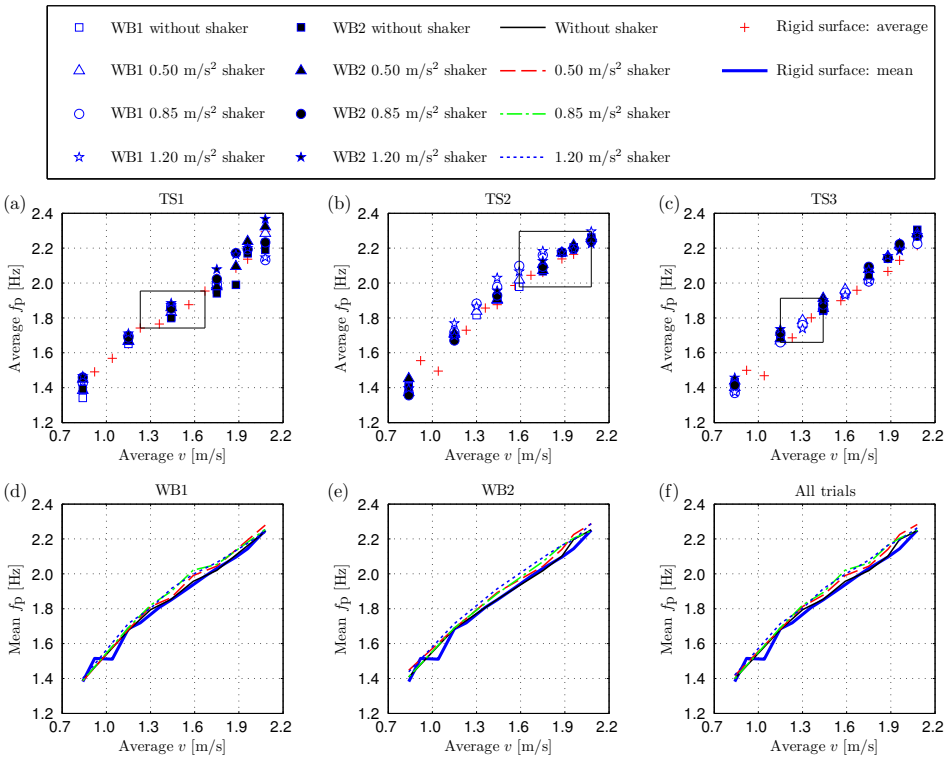

Figure 5.11: Pacing rate in experiments **(a)** by TS1, **(b)** by TS2, **(c)** by TS3, **(d)** on WB1, **(e)** on WB2 and **(f)** in all trials.

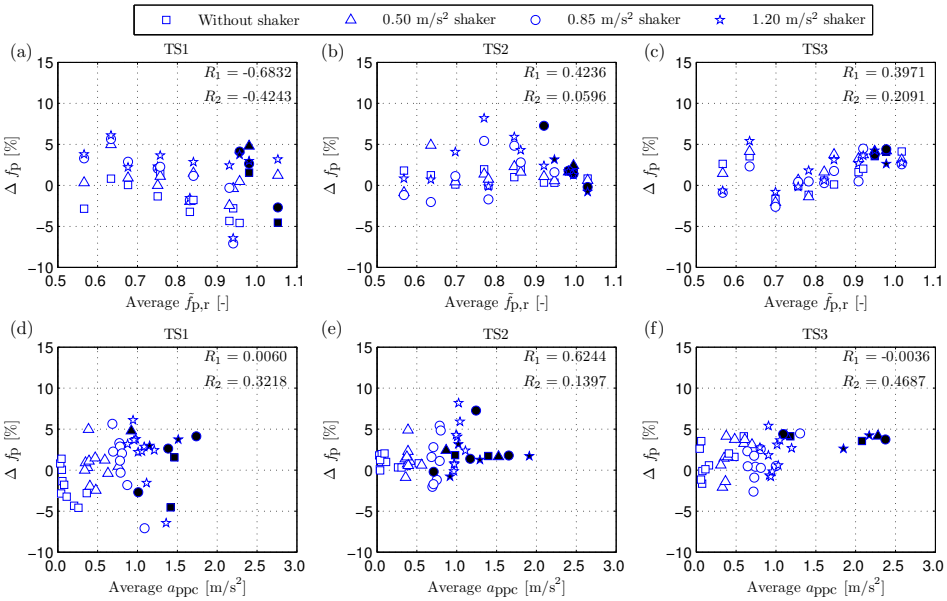

Figure 5.12: Percentage discrepancy of individual average pacing rate as a function of normalised pacing rate **(a–c)** and average peak-per-cycle acceleration **(d–f)**. Unfilled and filled symbols represent non-resonant and resonant trials, respectively.

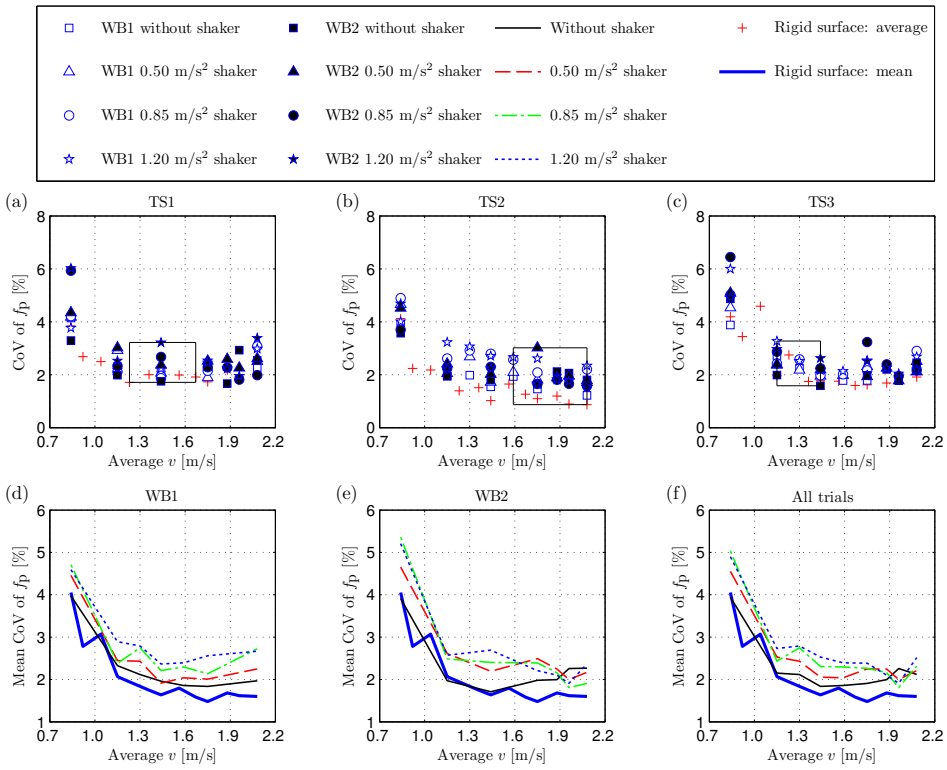

Figure 5.13: CoV of pacing rate in experiments **(a)** by TS1, **(b)** by TS2, **(c)** by TS3, **(d)** on WB1, **(e)** on WB2 and **(f)** in all trials.

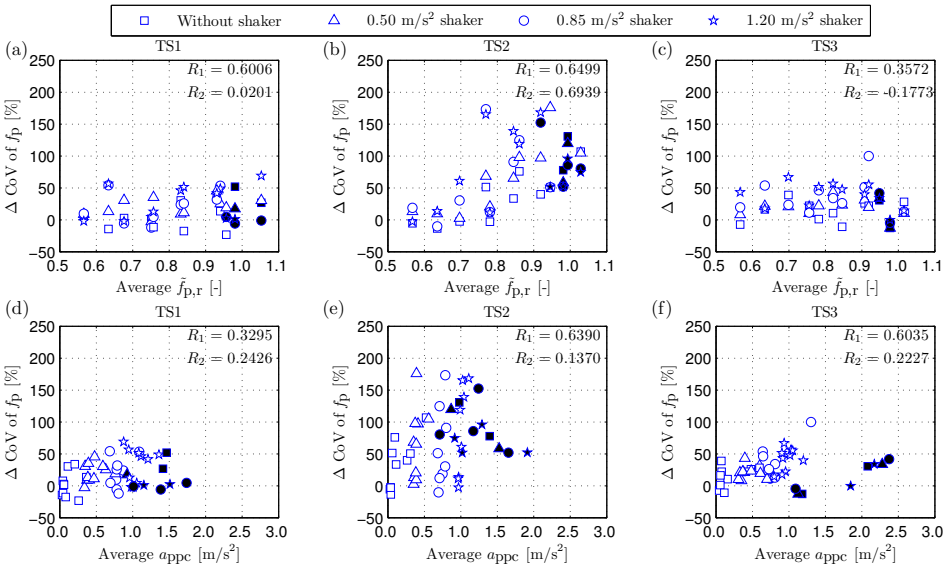

Figure 5.14: Percentage discrepancy of individual CoV of pacing rate as a function of normalised pacing rate **(a–c)** and average peak-per-cycle acceleration **(d–f)**. Unfilled and filled symbols represent non-resonant and resonant trials, respectively.

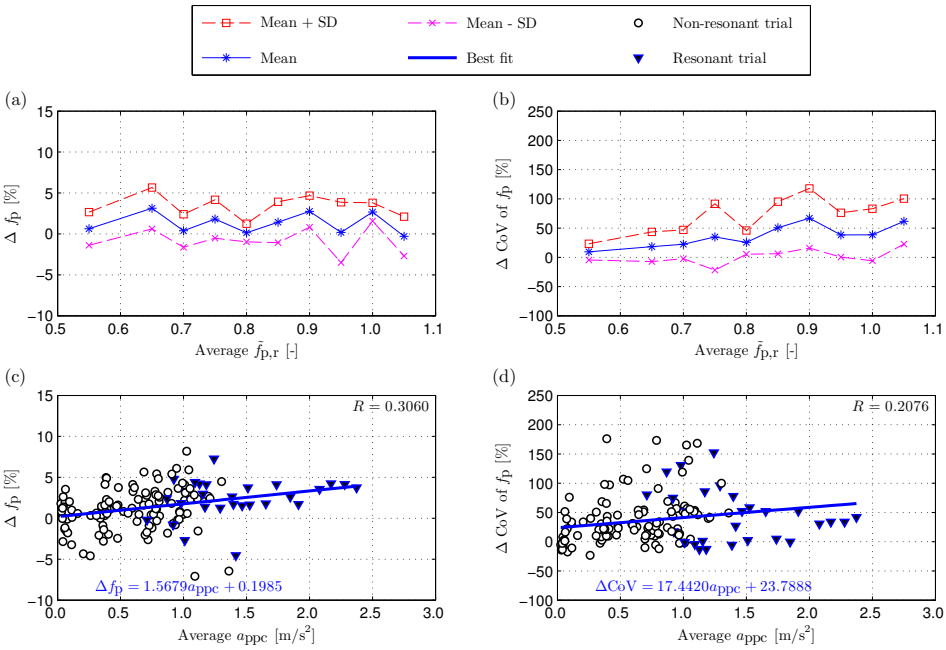

Figure 5.15: Percentage discrepancies of pacing rate and its CoV as functions of normalised pacing rate **(a–b)** and average peak-per-cycle acceleration **(c–d)**.

5.5.2 Step length

CDF for the p-value of step length, d, is plotted in Figure 5.16. There is no significant discrepancy between the results of rigid and lively trials (Figure 5.16f). The analysis shows that 96 % of the lively trials (average of lines representing lively trials in Figure 5.16f) fail to reject the normal distribution hypothesis at the significance level of 5 %, which is the same result as for the rigid trials. Therefore, the step length can be modelled as normal distribution regardless of the type of walking surfaces.

The step length is shown in Figure 5.17 as a function of the average speed. The average d in lively trials is mostly (83 %) lower than the corresponding value in the rigid trials (Figures 5.17a–c). The mean results indicate that the discrepancy in d becomes more noticeable when increasing the pre-induced vibration level (Figures 5.17d–f). Unlike in the case of the pacing rate, the data collected when the shaker is not in operation are not so close to the data collected on the rigid surface. This result indicates that the step length on the lively surface is influenced even when the perceived vibration is small. This observation also shows a noticeable intra-subject variability on different days of testing.

Discrepancy of step length Δd between lively and rigid trials is plotted in Figure 5.18. The ranges of Δd are from -7.1 % to 7.5 % for TS1, from -7.7 % to 3.0 % for TS2 and from -8.8 % to 0.7 % for TS3. Apart from TS1, absolute Δd tends to increase with an increase of the average $\tilde{f}_{\mathrm{p,r}}$ and the average a_{ppc} (Figure 5.18). Overall, the results suggest that the TSs shorten step length in lively trials. The observation of reducing step length is compatible with

the observed increase in the pacing rate shown in Figure 5.11f (based on the relation of $v = f_{\mathrm{p}} d$).

CoV of step length is plotted in Figure 5.19 as a function of the average speed. CoV in the lively trials is mostly (70 %) larger than that in the rigid trials (Figures 5.19a–c). The mean results in Figures 5.19d–f show that variations in step length in trials without shaker are similar to those in rigid trials, while increasing the vibration increases the variations.

Discrepancy of CoV of step length is shown in Figure 5.20. The ranges of ΔCoV are from -22.0 % to 60.0 % for TS1, from -51.9 % to 108.3 % for TS2 and from -0.4 % to 96.6 % for TS3. Similar to the analysis of the pacing rate, these ranges of CoV are much higher than those seen in the discrepancy of the average value. The correlation between ΔCoV and the average $\tilde{f}_{\mathrm{p,r}}$ is weakest for trials of TS3 (Figures 5.20a–c). On the other hand, the correlation between ΔCoV and the average a_{ppc} is moderate apart from trials of TS1 on WB1 (Figures 5.20d–f). These observations indicate that TSs introduce higher variations in step length in lively trials.

Δd and ΔCoV of all trials are plotted in Figures 5.21a and 5.21b as functions of the average $\tilde{f}_{\mathrm{p,r}}$. The mean is from -4.3 % to -0.3 % for Δd and 3.1–43.8 % for ΔCoV, while the standard deviation is 1.2–4.7 % and 18.6–42.2 %, respectively. Best fitting functions to Δd and ΔCoV, with respect to the average a_{ppc}, are given in Figures 5.21c and 5.21d.

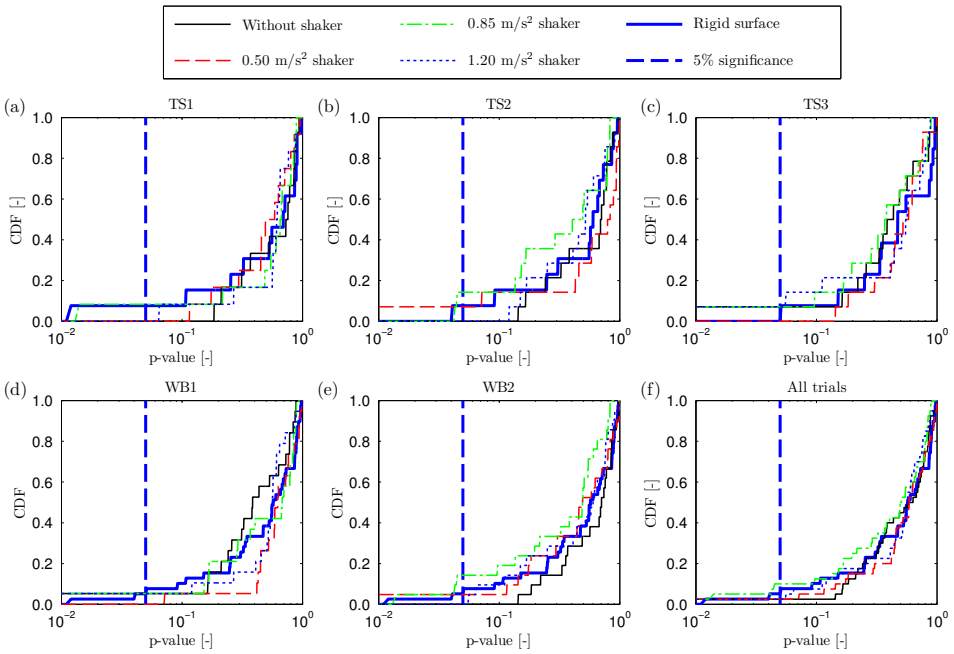

Figure 5.16: CDF of p-value of step length in experiments **(a)** by TS1, **(b)** by TS2, **(c)** by TS3, **(d)** on WB1, **(e)** on WB2 and **(f)** in all trials.

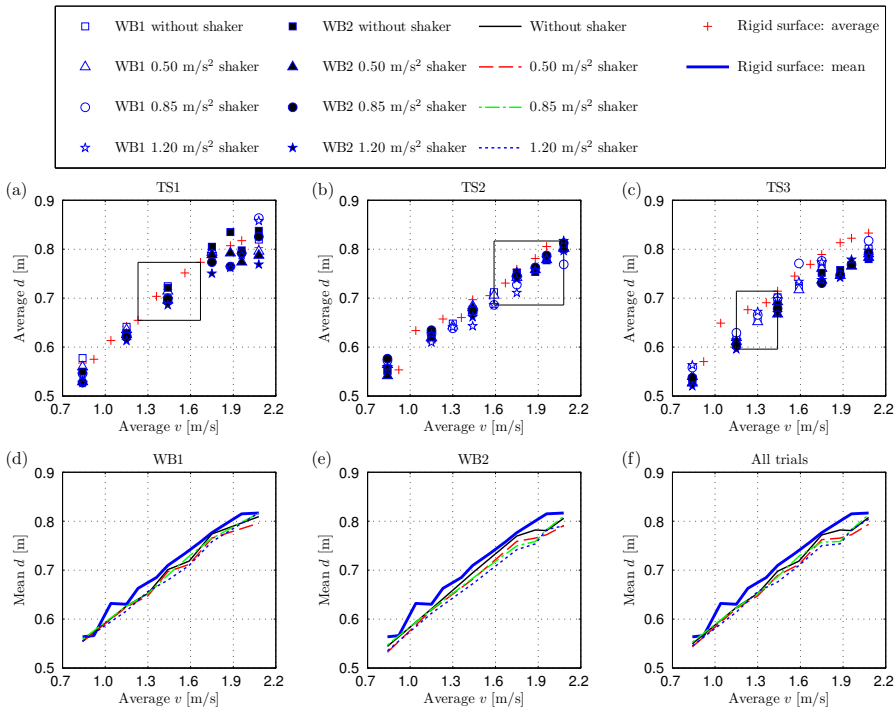

Figure 5.17: Step length in experiments **(a)** by TS1, **(b)** by TS2, **(c)** by TS3, **(d)** on WB1, **(e)** on WB2 and **(f)** in all trials.

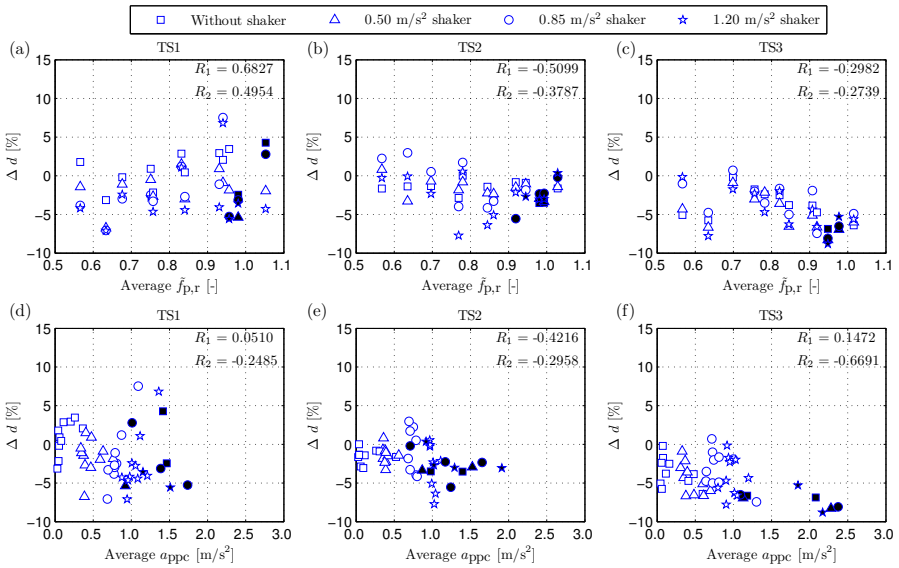

Figure 5.18: Percentage discrepancy of individual average step length as a function of normalised pacing rate **(a–c)** and average peak-per-cycle acceleration **(d–f)**. Unfilled and filled symbols represent non-resonant and resonant trials, respectively.

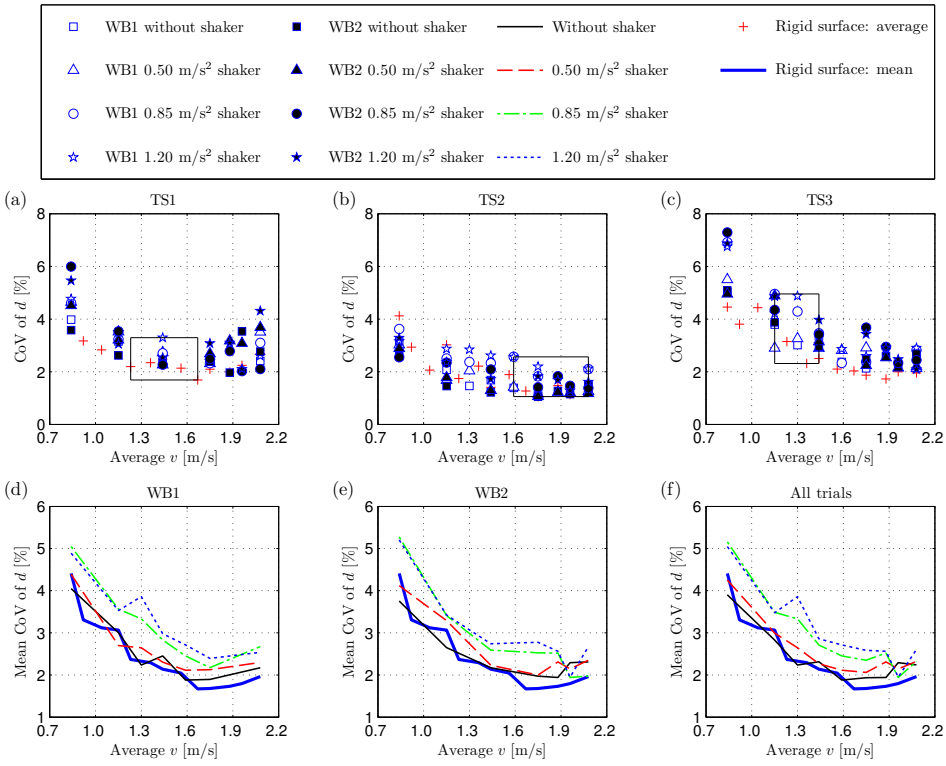

Figure 5.19: CoV of step length in experiments **(a)** by TS1, **(b)** by TS2, **(c)** by TS3, **(d)** on WB1, **(e)** on WB2 and **(f)** in all trials.

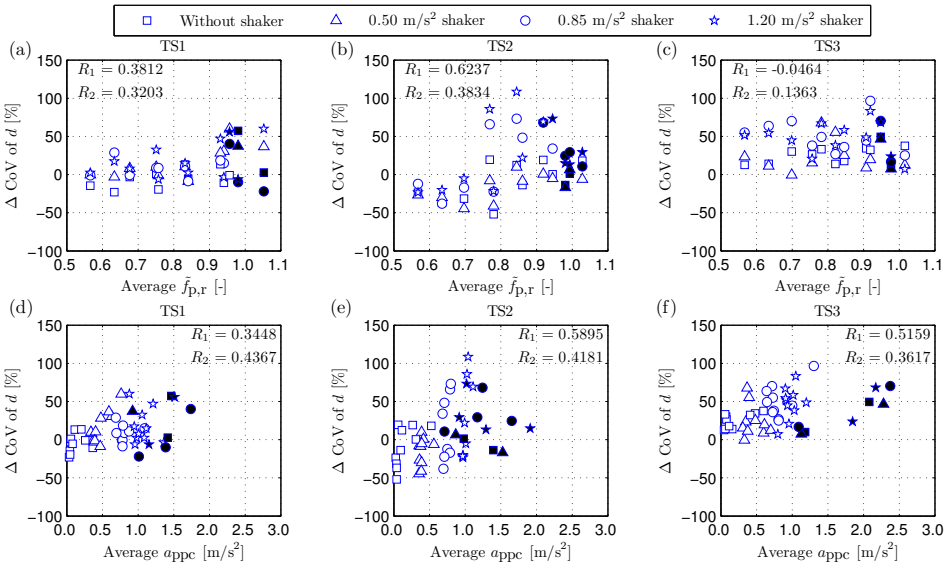

Figure 5.20: Percentage discrepancy of individual CoV of step length as a function of normalised pacing rate **(a–c)** and average peak-per-cycle acceleration **(d–f)**. Unfilled and filled symbols represent non-resonant and resonant trials, respectively.

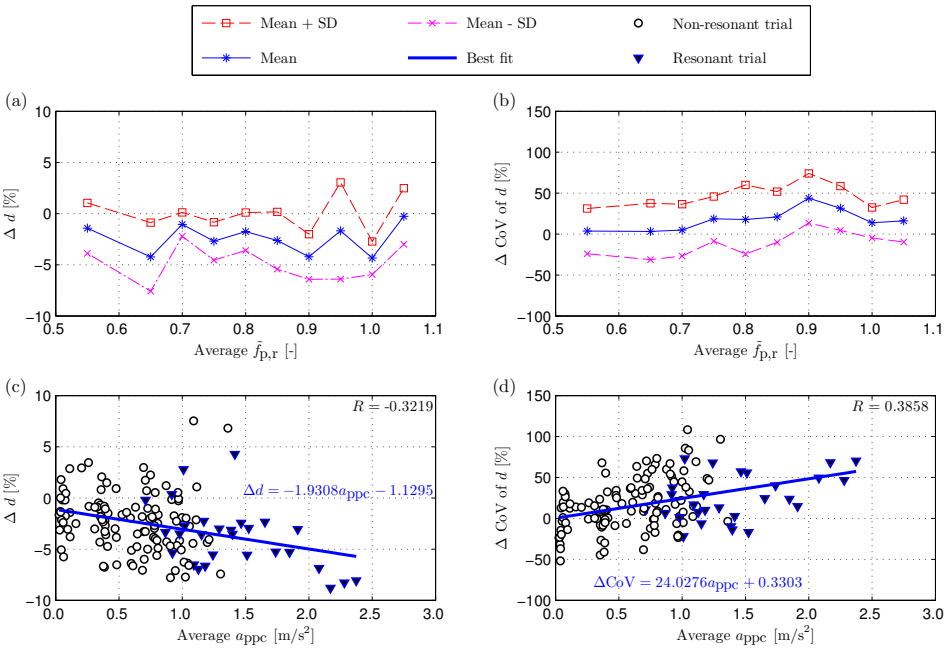

Figure 5.21: Percentage discrepancies of step length and its CoV as functions of normalised pacing rate **(a–b)** and average peak-per-cycle acceleration **(c–d)**.

5.5.3 Step width

CDF of p-value of step width w is plotted in Figure 5.22. The result shows that 100 % of all trials (both lively and rigid) fail to reject the normal distribution hypothesis at the significance level of 5 % (Figure 5.22f).

Step width is plotted in Figure 5.23. Apart from TS2 trials, the average w in lively trials is mostly larger than that in the rigid trials (Figures 5.23a and 5.23c). Also, it seems that the step width is independent from the induced-vibration level. Δw is shown in Figure 5.24, ranging from −18.8 % to 39.6 % for TS1, from −19.2 % to 50.5 % for TS2 and from −6.3 % to 34.7 % for TS3. Since the results of trials without shaker are significantly different from the rigid results, the observation of increase in step width might likely come from the intra-subject variability of testing on different days.

The CoV of step width is shown in Figure 5.25, and it tends to be lower in lively trials than in rigid trials (Figures 5.25a–c). ΔCoV is plotted in Figure 5.26. The ranges of ΔCoV are from −40.7 % to 24.2 % for TS1, from −50.6 % to 7.6 % for TS2 and from −39.6 % to 48.7 % for TS3. Unlike pacing rate and step length, these discrepancy ranges are comparable to those seen in the discrepancy of the average value. In Figure 5.26, there is no clear trends of correlations between ΔCoV and the average $\tilde{f}_{\mathrm{p,r}}$. Apart from trials of TS2 on WB1, the results suggest that the vibration has no influence on the step width.

Δw and ΔCoV are plotted in Figures 5.27a and 5.27b. The mean is 0.6–14.6 % for Δw and between −24.7 % and 4.0 % for ΔCoV, while the standard deviation is 8.0–21.5 % and 8.5–25.7 %, respectively. Best fitting functions of Δw and ΔCoV with the average a_{ppc} are given in Figures 5.27c and 5.27d.

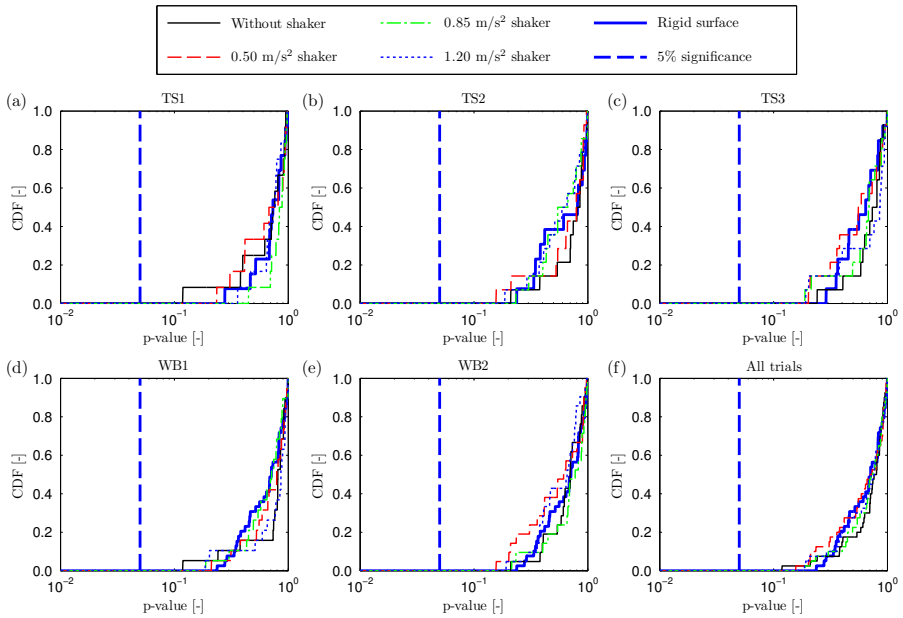

Figure 5.22: CDF of p-value of step width in experiments **(a)** by TS1, **(b)** by TS2, **(c)** by TS3, **(d)** on WB1, **(e)** on WB2 and **(f)** in all trials.

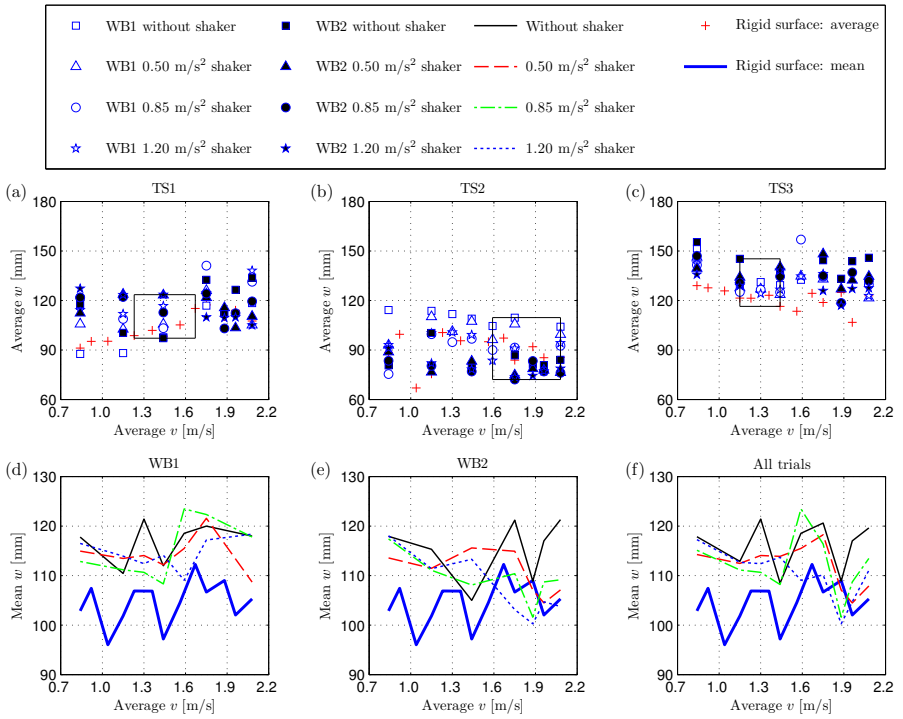

Figure 5.23: Step width in experiments **(a)** by TS1, **(b)** by TS2, **(c)** by TS3, **(d)** on WB1, **(e)** on WB2 and **(f)** in all trials.

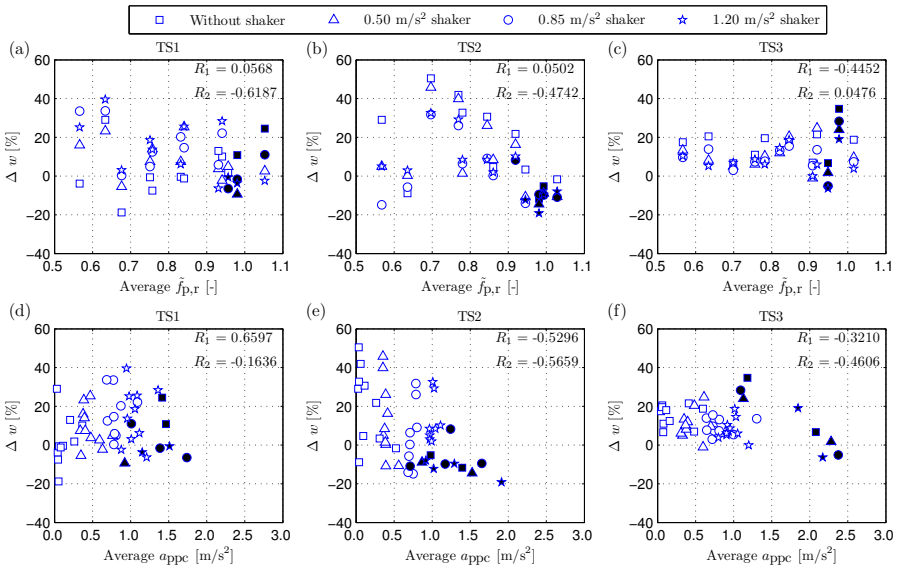

Figure 5.24: Percentage discrepancy of individual average step width as a function of normalised pacing rate **(a–c)** and average peak-per-cycle acceleration **(d–f)**. Unfilled and filled symbols represent non-resonant and resonant trials, respectively.

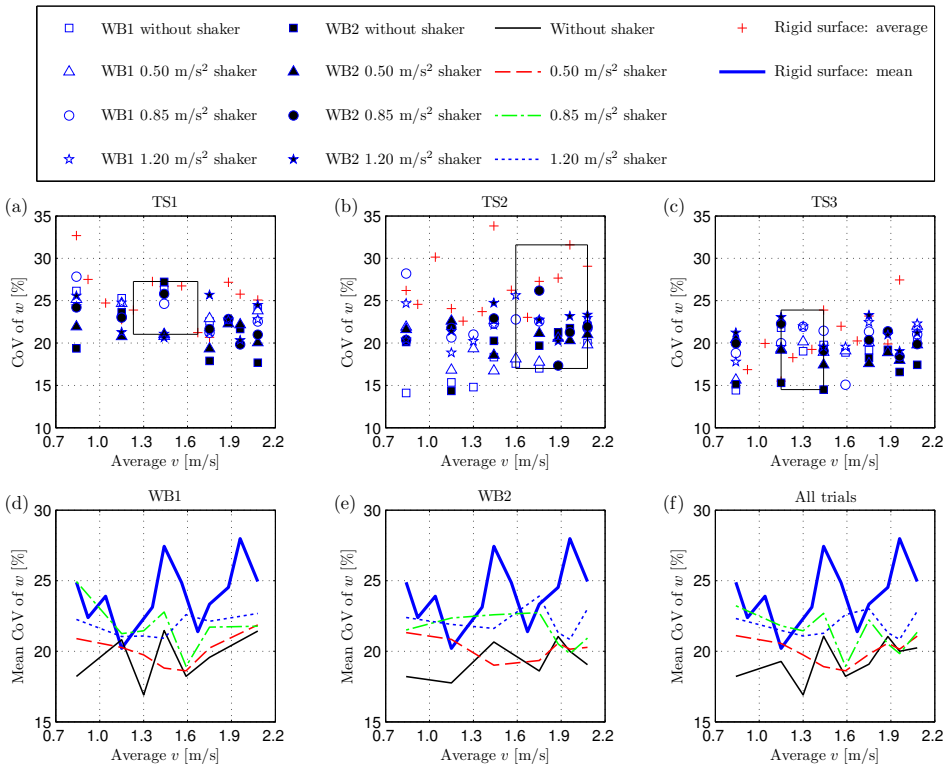

Figure 5.25: CoV of step width in experiments **(a)** by TS1, **(b)** by TS2, **(c)** by TS3, **(d)** on WB1, **(e)** on WB2 and **(f)** in all trials.

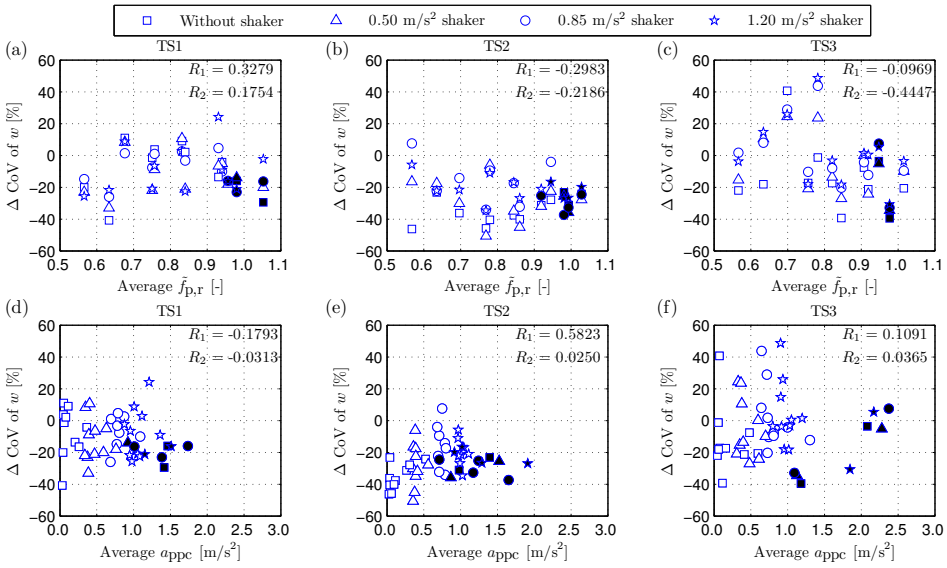

Figure 5.26: Percentage discrepancy of individual CoV of step width as a function of normalised pacing rate **(a–c)** and average peak-per-cycle acceleration **(d–f)**. Unfilled and filled symbols represent non-resonant and resonant trials, respectively.

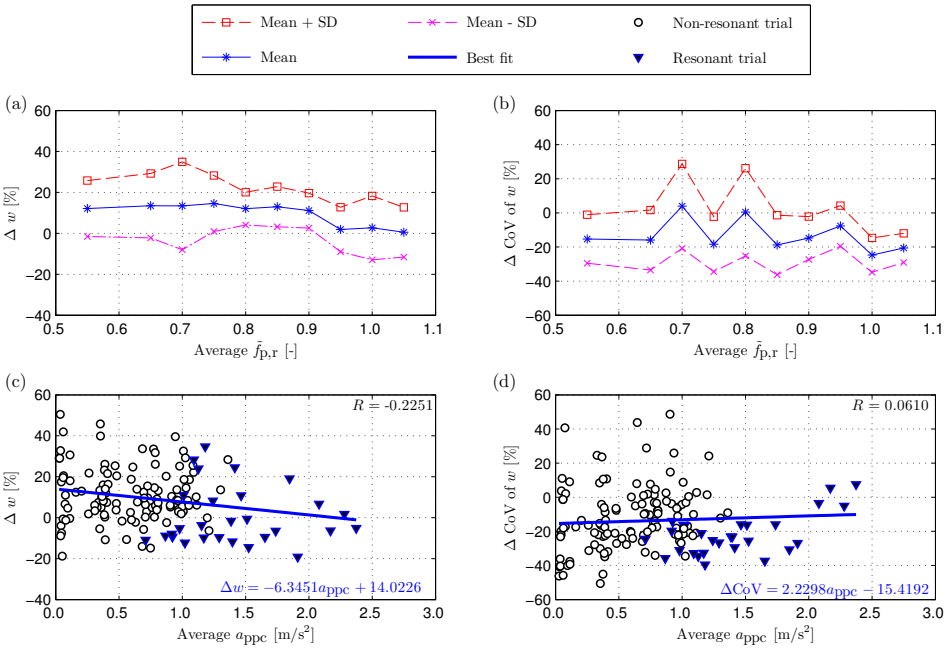

Figure 5.27: Percentage discrepancies of step width and its CoV as functions of normalised pacing rate **(a–b)** and average peak-per-cycle acceleration **(c–d)**.

5.5.4 Attack angle

CDF of p-value of attack angle θ_0 is plotted in Figure 5.28. The result shows that 94 % of the lively trials (average of lines representing lively trials in Figure 5.28f) fail to reject the normal distribution hypothesis at the significance level of 5 %, which is slightly smaller than the result of 97 % on rigid trials. Thus, the attack angle can be modelled as normal distribution in the lively trials.

The attack angle is plotted in Figure 5.29 as a function of the average speed. Apart from TS2 trials, the average θ_0 in lively trials is mostly higher than that in rigid trials (Figures 5.29a and 5.29c). The mean results presented in Figures 5.29d–f suggest that even though the attack angle tends to become higher in lively trials, such an increase does not depend on the vibration level. $\Delta\theta_0$ for individual TSs is plotted in Figure 5.30. The ranges of $\Delta\theta_0$ are from -2.5 % to 3.0 % for TS1, from -4.3 % to 3.7 % for TS2 and from 0.0 % to 7.3 % for TS3. The correlation between $\Delta\theta_0$ and the average $\tilde{f}_{\mathrm{p,r}}$ is moderate, apart from trials of TS1 on WB2 (Figures 5.30a–c). Besides, the correlation between $\Delta\theta_0$ and the average a_{ppc} is generally weak, apart from trials of TS1 on WB1 and TS3 on WB2 (Figures 5.30d–f). Overall, TSs tend to increase attack angle in lively trials. Such an increase of θ_0 corresponds to the reduction in step length as shown in Figure 5.17f.

CoV of θ_0 is shown in Figure 5.31 as a function of the average speed. Most of the lively trials (86 %) have higher CoV than rigid trials (Figures 5.31a–c). The mean results presented in Figure 5.31f indicate that ΔCoV becomes more significant when increasing the vibration level. Also, the results without shaker are closest to the results on rigid trials suggesting that the

intra-subject variability of TSs on different days is quite small. Thus, the TSs were directly affected by the structural vibration and consequently increased the CoV. ΔCoV is plotted in Figure 5.32. The ranges of ΔCoV are from $-23.3\,\%$ to $74.5\,\%$ for TS1, from $-35.9\,\%$ to $154.8\,\%$ for TS2 and from $-4.9\,\%$ to $169.4\,\%$ for TS3. These ranges are much higher than those seen in $\Delta\theta_0$, suggesting the high intra-subject variability within a trial due to perceptible vibration. The results show that ΔCoV of all TSs tends to increase with an increase of the normalised pacing rate and the acceleration level.

$\Delta\theta_0$ and ΔCoV of all trials are plotted in Figures 5.33a and 5.33b as functions of the average $\tilde{f}_{\mathrm{p,r}}$. The mean is from $-1.1\,\%$ to $2.6\,\%$ for $\Delta\theta_0$ and between $-8.1\,\%$ and $55.9\,\%$ for ΔCoV, while the standard deviation is 0.8–3.1 % and 14.5–58.2 %, respectively. Best fitting functions of $\Delta\theta_0$ and ΔCoV with regard to the average a_{ppc} are given in Figures 5.33c and 5.33d.

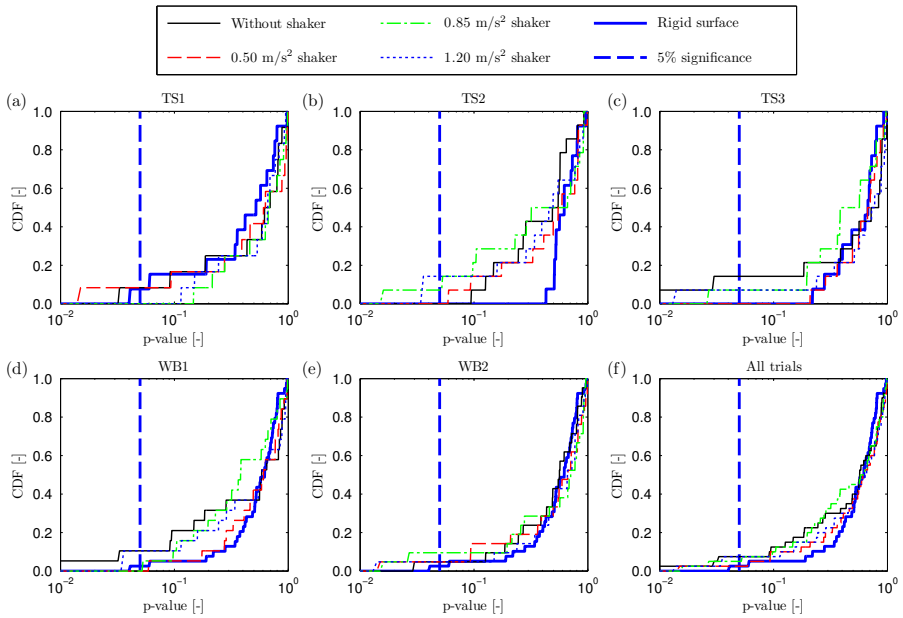

Figure 5.28: CDF of p-value of attack angle in experiments **(a)** by TS1, **(b)** by TS2, **(c)** by TS3, **(d)** on WB1, **(e)** on WB2 and **(f)** in all trials.

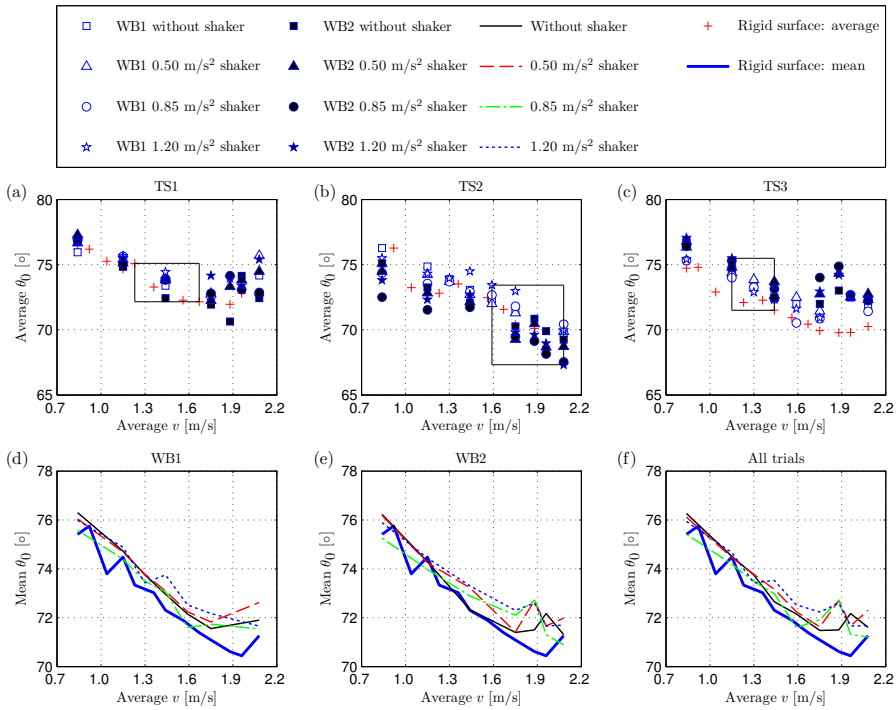

Figure 5.29: Attack angle in experiments **(a)** by TS1, **(b)** by TS2, **(c)** by TS3, **(d)** on WB1, **(e)** on WB2 and **(f)** in all trials.

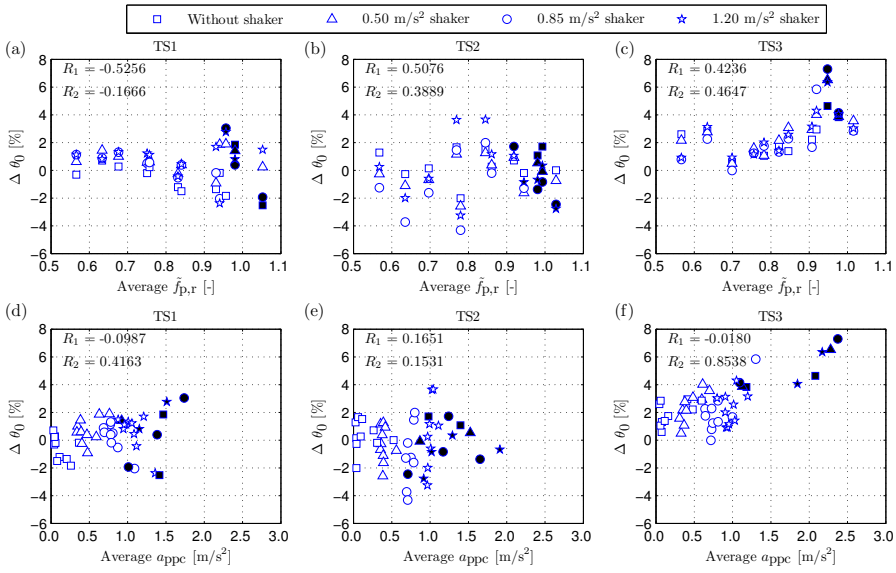

Figure 5.30: Percentage discrepancy of individual average attack angle as a function of normalised pacing rate **(a–c)** and average peak-per-cycle acceleration **(d–f)**. Unfilled and filled symbols represent non-resonant and resonant trials, respectively.

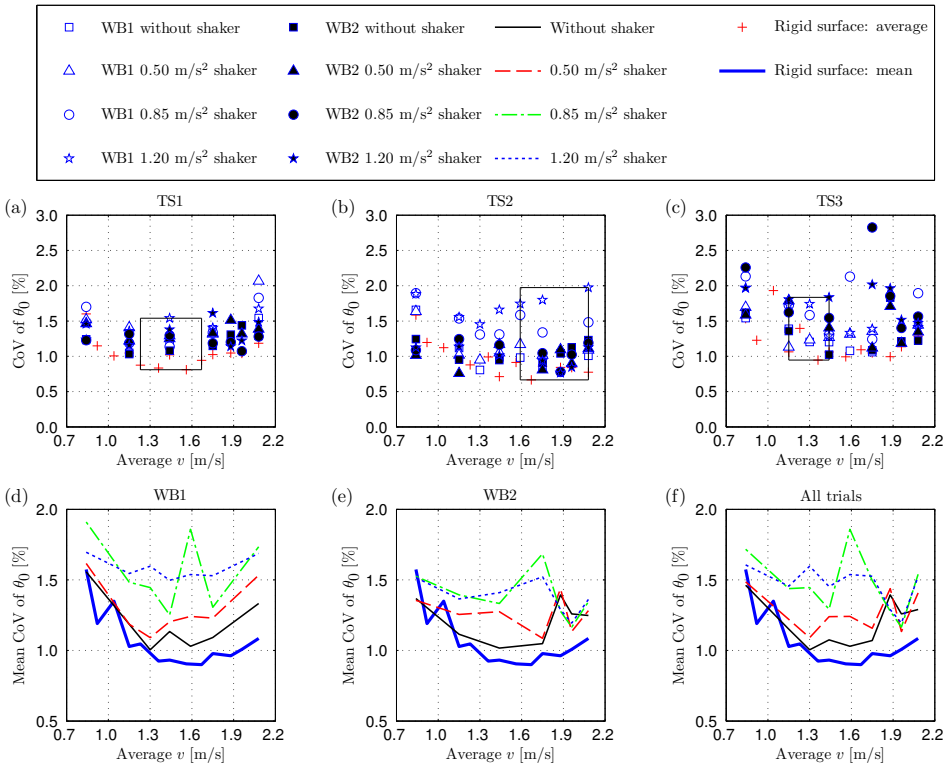

Figure 5.31: CoV of attack angle in experiments **(a)** by TS1, **(b)** by TS2, **(c)** by TS3, **(d)** on WB1, **(e)** on WB2 and **(f)** in all trials.

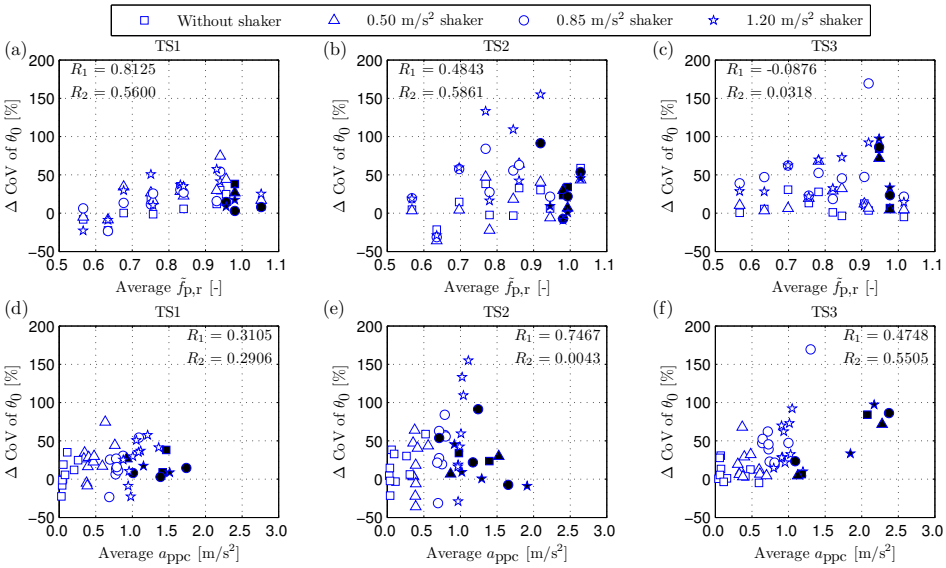

Figure 5.32: Percentage discrepancy of individual CoV of attack angle as a function of normalised pacing rate **(a–c)** and average peak-per-cycle acceleration **(d–f)**. Unfilled and filled symbols represent non-resonant and resonant trials, respectively.

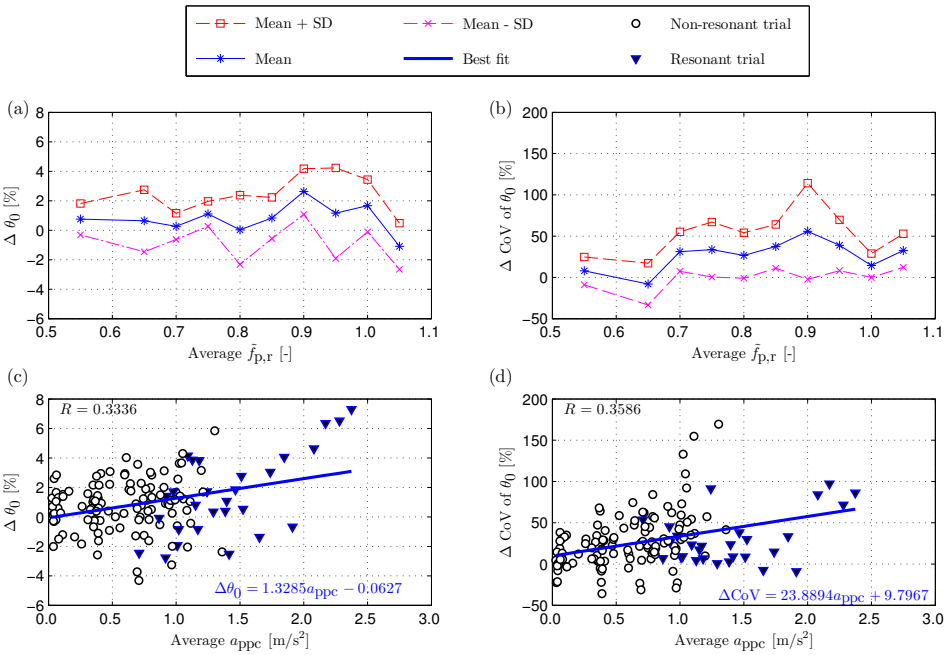

Figure 5.33: Percentage discrepancies of attack angle and its CoV as functions of normalised pacing rate **(a–b)** and average peak-per-cycle acceleration **(c–d)**.

5.5.5 End-of-step angle

CDF of p-value of end-of-step angle θ_e is plotted in Figure 5.34. Of all lively trials, 82 % trials (average of lines representing lively trials in Figure 5.34f) fail to reject the normal distribution hypothesis at the significance level of 5 %, which is significantly lower than the result of 100 % for rigid trials. Though normal distribution can still be used to model θ_e, walking on the lively surface reduces the likelihood of this happening.

Average end-of-step angle is plotted in Figure 5.35 as a function of the average speed. The average θ_e in lively trials is similar to that observed in the rigid trials (Figures 5.35d–f). $\Delta\theta_e$ for individual TS is shown in Figure 5.36. The ranges of $\Delta\theta_e$ are from −0.6 % to 3.5 % for TS1, from −1.8 % to 1.4 % for

TS2 and from −1.6 % to 0.8 % for TS3. For majority of trials (72 %), $|\Delta\theta_\mathrm{e}|$ is less than 1 %. Such small values indicate that θ_e does not change much even when structural vibrations are substantial. Besides, correlations between $\Delta\theta_\mathrm{e}$ and the average $\tilde{f}_\mathrm{p,r}$ and average a_ppc for all TSs are mostly weak (Figure 5.36).

CoV of θ_e is shown in Figure 5.37 as a function of the average speed. Most of lively trials (79 %) have higher CoV than rigid trials (Figures 5.37a–c). Also, the discrepancy in CoV of θ_e tends to increases with an increase of the vibration level pre-induced by the shaker (Figures 5.37d–f). ΔCoV is plotted in Figure 5.38. The ranges of ΔCoV are from −35.0 % to 114.2 % for TS1, from −31.8 % to 257.2 % for TS2 and from −6.1 % to 106.1 % for TS3. Similar to the analysis of the attack angle, these ranges of CoV are much higher than those observed for the average value. In TS1 and TS2 trials (Figures 5.38a, 5.38b, 5.38d and 5.38e), ΔCoV tends to increase with an increase of the normalised pacing rate and acceleration level. Such an increase tendency of ΔCoV with an increase of the average $\tilde{f}_\mathrm{p,r}$ is not seen in TS3 trials (Figure 5.38c) while the ΔCoV is quite independent from the average a_ppc (Figure 5.38f). These observations indicate that though the average values are mostly the same between lively and rigid trials, TSs generally induce higher intra-subject variability of end-of-step angle in lively trials.

$\Delta\theta_\mathrm{e}$ and ΔCoV of all trials are plotted in Figures 5.39a and 5.39b as functions of the average $\tilde{f}_\mathrm{p,r}$. The mean is from −0.4 % to 1.2 % for $\Delta\theta_\mathrm{e}$ and between 2.2 % and 72.6 % for ΔCoV, while the standard deviation is 0.5–1.2 % and 19.3–71.2 %, respectively. Best fitting functions of $\Delta\theta_\mathrm{e}$ and ΔCoV with respect to the average a_ppc are given in Figures 5.39c and 5.39d.

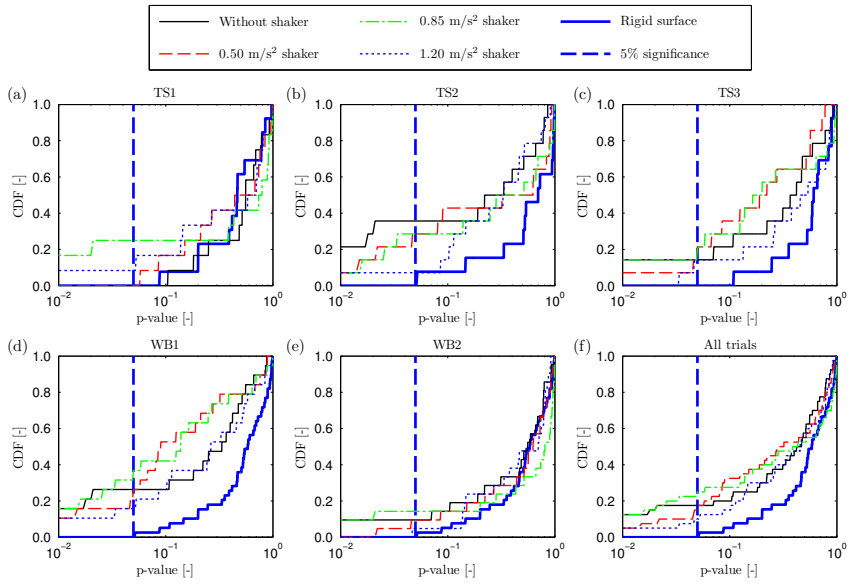

Figure 5.34: CDF of p-value of end-of-step angle in experiments **(a)** by TS1, **(b)** by TS2, **(c)** by TS3, **(d)** on WB1, **(e)** on WB2 and **(f)** in all trials.

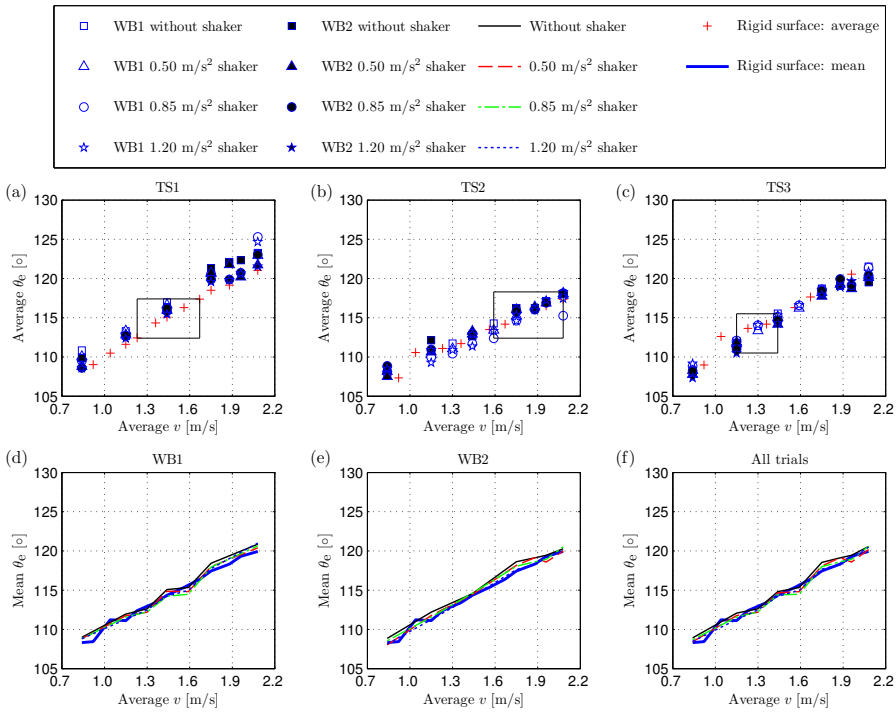

Figure 5.35: End-of-step angle in experiments **(a)** by TS1, **(b)** by TS2, **(c)** by TS3, **(d)** on WB1, **(e)** on WB2 and **(f)** in all trials.

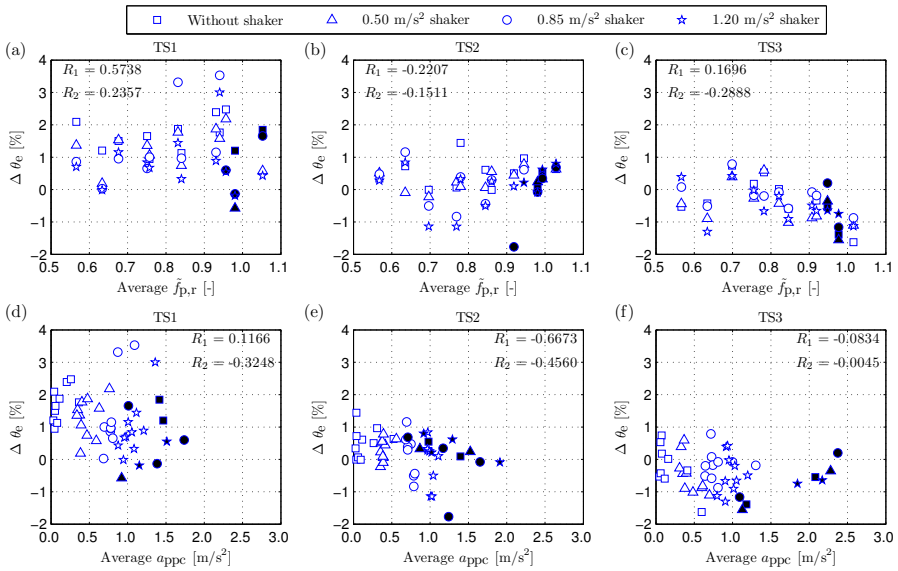

Figure 5.36: Percentage discrepancy of individual average end-of-step angle as a function of normalised pacing rate **(a–c)** and average peak-per-cycle acceleration **(d–f)**. Unfilled and filled symbols represent non-resonant and resonant trials, respectively.

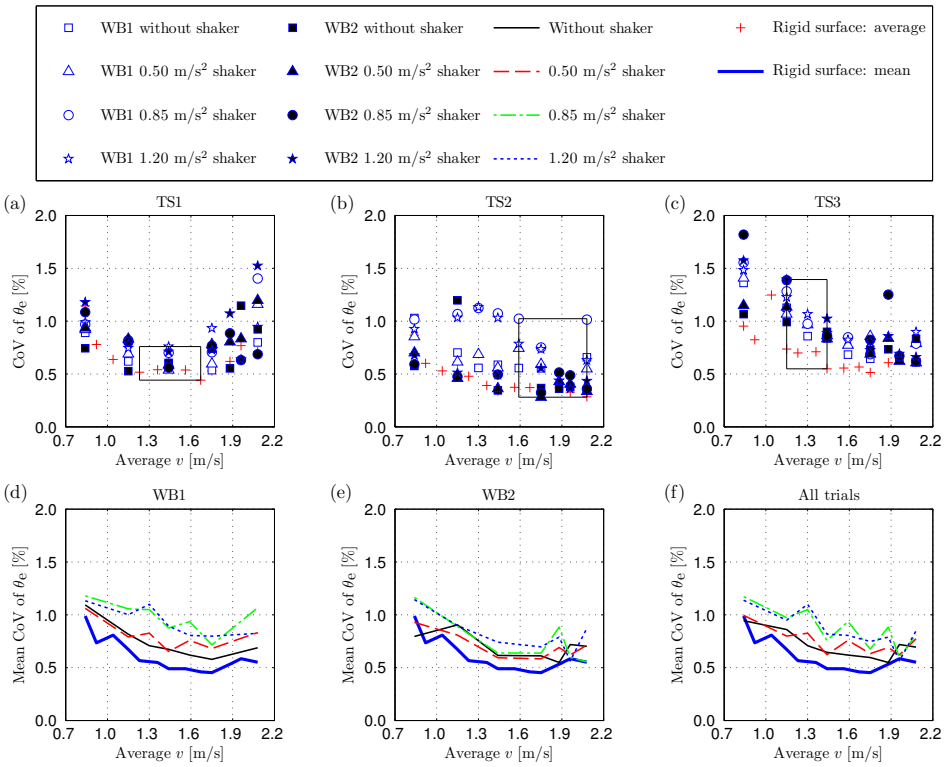

Figure 5.37: CoV of end-of-step angle in experiments **(a)** by TS1, **(b)** by TS2, **(c)** by TS3, **(d)** on WB1, **(e)** on WB2 and **(f)** in all trials.

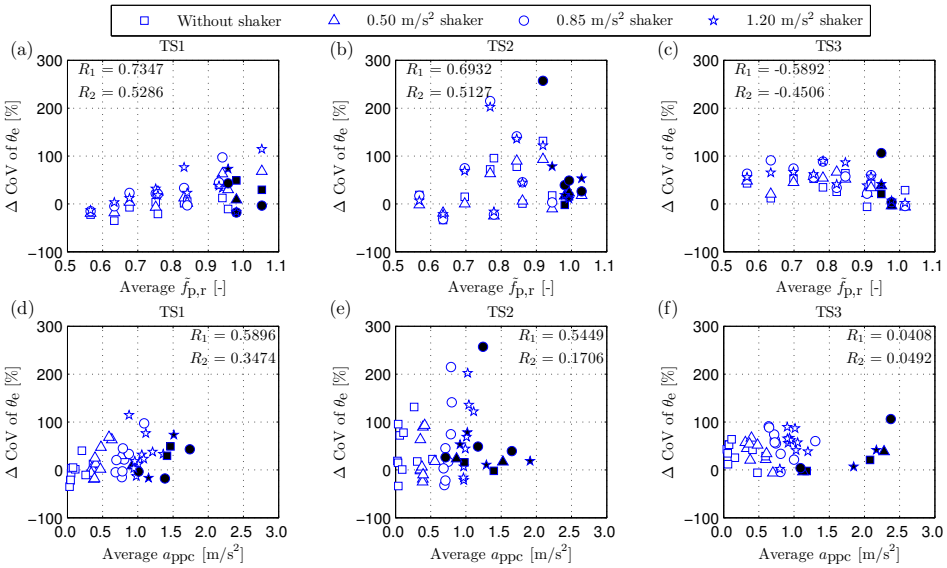

Figure 5.38: Percentage discrepancy of CoV of individual end-of-step angle as a function of normalised pacing rate **(a–c)** and average peak-per-cycle acceleration **(d–f)**. Unfilled and filled symbols represent non-resonant and resonant trials, respectively.

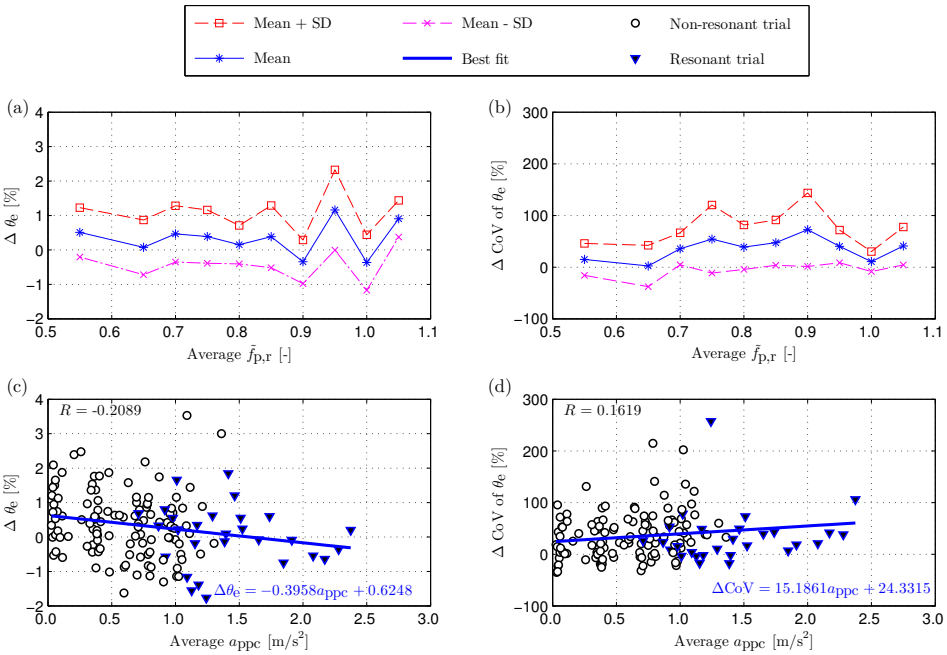

Figure 5.39: Percentage discrepancies of end-of-step angle and its CoV as functions of normalised pacing rate **(a–b)** and average peak-per-cycle acceleration **(c–d)**.

5.5.6 Trunk angle

CDF of p-value of trunk angle θ_{tr} is plotted in Figure 5.40. The result shows that 94 % of the lively trials (average of lines representing lively trials in Figure 5.40f) fail to reject the normal distribution hypothesis at the significance level of 5 %, which is slightly higher than the result of 92 % in the rigid trials. Therefore, the trunk angle can be modelled as normal distribution in the lively trials.

The trunk angle is plotted in Figure 5.41 as a function of the average speed. Most lively trials (83 %) have the average θ_{tr} higher than the rigid trials (Figures 5.41a–c). This observation suggests that while walking on the lively surface, the TSs tend to lean forwards slightly more than when walking on the rigid surface. Such an increase becomes more noticeable when increasing the vibration level (Figures 5.41d–f). The discrepancy of θ_{tr} is shown in Figure 5.42. The ranges of $\Delta\theta_{\mathrm{tr}}$ are from -1.5 % to 4.5 % for TS1, from 0.0 % to 3.7 % for TS2 and from -1.7 % to 6.2 % for TS3. There is a weak correlation between $\Delta\theta_{\mathrm{tr}}$ and the average $\tilde{f}_{\mathrm{p,r}}$ for all TSs (Figures 5.42a–c). The correlation between $\Delta\theta_{\mathrm{tr}}$ and the average a_{ppc} is also weak, apart from trials of TS1 on WB1 and TS3 on WB2 (Figures 5.42d–f). Overall, the data show that TSs tend to increase the average θ_{tr} in the lively trials.

CoV of θ_{tr} is shown in Figure 5.43 as a function of the average speed. Most of the lively trials (65 %) have higher CoV than in the rigid trials (Figures 5.43a–c). ΔCoV is plotted in 5.44. The ranges of ΔCoV are from -26.1 % to 34.0 % for TS1, from -15.7 % to 72.7 % for TS2 and from -20.1 % to 61.3 % for TS3. Similar to the analysis of θ_0 and θ_{e}, these ranges for CoV are much

higher than those obtained from the average value. There is a weak correlation between ΔCoV and the average $\tilde{f}_{\mathrm{p,r}}$, apart from trials of TS1 on WB1 and TS3 on WB2 (Figures 5.44a–c). In trials of TS2 and TS3, ΔCoV tends to increase with an increase of the acceleration level (Figures 5.44e and 5.44f) while such an increase trend is not seen for trials of TS1 (Figure 5.44d).

Mean results in Figures 5.41f and 5.43f suggest that θ_{tr} and its CoV increases in lively trials. Also, such an increase becomes more noticeable when increasing the vibration level.

$\Delta\theta_{\mathrm{tr}}$ and ΔCoV of all trials are plotted in Figures 5.45a and 5.45b as functions of the average $\tilde{f}_{\mathrm{p,r}}$. The mean is from 0.5 % to 2.3 % for $\Delta\theta_{\mathrm{tr}}$ and between 0.5 % and 17.7 % for ΔCoV, while the standard deviation is 0.8–1.8 % and 11.3–28.7 %, respectively. Best fitting functions for $\Delta\theta_{\mathrm{tr}}$ and ΔCoV, with regard to the average a_{ppc}, are given in Figures 5.45c and 5.45d.

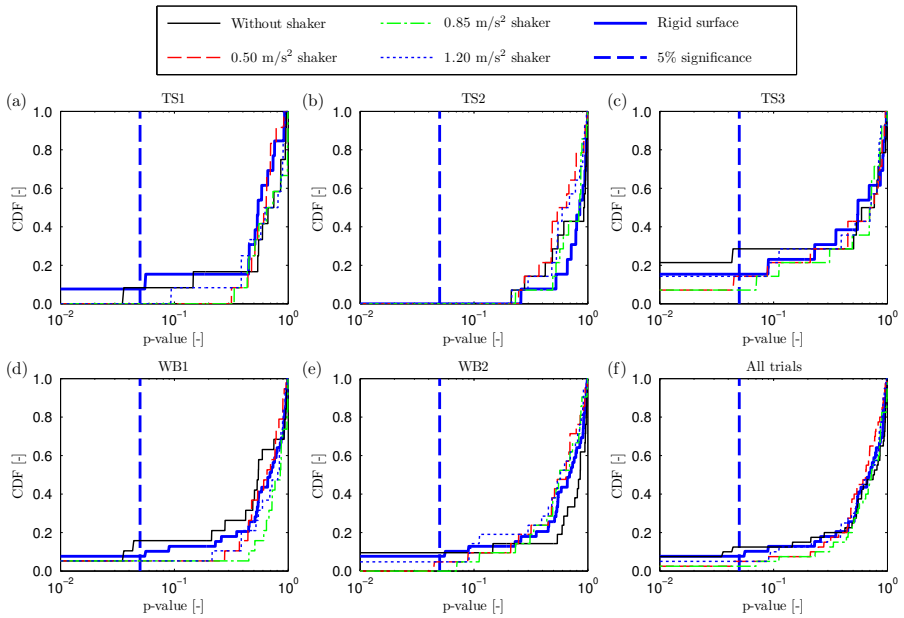

Figure 5.40: CDF of p-value of trunk angle in experiments **(a)** by TS1, **(b)** by TS2, **(c)** by TS3, **(d)** on WB1, **(e)** on WB2 and **(f)** in all trials.

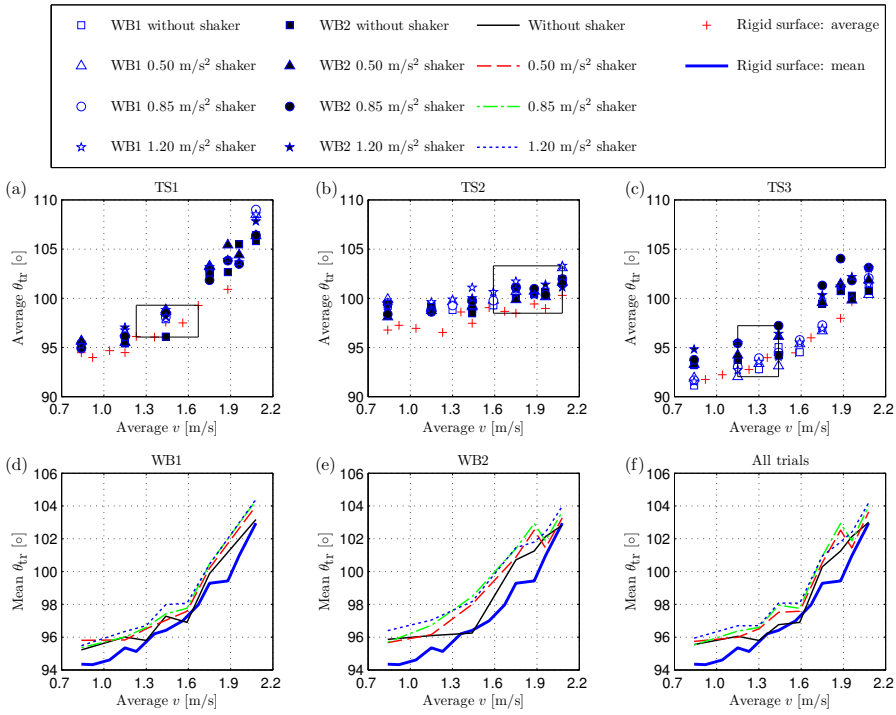

Figure 5.41: Trunk angle in experiments **(a)** by TS1, **(b)** by TS2, **(c)** by TS3, **(d)** on WB1, **(e)** on WB2 and **(f)** in all trials.

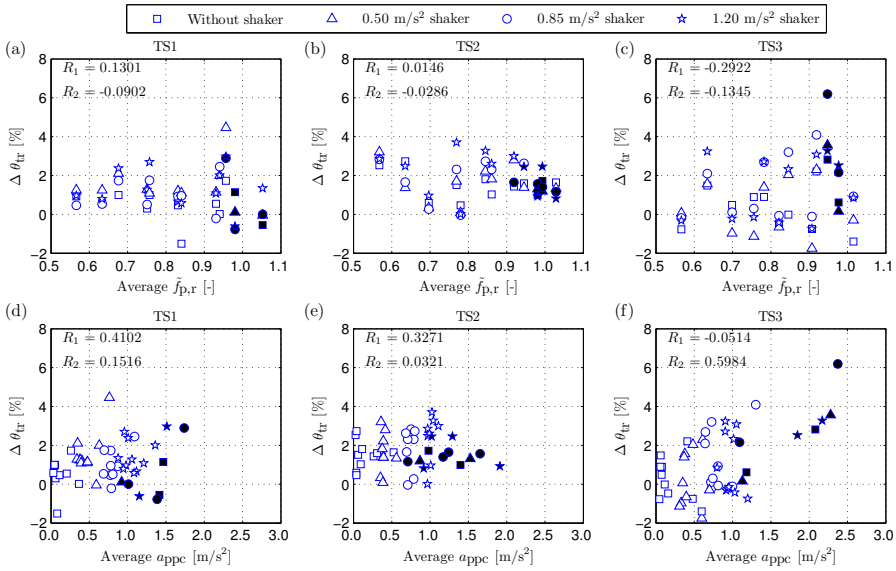

Figure 5.42: Percentage discrepancy of individual average trunk angle as a function of normalised pacing rate **(a–c)** and average peak-per-cycle acceleration **(d–f)**. Unfilled and filled symbols represent non-resonant and resonant trials, respectively.

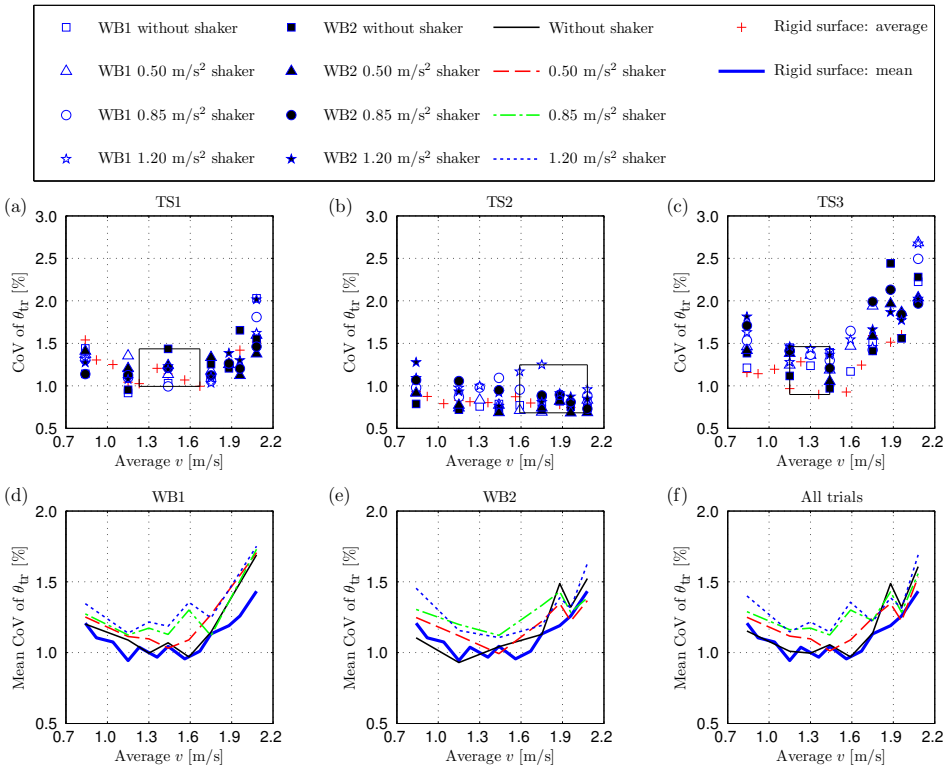

Figure 5.43: CoV of trunk angle in experiments **(a)** by TS1, **(b)** by TS2, **(c)** by TS3, **(d)** on WB1, **(e)** on WB2 and **(f)** in all trials.

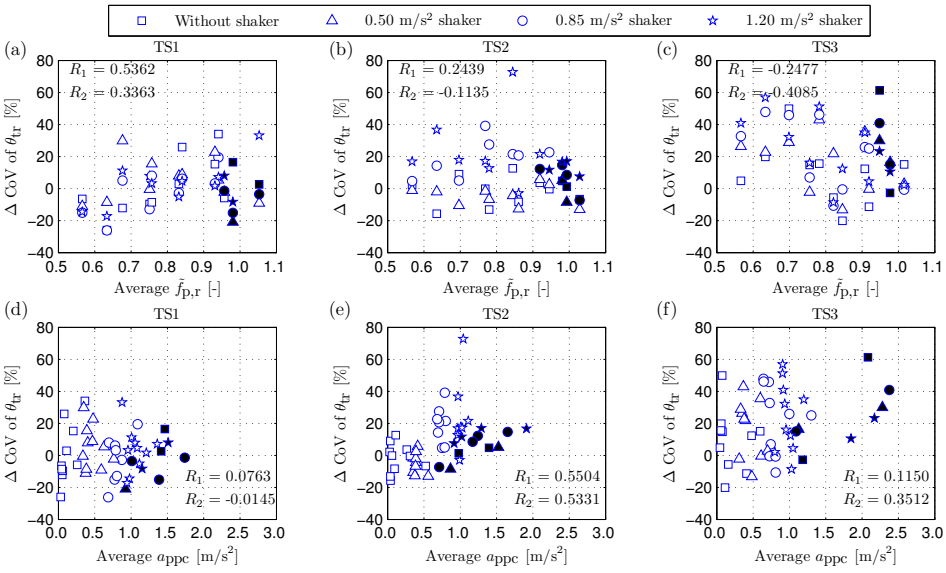

Figure 5.44: Percentage discrepancy of individual CoV of trunk angle as a function of normalised pacing rate **(a–c)** and average peak-per-cycle acceleration **(d–f)**. Unfilled and filled symbols represent non-resonant and resonant trials, respectively.

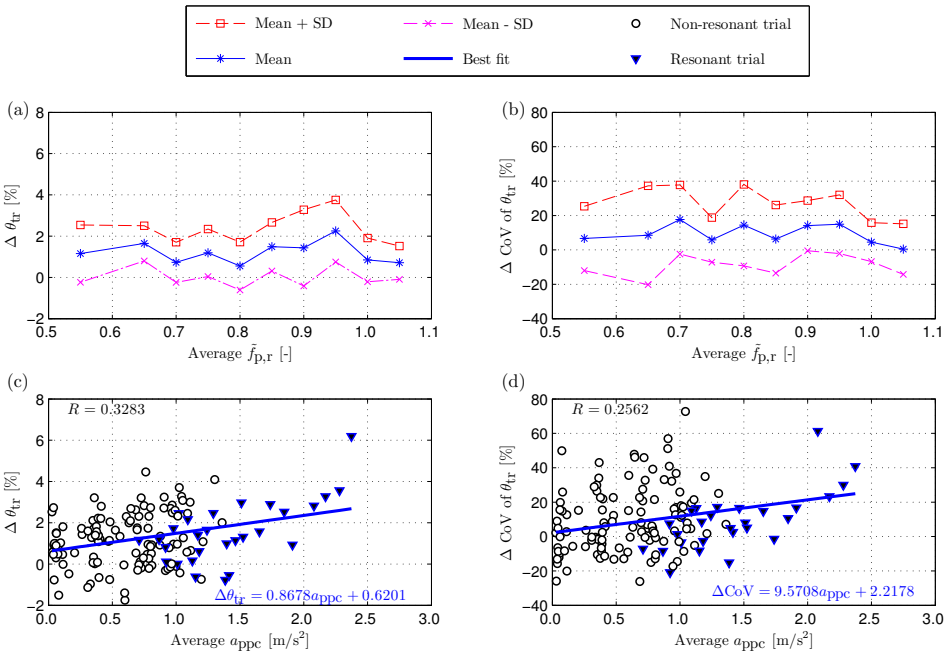

Figure 5.45: Percentage discrepancies of trunk angle and its CoV as functions of normalised pacing rate **(a–b)** and average peak-per-cycle acceleration **(c–d)**.

5.5.7 Ground reaction force

This section first evaluates accuracy of GRF's reconstruction in the experiments performed on the WB. Then, characteristics of the GRF spectrum on the lively surface is commented upon, followed by the analysis of the GRF.

5.5.7.1 Evaluation of measurement method

The GRF in trials on the WB was indirectly measured using the Vicon system only, i.e. there was no benchmark measurement that could be used for comparison. To evaluate the accuracy of the GRF's reconstruction, the measured force was input for a numerical model of the bridge to simulate the structural vibration response. The calculated response was then compared to that

measured at TP61 (Figure 5.2a).

For this simulation, the structure was modelled as a SDoF system having dynamic characteristics described in Section 5.2.2. Since the structural damping and natural frequency are functions of vibration amplitude, their values are updated in simulations on a cycle-by-cycle basis. The relationship of these two dynamic properties and the vibration amplitude was shown in Figure 5.4 for an acceleration level less than $1.4\,\mathrm{m/s^2}$. In the absence of the experimental data for accelerations greater than $1.4\,\mathrm{m/s^2}$, the natural frequency and damping ratio were assumed to be constant. The natural frequencies are kept at 2.422 Hz for WB1 and 2.164 Hz for WB2, while the corresponding damping ratios are assumed to be 0.479 % and 0.523 %, respectively.

Depending on the trial analysed, the external force acting on the bridge is either GRF alone or GRF and the shaker-induced force. Since the shaker was positioned on the bridge, there existed interaction between the shaker and the WB. In the scope of this thesis, such an interaction is assumed to be small and disregarded. The simulated and measured accelerations are band-pass filtered so that the bandwidth includes the first dominant harmonic of GRF and the first bending mode of the WB. The frequency range used in most cases was 1–3 Hz.

The measured acceleration represents the benchmark data. Any discrepancy between the simulated and the measured accelerations is considered as the measurement error (this discrepancy also includes the errors associated with the estimation of modal properties). At this stage, it is assumed that this type of error is negligible.

Examples of representative results are presented in Figure 5.46. In this

figure, f_p/f_n is the frequency ratio, where f_p and f_n are the average pacing rate and natural frequency of the structure, respectively. Three cases of pacing rate are presented: non-resonant trials (Figures 5.46a and 5.46b), near-resonant trials, i.e. beating phenomenon (Figures 5.46c and 5.46d) and resonant trials

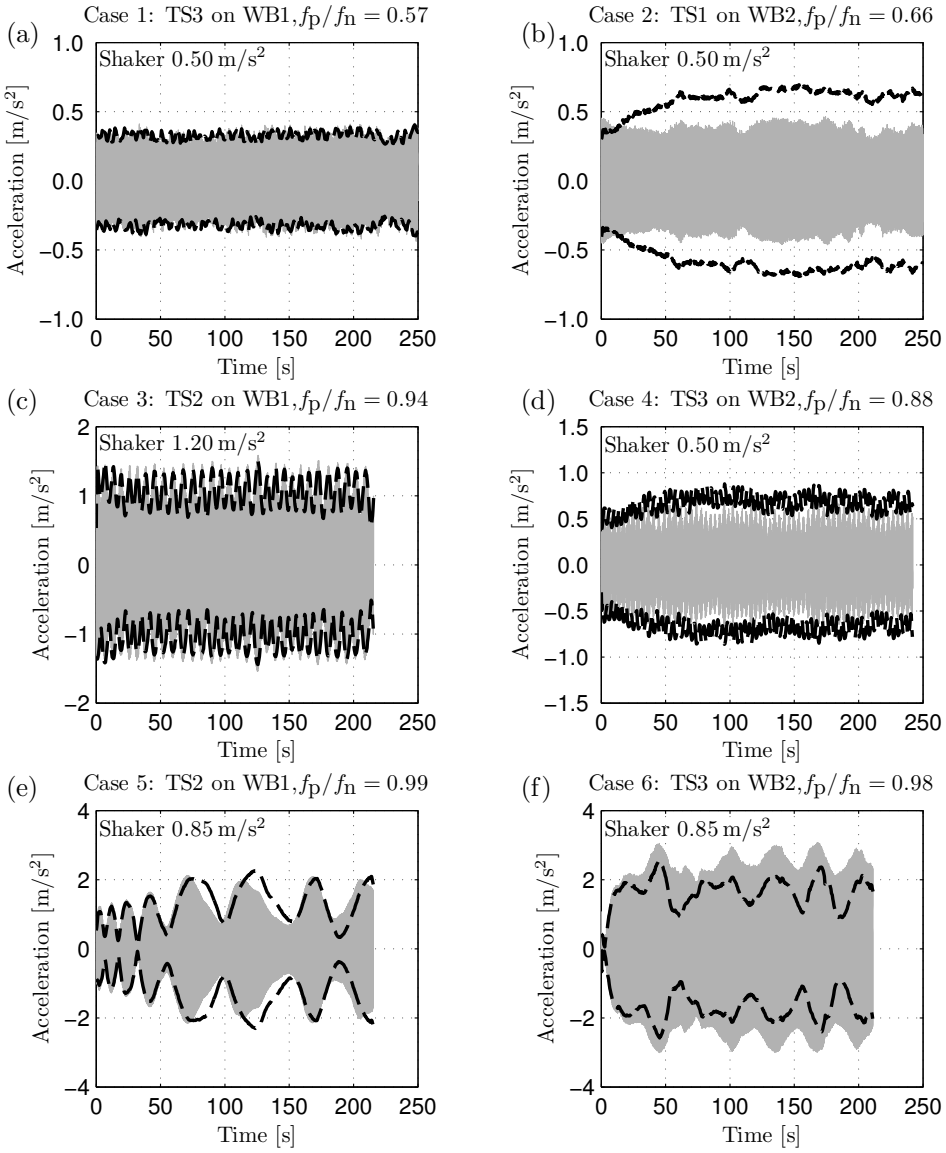

Figure 5.46: Measured acceleration (grey shaded areas) and the envelopes of simulated acceleration (dashed lines). Figures **(a–f)** represent Cases 1–6, respectively.

(Figures 5.46e and 5.46f). The left-column graphs (Cases 1, 3 and 5) represent trials where the simulated accelerations closely matched the measured accelerations while the right-column graphs (Cases 2, 4 and 6) show the cases in which discrepancies between the two acceleration signals were easily noticeable.

To quantify the discrepancy between simulated and measured acceleration, the average a_{ppc} is determined for every simulation. The percentage discrepancy of average a_{ppc} between simulated and measured data is calculated using Equation 4.3, in which Δ, X and Y represent the discrepancy, simulated response and measured response, respectively.

Δa_{ppc} for all simulations is shown in Figure 5.47 as a function of the measured average a_{ppc}. The three poor cases (2, 4 and 6) in Figure 5.46 are presented in Figure 5.47. Since they represent three of the largest observed percentage discrepancies between simulated and measured responses. In majority of cases, $|\Delta a_{\mathrm{ppc}}| \leq 15\,\%$ (inside the boundaries presented by dashed lines in Figure 5.47). The cumulative distribution function of the absolute discrepancy is plotted in Figure 5.48. Out of 160 trials, 79 % have the absolute discrepancy $\leq 15\,\%$. Among trials with larger discrepancy (i.e. $> 15\,\%$), 85 % of them are related to the trials when the average $a_{\mathrm{ppc}} \leq 1.4\,\mathrm{m/s^2}$ (where $1.4\,\mathrm{m/s^2}$ was the maximum acceleration level for which amplitude dependency of f_{n} and ζ were evaluated, see Figure 5.4). The remaining 15 % of trials having the larger discrepancy are resonant trials. This is most likely a consequence of errors introduced in evaluating the bridge dynamics.

$|\Delta a_{\mathrm{ppc}}| \leq 15\,\%$ in majority of trials implies that the discrepancy in the measured DLF_1 should be up to $\pm 15\,\%$. This accuracy level will be commented in Section 5.5.7.3 to justify the measurement method for the study of PSDI.

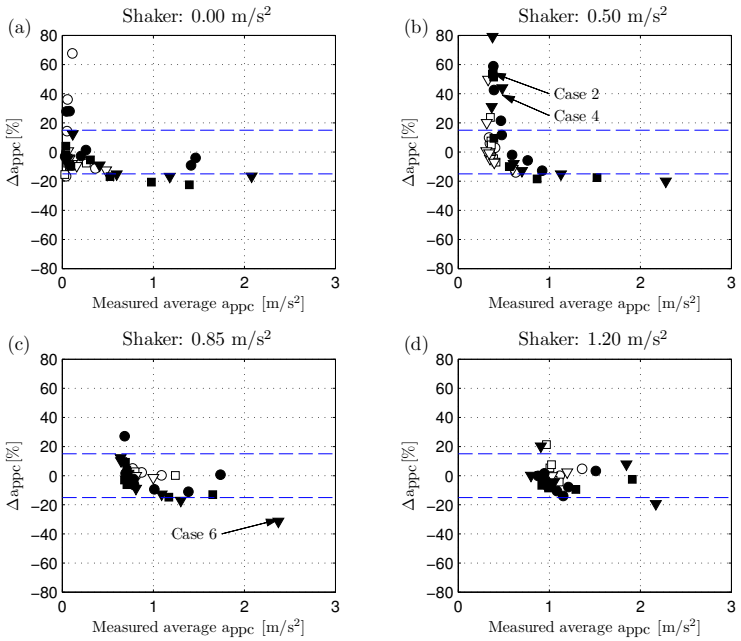

Figure 5.47: Normalised average discrepancy between simulated and measured accelerations as a function of average peak-per-cycle acceleration in experiments **(a)** without shaker and with shaker inducing vibration level of **(b)** 0.50 m/s^2, **(c)** 0.85 m/s^2 and **(d)** 1.20 m/s^2. Circles, squares and triangles represent trials of TS1, TS2 and TS3, respectively. Unfilled and filled symbols represent data on WB1 and WB2, respectively. Dashed lines indicate the boundaries for ±15 % discrepancies.

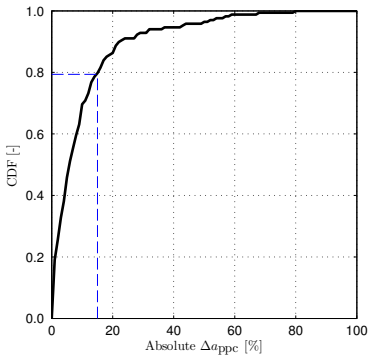

Figure 5.48: Cumulative distribution function of the absolute discrepancy of average peak-per-cycle acceleration. Horizontal and vertical dashed lines represent 79 % trials having the absolute normalised discrepancy less than 15 %.

5.5.7.2 Characteristics of force spectrum on lively surface

Figures 5.49a and 5.49b shows spectra of GRF in 14 trials performed by TS1 on WB2. The shaker was not in operation in the seven trials presented in Figure 5.49a, i.e. the TS's walking force was the only source of structural excitation. In these trials, the usual scenario of peaks at dominant harmonics can be seen. Figure 5.49b shows results for trials with pre-induced vibration at 1.2 m/s^2. Besides the peaks at the dominant harmonics induced by the TS, there were peaks at the dominant vibration frequency, i.e. the natural frequency of the bridge (2.18 Hz in this case). The zoomed views at the structural frequency are also shown in Figure 5.49. The additional peaks at 2.18 Hz in trials with shaker operation are the consequence of the interaction between the structure and the pedestrian, and they represent the, so called, self-excited force. This type of force was reported in the experiments of walking over a laterally oscillating surface by Ingólfsson et al. (2011) and in the analytical model developed by Bocian et al. (2013).

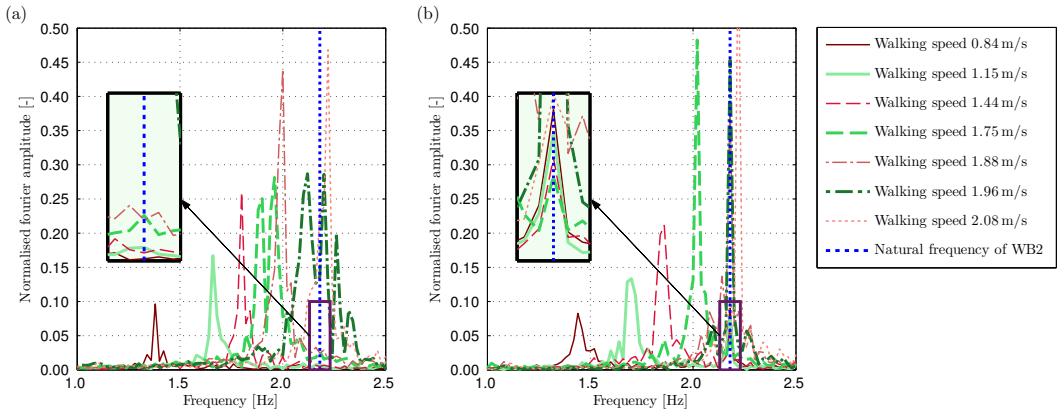

Figure 5.49: Spectrum of ground reaction force in trials on the lively surface: **(a)** without and **(b)** with shaker operation.

DLF_1 is calculated as the average amplitude of band-pass filtered GRF, with bandwidth from $f_p - 0.2\,Hz$ to $f_p + 0.2\,Hz$. This bandwidth is chosen to cover the spread of energy around the first harmonic for all trials. Due to the presence of the self-excited force, the filtered process results in a mixture of the first harmonic and the self-excited force in a number of trials. Four representative cases for the spectrum of GRF induced on the lively surface are shown in Figure 5.50. In Case 1 (Figure 5.50a), the self-excited force does not exist and only DLF_1 is presented. This case happens in trials without shaker-

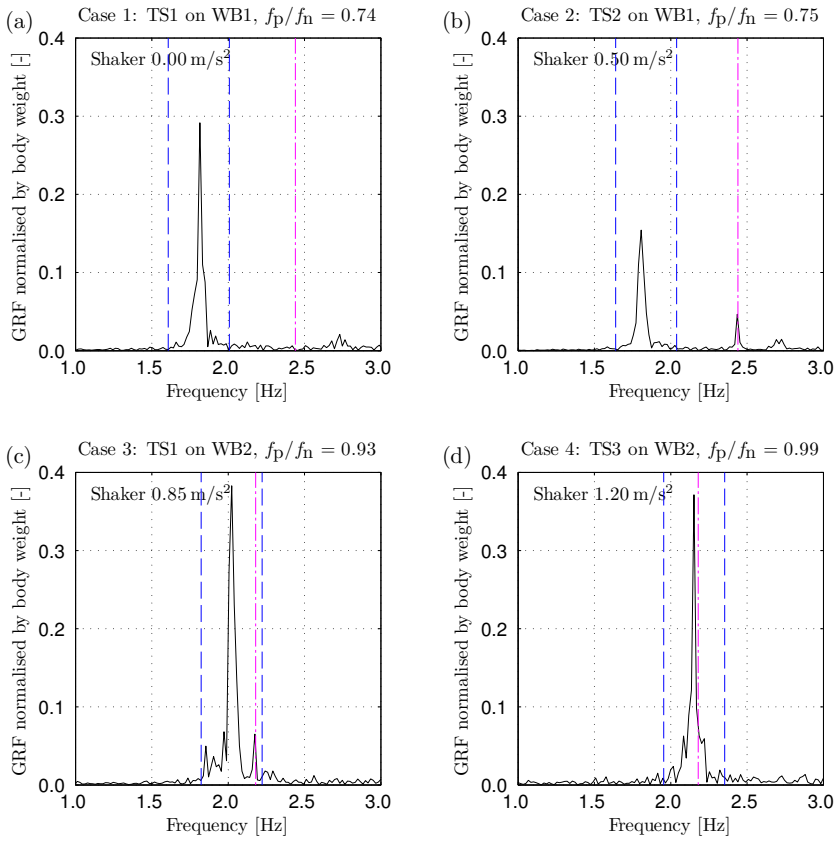

Figure 5.50: (a-d) Spectra of ground reaction force in four representative cases. Dashed lines represent the bandwidth of $f_p \pm 0.2\,Hz$ while dash-dotted lines represent the structural frequency.

induced vibration. In Case 2 (Figure 5.50b), the self-excited force exists while the bandwidth used in the calculation of DLF_1 does not cover the self-excited force. Both DLF_1 and self-excited force can be separately presented. Case 3 (Figure 5.50c) is similar to Case 2, apart from that the bandwidth includes these two components. The filtered force, therefore, consists of both DLF_1 and self-excited force. This joint contribution in the filtered force is hereafter referred to as the total force while its average amplitude is referred to as total force factor (TFF). In this case, both the self-excited force and TFF are presented. In Case 4 (Figure 5.50d), the pacing rate is so close to the structural frequency that the self-excited force merges into the first harmonic force. Only TFF is presented in Case 4.

The next two sections quantify walking force on the lively surface. DLF_1 is first presented, followed by the analysis of the self-excited force.

5.5.7.3 Dynamic load factor of first harmonic and total force factor

In this section, TFF will be included in graphs for DLF_1. Presented Pearson coefficients and fitting functions are for DLF_1 results only. The figures in this section mostly follow the format used in the analysis of kinematic parameters. Mean data are not presented in some graphs to avoid misleading results due to the mix of DLF_1 and TFF.

CDF of p-value for DLF_1 is plotted in Figure 5.51. There are 62 % of trials that fail to reject the normal distribution hypothesis (average of lines representing lively trials in Figure 5.51f). This result is lower than the result achieved on the rigid surface (82 %), which suggests that the presence of pre-induced vibration increases the likelihood of the hypothesis being rejected.

Among all gait parameters investigated in this chapter, DLF_1 has the lowest percentage of trials that fail to reject the hypothesis, suggesting that the normal distribution should not be used when modelling DLF_1 with a lively surface.

The average DLF_1 and TFF are plotted as a function of the average walking speed in Figures 5.52a–c. Since DLF_1 is often presented as a function of the average pacing rate, e.g. Kerr (1998), DLF_1 and TFF are also plotted versus the average f_p in Figures 5.52d–f. The discrepancies of these parameters (ΔDLF_1 and ΔTFF) when compared to data in rigid trials are shown in Figure 5.53. The ranges of ΔDLF_1 are from $-6.1\,\%$ to $17.7\,\%$ for TS1, from $-44.0\,\%$ to $5.0\,\%$ for TS2 and from $-15.1\,\%$ to $17.3\,\%$ for TS3. The ranges of ΔTFF are from $-25.3\,\%$ to $14.8\,\%$ for TS1, from $-53.1\,\%$ to $3.6\,\%$ for TS2 and from $-21.1\,\%$ to $17.1\,\%$ for TS3. When $\tilde{f}_{p,r} \leq 0.95$, $|\Delta DLF_1|$ is mostly smaller than $15\,\%$ (apart from several trials of TS2 presented in Figure 5.53b). In many trials when $0.95 < \tilde{f}_{p,r} \leq 1.10$, there is a significant reduction in TFF when compared with the corresponding DLF_1 from rigid trials ($\pm 15\,\%$ boundaries are presented as dashed lines in Figure 5.53). Such a reduction in many trials exceeds the expected uncertainty about the mean of $\pm 15\,\%$ associated with the measurement method. This result indicates that the chosen MCS is sensitive enough to be used for quantifying the influence of PSDI on the GRF in majority of (near) resonant trials. Figures 5.53d–f shows that the discrepancies in trials without shaker, generally characterised by low vibration level, are mostly small, suggesting that there is no significant difference of measurement errors (using MCS) on different days. Also, ΔTFF tends to increase with an increase of the vibration level.

CoVs of DLF_1 and TFF are plotted in Figure 5.54 as functions of the average walking speed and the average pacing rate while the discrepancy for CoVs are shown in Figure 5.55. Majority of lively trials (82 %) have the CoV greater than that measured on the rigid surface. The ranges of ΔCoV of DLF_1 are from -36.1 % to 281.3 % for TS1, from -38.4 % to 438.9 % for TS2 and from -15.5 % to 544.6 % for TS3. Similar to the analysis for ΔDLF_1, ΔCoV for DLF_1 from trials without shaker is normally small, indicating relatively similar measurement errors on different days. For the TFF, the CoV is generally much higher when compared to corresponding values of CoV of DLF_1 in rigid trials. The ranges of ΔCoV of TFF are from 27.7 % to 491.9 % for TS1, from 63.5 % to 708.4 % for TS2 and from 53.7 % to 348.3 % for TS3. ΔCoV of both DLF_1 and TFF tends to increase with an increase of the average $\tilde{f}_{\mathrm{p,r}}$ and the average a_{ppc}. The high values of intra-subject variability when the pacing rate is close to the structural frequency indicates that the GRF induced by the TSs is greatly influenced by the vibration.

Differences to DLF_1 and TFF are plotted in Figure 5.56a while ΔCoV of these parameters are given in Figure 5.56b. The mean is from -22.7 % to 7.9 % for ΔDLF_1 and between 13.1 % and 170.9 % for ΔCoV of DLF_1, while the standard deviation is 5.8–16.4 % and 25.9–193.9 %, respectively. For TFF, the mean is from -23.0 % to 1.9 % for ΔTFF and 140.0–267.9 % for ΔCoV, while the standard deviation is 5.3–18.4 % and 86.3–205.3 %, respectively. Best fitting functions of discrepancies of DLF_1 and its CoV with regard to the average a_{ppc} are given in Figures 5.56c and 5.56d.

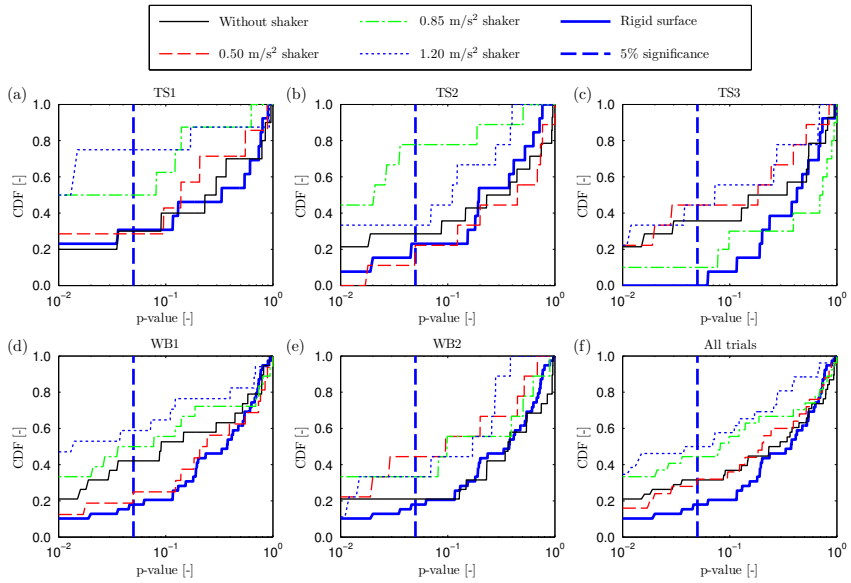

Figure 5.51: CDF of p-value of DLF_1 in experiments **(a)** by TS1, **(b)** by TS2, **(c)** by TS3, **(d)** on WB1, **(e)** on WB2 and **(f)** in all trials.

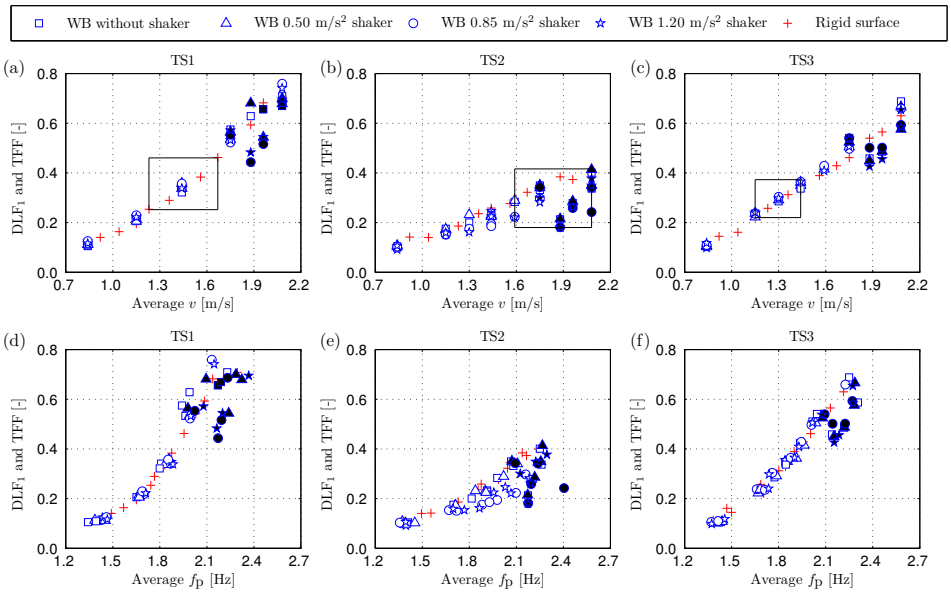

Figure 5.52: Average DLF_1 (unfilled symbols) and TFF (filled symbols) as a function of **(a–c)** average walking speed and **(d–f)** average pacing rate.

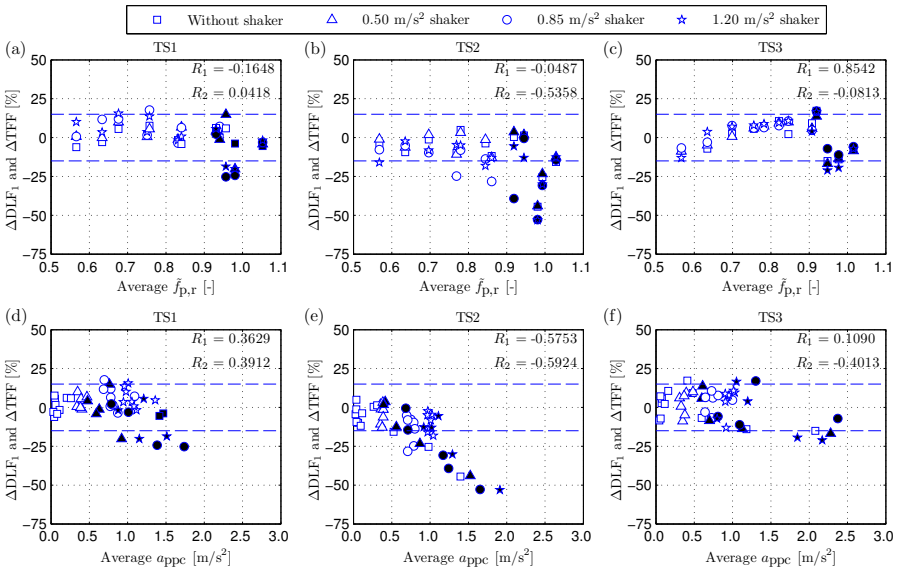

Figure 5.53: Percentage discrepancies of individual average DLF_1 (unfilled symbols) and TFF (filled symbols) as functions of normalised pacing rate **(a–c)** and average peak-per-cycle acceleration **(d–f)**. Pearson's coefficient R is calculated for only DLF_1 in each sub-figure. Dashed lines represent boundaries of $\pm 15\,\%$

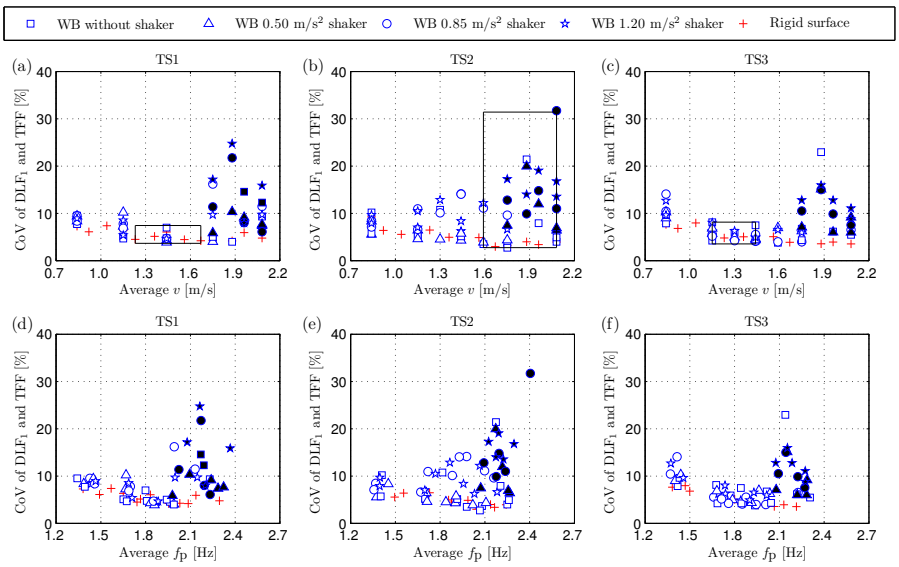

Figure 5.54: CoVs of DLF_1 (unfilled symbols) and TFF (filled symbols) as functions of **(a–c)** average walking speed and **(d–f)** average pacing rate.

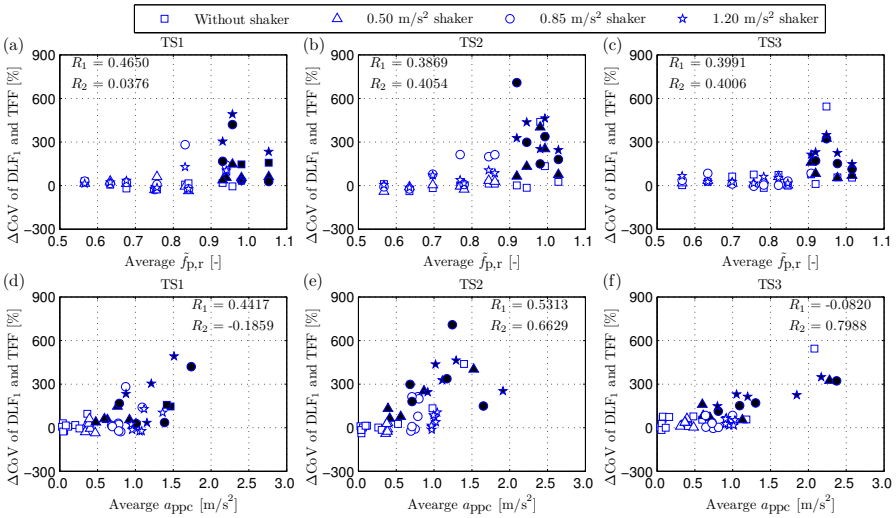

Figure 5.55: Percentage discrepancies of individual CoV of DLF_1 (unfilled symbols) and TFF (filled symbols) as functions of normalised pacing rate **(a–c)** and average peak-per-cycle acceleration **(d–f)**. Pearson's coefficient R is calculated for only DLF_1 in each sub-figure.

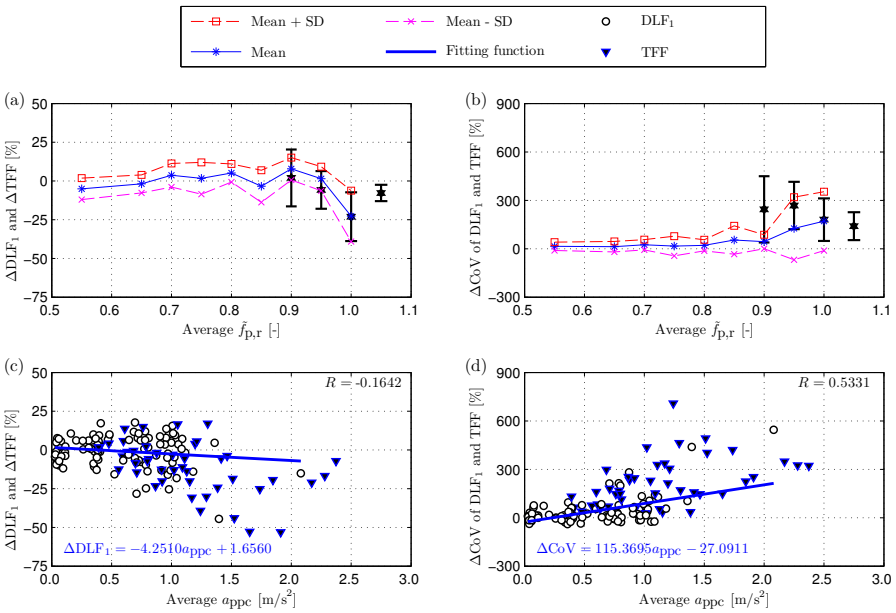

Figure 5.56: Percentage discrepancies of DLF_1 and its CoVs as functions of normalised pacing rate **(a–b)** and average peak-per-cycle acceleration **(c–d)**. Percentage discrepancies of TFF are presented as vertical lines in **(a–b)** and filled symbols in **(c–d)**. Pearson's coefficient R and best fitting functions are calculated for DLF_1 only.

5.5.7.4 Self-excited force

Similar to DLF_1, the self-excited force was calculated as the average amplitude of the band-pass filtered GRF around the natural frequency of the bridge, with 0.05 Hz bandwidth (Ingólfsson et al., 2011). The amplitude of the self-excited force was then averaged and normalised to the body weight to get non-dimensional value, hereafter called the self-excited factor (SEF).

The average SEF is plotted in Figure 5.57 as a function of the normalised average pacing rate in lively trials. The average $\tilde{f}_p$ is used in this graph for ease of presentation of the average SEF. The data show that the average SEF generally increases with an increase in the vibration level pre-induced by the shaker. This observation suggests that the amplitude of SEF depends on the perceived vibration level. When $\tilde{f}_p < 0.80$, the average SEF does not change much with the pacing rate. As the pacing rate approaches the natural frequency of the structure ($0.80 \leq \tilde{f}_p < 1.00$), the average SEF tends to decrease. The reduction is most pronounced for TS1 and TS3 (Figures 5.57a and 5.57c)

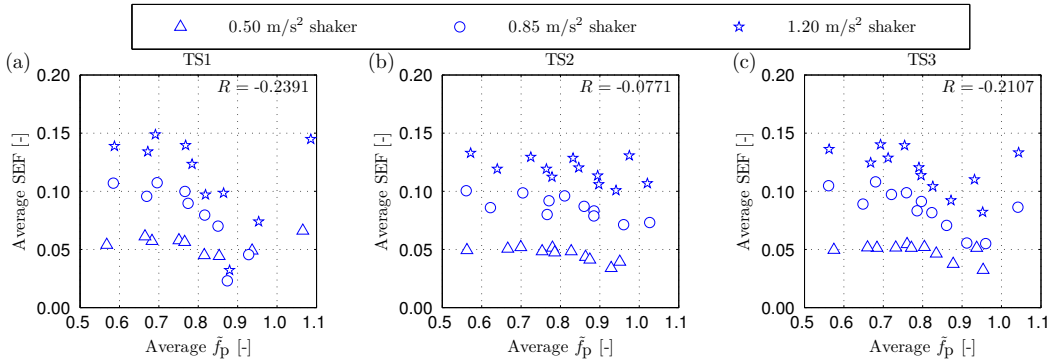

Figure 5.57: Amplitude of average self-excited factor as a function of normalised average pacing rate in experiments of **(a)** TS1, **(b)** TS2 and **(c)** TS3. Pearson's coefficient R is calculated for data points in each sub-figure.

while the decrease for TS2 is less noticeable (Figure 5.57b). The limited number of six trials when $\tilde{f}_{\mathrm{p}} > 1.00$ suggests that the average SEF tends to return to the same level as it was for $\tilde{f}_{\mathrm{p}} \leq 0.80$. Based on the presented data, there might be a critical range when the pacing rate is close to and smaller than the structural frequency, in which a drop in the SEF occurs.

Figure 5.58a presents the average SEF as a function of the average a_{ppc} and shows the best fitting function that can be used to predict the average SEF. The data suggests that average SEF tends to increase with an increase of the acceleration level. The ratio of SEF to DLF_1 is presented in Figure 5.58b as a function of the average pacing rate. The ratio is found to decrease with an increase of the average pacing rate. The reason is because DLF_1 tends to increase with an increase of average f_{p} (Figures 5.52a–c). As a result, the amplitude of the SEF is quite significant at lower pacing rate when compared to DLF_1 (even greater than DLF_1 in some trials with f_{p} less than 1.5 Hz). As the pacing rate increases, the average SEF becomes smaller than the average DLF_1.

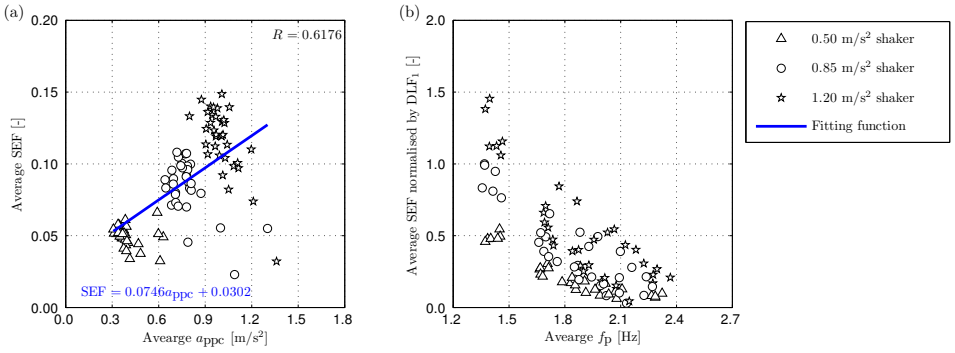

Figure 5.58: **(a)** Average self-excited factor as a function of average peak-per-cycle acceleration, Pearson's coefficient R is calculated for all data points. **(b)** Average self-excited factor normalised by average DLF_1 as a function of average pacing rate.

5.6 Conclusions

An experimental programme was completed to investigate the walking gait on a full-scale lively structure. As presented in Chapter 4, the parameters measured were six kinematic parameters (i.e. pacing rate, step length, step width, attack angle, end-off-step angle and trunk angle) and one kinematic parameter of walking force. All parameters were studied in relation to nine walking speeds (ranging from 0.8 m/s to 2.1 m/s). Three TSs completed two test sessions, each consisting of 20–28 trials. 400 steps were recorded in each trial. In total, the experimental programme consisted of 160 trials, in which the three TSs completed about 64,000 steps, equivalent to walking around 45 km.

After each trial, TSs provided answers of whether the vibration level was perceptible and, if the answer was positive, whether/how their walking was affected by the structural vibration. A complaint threshold was defined as the acceleration from which the walking started to be influenced by the vibration. It was found that this threshold, ranging between 0.86 m/s^2 and 2.25 m/s^2, increases with an increase of the average pacing rate.

The experimental data acquired on WB are compared against the benchmark data measured on the rigid surface. Step width is the kinematic parameter whose average value exhibits the largest discrepancy (from -20 % to 50 %) on the lively surface when compared to the equivalent measurement on the rigid surface. For other kinematic parameters, the discrepancies in average values are less dramatic, i.e. often within ± 10 %. In comparison with walking over the rigid surface, average pacing rate, attack angle and trunk angle

increased when walking on lively bridges, while step length decreased and end-of-step angle remained unchanged. The analysis also shows that step width is the only kinematic parameter for which the CoV tend to decrease in lively trials, with the mean value of ΔCoV is between $-24.7\,\%$ and $4.0\,\%$. However, the observation of such a decrease is not conclusive and likely comes from the inherent changes of measurement on different days. For other kinematic parameters, the discrepancy in CoV is much more dramatic than in the average value. Majority of lively trials have CoV larger than in the rigid trials. The ranges of mean ΔCoV for these parameters are: 9.3–66.9 % for pacing rate, 3.1–43.8 % for step length, from $-8.1\,\%$ to $55.9\,\%$ for attack angle, 2.2–72.6 % for end-of-step angle, and 0.5–17.7 % for trunk angle.

Based on the results for step width, it seems that this parameter is not influenced by the structural vibration. It has been shown that the discrepancies in average values for pacing rate, step length, attack angle and trunk angle are all directly dependent on the vibration level. The discrepancies of these parameters become more pronounced when the pre-induced vibration was increased. This observation is also correct for discrepancies in CoV for all kinematic parameters apart from step width. Such an increase in intra-subject variability indicates that the TSs were influenced by the structural vibration and consequently generating more variations during walking. It was also found that discrepancies of average values (apart from step width, attack angle and end-of-step angle) and CoV (apart from step width) of kinematic parameters in the lively trials without shaker were closest to the corresponding data in the rigid trials. This observation suggests that the intra-subject variability of TSs in experiments on different days was small for some parameters, justifying the

use of data for those parameters in rigid trials as benchmark data.

In the analysis of the walking force, DLF_1 and SEF are two components contributing to the GRF during walking on lively structures. When $f_p \leq 0.95f_n$, the discrepancies in DLF_1 and TFF (consisting of the first forcing harmonic and the self-excited force) was mostly in the range from $-15\,\%$ to $15\,\%$ and it seemed to be independent of the pacing rate and vibration level. In many trials when the pacing rate was closer to the structural frequency ($0.95f_n < f_p < 1.10f_n$), there was a significant reduction in DLF_1 and TFF when compared with DLF_1 recorded on the rigid surface at nominally the same walking speed. This result confirms rare previous experimental observations of the attenuation of structural vibration in resonant experiments on lively full-scaled structures (Pimentel et al., 2001; Živanović et al., 2005a). The reduction of TFF in many trials was higher than the measurement error of $\pm 15\,\%$ associated with the use of the motion capture system. This result shows that the chosen measurement method could be used to record the influence of PSDI on the GRF when the pacing rate was close to the structural frequency.

SEF, for a given specific vibration level, was constant when the pacing rate is away from the vibration frequency ($f_p < 0.8f_n$). SEF tends to decrease when the pedestrian's pacing rate approaches the vibration frequency. It was found that the SEF increases with an increase in vibration level.

In the analysis of changes of pedestrian behaviour when walking on the lively surface, the data for different TSs often contradicted each other, i.e. there was no unified trend. The observed differences in behaviour reflect complexity of human behaviour when being exposed to vibration and the inherent inter-subject variability. A further study that includes larger number of TSs

is required to further understanding of differences in human behaviour.

The Kolmogorov-Smirnov test was completed for each parameter to test the normal distribution hypothesis. Comparison with the data acquired on the rigid surface revealed that walking on the lively surface does not change the outcome of the test for step length and step width, while the likelihood of the hypothesis being rejected decreases for trunk angle, and increases for pacing rate, attack angle, end-of-step angle and DLF_1. Overall, all parameters, apart from DLF_1, can be recommended using a normal distribution.

The purpose of the experimental programme in this chapter was to establish a database of walking parameters on vertically vibrating surfaces and to quantify the influence of the PSDI phenomenon on the walking gait. Both aims were achieved within the available resources. A limitation of this study is the small number of TSs, which is dictated by the limited time available for the study. However, it is believed that the collected data provide unique insight into the human locomotion on the vibrating surface, which will contribute to develop understanding of PSDI in the vertical direction and motivate further research. Results of this experimental programme will be utilised in Chapter 6 for evaluation of a numerical model taking into account PSDI.

Chapter 6

Modelling pedestrian-structure dynamic interaction

6.1 Introduction

An experimental database of walking characteristics on surfaces that vibrate perceptibly in the vertical direction was presented in Chapter 5. The comparison with benchmark data collected on the rigid surface showed that the intra-subject variability of most gait parameters increased when walking on the lively surface. Besides, the experimental data indicated the existence of the self-excited force which, when walking to excite resonance, led to the attenuation of the force compared with the corresponding force generated on the rigid surface. These findings will be used for verification of the numerical model for pedestrian-structure dynamic interaction (PSDI) proposed in this chapter.

Among three bipedal walking models reviewed in Chapter 3, the inverted pendulum model (IPM) possesses several advantages. First, the IPM is the simplest model that is convenient for numerical calculation. In addition, the

model is capable of replicating the single support phase of a gait cycle that represents 80 % duration of a walking step. Furthermore, the parametric study in Chapter 3 showed that simulations using the IPM can provide full range of walking parameters, i.e. pacing rate, DLF_1 and walking speed, seen on as-built structures (Živanović, 2012). This feature of the IPM indicates ability of the model to describe variations in walking gaits among different pedestrians within a human population. Based on these features and preliminary analysis by Bocian et al. (2013) with promising results, the IPM will be used for modelling PSDI in this chapter.

To simulate the interaction between the pedestrian and the structure, a numerical model is established. This model builds on the model developed by Bocian et al. (2013), who used the IPM to represent the pedestrian walking on a surface with prescribed motion. In this chapter, a novel model, which includes two-way interaction between pedestrian and structure, will be developed. This model will be referred to as the interactive model (IM). To evaluate new features introduced by using the IM, simulation results will be compared with those produced by the moving harmonic model (MHM from Chapter 2), which ignores the interaction.

In simulations utilising the IPM on the rigid surface (Chapter 3), the initial conditions were reset to the same values at the beginning of each step. This assumption led to walking parameters (e.g. pacing rate and attack angle) being the same in each step. However, results in Chapter 4 indicate that there exists intra-subject variability in the gait parameters as represented by the coefficient of variation (CoV). Therefore, the assumption of repetitive initial conditions does not reflect accurately the non-periodic nature of the walking

gait. In an attempt to improve the modelling, initial conditions will be altered on a step-by-step basis to investigate if the actual features of human locomotion can be closely matched. Results in Chapter 5 showed that variations in many gait parameters become larger when pedestrians walked on the lively surface. Varying initial conditions will also target to model such an increase in variations of gait parameters.

The first aim of this chapter is to develop the interactive pedestrian-structure model. The second aim of the study is to validate the proposed model against experimental data.

In this chapter, the IM and its input parameters are first described. To investigate influence of different input parameters on the vibration response, a sensitivity analysis is then performed. Next, the IPM is calibrated to represent three test subjects (TSs) participating in the experimental programme on the rigid surface, followed by the evaluation of the performance of the calibrated model on the lively surface. Modelling the intra-subject variability on both rigid and lively surfaces is then presented and evaluated against experimental data. The chapter concludes with major findings.

6.2 Interactive pedestrian-structure model

Bocian et al. (2013) developed a numerical model consisting of the IPM walking on a lively surface characterised by a constant predefined vibration level (Chapter 2). In practice, this assumed level is often not known in advance. Moreover, vibration engineers are most interested to determine such an expected vibration level and, therefore, pre-defining it is a limitation of this

model. Another limitation is that it represents one-way interaction, i.e. effects of structural vibration on the pedestrian's walking gait are considered only. Therefore, the influence of changes in the pedestrian's walking on the structural vibration is neglected. The purpose of the study by Bocian et al. (2013) was to qualitatively investigate the changes of the walking locomotion when being exposed to vibration. This first step is useful for understanding some features of the model, but is insufficient for design purpose. This is the reason to extend use of the IPM on the lively surface in this study.

The features of the IM, consisting of input parameters and equations of motion, are first described in this section. Then a representative example is provided to compare modelling performance of the IM against the MHM, followed by a sensitivity analysis of the structural response.

6.2.1 Interactive model

IM consists of a pedestrian and a supporting structure (Figure 6.1). The chosen structure is a bridge susceptible to human-induced vibrations. The pedestrian is modelled using the IPM while the structure is modelled by a single degree-of-freedom (SDoF) system, which represents a single mode of vibration. To start the simulation, two sets of input parameters are needed: model parameters and initial conditions.

For the IPM, model parameters are the pedestrian mass m_{p} and pendulum length l. For the structure, the model parameters are the modal mass m_{b}, damping ratio ζ, natural frequency f_{n}, mode shape and span length L.

Motion in the IPM is influenced by the displacement $y_{\mathrm{b}}\phi_x$ at the pedes-

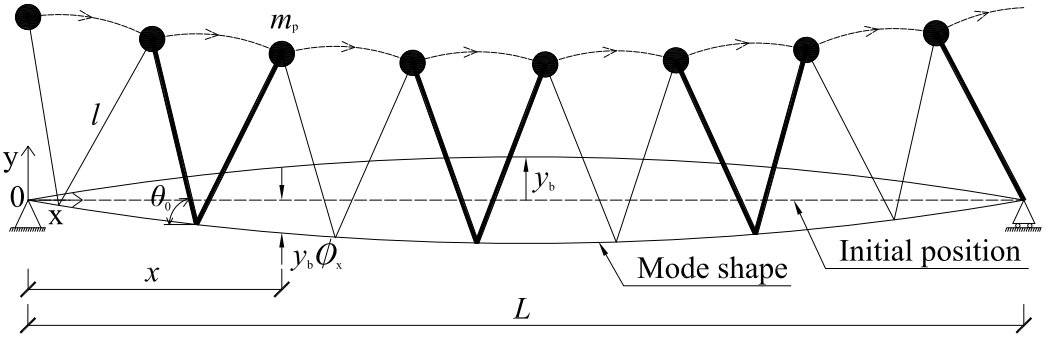

Figure 6.1: Interactive model for a pedestrian crossing a structure. Thick and thin lines represent the right and left legs, respectively. Bridge length is shortened for ease of illustration.

trian's position on the structure, where ϕ_x is the mode shape ordinate and y_b is the vertical modal displacement of the bridge (Figure 6.1). Using the Lagrangian approach, the coupled equations of motion for the pedestrian and the bridge can be derived (Appendix D):

$$\ddot{\theta} = \frac{\cos\theta}{l}(g - \phi_x \ddot{y}_\mathrm{b}) \tag{6.1}$$

$$\begin{aligned}(m_\mathrm{b} + m_\mathrm{p}\phi_x^2 \sin^2\theta)\ddot{y}_\mathrm{b} + 2\zeta m_\mathrm{b}(2\pi f_\mathrm{n})\dot{y}_\mathrm{b} + \\ m_\mathrm{b}(2\pi f_\mathrm{n})^2 y_\mathrm{b} - \phi_x m_\mathrm{p}(g\sin^2\theta + l\dot{\theta}^2\sin\theta) = 0\end{aligned} \tag{6.2}$$

where θ is the angle made between the leg and the ground while $\dot{\theta}$ and $\ddot{\theta}$ are its first and second derivatives, respectively; $\dot{y}_\mathrm{b}$ and $\ddot{y}_\mathrm{b}$ are the modal velocity and acceleration of the bridge, respectively. All derivatives in this chapter are calculated with respect to time. Equations 6.1 and 6.2 are applicable to a vibration mode of arbitrary shape.

The bridge is assumed to be stationary at the beginning of the simulation, i.e. initial conditions (modal displacement and velocity) are set to zeroes.

Initial conditions in the IPM are attack angle θ_0 and initial forward speed $\dot{x}_0$. Solver *ode45* from MATLAB library, that utilises the Runge-Kutta integration method with variable step size (Mathworks Inc., 2010), has been used in the simulation. The maximum time step utilised by the solver is set at 10^{-3} s. The absolute and relative error tolerances are set at 10^{-6}. All simulations in this section have the time step of 10^{-3} s.

The differential equation solver is paused at the end of every walking step. The condition $\theta_e + \theta_0 = 180^\circ$ is used as a criterion to end a walking step, where θ_e is the end-of-step angle (Chapter 3). At the end of the, say, n^{th} walking step, an upward impulse (I_n) is applied to m_p to redirect the mass of the IPM to the next step (Appendix A.1.2). The effect of this impulse on the supporting structure is represented by an instantaneous deduction of the modal velocity, denoted by $\Delta\dot{y}_{b,n}$, and is calculated from:

$$\Delta\dot{y}_{b,n} = -\frac{I_n \phi_x}{m_b} \tag{6.3}$$

The simulation is then resumed for the next walking step. The initial conditions for the bridge are taken as the modal displacement and velocity recorded at the end of the previous walking step, with addition that the velocity is altered by $\Delta\dot{y}_{b,n}$. The initial conditions for the IPM (θ_0 and $\dot{x}_0$) are kept constant for all steps. This unrealistic assumption of constant initial conditions is to be implemented first to test the applicability of the model before proceeding to implementing more representative initial conditions that will better replicate variations of gait parameters recorded in the experiments (Chapter 5). Despite repeatability of the initial conditions, the periodicity of

the walking gait on the lively surface is not preserved due to the influence of structural vibration during the time needed to complete each step. Therefore, variations in timing of individual steps offers a means of accounting for the human-structure interaction in this model.

To demonstrate differences in structural responses generated by using IM or MHM, a representative simulation is performed. Pedestrian mass and pendulum length are chosen to be 77.5 kg and 1.037 m, respectively (average values presented in Chapter 3). The initial conditions are selected as $\theta_0 = 69\,^\circ$ and $\dot{x}_0 = 1.61$ m/s. These parameters are chosen so to result in the average pacing rate f_p of 1.87 Hz and average walking speed v of 1.39 m/s that are frequently encountered in practice (Živanović, 2012). The DLF_1 determined with this parameter combination is 0.38. The natural frequency of the bridge is set to 1.87 Hz to match the pacing rate so that a large vibration can develop. Damping ratio of 0.5 % is chosen, which is within the range for lively bridges (Živanović et al., 2005b). The structure has the modal mass of 10,000 kg so that pedestrian to structure mass ratio is small (less than 1 %). The structure has a sufficient length ($L = 100$ m) to allow for the pedestrian's prolonged exposure to high-level vibrations so that there is enough time for the interaction effects to develop. A half-sine mode shape is assumed in this simulation. The stated parameters for the IPM and the structure are hereafter referred to as the benchmark pedestrian and the benchmark structure, respectively, while the simulation including these parameters is referred to as the benchmark simulation.

Figure 6.2 shows envelopes of the resulting modal acceleration responses using the IM and the MHM. For simulation utilising the MHM, DLF_1 and the pacing rate are chosen to correspond to those generated by the IPM on the rigid surface (i.e 0.38 and 1.87 Hz, respectively). The two responses agree well during first 17 s of the response build-up (before the dash-dotted line), after which they start to diverge from each other. This observation suggests that for the low vibration level, the pedestrian is mostly unaffected by the structural vibration, and only when the vibration level becomes more significant, the interaction starts taking place resulting in significantly lower peak response than in the case of the traditional model (1.03 m/s^2 versus 2.37 m/s^2). Such an attenuation of the structural response has been noticed on some as-built footbridges (Živanović et al., 2005a).

Figure 6.3 shows the spectra of structural response and GRF. Since the interaction is disregarded, the dominant frequency of both response and force in the MHM case stays at the structural frequency of 1.87 Hz (dashed lines).

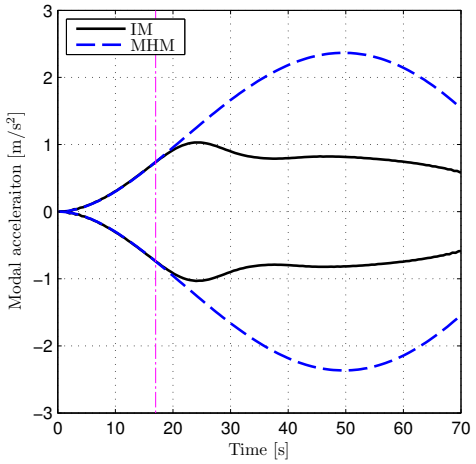

Figure 6.2: Envelopes of modal accelerations.

In Figure 6.3a, the spectrum of the structural response resulting from the IM simulation (solid line) shows that the peak response occurs at a lower frequency of 1.85 Hz. From the spectrum of the corresponding GRF in Figure 6.3b (calculated using an integer number of force cycles), it can be seen that this reduction is a consequence of the reduction of the forcing frequency to 1.85 Hz and leakage of the forcing energy into neighbouring frequency lines. The result indicates that the pacing rate of 1.87 Hz that would be established by the IPM on the rigid ground drops to 1.85 Hz when walking on this lively structure. This small change is sufficient to change the dynamics of the system and cause the peak response that is approximately two times lower than the response initially expected using the result from the MHM simulation.

To distinguish the parameter (e.g. pacing rate) achieved using the IPM on a rigid surface from that achieved on a lively structure using the same input parameters, the former will be referred to as the target parameter hereafter.

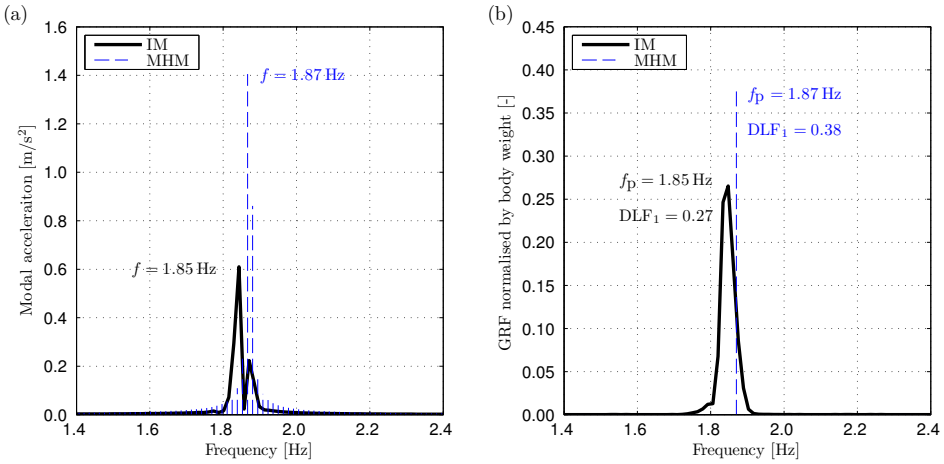

Figure 6.3: Spectra of **(a)** structural responses and **(b)** ground reaction forces.

6.2.2 Sensitivity analysis

A detailed analysis is completed in this section to study the sensitivity of the structural response to both pedestrian and structural parameters. Pedestrian parameters include the pedestrian mass and the pacing rate. The pacing rate is a secondary parameter that is determined by the choice of the angle of attack and the initial forward speed. The pendulum length of the IPM is chosen as 1.037 m. The single pendulum length is considered only since it is known that this length can provide wide ranges of walking parameters required for the study (Figure 3.3). The varying structural parameters consist of the modal (i.e. mass, damping ratio and natural frequency) and physical (i.e. length) properties of the structure, while the mode shape is kept as half-sine wave. The analysis is performed by sweeping one parameter through its realistic domain while all other parameters remain constant.

The use of the IM is applicable to low frequency structures, i.e. when the natural frequency of the vibration mode of interest is excitable by the first harmonic of the walking force only. This limitation is due to the inability of the IPM to generate realistic amplitudes of the higher harmonics to the GRF. As a result, structural responses in simulations are band-pass filtered to remove the effect of higher forcing harmonics (the filter bandwidth is set to 1–3 Hz in most cases). Comparison between the IM and the MHM is made whenever it is possible. Prior to the comparison, the peak modal accelerations resulting from the two models are normalised by the peak response of 1.03 $\mathrm{m/s^2}$ obtained in the benchmark simulation, unless stated otherwise.

Analyses of the structural response to pedestrian and structural param-

eters are consecutively presented, followed by major concluding remarks.

Pedestrian parameters

To investigate sensitivity of the peak response, first the pedestrian mass is varied from 30 kg to 200 kg (in 1 kg increment), which covers the range of body mass reported in a study of nearly 7,000 people (aged 16–96) of the UK population (NHS, 2010). For the MHM, an increase in the mass leads to an increase in the dynamic forcing amplitude and consequently results in the expected proportional increase in the structural response (dashed line in Figure 6.4). The acceleration calculated using the IM (solid line in Figure 6.4) still increases for larger pedestrian mass, but it is much less sensitive to the change in the mass.

It is known that the structural response is most sensitive to the pacing rate (Pedersen and Frier, 2010). However, the pacing rate is not a direct input

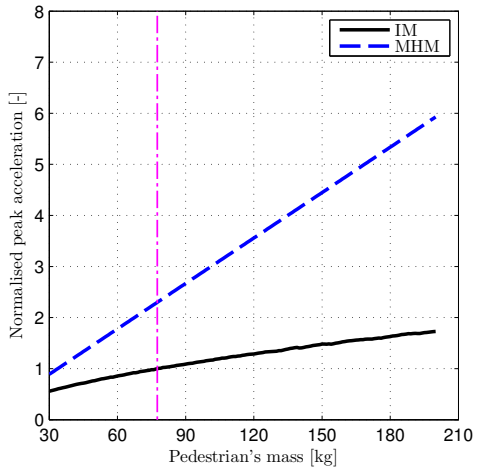

Figure 6.4: Sensitivity of structural response to pedestrian mass. Dash-dotted line represents the pedestrian mass used in the benchmark simulation.

parameter in the IM, and therefore can be varied only indirectly by changing either the attack angle or the initial forward speed or both. First, the angle of attack is kept at 69° and the initial forward speed is varied from 1.4 m/s to 1.9 m/s (in 0.01 m/s increment), resulting in the target pacing rate of 1.4–2.4 Hz. Figure 6.5a shows the normalised peak modal acceleration as a function of the target pacing rate. The structural response is largest in the range of $0.97f_{\mathrm{n}}$–$1.03f_{\mathrm{n}}$ (the boundaries presented by dotted lines in Figure 6.5a). More interestingly, it can be seen that the extreme response is achieved when the target pacing rate is 1.89 Hz, i.e. for $\Delta f = 0.02$ Hz larger than the natural frequency of the structure. This result is in line with observations shown in Figure 6.3.

To investigate the range of the frequency shift, the attack angle and initial forward speed are varied in the ranges of 65–78° and 1.0–1.9 m/s, respectively. The frequency shift Δf normalised by the natural frequency decreases with an

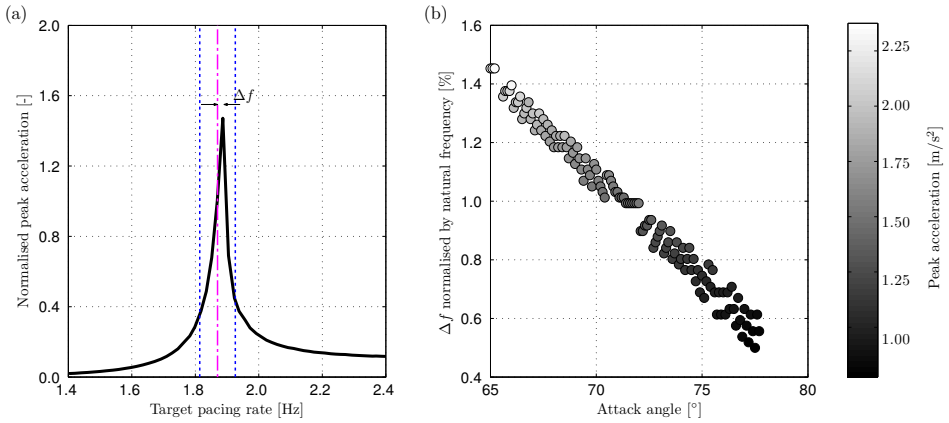

Figure 6.5: **(a)** Structural response as a function of target pacing rate (for $\theta_0 = 69°$); dash-dotted and dotted lines represent the natural frequency and ±3 % boundaries, respectively. **(b)** Normalised frequency shift as a function of attack angle.

increase in the attack angle (Figure 6.5b). To achieve the same target pacing rate, the larger attack angle has to be accompanied by a lower DLF_1 value (Figures 3.3a and 3.3b). This combination results in a lower peak vibration response, as it can be seen from the greyscale-coloured map in Figure 6.5b. Therefore, Δf is generally smaller for lower level vibration responses.

An additional way to consider the effects of the frequency shift is to compare the performance of the IM and the MHM over a range of pacing rates generated by the IPM ($\theta_0 = 69°$, $\dot{x}_0$ =1.4–1.9 m/s). In this comparison, three virtual bridges with natural frequencies of 1.6, 1.9 and 2.2 Hz are introduced. Other dynamic properties of the bridges are the same as for the benchmark structure. The ratio of the peak response obtained using the IM over that from the MHM is shown as a function of the target pacing rate in Figure 6.6a. When the pacing rate is away from the natural frequency (i.e. $f_p < 0.95 f_n$

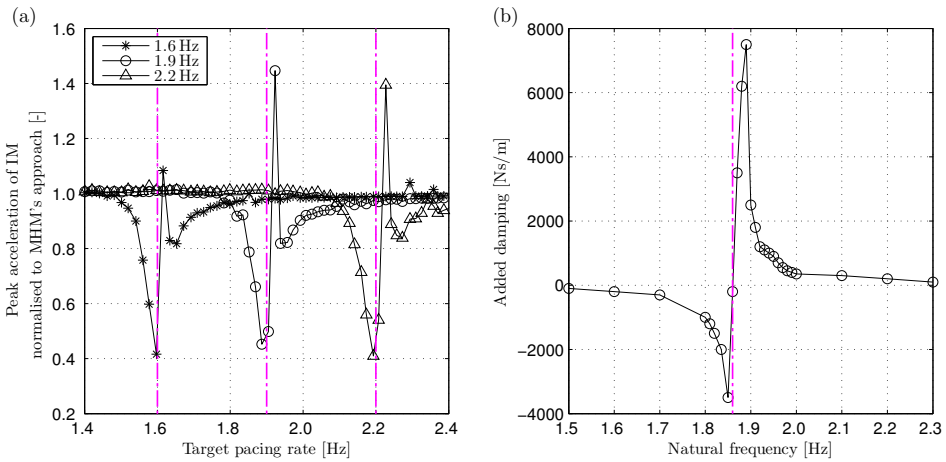

Figure 6.6: (a) Normalised peak acceleration of interactive model under a range of pacing rates; dash-dotted lines represent natural frequencies. **(b)** Added damping as a function of structural frequency (after Bocian et al., 2013); dash-dotted line represents the target pacing rate of 1.86 Hz.

and $f_{\mathrm{p}} > 1.10 f_{\mathrm{n}}$), the discrepancy between accelerations estimated by the two models is less than 5 % (this scenario is referred to as Case 1 in this section). Large discrepancy between the two models can be seen in the vicinity of the natural frequencies. Most of the time, the IM generates a lower structural response than the MHM. The most extreme reduction occurs when the pacing rate is close to and lower than f_{n} (Case 2). The reduction is less significant when the pacing rate is close to and higher than f_{n} (Case 3). Only in a small number of simulations when the target pacing rates are slightly higher than the natural frequencies, the IM generates a higher response than the MHM (Case 4).

Results in Figure 6.6a can be qualitatively compared to results obtained by Bocian et al. (2013) in Figure 6.6b, in which the effect of a pedestrian walking at the target pacing rate of 1.86 Hz on structures with natural frequency ranging from 1.5 Hz to 2.3 Hz is presented as the equivalent added damping. Similar to Case 1 of the IM when the pacing rate is away from the structural frequency, the walking locomotion does not have any effect on structural dynamics, i.e. added damping is almost zero. The locomotion is considered beneficial to the structural vibration (i.e. positive damping) when the pacing rate is close to and lower than f_{n}, which is similar to Case 2. On the other hand, the walking effect is considered adverse (i.e. negative damping) when the pacing rate is close to and higher than f_{n}. This result is in agreement with Case 4 while it is contrary to Case 3. The discrepancy between Bocian et al.'s model and results in Case 3 results can be attributed to consideration of one-way interaction only in their model, i.e. the two graphs in Figure 6.6 are not directly comparable.

Structural parameters

The benchmark simulation was repeated for varying modal mass of the structure from 1,000 kg to 100,000 kg (in 1,000 kg increment) and then for damping ratio being varied from 0.1 % to 5 % (in 0.1 % increment). Normalised peak acceleration is plotted as a function of the modal mass and damping ratio in Figure 6.7. As expected, all simulation results show that the increase of the modal mass and the damping ratio is beneficial for reducing the vibration response of the structure. The discrepancy between estimates by the IM and the MHM is more significant for low modal mass and damping ratio. When the modal mass and the damping ratio increase, the vibration response reduces and the two models provide similar vibration estimates.

Figure 6.8a shows results for the benchmark pedestrian crossing the structure having natural frequency from 1.4 Hz to 2.4 Hz (in 0.01 Hz increment). The maximum response generated using the IM is lower than that under the MHM.

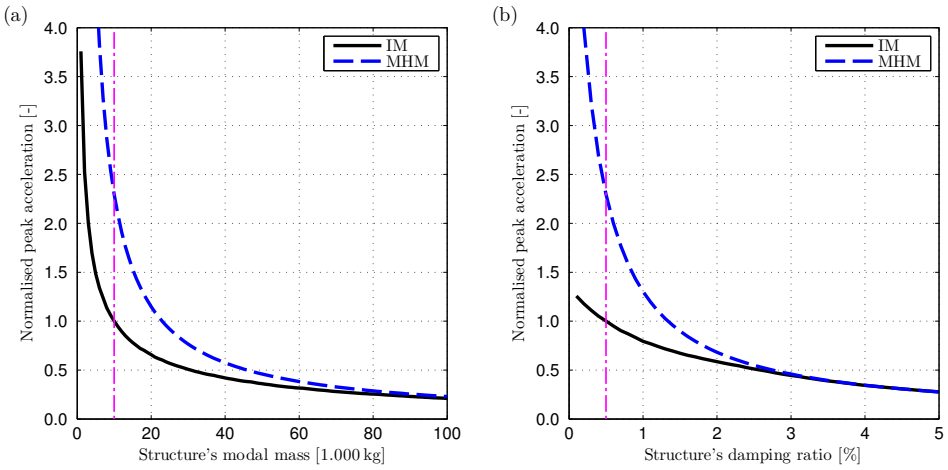

Figure 6.7: Sensitivity of structural response to **(a)** modal mass and **(b)** damping ratio. Dash-dotted lines represent the parameters used in the benchmark simulation.

Due to the effect of frequency shift identified in Figure 6.5a, and confirmed in Figure 6.6a, the response by the IM slightly exceeds the corresponding response of the MHM in a narrow frequency range only (zoomed view in Figure 6.8a).

Finally, Figure 6.8b shows the influence of the span length, ranging from 10 m to 200 m (in 1 m increment), on the structural response. When the span length is short (less than 20 m), the response estimates between the two models are similar. In this case, the duration required for a pedestrian to cross the bridge is short, and there is, therefore, little time for the effect of the interaction to develop. As L increases, there is much larger discrepancy between results of the two models. Since the MHM neglects the interaction, the peak response increases as the structural length increases and more time for vibration development is available. On the contrary, the response estimates using the IM do not change much when the span varies from 20 m to 200 m.

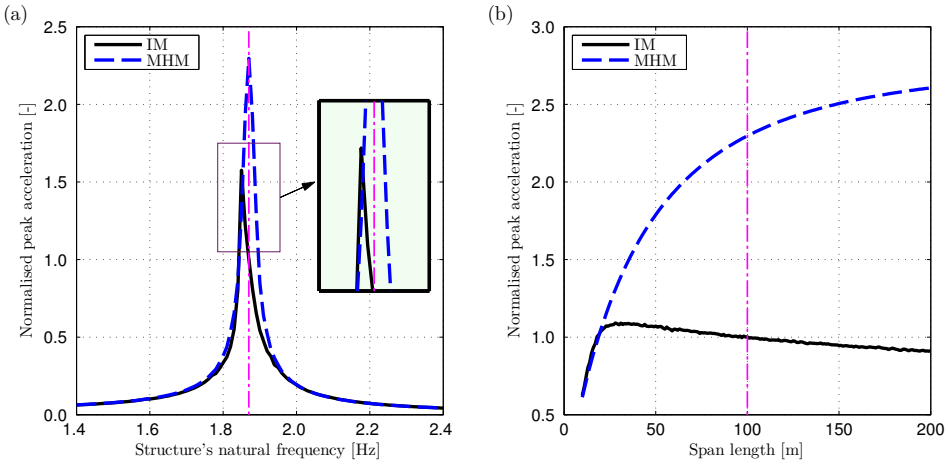

Figure 6.8: Sensitivity of structural response to **(a)** natural frequency and **(b)** span length. Dash-dotted lines represent the parameters used in the benchmark simulation.

Concluding remarks

In this section, the sensitivity of the structural response to input parameters of the model was investigated. As for the pedestrian parameters, it was first found that the vibration estimate when using the IM was less sensitive to the pedestrian mass than in the case of using the MHM. Due to the interaction effect, the increase of the pedestrian mass did not result in the proportional increase in the structural response. Second, the IM generated the largest vibration response when the target pacing rate was slightly higher than the natural frequency. The effect of this frequency shift originated from the change in the pacing rate when the IPM was interacting with the structural vibration.

For the structural parameters, the results showed that the discrepancy between the IM and the MHM was small when the structure was either heavy, heavily damped or short. In those cases, designers could use the simpler MHM for response estimation. For either light, lightly damped or long structures, which are increasingly popular in modern footbridge design, the vibration estimate calculated using the IM was, in majority of cases, lower than that generated using the MHM. This result is in line with scarce experimental evidence (Pimentel et al., 2001; Živanović et al., 2005a), implying that the IM could be used, at least qualitatively, to explain experimental observations.

In general, the sensitivity analysis shows the discrepancies in vibration estimates produced by the IM and the MHM. All simulations have been performed on virtual bridges. As a result, no firm conclusions can be made about the applicability of the IM for vibration assessment in practice. The next section aims to address this issue.

6.3 Validation of interactive model

The aim of this section is to validate the performance of the IM using experimental data for the three TSs presented in Chapter 5. The shaker-induced force and the structural response in the experiments were recorded with the sampling rate of 200 Hz (i.e. for time step of 0.005 s as explained in Chapter 5). This is the justification for choosing the same sampling rate in this section for presenting outputs of simulations (e.g. modal response and GRF).

In this section, a parameter can be referred to as either the simulated or measured parameter on either a rigid or lively surface. To distinguish between different types of parameters, subscripts "s" and "m" are used to represent the simulated and measured parameters, respectively, while subscripts "r" and "l" indicate the parameter on rigid and lively surfaces, respectively. For example, $f_{\mathrm{p,ml}}$ represents the pacing rate measured on the lively surface.

Before the validation of the IM can be performed, the IPM has to calibrated to genuinely represent characteristics of the three TSs when walking on the rigid surface. The calibrated model will then be used in the IM required for simulations on the Warwick Bridge (WB).

6.3.1 Calibration of inverted pendulum model

In this section, the IPM is calibrated with respect to the measured locomotion data recorded on the rigid surface for each TS. The body masses of three test subjects TS1, TS2 and TS3 are taken as measured values, i.e. 62.4, 70.0 and 72.7 kg, respectively. The pendulum length l of the IPM is first calculated for

individual TS from the model geometry:

$$l = \frac{d}{2\cos\theta_0} \tag{6.4}$$

where d is the step length. Based on the average d and average θ_0 measured in the experiments, l is calculated for each trial. It is noted that the resulting l for individual TS varies for trials with different walking speeds. The reason for this issue is because IPM is a simplified representation of the walking gait and, therefore, cannot reflect truly the walking locomotion. The identified pendulum length is then averaged across 13 trials performed by each TS. The average l is found to be approximately 1.3 m for TS1 while the corresponding value for both TS2 and TS3 is about 1.1 m.

The attack angle is chosen to match the average value measured in each trial (absolute discrepancy less than 0.1 %). The initial forward speed is then selected on a trial-by-trial basis so that the gait parameters (i.e. pacing rate, walking speed and DLF_1) produced by the IPM are close to those measured on the rigid surface. Since these gait parameters are interdependent and there usually does not exist a single combination of initial conditions resulting in all gait parameters matching the corresponding values measured in the experiments, the selection of the initial forward speed for each simulation is made in the following priority. First, a range of the initial forward speeds that results in the pacing rate that is close to the measured value is identified. Among the pacing rate, walking speed and DLF_1, the pacing rate is chosen to be matched first since it is a gait parameter to which the structural response is most sensitive to. The second parameter to match is the walking speed. This parameter

was given priority over DLF_1 since it was measured with much greater accuracy. As shown in Chapter 5, DLF_1 was least accurate of all measured parameters, which is justification for giving it the lowest priority.

The discrepancy between the simulated (s) and measured (m) values of a parameter is calculated using Equation 4.3, in which Δ, X and Y represent the percentage discrepancy, simulated data and measured average data on the rigid surface, respectively.

Discrepancies for the three parameters are shown in Figure 6.9 as functions of the corresponding measured values. In Figure 6.9a, it can be seen that $|\Delta f_p|$ is quite small in all cases (less than 1 %). On the other hand, the simulated walking speed underestimates the measured data in majority of cases (Figure 6.9b). This discrepancy ranges from -18 % to 1 %. With regard to DLF_1, the discrepancy for TS3 is smallest and ranging between -13 % and 9 % (Figure 6.9c). Simulated DLF_1 for TS1 and TS2 significantly underestimates and overestimates the measured values, respectively. Overall, the results show that using the calculated pendulum lengths, measured attack angle and the

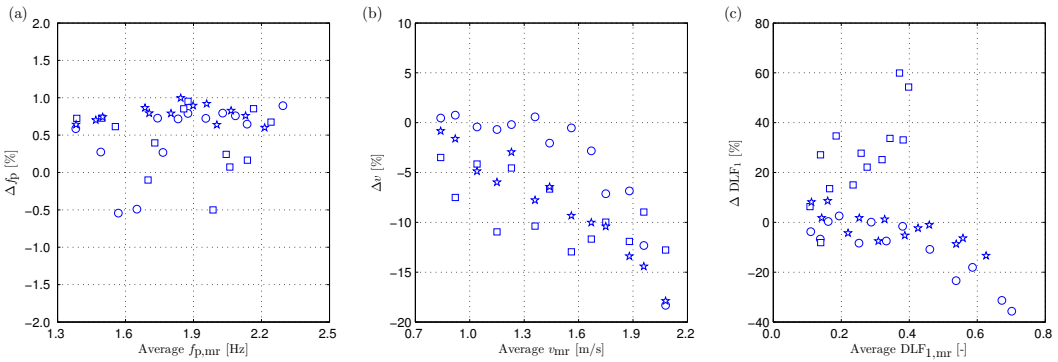

Figure 6.9: Discrepancies between simulated and measured values of **(a)** pacing rate, **(b)** walking speed and **(c)** DLF_1. Circles, squares and stars represent TS1, TS2 and TS3, respectively.

"best" optimised initial forward speed in the simulations led to absolute discrepancies in the walking speed and DLF_1 up to 18 % and 60 %, respectively.

To check if the absolute discrepancy for walking speed and DLF_1 could be reduced, the pendulum length is varied between 0.9 m and 1.4 m (in 0.1 m increment) for all TSs and the selection procedure of initial conditions is repeated. The cumulative distribution function (CDF) of the absolute discrepancy of f_p, v and DLF_1 for an individual TS is shown in Figure 6.10. For

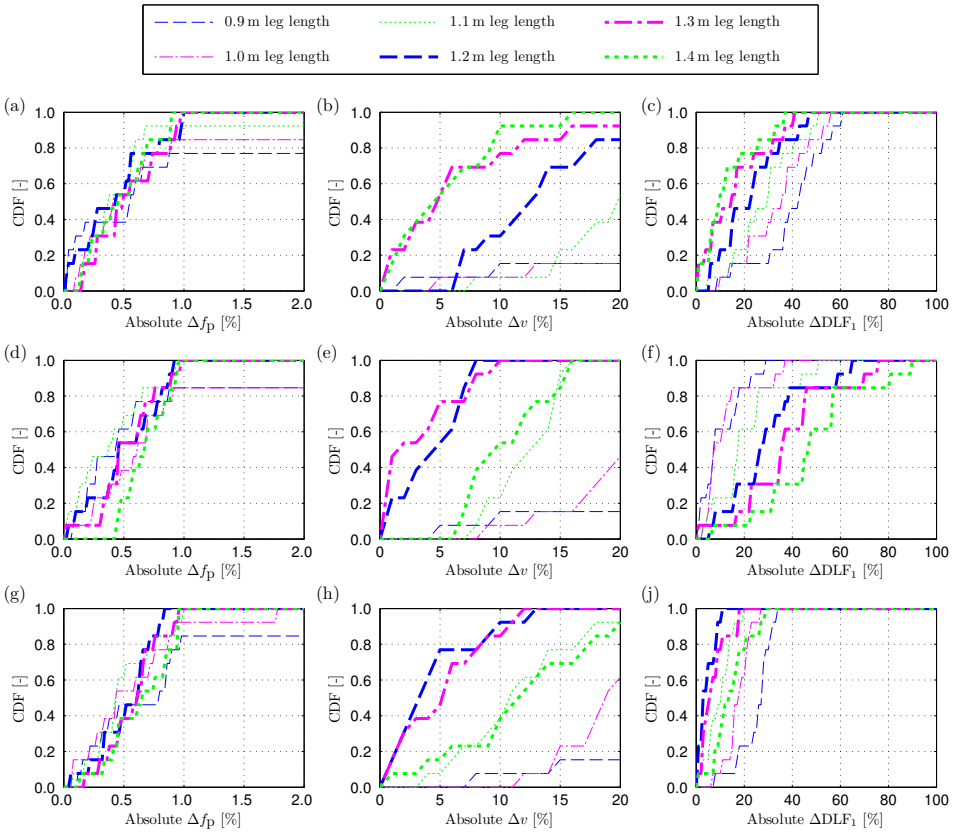

Figure 6.10: Cumulative distribution function of absolute discrepancies between simulated and measured gait parameters on rigid surface using different pendulum lengths. Top, middle and bottom rows represent results of TS1, TS2 and TS3, respectively. First, second and third columns represent results for absolute discrepancy of pacing rate, walking speed and DLF_1, respectively.

TS1 (Figures 6.10a–c), the absolute Δf_{p} is less than 1 % when $l \geq 1.2$ m while simulations using l of 1.4 m provide the smallest absolute discrepancies of both Δv (less than 16 %) and $\Delta \mathrm{DLF}_1$ (less than 37 %). For TS2 (Figures 6.10d–f), the absolute Δf_{p} is less than 1 % when $l \geq 1.1$ m. The simulations using l of 1.2 m provide the smallest absolute discrepancy of Δv (less than 8 %) while the corresponding absolute $\Delta \mathrm{DLF}_1$ is less than 65 %. For TS3 (Figures 6.10g–j), the absolute Δf_{p} is less than 1 % when $l \geq 1.1$ m. The simulations using l of 1.3 m provide the smallest range of absolute Δv (less than 12 %) while the absolute $\Delta \mathrm{DLF}_1$ is less than 18 %. Based on this analysis, the pendulum lengths of 1.4 m, 1.2 m and 1.3 m are chosen in further simulations for TS1, TS2 and TS3, respectively, since these values, on average, best fit the experimental data than those calculated using Equation 6.4.

6.3.2 Simulations for the Warwick Bridge

This section aims to validate the IM against the data collected on the lively surface presented in Chapter 5. The main objective is to investigate if the IM can provide numerical results comparable to the measured data.

The WB is modelled as a SDoF system in the same way as explained in Section 5.5.7.1. Initial conditions for the bridge, in form of modal displacement and velocity, are set to the measured values. Since the TSs walked on the treadmill that was located at the midspan of the bridge, mode shape ordinate ϕ_x is set to 1 in Equations 6.1 and 6.2.

Simulations are performed to represent conditions in 144 trials completed by three TSs walking on two bridge configurations. The pedestrian mass re-

quired for simulation is set to the actual mass of each TS, i.e. 62.4, 70.0 and 72.7 kg while the pendulum length is set to be 1.4, 1.2 and 1.3 m for TS1, TS2 and TS3, respectively. The initial conditions for the IPM are chosen to match the measured gait parameters on the rigid surface when TS walked at nominally the same speed, following procedure explained in Section 6.3.1.

Among 144 trials to be used for validation of the IM, there were 36 trials in which the shaker was off and 108 trials in which the shaker induced a harmonic force onto the structure. In simulations with zero shaker force, the walking force F_{p} generated by the IPM (calculated in Appendix D) was the only excitation to be input into Equations 6.1 and 6.2. In simulations that include shaker operation, the shaker-induced force, F_{s}, measured in a particular trial is used in the simulation as an additional external force. In this case, Equation 6.2 becomes:

$$\begin{aligned}(m_{\mathrm{b}} + m_{\mathrm{p}}\phi_x^2 \sin^2\theta)\ddot{y}_{\mathrm{b}} + 2\zeta m_{\mathrm{b}}(2\pi f_{\mathrm{n}})\dot{y}_{\mathrm{b}} + \\ m_{\mathrm{b}}(2\pi f_{\mathrm{n}})^2 y_{\mathrm{b}} - \phi_x m_{\mathrm{p}}(g\sin^2\theta + l\dot{\theta}^2\sin\theta) + \phi_{\mathrm{s}}F_{\mathrm{s}} = 0\end{aligned} \tag{6.5}$$

where ϕ_{s} is the (unity-scaled) mode shape ordinate at the shaker location (TP57 in Figure 5.2a). This ordinate is equal to 0.70 and 0.82 for WB1 and WB2, respectively.

To successfully simulate trials with shaker in operation, it is necessary to check if the simulated vibration response is sensitive to the chosen phase difference between the shaker force and the walking force. To investigate this sensitivity, all possible phase differences are accounted for through multiple simulations. Namely, the starting point of the shaker force time history re-

quired for simulations is chosen so that all possible phase differences within a full cycle of the harmonic force are covered.

Resulting envelopes of vibration responses obtained when modelling conditions in two chosen trials are shown in Figures 6.11a and 6.11b. Full information about each trial is included in the figures. In each figure, the results of two simulations, which differ in the choice of the pedestrian-shaker phase only,

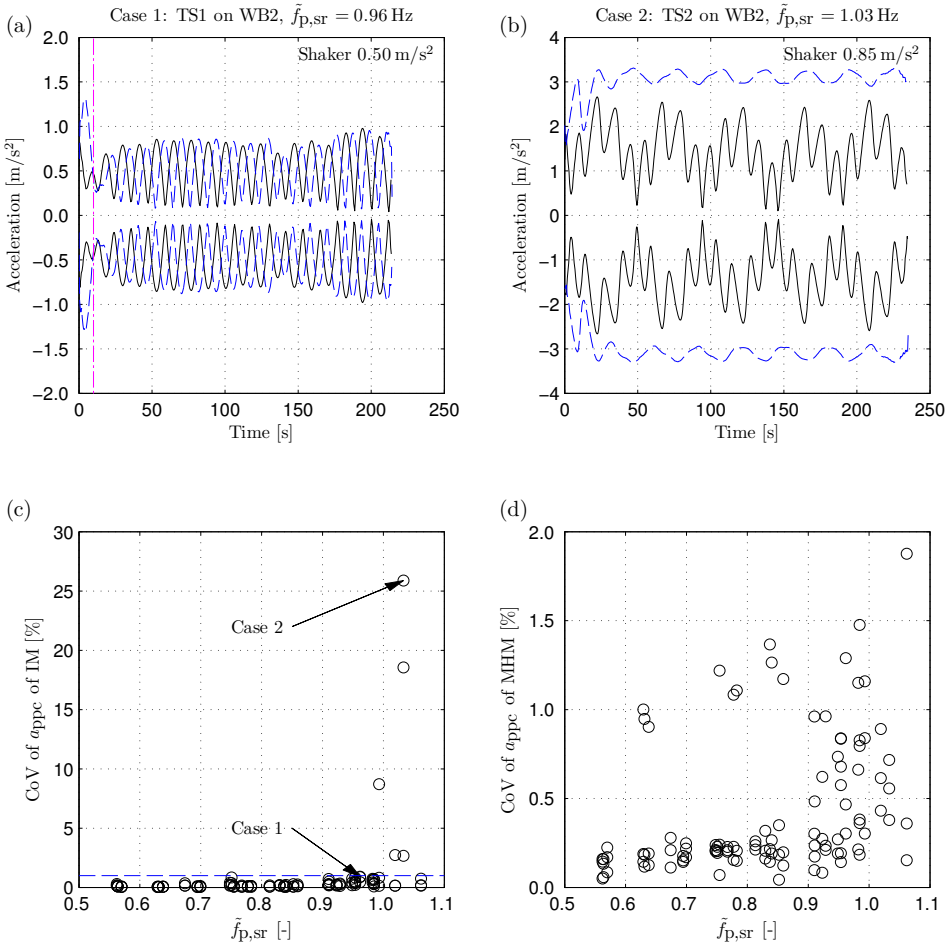

Figure 6.11: Phase difference between walking force and shaker force results in vibration responses with **(a)** small discrepancy and **(b)** large discrepancy. Coefficient of variation of average peak-per-cycle acceleration of all simulations in each case for **(c)** the interactive model and **(d)** the moving harmonic model.

are presented. The two simulations chosen for presentation are those which result in minimum (solid lines) and maximum (dashed lines) average peak-per-cycle acceleration (average a_{ppc}). In Figure 6.11a (referred to as Case 1 in this section), the amplitudes and shapes of the envelopes of the two simulations are relatively similar, apart from the initial 10 s (i.e. before the dash-dotted line). On the other hand, the two envelopes in Figure 6.11b (Case 2) differ both quantitatively and qualitatively over the entire simulation time. In this particular example, the average a_{ppc} of the maximum response is 110 % greater than that of the minimum response.

Because of the transient effect (such as the responses seen in Figure 6.11a), the first 30 s of all simulated responses is disregarded before further analysis. Average a_{ppc} is then calculated corresponding to all possible phase differences for each of 108 trials with shaker operation. Then the CoV of average a_{ppc} is calculated in relation to each trial and shown in Figure 6.11c as a function of the normalised pacing rate simulated on rigid surface ($\tilde{f}_{\mathrm{p,sr}} = f_{\mathrm{p,sr}}/f_{\mathrm{n}}$). In majority of cases, the CoV of average a_{ppc} is quite small, i.e. less than 1 % (dashed line in Figure 6.11c). In this category, Case 1 (Figure 6.11a) is the simulation with the highest CoV (0.9 %). There are five cases in which CoV was larger than 1 % with maximum value of 25.9 % achieved for Case 2 shown in Figure 6.11b. It can be concluded that for further analysis, it is acceptable to choose an arbitrary phase in cases when CoV in Figure 6.11c is below 1 %. For the five cases with higher CoV and in the absence of any criterion for appropriate choice of the phase angle, all possible phase combinations will be considered in further analysis. The cases with low and high CoV are hereafter referred to as normal and special cases, respectively.

The MHM is also used in simulations on WB. Pedestrian mass, pacing rate, DLF_1 and walking speed are chosen to match the measured data on the rigid surface. Investigation of effects of the phase difference for this model in the simulations with shaker operation is performed in the same way as presented for the IM. CoV of average a_{ppc} for simulations of the MHM is below 2 % as shown in Figure 6.11d. The result shows that the choice of phase angle when using the MHM is relatively insensitive to the structural response. Thus, an arbitrary phase is used in MHM simulations.

The analysis starts with the evaluation of capability of the IM and the MHM to predict measured vibration responses. This is followed by the analysis of the pacing rate and DLF_1 produced by the IM. For each parameter, the average value achieved is compared to the corresponding value obtained in the simulation (with the same input parameters) on the rigid surface. The objective is to check whether the discrepancy between simulated results on rigid and lively surfaces can reflect that seen in the measured data. Ranges of CoV of simulated parameters on the WB are then quantified and compared to the measured data.

6.3.2.1 Structural vibration response

Measured vibration responses are used to evaluate the responses produced by the IM and the MHM. The percentage discrepancy of the average a_{ppc} used in the validation is calculated using Equation 4.3, in which Δ, X and Y represent Δa_{ppc}, simulated average response and measured average response, respectively. The measured signal is band-pass filtered and then truncated to have the same data points with the simulated acceleration signal.

Discrepancy in a_{ppc} when using IM is shown as a function of $\tilde{f}_{\mathrm{p,sr}}$ in Figure 6.12a and of the average $a_{\mathrm{ppc,m}}$ in Figure 6.12b. Results of the normal cases are plotted as unfilled symbols while the special cases are presented as vertical lines (drawn to connect minimum and maximum values with a mean value represented using a filled symbol). In these five cases, simulation results can only be interpreted within the obtained range and no firm conclusions can be drawn due to the unknown initial phase difference. This way of presenting

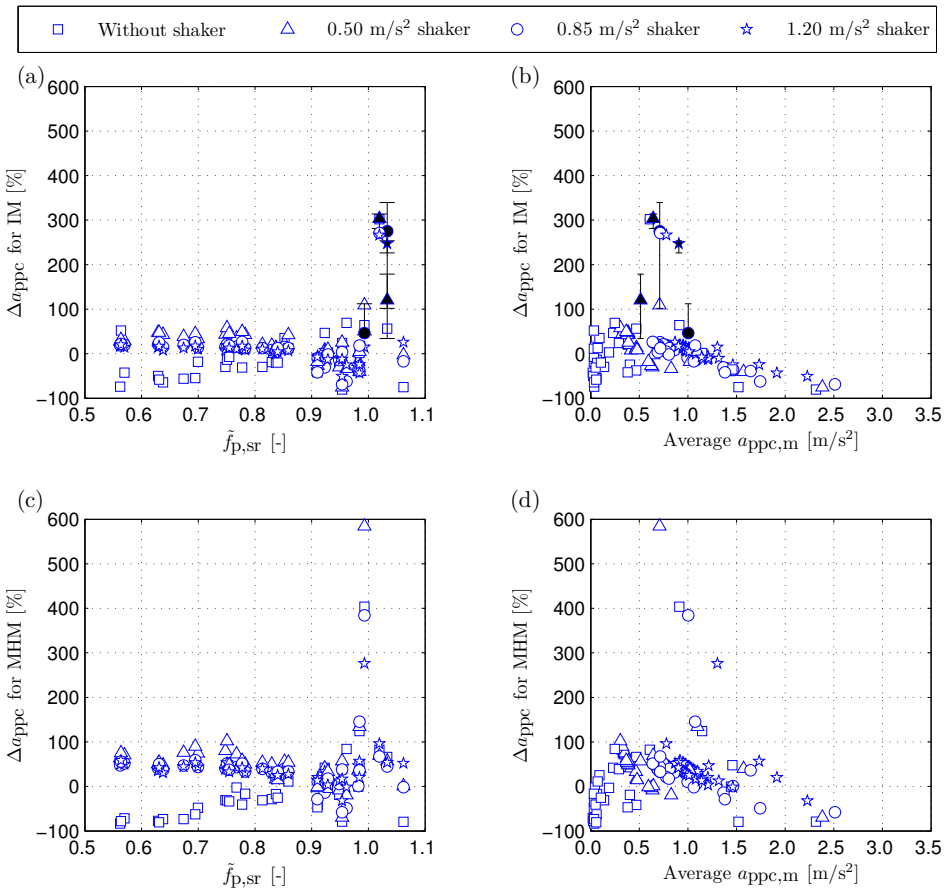

Figure 6.12: Discrepancy of average peak-per-cycle acceleration generated by **(a–b)** the interactive model and **(c–d)** the moving harmonic model. Unfilled and filled symbols in **(a–b)** represent normal and special cases, respectively.

and interpreting the simulation data will be used in the remainder of Section 6.3.

For $\tilde{f}_{\mathrm{p,sr}} < 0.90$, Δa_{ppc} ranges from $-74\,\%$ to $58\,\%$, in which largest discrepancies happen in simulations of trials without shaker. These cases mostly corresponds to low vibration cases (squares in Figure 6.12b). On the other hand, the IM mostly underestimates the measured response when $0.90 < \tilde{f}_{\mathrm{p,sr}} < 1.00$ and $\tilde{f}_{\mathrm{p,sr}} > 1.05$ (Δa_{ppc} is up to $-81\,\%$, corresponding to high vibration cases of greater than $1.5\,\mathrm{m/s^2}$ in Figure 6.12b). For $1.00 \leq \tilde{f}_{\mathrm{p,sr}} \leq 1.05$, the IM overestimates the measured response (up to about $300\,\%$). For the special cases having pacing rate within this range, the IM overestimates the measured response regardless of phase angle chosen (Δa_{ppc} is approximately 30–$340\,\%$). The estimated results of high vibration in cases of $f_{\mathrm{p,sr}}$ slightly higher than f_{n} is in agreement with the result presented in Figure 6.5a. However, this observation of frequency shift in the simulations does not agree with the experimental data, leading to excessive discrepancies of vibration estimates in many cases.

Discrepancy of a_{ppc} for the MHM is plotted in Figures 6.12c and 6.12d. Results provided by the MHM are generally worse than those by the IM. The difference between results of the IM and the MHM is most pronounced when the target pacing rate is around the structural frequency, in which the MHM overestimates the measured response by at least two times more than the IM.

Overall, both the IM and the MHM produce vibration responses with high discrepancies when compared to the measured data. More importantly, vibration estimates have are not reliable when the target pacing rate is close to the structural frequency ($0.9 < \tilde{f}_{\mathrm{p,sr}} < 1.1$). For the IM, a source of large

discrepancies could be the unrealistic assumption of constant initial conditions used in simulations.

While the discrepancies in Figure 6.12 are calculated on a trial-by-trial basis, it is useful to investigate the range of vibration response estimated by the two models in comparison with that of the measured data. Figure 6.13a shows the average a_{ppc} measured in the experiments. It can be seen that estimates provided by the IM (Figure 6.13b) are in better agreement with the measured data than those produced by the MHM (Figure 6.13c). The maximum a_{ppc} in simulations of the IM and the MHM are $3.1\,\mathrm{m/s^2}$ and $4.9\,\mathrm{m/s^2}$ respectively, while the corresponding measured value is $2.5\,\mathrm{m/s^2}$.

In general, using the IM leads to the vibration estimates being closer to the measured data, and therefore less conservative in overestimated cases, than the MHM.

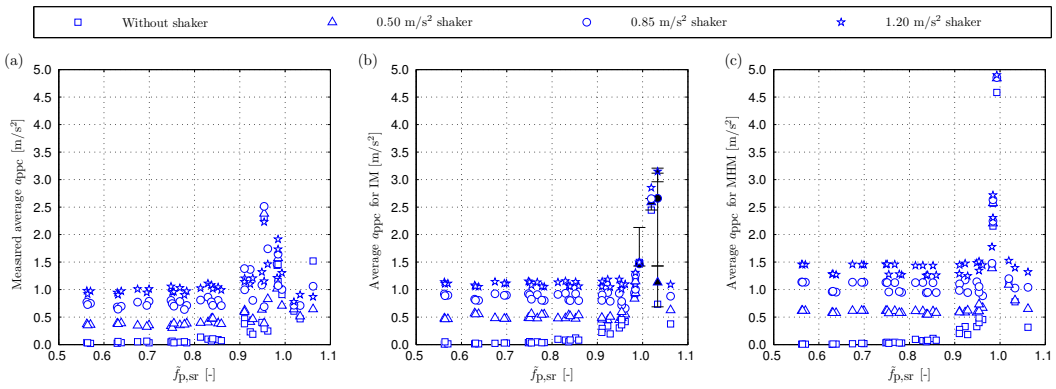

Figure 6.13: Average peak-per-cycle acceleration **(a)** in experiments, **(b)** produced by the interactive model and **(c)** produced by the moving harmonic model. Unfilled and filled symbols in **(b)** represent normal and special cases, respectively.

6.3.2.2 Pacing rate

The percentage discrepancy of average pacing rate (Δf_{p}) is calculated using Equation 4.3, in which Δ, X and Y represent Δf_{p}, the average pacing rate simulated on the lively surface and the target pacing rate simulated on the rigid surface, respectively.

Δf_{p} is shown as a function of $\tilde{f}_{\mathrm{p,sr}}$ and simulated average $a_{\mathrm{ppc,s}}$ in Figures 6.14a and 6.14b, respectively. The target pacing rate is reduced in a majority

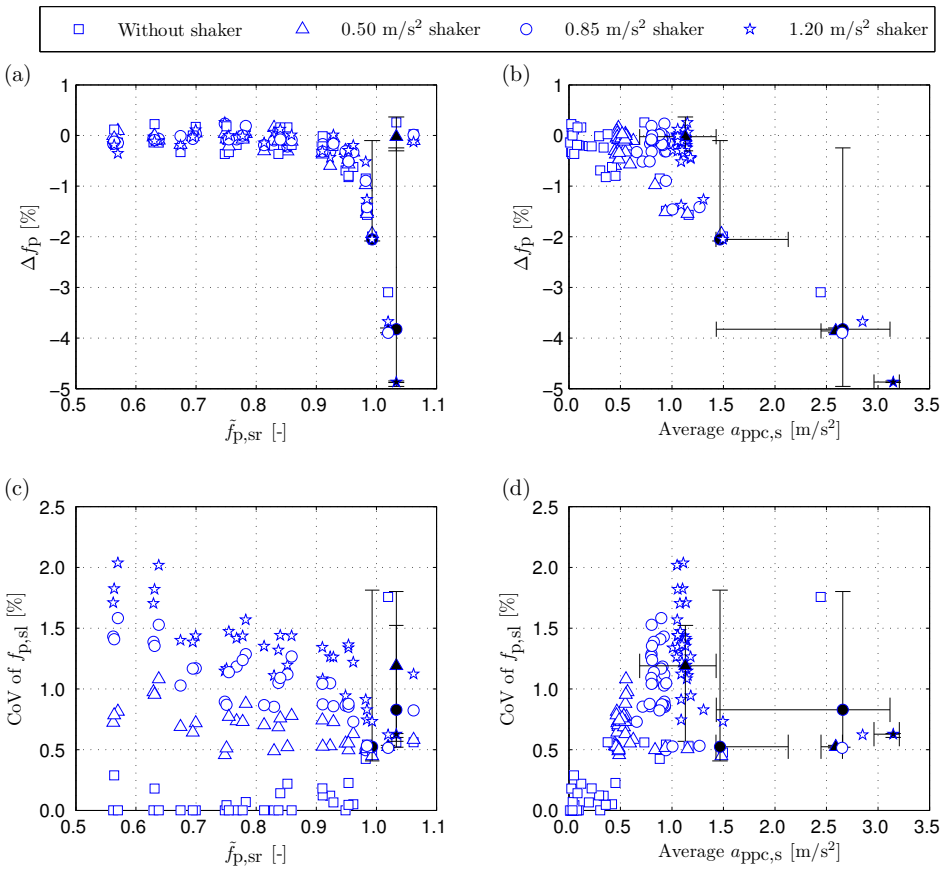

Figure 6.14: **(a–b)** Percentage discrepancy of pacing rate between simulations on rigid and lively surfaces and **(c–d)** CoV of pacing rate simulated on the lively surface. Unfilled and filled symbols represent normal and special cases, respectively.

of cases (80 %), with the most pronounced reduction happening when $0.90 < \tilde{f}_{\mathrm{p,sr}} < 1.05$ (Figure 6.14a). Within this range of pacing rate, Δf_{p} ranges from -3.9 % to 0.3 % for the normal cases and -5.0 % to 0.4 % for the special cases. The general reduction of f_{p} is in agreement with the finding that simulations of the IM result in decrease in the pacing rate, as demonstrated in Figure 6.3b. Such a reduction is likely the reason for the overestimation of vibration estimate when the pacing rate is slightly higher than the natural frequency as presented in Figure 6.12a. In addition, Figure 6.14b shows that $|\Delta f_{\mathrm{p}}|$ tends to increase with an increase of the acceleration.

CoV of the pacing rate simulated on the lively surface $f_{\mathrm{p,sl}}$ is shown in Figures 6.14c and 6.14d. The CoV tends to increase with an increase of the pre-induced vibration level (Figure 6.14c) and the acceleration level (Figure 6.14d). The CoV has the maximum at 2 % while it is close to zero for walking over bridge exhibiting low vibration level, which is almost the same as the IPM walking on the rigid surface.

Overall, the IPM tends to reduce the pacing rate when walking on the lively surface. Such a reduction contradicts the experimental data (Figure 5.11f). On the other hand, the CoV of pacing rate increases with an increase of the vibration level, which is in agreement with the measured data (Figure 5.13f). However, the range of CoV of the pedestrian (0–2 %) is lower than the measured range (1.2–6.4 %, Figures 5.13a–c). A factor contributing to these shortcomings is the constant initial conditions (used in the IPM) that cannot adequately replicate the human gait measured in the experiments.

6.3.2.3 Ground reaction force

Examples of spectra of the simulated GRF on the WB2 are presented in Figure 6.15. When the shaker is not in operation (Figure 6.15a), there is a peak at the first dominant harmonic as seen in the simulation on the rigid surface (Figure 3.2b). In the case with pre-induced vibration by the shaker at the natural frequency of the structure (Figure 6.15b), there is an additional peak at the vibration frequency. The simulation results agree qualitatively with the measured data (Figure 5.49) and the IM is, therefore, able to account for the self-excited force. In this section, average DLF_1, self-excited factor (SEF) and total force factor (TFF consisting of DLF_1 and SEF) are calculated in the same way as presented in Chapter 5.

Percentage discrepancies of average DLF_1 and total force factor (TFF) when compared to the target DLF_1 (ΔDLF_1 and ΔTFF, respectively) are

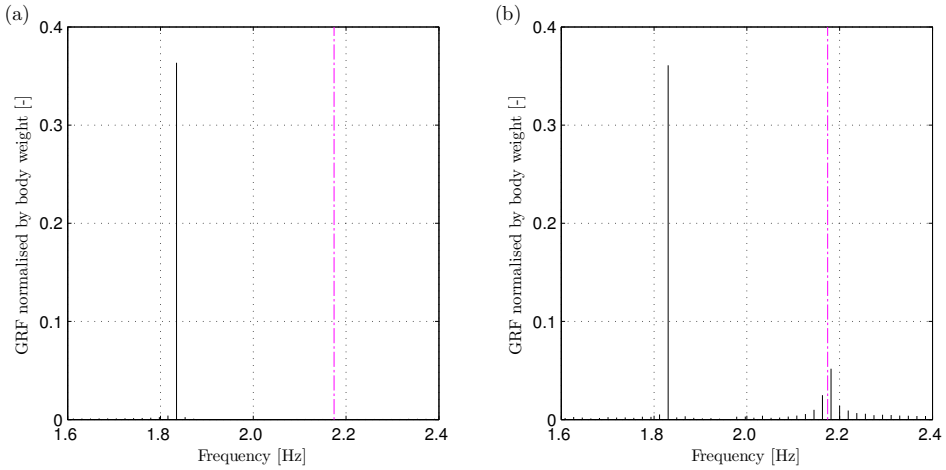

Figure 6.15: Spectrum of ground reaction force induced by the inverted pendulum model on the lively surface in the case **(a)** without shaker operation and **(b)** with shaker-induced vibration of 0.85 m/s^2 at 2.18 Hz. Input parameters for simulations belong to trials performed by TS3 on WB2 walking with target pacing rate of 1.83 Hz. Dash-dotted lines represent the natural frequency of WB2.

calculated using Equation 4.3, in which Δ, X and Y represent the discrepancy, average data simulated on the lively surface and average data simulated on the rigid surface, respectively. The discrepancies of average DLF_1 and TFF are shown in Figures 6.16a and 6.16b as functions of $\tilde{f}_{p,sr}$ and $a_{ppc,s}$, respectively. When $\tilde{f}_{p,sr} < 0.9$, the absolute discrepancy is small, i.e. less than 2 % (Figure 6.16a). When $f_{p,sr}$ approaches f_n, there is a significant increase in ΔDLF_1 and ΔTFF for normal cases (up to 40 %). The discrepancy is negative (up

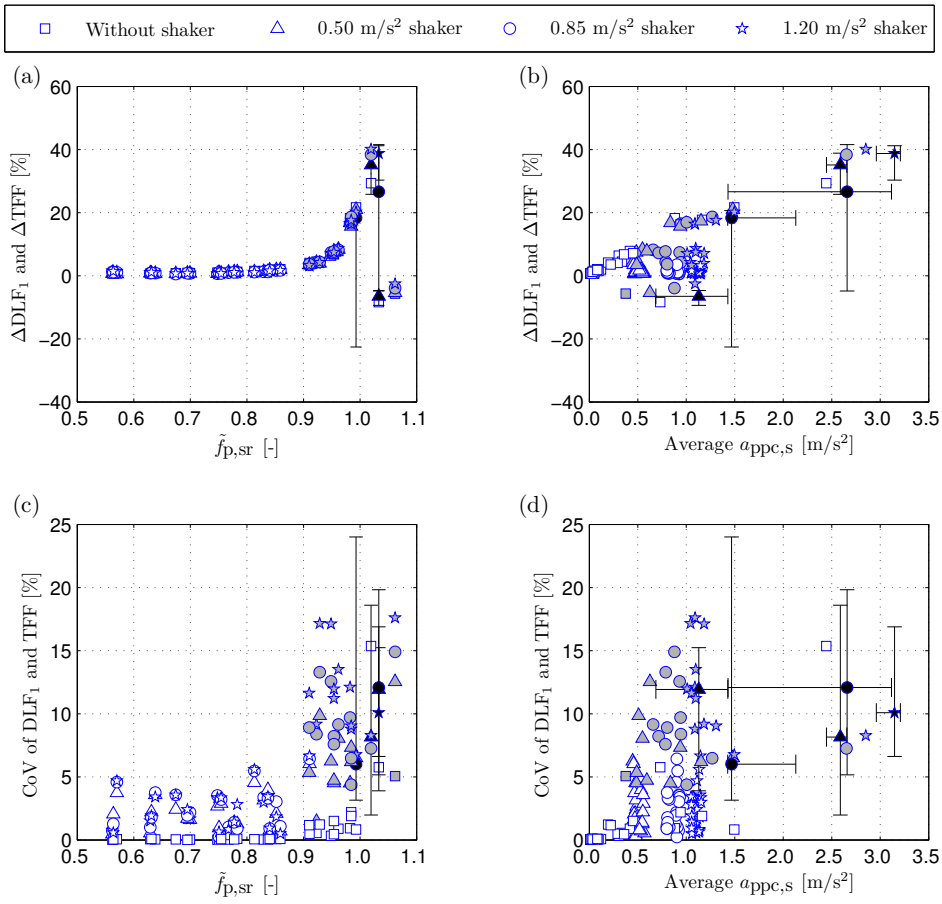

Figure 6.16: (a–b) Percentage discrepancy of average DLF_1 and TFF between simulations on rigid and lively surfaces and **(c–d)** CoV of DLF_1 and TFF in simulations on the lively surface. Unfilled and filled symbols represent average DLF_1 and TFF, respectively. Black filled symbols represent special cases.

to −8 %) in several cases when $f_{\mathrm{p,sr}}$ is close to and higher than f_{n}. For the special cases, the mean values (black-filled symbols in Figure 6.16a) seems to follow the observed trend for the normal cases. However, $\Delta\mathrm{DLF}_1$ and $\Delta\mathrm{TFF}$ in these cases have a large range (from −23 % to 41 %). Figure 6.16b shows that $\Delta\mathrm{DLF}_1$ and $\Delta\mathrm{TFF}$ tend to increase with an increase of the acceleration level.

CoV of DLF_1 and TFF are plotted in Figures 6.16c and 6.16d. The CoV tends to increase with an increase of the pre-induced vibration level (Figures 6.16c). Moreover, the range of CoV increases when $f_{\mathrm{p,sr}}$ is closer to the structural frequency. The CoV is 0–18 % for the normal cases and 2–24 % for the special cases. There is no particular trend of CoV of DLF_1 and TFF with respect to the average $a_{\mathrm{ppc,s}}$ (Figures 6.16d).

The increase of average DLF_1 and TFF shown in Figure 6.16a contradicts the measured results presented in Figures 5.53, in which the reduction of DLF_1, when the pacing rate was close to the natural frequency, exceeded 15 %. This finding indicates that the IM cannot replicate all aspects of walking characteristics encountered in the experiments. On the other hand, increase in CoV for cases when the target pacing rate is closer to the structural frequency is in agreement with the measured data (Figures 5.55a–c). Similar to the analysis of the pacing rate, the range of CoV of DLF_1 and TFF (0–24 %) generally underestimates that of the measured data (3–31 %, Figures 5.54a–c).

The average SEF is shown in Figure 6.17a as a function of the average normalised pacing rate on the lively surface ($\tilde{f}_{\mathrm{p,sl}}$). At each pre-induced vibration level, the average SEF tends to decrease when the pacing rate becomes closer to and smaller than f_{n}. The SEF data are not presented for cases in

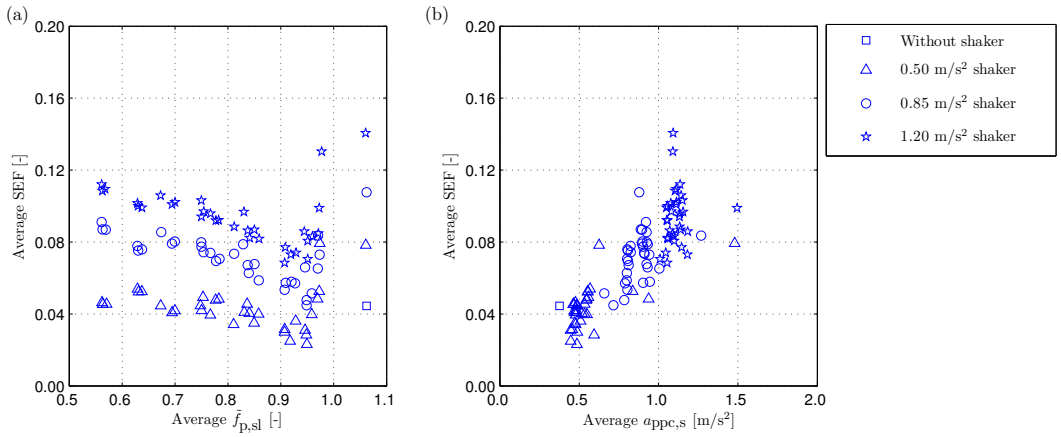

Figure 6.17: Simulated self-excited factor as a function of **(a)** average normalised pacing rate and **(b)** average peak-per-cycle acceleration.

which this force merges with DLF_1 into one peak in the spectrum. Results of few simulations with the pacing rate greater than f_n suggest that the average SEF increases in comparison with values obtained when the pacing rate is less than f_n. Figure 6.17b shows that the average SEF tends to increase with an increase of the vibration level. The results in Figure 6.17 are mostly in agreement with the measured data presented in Figures 5.57 and 5.58a.

6.3.2.4 Evaluations of simulation results

Simulation results on the lively surface show that there is a large discrepancy in vibration estimate in comparison with the measured responses. When the target pacing rate is close to and smaller than the structural frequency, the pacing rate decreases while the average DLF_1 and TFF increase in comparison to the simulations on the rigid surface. These trends oppose those observed in the measured data.

On the positive side, the range of vibration estimates produced by the IM is closer to the measured responses than that provided by the MHM. In ad-

dition, the IM allows the pedestrian to interact with the lively surface. In this process, the timing of each step of the pedestrian is affected by the vibration of the supporting structure. As a result, the intra-subject variability (CoV) is introduced in the pacing rate and DLF_1/TFF when walking on the lively surface, reflecting the non-periodic nature of the walking gait. Nevertheless, the range of CoV in simulations is lower than that seen in the experiments. This feature is most likely consequence of repetitive initial conditions. Another positive feature of the IM is its ability to model the self-excited force. The feature might be helpful for the further application of the model in modelling structural vibration due to multi-pedestrian traffic as one pedestrian is under influence of the vibration generated by others and consequently producing the self-excited force. Since the IM can reproduce this forcing component, its application is likely to produce better estimates of response to multi-pedestrian traffic than the MHM.

Overall, the results show that the IM can reproduce well some experimental data. Since the assumption of constant initial conditions is restrictive and it cannot represent natural variations in the human gait, the intention of the next section is to investigate if introducing variations of initial conditions can improve the overall performance of the IM.

6.4 Modelling intra-subject variability of gait parameters

Since the constant initial conditions of the IPM cannot provide any variation in gait parameters in simulations on the rigid surface and it underestimates

the variation that occurs when walking on the lively surface, a possible improvement of the IPM would be to introduce variations to initial conditions on a step-by-step basis. Such variations could alter the simulated parameters in each step and consequently create the desired effect of gait variability.

The aim of the study in this section is first to investigate if variations of gait parameters seen in the experiments on both rigid and lively surfaces can be replicated. The priority in this process is to achieve good agreement with measured variations in the pacing rate. Also, it is aimed to test if improving the intra-subject variability in gait parameters could lead to more accurate vibration estimates. Data collected in 39 trials on the rigid surface and 144 trials on the lively surfaces will be used for validation. Pedestrian mass and the pendulum length corresponding to each TS are chosen in the same way as in simulations performed in Section 6.3.2.

This section first describes the modelling of intra-subject variability using the IPM on the rigid surface, followed by the application of the modelling method for the simulations on the lively surface.

6.4.1 Modelling gait variability on rigid surface

Methods of introducing variations to the initial conditions of the IPM (i.e. attack angle and initial forward speed) could be to keep one parameter constant and vary the other, or to vary both parameters at the same time. Since the variability of the attack angle was experimentally observed and quantified in Chapters 4 and 5, the option of keeping the attack angle constant while varying the initial forward speed is disregarded in this analysis.

The attack angle only is first randomised for each step while the initial forward speed is kept constant. Normal distribution is used for the distribution of the attack angle (Chapter 4) with the mean value equal to the measured average value. Although the CoV of attack angle is known in the experiments, a range of CoV of θ_0 is used in the simulations (0.0–2.5 %) to test the performance of the randomisation method. The initial forward speed is chosen so that, together with the mean θ_0, the simulated gait parameters match the measured average data on the rigid surface on a trial-by-trial basis (following the matching procedure presented in Section 6.3.1).

Figure 6.18 shows a simulation example of pacing rate and DLF_1 when the CoV of θ_0 is set at 0.7 %. Randomisation in the attack angle provides the variability in the pacing rate on a step-by-step basis (Figure 6.18a). The spectrum of the GRF produced by the IPM over 50 steps is shown in Figure 6.18b. Unlike the simulation result of constant initial conditions (Figure 3.2b), spectrum of the GRF with varying attack angle reflects the narrow-band nature seen in the experiments (Figure 4.28b). Figure 6.18c shows the pacing rate and its CoV averaged over increasing number of steps within a single simulation. Similar information is shown in Figure 6.18d for the DLF_1 and its CoV. The averaged f_p and DLF_1 have negligible variations after the number of steps exceeds 1,000 in this particular example (dash-dotted lines in Figures 6.18c and 6.18d). On the other hand, CoVs of f_p and DLF_1 require more steps to achieve values that have negligent variations. In this section, 5,000 steps are used in each simulation for calculations of CoVs of f_p and DLF_1.

Contour plots of CoVs of f_p and DLF_1 for the three TSs are shown in Figure 6.19. CoV of θ_0 tends to increase to reach the same level of CoV of

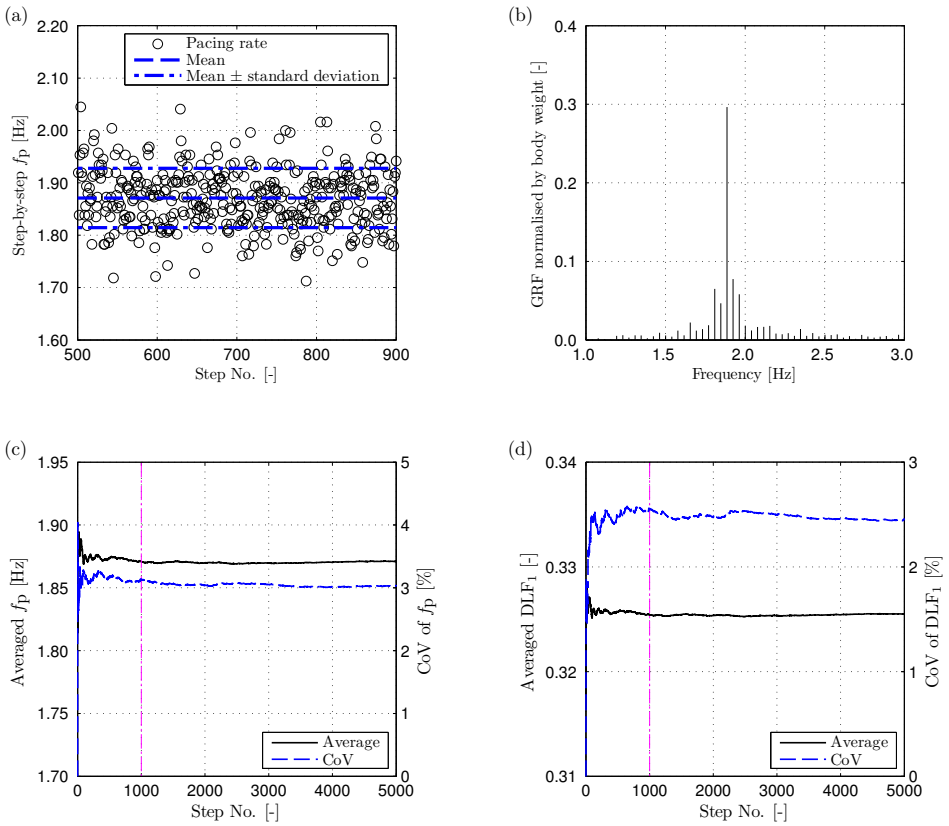

Figure 6.18: **(a)** Step-by-step pacing rate, **(b)** spectrum of GRF generated in 50 steps. **(c)** Averaged pacing rate and its coefficient of variation and **(d)** Averaged DLF_1 and its coefficient of variation as a function of step number. Input parameters for the simulation belong to the trial performed by TS2 walking at 1.45 m/s on rigid surface.

f_p and DLF_1 when the pacing rate increases. When the measured CoV of attack angle is used in the randomisation, the achieved CoV of f_p is between 2.5–13.0 % for all TSs (circles in left column). The achieved CoV of f_p is significantly higher than the measured range of CoV (0.9–4.6 %). To achieve the measured CoV of f_p, CoV of θ_0 for each trial is customised (squares). In all simulations, the customised CoV of θ_0 is always lower than the measured value. For the CoV of DLF_1, the application of the measured CoV of θ_0 (circles in

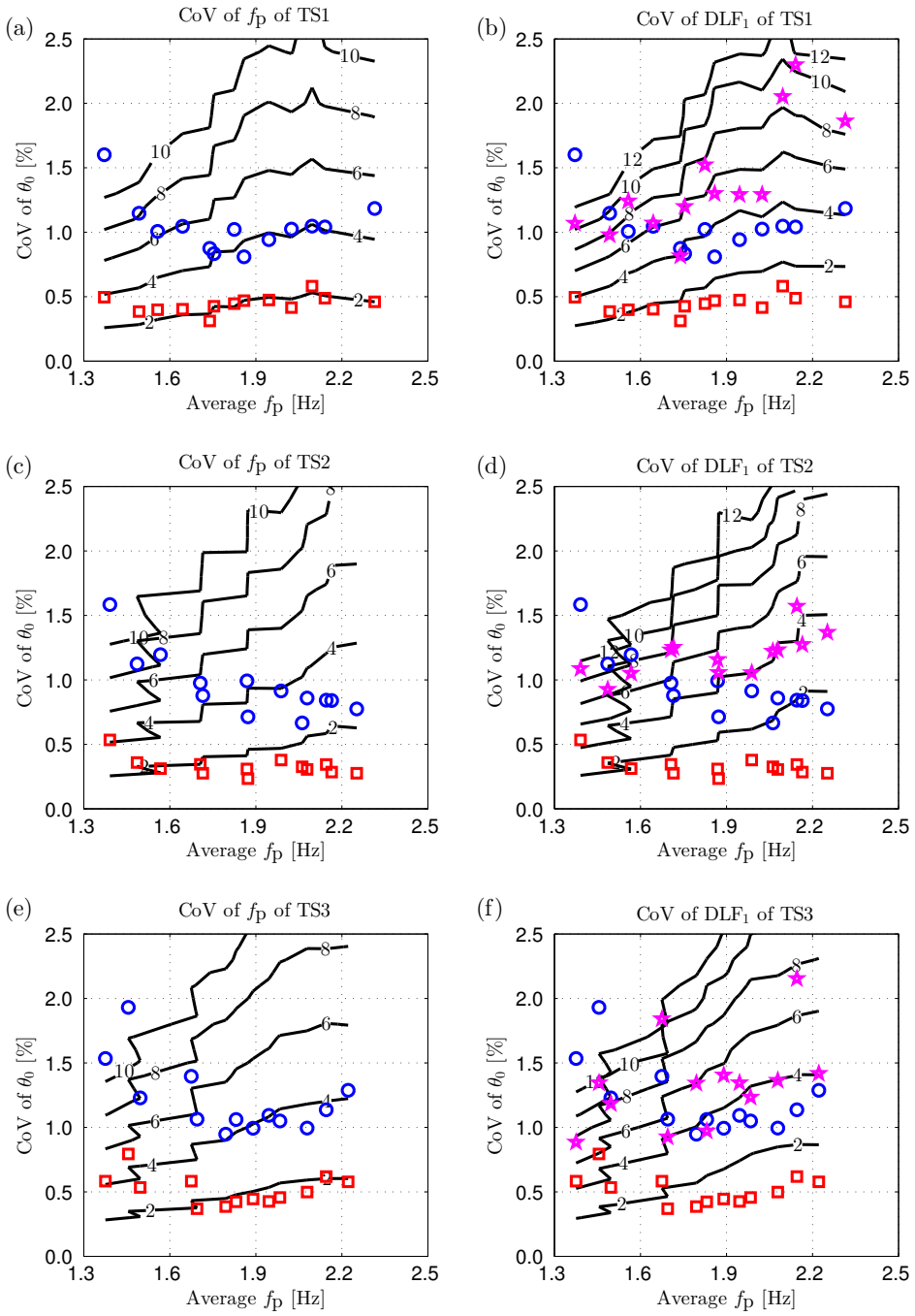

Figure 6.19: CoV of pacing rate and DLF$_1$ for simulations of TS1 in **(a)** and **(b)**, of TS2 in **(c)** and **(d)**, and of TS3 in **(e)** and **(f)**, respectively.

right column) generally results in lower CoV than the measured data (stars). The discrepancy is even higher when the CoV of θ_0 is optimised to match the CoV of pacing rate (squares).

Results in Figure 6.19 suggest that applying the measured CoV of θ_0 while keeping the initial forward speed constant produces the CoV of f_p being higher than the measured values. The implementation of randomisation of both initial conditions (results not shown here) produces even higher, and therefore unrealistic, CoV of f_p. Given the importance of replicating variations in the pacing rate as best as possible, the option of randomising both θ_0 and $\dot{x}_0$ is no longer considered.

Overall, the randomisation method in this section succeeds in replicating the measured CoV of f_p through using customised CoV of θ_0 identified for each trial. Acknowledging that this customised CoV results in the CoV of DLF_1 being lower than that measured, it will be applied for modelling intra-subject variability on the lively surface in the next section.

6.4.2 Modelling gait variability on lively surface

Simulations are performed on the WB using the same methodology as presented in Section 6.3.2. The only addition is the randomisation of the attack angle using the customised CoV to replicate the CoV of f_p on the rigid surface. This randomisation method generates different pacing rate on a step-by-step basis, leading to the continuous variations of phase between the walking force and shaker force in a randomised manner. Thus the check of effects of the phase difference between these two types of forces is not as critical as in Sec-

tion 6.3.2. As a result, this check is disregarded in this section.

Since the randomisation method using the stochastic representation of attack angle (i.e. mean and CoV) and given the limited number of steps (i.e. 400) in each trial, each simulation will produce different responses using the same stochastic input. Therefore, multiple simulations are performed for each trial to achieve statistically reliable results. Figure 6.20 shows three examples, each consists of 50 simulations using the randomisation method. The three chosen examples represent a non-resonant trial (top row, normalised target pacing rate $\tilde{f}_{\mathrm{p,sr}} = 0.84$), a near resonant trial resulting in the beating response (middle row, $\tilde{f}_{\mathrm{p,sr}} = 0.92$) and a resonant trial (bottom row, $\tilde{f}_{\mathrm{p,sr}} = 0.98$). For each example, average a_{ppc}, Δf_{p}, CoV of f_{p}, $\Delta\mathrm{DLF}_1$ and CoV of DLF_1 are investigated (definitions for these parameters are the same as presented in Section 6.3.2). For each of the five parameters, results of individual simulations are presented (circles), along with the averaged value as a function of number of simulations (solid lines). Even though there are, as expected, variations in the results of individual simulations, Figure 6.20 shows the convergence of the averaged values within 50 simulations.

To represent each of 144 trials on WB, the simulation is repeated 50 times, and the averaged data are then acquired using all simulations. Averaged results for the average a_{ppc}, Δf_{p}, $\Delta\mathrm{DLF}_1$ and average SEF are shown in Figures 6.21a–d as functions of $\tilde{f}_{\mathrm{p,sr}}$, respectively. The results from simulations with randomisation (WR) are relatively similar to the results of non-randomisation (NR) simulations presented in Section 6.3.2. This observation indicates that even when the variability of gait parameters is introduced, the performance of the IM does not improve. Namely, there are excessive errors in vibration

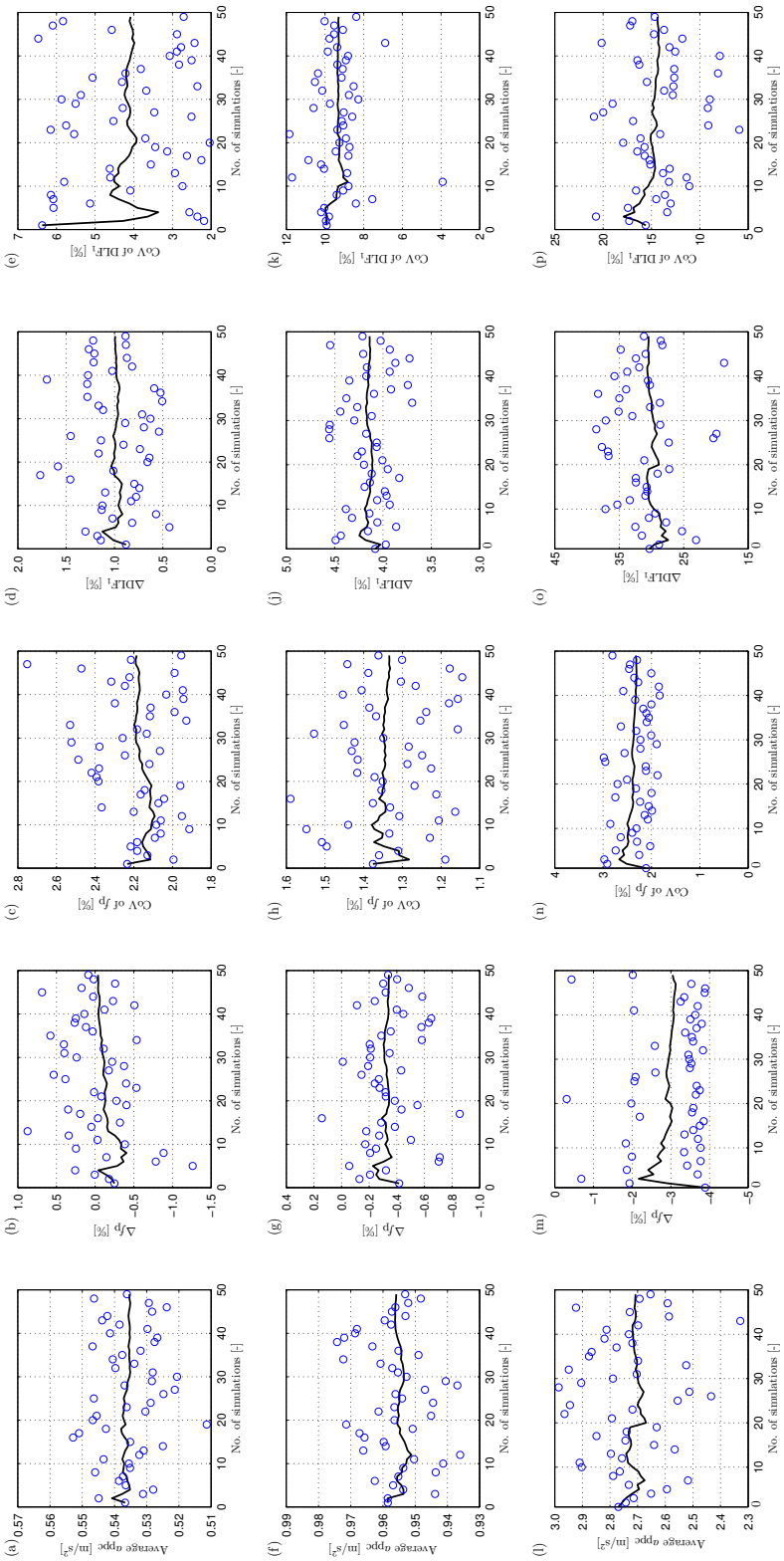

Figure 6.20: Examples of multiple simulations using randomisation of attack angle. Circles and solid lines represent individual data and averaged data as a function of number of simulations, respectively. First, second, third, fourth and fifth columns represent results of average a_{ppc}, Δf_{p}, CoV of f_{p}, $\Delta \mathrm{DLF}_1$ and CoV of DLF_1, respectively. Top, middle and bottom rows represent TS1 on WB2 (walking at $\tilde{f}_{\mathrm{p,sr}} = 0.84$, shaker 0.50 m/s^2), TS2 on WB1 (walking at $\tilde{f}_{\mathrm{p,sr}} = 0.92$, shaker 0.85 m/s^2), and TS3 on WB2 (walking at $\tilde{f}_{\mathrm{p,sr}} = 0.98$, shaker 1.20 m/s^2), respectively.

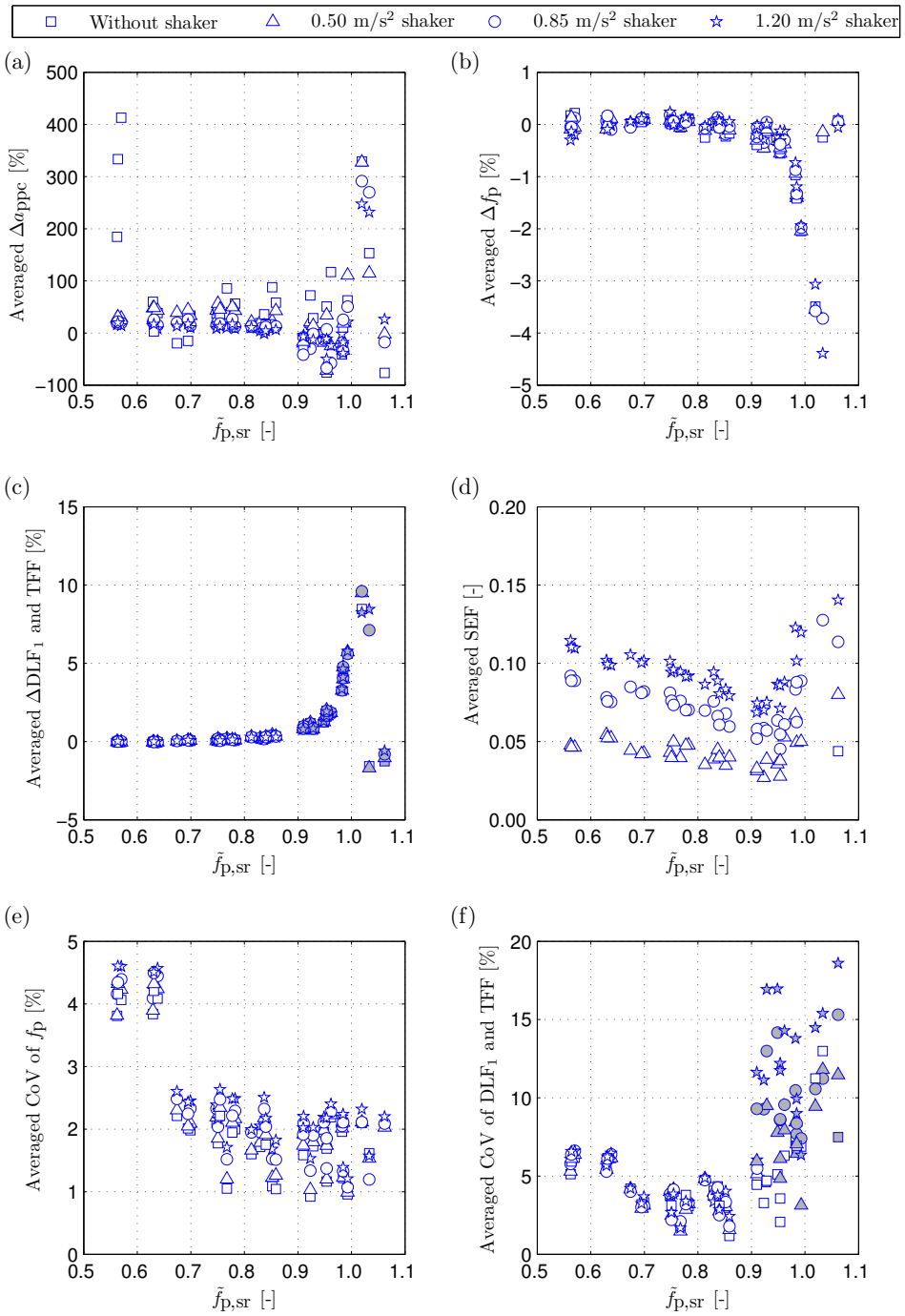

Figure 6.21: Averaged results of **(a)** average a_{ppc}, **(b)** Δf_{p}, **(c)** $\Delta\mathrm{DLF}_1$, **(d)** SEF, **(e)** CoV of f_{p} and **(f)** CoV of DLF_1. Unfilled and filled symbols in **(c)** and **(e)** represent DLF_1 and TFF, respectively.

responses while the trends of reduction in pacing rate and increase in average DLF_1 and TFF when the pacing rate is close to the natural frequency still contradict the measured data. It is seen that the capability of the model in producing the self-excited force is still maintained.

Averaged CoV of f_p is shown in Figures 6.21e, which ranges from 0.9–4.6 %. This range, though higher than the range in NR simulations, is the same with that measured on the rigid surface, i.e. the target CoV when applying the randomisation method. This result indicates that the simulations on the lively surface do not change the target CoV of pacing rate. The reason is likely because the duration of each step is not long enough for the IPM to respond to the vibration and thus maintain the target CoV during the WR simulations.

Averaged CoV of DLF_1 and TFF is shown in Figure 6.21f. The range of averaged CoV in the WR simulations is similar to the CoV achieved in the NR simulations (Figure 6.16c). This range is lower than that seen in the measured data (3–31 %, Figures 5.54a–c).

In general, the randomisation method produces similar results in comparison to the NR simulations, apart from the improvement in the CoV of pacing rate. This result suggests that even when the variability of the pacing rate is modelled close to the measured data (at least on the rigid surface), the IM still cannot produce vibration estimates with better accuracy. In addition, the trends of discrepancies in pacing rate and DLF_1/TFF are built-in characteristics of the IM and they cannot be changed when the current randomisation method is applied. Also, the target CoV of pacing rate is maintained in the simulations on the WB, suggesting that the application of measured CoV on the rigid surface is not sufficient to replicate the increase trend of variations

of gait parameters when walking on the lively surface.

6.5 Conclusions

In this chapter, a numerical model (IM) was established with the aim to model the dynamic interaction between a pedestrian walking and a lively structure. The pedestrian is represented by a simple bipedal model (IPM) while the structure is modelled as a SDoF system. The novelty feature of the model is that it takes into account the two-way interaction, i.e. effects of the structural vibration on the walking gait and vice versa. The initial conditions of the IPM were first kept constant for every step, then a randomisation method was applied with the aim of providing genuine representations of gait variabilities.

A sensitivity analysis was conducted to test the performance of the IM, and compare it with the traditional model (i.e. MHM) that disregards the interaction. The analysis showed that the IPM tended to decrease the pacing rate when walking on a lively surface. This result led to a shift in the pacing rate. This shift meant that the maximum vibration estimate was achieved when the target pacing rate was slightly higher than the natural frequency of the structure. In addition, the sensitivity analysis showed that the estimates provided by the IM and the MHM were similar when the structure was either heavy, heavily damped or short. In these cases, it is recommended to use the simpler MHM. On the other hand, the discrepancy in results produced by the two models was more pronounced when the structure was either light, lightly damped or long. The IM generally produced lower vibration estimates than the MHM in resonance cases while the two methods provide relatively similar

results in non-resonance cases. This result agrees qualitatively with (rarely available) experimental observations and, therefore, it suggests that the IM has potential to be used to qualitatively explain the attenuation in measured structural response when walking to excite resonance.

Validation of the IM against experimental data was also attempted in this chapter. Input parameters of the IPM were first calibrated to represent walking characteristics of TSs on the rigid surface. Due to the simplification of the model, the IPM could not replicate all measured parameters. Nevertheless, the model was calibrated to match the average attack angle and the average pacing rate measured in the experiments. The calibrated IPM was then used in simulations on the WB. The structural response produced by the IM was compared against the experimental data and that produced by the MHM. It was found that the discrepancy between the two models are more pronounced when the pacing rate was close to the natural frequency. In this range, there was a large discrepancy between vibration estimates and the measured data when making the comparison on a trial-by-trial basis. However, the investigation of the range of simulated responses indicated that the results from the IM were in better agreement with the measured data than those from the MHM. In addition, the maximum estimate produced by the IM was much closer to the measured data, and therefore less conservative than the MHM. This result highlights the better performance of the IM over the MHM. Another positive feature of the IM was the capability to produce the self-excited force that was quantitatively in line with the measured data.

It was also found that there was a significant reduction in the average pacing rate (up to about 5 %) and increase in average DLF_1 and TFF (up to

about 40 %) when the target pacing rate was close to the natural frequency of the structure. These results oppose the trends seen in the measured data. Analysis of the intra-subject variability showed that although there existed variations, in the form of CoV, ranges of variability of gait parameters were lower than those of the measured data.

A randomisation method using normal distribution of initial conditions was applied with the aim to improve the performance of the IM in producing gait variability. The option of maintaining the initial forward speed and randomising the attack angle was chosen for this method. It was difficult to replicate gait variability for all parameters at the same time so it was decided to put the priority on the pacing rate due to its greatest influence on the structural vibration. In the simulations on the rigid surface, it was shown that a customised CoV of attack angle should be implemented so that the achieved CoV of pacing rate could match the measured values. This customised range of CoV of attack angle was lower than that measured in the experiments. These customised values were then used for simulations on the WB. It was found that simulated response, average pacing rate, average DLF_1/TFF and their CoVs, and average SEF were relatively similar to the simulations without randomisation. CoV of pacing rate was the only parameter that was higher when compared to that in simulations with constant initial conditions. This observation indicated that even with better represent of variability of pacing rate, the IM still cannot improve its vibration estimates.

In summary, the IM contains several shortcomings (e.g. incapability to simulate the decrease trend of pacing rate and the reduced DLF_1/TFF at resonant cases). However, the IM possesses advantages over the MHM (e.g.

more accurate vibration estimate and better represent of the GRF in terms of the SEF) and, therefore, represents an improvement in modelling PSDI.

Chapter 7

Conclusions and recommendations for further work

Throughout this thesis, it has been shown that pedestrian-structure dynamic interaction (PSDI) is a complicated phenomenon. To investigate PSDI, experimental and modelling work was conducted. The literature review in Chapter 2 suggested that representing a pedestrian as a bipedal model can replicate some features of the human locomotion and, therefore, has the potential for the application of PSDI modelling. Six bipedal models were reviewed, three of which were quantitatively studied in Chapter 3 and one (the inverted pendulum model) was chosen for further development in this thesis. Experimental programmes were performed on both rigid (Chapter 4) and lively (Chapter 5) surfaces to quantify characteristics of walking locomotion. An interactive model of pedestrian and structure was then developed and evaluated in Chapter 6.

In this chapter, conclusions of main findings are first presented, followed by recommendations for further work.

7.1 Conclusions

Main findings over the course of this thesis are presented in this section. First, the investigation of using motion capture systems (MCS) for measurement of ground reaction force (GRF) is summarised. Conclusions related to the experimental work are then presented. Next, quantitative studies of bipedal models are recapped, followed by the summary of the interactive model of pedestrian and structure.

Motion capture system for measurement of ground reaction force

A MCS was utilised for monitoring of walking locomotion parameters (Chapter 4). Although use of such a system in civil engineering research is growing, there exists no guidance for a marker layout that can provide good accuracy for measurement of GRF. Based on review of MCS applications from multidisciplinary research, four marker models were proposed with detailed description of marker placements to investigate their performances in the reconstruction of GRF. An experimental programme of stamping activity involving ten test subjects (TSs) was conducted. The reconstructed force by the MCS was evaluated against the directly measured force by a force plate, which was assumed to be accurate represent of the GRF. Dynamic load factor of the first harmonic (DLF_1) was used in this comparison. Quantifications of measurement error are provided for all four models, allowing other researchers to make informed choices of using any particular model in future work. It was found that two models (Models C and D, consisting of 19 and 27 markers, re-

spectively) provide the lowest absolute discrepancy between the two methods (less than 15 % for 90% of recorded trials). Model C of 19 markers was chosen for further study.

Characteristics of walking locomotion on rigid and lively surfaces

Ten TSs participated in an experimental programme of walking activity on the rigid surface. TSs were instrumented with markers and asked to walk on a treadmill (located on the ground) over a realistic range of walking speed, i.e. 0.8–2.1 m/s. Three TSs then repeated a number of trials on a lively structure under different pre-induced vibration levels. Gait parameters were measured, including six kinematic parameters (pacing rate, step length, step width, attack angle, end-of-step angle and trunk angle) and one kinetic parameter (DLF_1). Overall, there were 130 trials conducted on the rigid ground and 160 trials performed on the lively structure, consisting of approximately 120,000 recorded steps.

In the experiments on the rigid surface (Chapter 4), average value and coefficient of variation (CoV) of each parameter were calculated for each trial. The mean value of both quantities as well as their standard deviation bands were then calculated across the TS population. The ranges for parameters recorded when walking at normal (i.e. self-assessed) walking speeds were found to be: 1.66–2.22 Hz for pacing rate, 0.56–0.84 m for step length, 60–143 mm for step width, 69.1–77.3° for attack angle, 111.0–125.0° for end-of-step angle, 89.2–102.3° for trunk angle, and 0.11–0.50 for DLF_1. The CoV over the normal speed range was less than 5 % for most parameters. The only ex-

ceptions were DLF_1 (CoV=3.1–12.8 %) and a large variation for step width (CoV=13.4-39.2 %). These results represent the most comprehensive description of locomotion parameters, with particularly detailed characterisation of intra-subject variability, i.e. variations on a step-by-step basis.

The experimental programme was extended to investigate the walking gait on a full-scale lively structure (Chapter 5). Gait parameters were measured in nominally the same way as those collected on the rigid surface. It was assumed that the discrepancy between two sets of data (i.e. collected on rigid and lively surfaces) was attributed to the PSDI phenomenon. This assumption was justified for some parameters (i.e. pacing rate, step length, trunk angle and DLF_1), in which the data collected on the rigid surface was similar to those measured in trials on the lively surface without shaker-induced vibrations (often characterised as low vibration cases).

Step width was the only kinematic parameter that had large discrepancy between measurements on different days. The results also indicated that this parameter was unaffected by the structural vibration. For other kinematic parameters, the discrepancies in average values were within ± 10 % while there were dramatic increases in the CoV. Such an increase in intra-subject variability became more pronounced when the pre-induced vibration was increased. This result indicates that the TSs were influenced by the structural vibration and consequently they generated more variations during walking.

As for the analysis of the walking force, the DLF_1 and self-excited factor (SEF) were two components contributing to the GRF during walking on the lively surface. When the pacing rate f_p is away from the natural frequency f_n of the structure (i.e. $f_p \leq 0.95 f_n$), the discrepancy in the DLF_1 and the total force

factor (TFF, consisting of the first forcing harmonic and the self-excited force) was mostly in the range from $-15\,\%$ to $15\,\%$. These discrepancies seemed to be independent from the pacing rate and vibration level. In many trials when the pacing rate was closer to the structural frequency ($0.95f_\mathrm{n} < f_\mathrm{p} < 1.10f_\mathrm{n}$), there was a significant reduction of the DLF_1 and the TFF when compared with the DLF_1 recorded on the rigid surface at nominally the same walking speed. This result confirms rare experimental observations of the attenuation of structural vibration in resonant experiments on lively as-built structures. In addition, the reduction of the TFF in many trials was higher than the measurement error of $\pm 15\,\%$ associated with the use of the MCS. This result suggests that the MCS could be used to quantify the influence of PSDI on the GRF when the pacing rate was close to the structural frequency.

The SEF, given a specific vibration level, was constant when the pacing rate is away from the vibration frequency ($f_\mathrm{p} < 0.8f_\mathrm{n}$). The SEF tends to decrease when the pedestrian's pacing rate approaches the vibration frequency. It was found that the SEF increases with an increase of vibration level.

Overall, a database of characteristics of walking locomotion on both rigid and lively surfaces was provided. The influence of the PSDI phenomenon on the walking gait was also quantified. A limitation of this experimental study is the small number of TSs, which is dictated by the limited time available for the study. However, it is believed that the collected data provide unique insight into human locomotion on the vibrating surface, which will contribute to develop understanding of PSDI in the vertical direction.

Quantitative study of bipedal models

Three bipedal models were quantitatively studied in Chapter 3. They were the inverted pendulum model (IPM), the rocker foot model (RFM) and the spring mass model (SMM).

It was found that the IPM, the simplest model reviewed, could accurately reproduce neither all phases of walking gait nor the trajectory of the body's centre of mass (BCoM). However, the IPM provides a good approximation of human walking gait in the single stance phase, which represents 80 % of a gait cycle. The parametric scan shows that a wide range of walking parameters seen in experimental data can be reproduced by the IPM. Furthermore, the model produces realistic range of DLF_1, which is the most important force component for modelling human walking on low-frequency structures (i.e. with natural frequency below 2.5 Hz).

The introduction of the rocker foot feature in the RFM contributes to the reduced, i.e. more realistic, excursion of BCoM. Overall, the RFM possesses a number of improvements when compared to the IPM. However, as only a minor upgrade of the IPM, the RFM still has limitations that are inherited from the IPM (e.g. neglects the double support phase and provides unrealistic DLFs for second and higher harmonics). Thus, it is unlikely that utilising the RFM can provide significant improvements in PSDI modelling when compared with the application of the IPM.

Among three models reviewed, the SMM is capable of best replicating the trajectory of BCoM. Moreover, the spring-like legs contribute to the qualitatively accurate replication of the typical M-shaped GRF pattern. Therefore,

DLFs for the higher harmonics are in realistic ranges. The parametric scan shows that the SMM has difficulties in covering range of human walking speed. Also, the scan only determines limited number of stable solutions that have realistic DLF_1 in the low range of pacing rate (1.4–1.7 Hz). These limitations, along with the complexity in selecting initial conditions to result in stable solutions, indicate that the SMM is not the best choice for further investigation of PSDI.

Overall, the quantitative studies of three bipedal models show that the IPM, despite its limitations, has potential to be used in the study of PSDI. In addition, the IPM is the simplest bipedal model reviewed and, therefore, the development for PSDI modelling would be easier than the application of more complicated bipedal models. Thus, the IPM was chosen for further study.

Numerical model of two-way interaction

An interactive model (IM) was established with the aim to model the dynamic interaction between a pedestrian walking and a lively structure (Chapter 6). The pedestrian is represented by the IPM while the structure is modelled as a single degree-of-freedom system. The novelty feature of the model, compared with the model developed by Bocian et al. (2013), is that it takes into account the two-way interaction, i.e. effects of the structural vibration on the walking gait and vice versa. In the application of the IPM, the initial conditions were first kept constant for every step, then a randomisation method was developed with the aim of providing genuine representations of gait variabilities.

A sensitivity analysis was conducted to test the performance of the IM,

and compare it with the traditional model (i.e. MHM). The results showed that the estimates provided by the IM and the MHM were similar when the structure was either heavy, heavily damped or short. On the other hand, the discrepancy in results produced by the two models was more pronounced when the structure was either light, lightly damped or long.

Validation of the IM against experimental data was also attempted in this thesis. Input parameters of the IPM were first calibrated to represent walking characteristics of TSs on the rigid surface and then used in simulations on the Warwick Bridge. The structural response produced by the IM was much closer to the measured data than that produced by the MHM. Another positive feature of the IM was the capability to produce the self-excited force that was quantitatively agreed with the measured data. It was also found that there was a significant reduction in the average pacing rate (up to about 5 %) and increase in average DLF_1 and TFF (up to about 40 %) when the target pacing rate was close to the natural frequency of the structure. These results oppose the trends seen in the measured data. Analysis of the intra-subject variability showed that although there existed variations, in the form of CoV, ranges of variability of gait parameters were lower than those in the measured data.

A randomisation method assuming normal distribution of the attack angle was applied with the aim to improve the performance of the IM in producing gait variability. Customised CoV of attack angle was determined to match the measured CoV of pacing rate while the initial forward speed was kept constant. When this approach was implemented in simulations on the Warwick Bridge, it was found that the simulated response was relatively similar to the simulation without randomisation. This result indicated that even

when simulating the variability of pacing rate, the IM still could not improve the vibration estimates.

In summary, the IM contains several shortcomings (e.g. incapability to simulate the decrease trend of pacing rate and the reduced DLF_1/TFF at resonant cases). However, the IM possesses advantages over the MHM (e.g. more accurate vibration estimate and better represent of the GRF in terms of the SEF) and, therefore, represents an improvement in modelling pedestrians on lively structures.

7.2 Further work

The research in this thesis provides novel insight into information of human locomotion on perceptibly vibrating surfaces and establishes an interactive pedestrian-structure model. To gain better understanding and improve accuracy in the modelling of PSDI, more research in this phenomenon is needed. Some aspects of further work are recommended as follows:

- The experimental programme in this thesis was conducted on two as-built bridges only, both having natural frequencies in the upper range of pacing rate induced by humans (2.18 Hz and 2.44 Hz). Therefore, experimental data performed on other bridges is necessary so that the results can be generalised for practical applications. In addition, experiments with larger number of TSs are strongly recommended to be able to strengthen findings from this thesis.
- The analysis in Chapter 5 reported the existence of self-excited force. However, the effect of this force component on the structural response is not investigated yet. Better understanding of phase angle between the self-excited force and the structural vibration to

improve understanding of the PSDI phenomenon is required. This goal could be achieved by conducting further analysis of the GRF with respect to the structural vibration.

- There were shortcomings when utilising the IPM to model the pedestrian in the interactive model. These shortcomings are partly due to the simplicity of the model that cannot genuinely represent human gait. Thus, the development of more detailed bipedal models (reviewed in Chapter 2) for PSDI modelling should be investigated as a potential means of further improvement of model performance.

- Simulations involving a single pedestrian only were studied in this thesis. The model could be extended to the multi-pedestrian traffic scenario. Also, such a model could be evaluated against experimentally acquired database (both existing and to be developed) of crowd traffic.

References

Alexander, N.A. Theoretical treatment of crowd-structure interaction dynamics. *Proceedings of the Institution of Civil Engineers - Structures and Buildings*, 159(6):329–338, 2006.

AMTI, Force plate manual - Model OR6-7. Advanced Mechanical Technology Inc., Watertown, Massachusetts, USA., 2007.

APS Dynamics, APS 400 ELECTRO-SEIS Instrution manual. Dresden, Germany, 2011.

Archbold, P., Keogh, J., Caprani, C., and Fanning, P. A parametric study of pedestrian vertical foce models for dynamic analysis of footbridges. In *EVACES Conference*, 3–5th October, 2011.

Ayyappa, E. Normal human locomotion, Part 2: motion, ground-reaction force and muscle activity. *Prosthetics and Orthotics*, 9(2):49–57, 1997.

Bachmann, H. *Vibrations in Structures*. Birkhauser, 2nd edition, 1995.

Bauby, C.E. and Kuo, A.D. Active control of lateral balance in human walking. *Journal of Biomechanics*, 33(11):1433–1440, 2000.

Bell, A.L., Brand, R.A., and Pedersen, D.R. Prediction of hip joint centre location from external landmarks. *Human Movement Science*, 8(1):3–16, 1989.

Belli, A., Bui, P., Berger, A., Geyssant, A., and Lacour, J.R. A treadmill ergometer for three-dimensional ground reaction forces measurement during walking. *Journal of Biomechanics*, 34(1):105–112, 2001.

Blicknan, R. The spring-mass model for running and hopping. *Journal of Biomechanics*, 22 (11–12):1217–1227, 1989.

Bobbert, M.M., Schamhardt, H.C., and Nigg, B.M. Calculation of vertical ground reaction force estimates during running from positional data. *Journal of Biomechanics*, 24(12): 1095–1105, 1991.

Bocian, M., Macdonald, J.H.G., and Burn, J.F. Biomechanically inspired modelling of pedestrian-induced forces on laterally oscillating structures. *Journal of Sound and Vibration*, 331(16):3914–3929, 2012.

Bocian, M., Macdonald, J.H.G., and Burn, J.F. Biomechanically-inspired modelling of pedestrian-induced vertical self-excited forces. *Journal of Bridge Engineering*, 18(12): 1336–1346, 2013.

Brownjohn, J.M.W. Energy dissipation from vibrating floor slabs due to human-structure interaction. *Shock and Vibration*, 8(6):315–323, 2001.

Brownjohn, J.M.W. and Pavic, A. Experimental methods for estimating modal mass in footbridges using human-induced dynamic excitation. *Engineering Structures*, 29(11): 2833–2843, 2007.

Brownjohn, J.M.W., Fok, P., Roche, M., and Omenzetter, P. Long span steel pedestrian bridge at Singapore Changi Airport - Part 2: Crowd loading tests and vibration mitigation measures. *Structural Engineer*, 82(16):28–34, 2004a.

Brownjohn, J.M.W., Pavic, A., and Omenzetter, P. A spectral density approach for modelling continuous vertical forces on pedestrian structures due to walking. *Canadian Journal of Civil Engineering*, 31(1):65–77, 2004b.

BSI, UK National Annex to Eurocode 1: Actions on structures, Part 2: Traffic loads on bridges. NA to BS EN 1991-2:2003, British Standards Institute, 2008.

Cavagna, G.A., Thys, H., and Zamboni, A. The sources of external work in level walking and running. *The Journal of Physiology*, 262(3):639–657, 1976.

Chandler, R.F., Clauser, C.E., McConville, J.T., Reynolds, H.M., and Young, J.W. Investigation of inertial properties of the human body. Technical report, Air Force Aerospace Medical Research Laboratory, Wright-Petterson Air Force Base, Ohio, USA, 1975.

Clauser, C.E., McConville, J.T., and Young, J.W. Weight, volume and centre of mass of segments of the human body. Technical report, 69-70, Aerospace Medical Research Laboratory, Wright-Petterson Air Force Base, Ohio, USA, 1969.

Comer, A., Blakeborough, A., and Williams, M.S. Grandstand simulator for dynamic human-structure interaction experiments. *Experimental Mechanics*, 50(6):825–834, 2010.

Cordero, A.F., Koopman, H.J.F.M., and van der Helm, F.C.T. Use of pressure insoles to calculate the complete ground reaction forces. *Journal of Biomechanics*, 37(9):1427–1432, 2004.

Dallard, P., Fitzpatrick, T., Flint, A., Low, A., Smith, R.R., Willford, M., and Roche, M. The london millennium footbridge: pedestrian-induced lateral vibration. *Journal of Bridge Engineering*, 6(6):412–417, 2001.

Data Physics, SignalCalc Dynamic Signal Analyser user manual. San Jose, California, USA, 2011.

de Leva, P. Adjustments to Zatsiorsky-Seluyanov's segment inertia parameters. *Journals of Biomechanics*, 29(9):1223–1230, 1996.

Dempster, W.T. Space requirements of the seated operator: geometrical, kinematic, and mechanical aspects of the body with special reference to the limbs. Technical report, Project no. 7214, Aerospace Medical Research Laboratory, Wright-Petterson Air Force Base, Ohio, USA, 1955.

Donelan, J.M., Kram, R., and Kuo, A.D. Mechanical and metabolic determinants of the preferred step width in human walking. *Proceedings of the Royal Society of London. Series B: Biological Sciences*, 268(1480):1985–1992, 2001.

Drillis, R., Contini, R., and Bluestein, M. Body segment parameters. *Artificial Limbs*, 8(1): 44–66, 1964.

Dytran Instrument Inc., Operating guide, dodels 3166B, 3166B1 and 3166B2 LIVM internally ground isolated accelerometers for machinery monitoring. Chatsworth, California, USA, 2003.

Eames, M.H.A., Cosgrove, A., and Baker, R. Comparing methods of estimating the total body centre of mass in three-dimensions in normal and pathological gaits. *Human Movement Science*, 18(5):637–646, 1999.

Ellis, B.R. and Ji, T. Human-structure interaction in vertical vibrations. *Proceedings of the Institution of Civil Engineers - Structures and Buildings*, 122(1):1–9, 1997.

Fuel Fitness, Treadmill user manual - model F63. Fuel Fitness Co., Ltd., Stoke-On-Trent, UK, 2013.

Gard, S.A. and Childress, D.S. The effect of pelvic list on the vertical displacement of the trunk during normal walking. *Gait & Posture*, 5(3):233–238, 1997.

Gard, S.A. and Childress, D.S. The influence of stance-phase knee flexion on the vertical displacement of the trunk during normal walking. *Archives of Physical Medicine & Rehabilitation*, 80(1):26–32, 1999.

Gard, S.A. and Childress, D.S. What determines the vertical displacement of the body during normal walking? *Journal of Prosthetics & Orthotics*, 13(3):64–67, 2001.

Gard, S.A., Miff, S.C., and Kuo, A.D. Comparison of kinematic and kinetic methods for computing the vertical motion of the body center of mass during walking. *Human Movement Science*, 22(6):597–610, 2004.

Geyer, H. *Simple Models of Legged Locomotion based on Compliant Limb Behavior*. PhD thesis, Friedrich-Schiller-Universität Jena, 2005.

Giakas, G. and Baltzopoulos, V. Time and frequency domain analysis of ground reaction forces during walking: an investigation of variability and symmetry. *Gait & Posture*, 5 (3):189–197, 1997.

Goldstein, H. *Classical Mechanics*. Addison-Wesley, 2nd edition, 1980.

Hansen, A., Gard, S., and Childress, D. The determination of foot/ankle roll-over shape: clinical and research applications. In *Pediatric Gait, 2000. A new Millennium in Clinical Care and Motion Analysis Technology*, pages 159–165, 2000.

Hasan, S.S., Robin, D.W., Szurkus, D.C., Ashmead, D.H., Peterson, S.W., and Shiavi, R.G. Simultaneous measurement of body center of pressure and center of gravity during upright stance. Part I: Methods. *Gait & Posture*, 4(1):1–10, 1996.

Hof, A.L., Gazendam, M.G.J., and Sinke, W.E. The condition for dynamic stability. *Journal of Biomechanics*, 38(1):1–8, 2005.

Honeywell Sensing & Control, Q-Flex QA-750 Accelerometer - Data sheet. Columbus, Ohio, USA, 2005.

Ingólfsson, E.T., Georgakis, C.T., Ricciardelli, F., and Jönsson, J. Experimental identification of pedestrian-induced lateral forces on footbridges. *Journal of Sound and Vibration*, 330(6):1265–1284, 2011.

Inman, V.T., Ralston, H., and Todd, F. *Human walking*. Edwin Mellen Press Ltd., 1989.

ISO, Bases for design of structures - Serviceability of buildings and walkways against vibration. ISO 10137:2007, International Organization for Standardization, 2007.

Kadaba, M.P., Ramakrishnan, H.K., and Wootten, M.E. Measurement of lower extremity kinematics during level walking. *Journal of Orthopaedic Research*, 8(3):383–392, 1990.

Kerr, S.C. *Human Induced Loading on Staircases*. PhD thesis, Mechanical Enginering Department, University College London, UK, 1998.

Kim, S. and Park, S. Leg stiffness increases with speed to modulate gait frequency and propulsion energy. *Journal of Biomechanics*, 44(7):1253–1258, 2011.

Kram, R., Griffin, T.M., Donelan, J.M., and Chang, Y.H. Force treadmill for measuring vertical and horizontal ground reaction forces. *Journal of Applied Physiology*, 85(2):764–769, 1998.

Lafond, D., Duarte, M., and Prince, F. Comparison of three methods to estimate the center of mass during balance assessment. *Journal of Biomechanics*, 37(9):1421–1426, 2004.

Leardini, A., Chiari, L., Croce, U.D., and Cappozzo, A. Human movement analysis using stereophotogrammetry: Part 3. Soft tissue artifact assessment and compensation. *Gait & Posture*, 21(2):212–225, 2005.

Lee, C.R. and Farley, C.T. Determinants of the center of mass trajectory in human walking and running. *The Journal of Experimental Biology*, 201(21):2935–2944, 1998.

Leonard, D.R. Human tolerance levels for bridge vibrations, TRRL Report No. 34. Technical report, Road Research Laboratory, 1966.

Macdonald, J.H.G. Lateral excitation of bridges by balancing pedestrians. *Proceedings of the royal society A: Mathematical, Physical and Engineering Sciences*, 2008.

Maia, N.M.M., Silva, J.N.M., He, J., Lieven, N.A.J., Lin, R.M., Skingle, G.W., To, W.M., and Urgeira, A.P.V. *Theoretical and experimental modal analysis*. Research Studies Press Ltd., 1997.

Massey, F.J.Jr. The Kolmogorov-Smirnov test for goodness of fit. *Journal of the American Statistical Association*, 46(253):68–78, 1951.

Mathworks Inc., MATLAB version 7.10.0.499 (R2010a). Natick, Massachusetts, USA, 2010.

Matsas, A., Taylor, N., and McBurney, H. Knee joint kinematics from familiarised treadmill walking can be generalised to overground walking in young unimpaired subjects. *Gait & Posture*, 11(1):46–53, 2000.

McGeer, T. Passive dynamic walking. *The International Journal of Robotics Research*, 9 (2):62–82, 1990.

Morawski, J.M. and Wojcieszak, I. Miniwalker - a resonant model of human locomotion. In *Proceedings of the 6th Int. Congress of Biomechanics*, pages 445–451, 1977.

Morbiato, T., Vitaliani, R., and Saetta, A. Numerical analysis of a synchronization phenomenon: Pedestrian-structure interaction. *Computers & Structures*, 89(17–18):1649–1663, 2011.

Murray, M.P., Spurr, G.B., Sepic, S.B., Gardner, G.M., and Mollinger, L.A. Treadmill vs. floor walking: kinematics, electromyogram, and heart rate. *Journal of Applied Physiology*, 59(1):87–91, 1985.

National Instruments, User guide NI USB-9162 portable bus-powered USB carrier for NI C Series I/O modules. National Instrments Corporation Ltd., Newbury, Berkshire, UK, 2013.

NHS, Health survey for England, United Kingdom. *National Health Service*, 2010.

Oppenheim, A.V., Willsky, A.S., and Nawab, S.H. *Signals & systems*. Prentice Hall International, 2nd edition, 1997.

Owings, T.M. and Grabiner, M.D. Measuring step kinematic variability on an instrumented treadmill: how many steps are enough? *Journal of Biomechanics*, 36(8):1215–1218, 2003.

Owings, T.M. and Grabiner, M.D. Variability of step kinematics in young and older adults. *Gait & Posture*, 20(1):26–29, 2004.

Oxford Metrics Group, Vicon MX Hardware: System Reference. Oxford Metrics Group, 2007.

Oxford Metrics Group, Vicon Nexus Revesion 1.4.1. Oxford Metrics Group, 2008.

Pedersen, L. and Frier, C. Sensitivity of footbridge vibrations to stochastic walking parameters. *Journal of Sound and Vibration*, 329(13):2683–2701, 2010.

Perry, J. and Burnfield, J.M. *Gait analysis: Normal and Pathological Function*. SLACK Incorporated, 2nd edition, 2010.

Pheasant, S.T. Anthropometric estimates for british civilian adults. *Ergonomics*, 25(11): 993–1001, 1982.

Pimentel, R.L., Pavic, A., and Waldron, P. Evaluation of design requirements for footbridges excited by vertical forces from walking. *Canadian Journal of Civil Engineering*, 28(5): 769–777, 2001.

Qin, J.W., Law, S.S., Yang, Q.S., and Yang, N. Pedestrian-bridge dynamic interaction, including human participation. *Journal of Sound and Vibration*, 332(4):1107–1124, 2013.

Racic, V. and Brownjohn, J.M.W. Stochastic model of near-periodic vertical loads due to humans walking. *Advanced Engineering Informatics*, 25(2):259–275, 2011.

Racic, V., Pavic, A., and Brownjohn, J.M.W. Experimental identification and analytical modelling of human walking forces: Literature review. *Journal of Sound and Vibration*, 326(1–2):1–49, 2009.

Racic, V., Brownjohn, J.M.W., and Pavic, A. Reproduction and application of pedestrian forces from visual marker data. In *IUTAM 2010: International Union of Theoretical and Applied Mechanics symposium on Human Movement Analysis and Simulation*, Leuven, Belgium, 2010a.

Racic, V., Brownjohn, J.M.W., and Pavic, A. Reproduction and application of human bouncing and jumping forces from visual marker data. *Journal of Sound and Vibration*, 329(16):3397–3416, 2010b.

Racic, V., Pavic, A., and Brownjohn, J.M.W. Modern facilities for experimental measurement of dynamic loads induced by humans: A literature review. *Shock and Vibration*, 20 (1):53–67, 2013.

Rainer, J.H., Pernica, G., and Allen, D.E. Dynamic loading and response of footbridges. *Canadian Journal of Civil Engineering*, 15(1):66–71, 1988.

Sachse, R., Pavic, A., and Reynolds, P. Human-structure dynamic interaction in civil engineering dynamics: A literature review. *Shock and Vibration Digest*, 35(1):3–18, 2003.

Saunders, J.B.D.M., Inman, V.T., and Eberhart, H.D. The major determinants in normal and pathological gait. *The Journal of Bone & Joint Surgery*, 53(3):543–558, 1953.

SETRA, Footbridges, assessment of vibrational behaviour of footbridges under pedestrian loading, technical guide. Service d'Etudes Techniques des Routes et Autoroutes, Paris, 2006.

Shin, K. and Hammond, J.K. *Fundamentals of signal processing for sound and vibration engineers*. John Wiley & Sons, 2008.

Smith, J.W. *The Vibration of Highway Bridges and the Effects on Human Comfort*. PhD thesis, University of Bristol, UK, 1969.

Taylor, R. Interpretation of the correlation coefficient: A basic review. *Journal of Diagnostic Medical Sonography*, 6(1):35–39, 1990.

Thirunarayan, M.A., Kerrigan, D.C., Rabuffetti, M., Croce, U.D., and Saini, M. Comparison of three methods for estimating vertical displacement of center of mass during level walking in patients. *Gait & Posture*, 4(4):306–314, 1996.

Vaughan, C.L., Davis, B.L., and O'Connor, J.C. *Dynamics of Human Gait*. Kiboho Publishers, 2nd edition, 1999.

Whittington, B.R. and Thelen, D.G. A simple mass-spring model with roller feet can induce the ground reactions observed in human walking. *Journal of Biomechanical Engineering*, 131(1), 2009.

Whittle, M.W. Three-dimensional motion of the center of gravity of the body during walking. *Human Movement Science*, 16(2–3):347–355, 1997.

Whittle, M.W. *Gait analysis: an introduction*. Butterworth-Heinemann, 3rd edition, 2002.

Willford, M. Dynamic actions and reactions of pedestrians. In *Proceedings of the International Conference on the Design and Dynamic Behaviour of Footbridges*, Paris, France, 2002.

Winter, D.A. Human balance and posture control during standing and walking. *Gait & Posture*, 3(4):193–214, 1995.

Winter, D.A. *Biomechanics and motor control of human movement*. John Wiley & Sons, Inc., 4th edition, 2009.

Yao, S., Wright, J.R., Pavic, A., and Reynolds, P. Experimental study of human-induced dynamic forces due to bouncing on a perceptibly moving structure. *Canadian Journal of Civil Engineering*, 31(6):1109–1118, 2004.

Yao, S., Wright, J.R., Pavic, A., and Reynolds, P. Experimental study of human-induced dynamic forces due to jumping on a perceptibly moving structure. *Journal of Sound and Vibration*, 296(1-2):150–165, 2006.

Zatsiorsky, V.M., Seluyanov, V.N., and Chugunova, L.G. Methods of determining mass-inertial characteristics of human body segments. In *Contemporary Problems of Biomechanics*, Massachusetts, USA, 1990.

Zeni, J.A.Jr., Richards, J.G., and Higginson, J.S. Two simple methods for determining gait events during treadmill and overground walking using kinematic data. *Gait & Posture*, 27(4):710–714, 2008.

Živanović, S. Benchmark footbridge for vibration serviceability assessment under the vertical component of pedestrian load. *Journal of Structural Engineering*, 138(10):1193–1202, 2012.

Živanović, S., Pavic, A., and Reynolds, P. Human-structure dynamic interaction in footbridges. *Proceedings of the Institution of Civil Engineers - Bridge Engineering*, 158(4): 165–177, 2005a.

Živanović, S., Pavic, A., and Reynolds, P. Vibration serviceability of footbridges under human-induced excitation: a literature review. *Journal of Sound and Vibration*, 279 (1–2):1–74, 2005b.

Živanović, S., Pavic, A., and Reynolds, P. Probability-based prediction of multi-mode vibration response to walking excitation. *Engineering Structures*, 29(6):942–954, 2007.

Živanović, S., Díaz, I.M., and Pavic, A. Influence of walking and standing crowds on structural dynamic properties. In *Proceedings of the IMAC-XXVII: Conference & Exposition on Structural Dynamics*. Society for Experimental Mechanics, 2009.

Živanović, S., Johnson, R.P., Dang, H.V., and Dobrić, J. Design and construction of a very lively bridge. In *Proceedings of the IMAC-XXXI: Conference & Exposition on Structural Dynamics*. Society for Experimental Mechanics, 2013.

Appendices

Appendix A

Bipedal models on rigid surface

A.1 Inverted pendulum model

A.1.1 Equation of motion

The simulation starts when one leg hits the ground at an attack angle θ_0 (Figure A.1). The coordinates of pedestrian mass m_p are presented in polar coordinates as:

$$x = l\cos\theta_0 - l\cos\theta + x_0 \tag{A.1}$$

$$y = l\sin\theta \tag{A.2}$$

where l is the pendulum length and x_0 is the longitudinal distance the pedestrian travelled from the beginning of the simulation to the end of the last walking step (Figure A.1).

The velocity of m_p in x- and y-direction are:

$$\dot{x} = l\dot{\theta}\sin\theta \tag{A.3}$$

$$\dot{y} = l\dot{\theta}\cos\theta \tag{A.4}$$

where the dot above variables represents the first derivative. All derivatives in

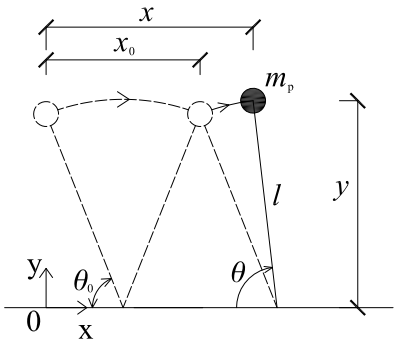

Figure A.1: Inverted pendulum model.

this appendix are calculated with respect to time, unless stated otherwise.

Kinetic energy (T) and potential energy (V) after using relationship in Equations A.3 and A.4 of the system are:

$$T = \frac{1}{2} m_{\mathrm{p}} (\dot{x}^2 + \dot{y}^2) = \frac{1}{2} m_{\mathrm{p}} l^2 \dot{\theta}^2 \tag{A.5}$$

$$V = -m_{\mathrm{p}} g y = -m_{\mathrm{p}} g l \sin\theta \tag{A.6}$$

where g is the gravity acceleration. Using the convention of upward direction as positive, $g = -9.81$ m/s^2. The equation of motion of the model is derived using the Lagrange equation (Goldstein, 1980). The Lagrangian $\mathcal{L}$ is calculated as:

$$\mathcal{L} = T - V = \frac{1}{2} m_{\mathrm{p}} l^2 \dot{\theta}^2 + m_{\mathrm{p}} g l \sin\theta \tag{A.7}$$

Derivatives of the Lagrangian with respect to $\dot{\theta}$ and θ are:

$$\frac{\mathrm{d}}{\mathrm{d}t}\left(\frac{\partial \mathcal{L}}{\partial \dot{\theta}}\right) = m_{\mathrm{p}} l^2 \ddot{\theta} \tag{A.8}$$

$$\frac{\partial \mathcal{L}}{\partial \theta} = m_{\mathrm{p}} g l \cos\theta \tag{A.9}$$

The Lagrange equation applied for the IPM is:

$$\frac{\mathrm{d}}{\mathrm{d}t}\left(\frac{\partial \mathcal{L}}{\partial \dot{\theta}}\right) - \frac{\partial \mathcal{L}}{\partial \theta} = 0 \tag{A.10}$$

The equation of motion of the IPM is:

$$\ddot{\theta} = \frac{\cos\theta}{l} g \tag{A.11}$$

where $\ddot{\theta}$ is the second derivative of θ.

The ground reaction force (GRF) can be calculated from Figure A.2 as:

$$F_{\mathrm{p}} = -m_{\mathrm{p}}(g - \ddot{y}) = -m_{\mathrm{p}}(g\sin^2\theta + l\dot{\theta}^2\sin\theta) \tag{A.12}$$

where $\ddot{y}$ is the second derivative of y.

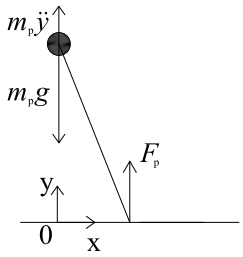

Figure A.2: Forces acting on body centre of mass and ground reaction force.

A.1.2 Amplitude of impulse at step transition

At step transition, m_{p} has the tendency of moving downwards and must be redirected upwards to initiate the next step. Free body diagram of m_{p} at the step transition is displayed in Figure A.3.

Amplitude of the impulse needed to redirect the mass m_{p} is:

$$\begin{aligned} I &= -m_{\mathrm{p}}\dot{y}_{\mathrm{e},n} + m_{\mathrm{p}}\dot{y}_{0,n+1} \\ &= -m_{\mathrm{p}}\dot{y}_{\mathrm{e},n} + m_{\mathrm{p}}\dot{x}_{0,n+1}\cot\theta_0 \end{aligned} \tag{A.13}$$

where subscripts "n" and "$n+1$" represent n^{th} and $(n+1)^{\mathrm{th}}$ steps, respectively. Subscripts "e" and "0" indicate the end and beginning of a step, respectively.

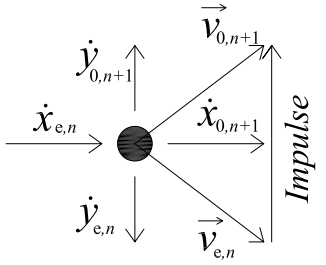

Figure A.3: Free body diagram of m_p at transition from n^{th} step to $(\mathrm{n+1})^{\mathrm{th}}$ step. $\dot{x}$, $\dot{y}$ and $\vec{v}$ are the horizontal, vertical and total velocity, respectively.

A.2 Rocker foot model

The simulation of the rocker foot model (RFM) starts when one leg hits the ground at an attack angle θ_0 (Figure A.4). The coordinates of pedestrian mass m_p are presented in polar coordinates as:

$$x = l\cos\theta_0 - l\cos\theta + r(\theta - \theta_0) + x_0 \tag{A.14}$$

$$y = l\sin\theta + r \tag{A.15}$$

where r is the radius of the rocker.

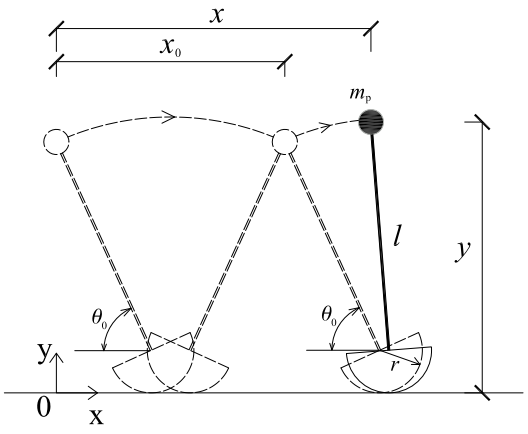

Figure A.4: Rocker foot model.

The velocity of m_p in x- and y-direction are:

$$\dot{x} = l\dot{\theta}\sin\theta + r\dot{\theta} \tag{A.16}$$

$$\dot{y} = l\dot{\theta}\cos\theta \tag{A.17}$$

Kinetic energy and potential energy of the system are calculated as:

$$T = \frac{1}{2}m_\mathrm{p}(l^2\dot{\theta}^2 + r^2\dot{\theta}^2 + 2rl\dot{\theta}^2\sin\theta) \tag{A.18}$$

$$V = -m_\mathrm{p}g(l\sin\theta + r) \tag{A.19}$$

Derivatives of the Lagrangian with respect to $\dot{\theta}$ and θ are:

$$\frac{\mathrm{d}}{\mathrm{d}t}\left(\frac{\partial\mathcal{L}}{\partial\dot{\theta}}\right) = m_\mathrm{p}(l^2\ddot{\theta} + r^2\ddot{\theta} + 2rl\ddot{\theta}\sin(\theta) + 2rl\dot{\theta}^2\cos(\theta)) \tag{A.20}$$

$$\frac{\partial\mathcal{L}}{\partial\theta} = m_\mathrm{p}l\cos\theta(g + r\dot{\theta}^2) \tag{A.21}$$

The equation of motion of the RFM can be derived as:

$$\ddot{\theta} = \frac{l\cos\theta(g - r\dot{\theta}^2)}{r^2 + l^2 + 2rl\sin(\theta)} \tag{A.22}$$

The GRF produced by the RFM is calculated as:

$$F_\mathrm{p} = -m_\mathrm{p}\left[g + l\dot{\theta}^2\sin\theta - \frac{l^2\cos^2\theta(g + 2r\dot{\theta}^2)}{r^2 + l^2 + 2rl\sin\theta}\right] \tag{A.23}$$

The amplitude of impulse at step transitions is calculated in the same way as in Section A.1.2.

A.3 Spring mass model

It is considered that in a walking step of the spring mass model (SMM), m_p travels from one apex, i.e. highest elevation, to another. As a result, each walking step contains two single support phases and one double support phase, shown in Figure A.5. This section first presents equations of motion for the

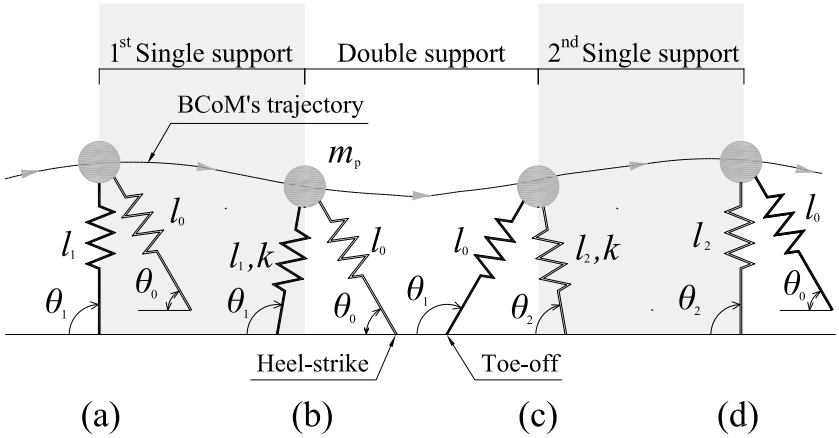

Figure A.5: Spring mass model (after Geyer, 2005). **(a)** Start of simulation, **(b)** heel-strike event of the leading leg, **(c)** toe-off event of the trailing leg and **(d)** end of a walking step.

single support phase, followed by equations for the double support phase.

A.3.1 Single support phase

The single support phase of the SMM is shown in Figure A.6. The coordinates of pedestrian mass m_p are presented in polar coordinates as:

$$x = -l_1 \cos\theta_1 + x_0 \tag{A.24}$$

$$y = l_1 \sin\theta_1 \tag{A.25}$$

where subscript "1" represents the first leg, i.e. the supporting leg in the stance phase.

Kinetic energy and potential energy of the system are calculated as:

$$T = \frac{1}{2} m_\mathrm{p} (\dot{l}_1^2 + l_1^2 \dot{\theta}_1^2) \tag{A.26}$$

$$V = -m_\mathrm{p} g l_1 \sin\theta_1 + \frac{1}{2} k (l_0 - l_1)^2 \tag{A.27}$$

where k is the stiffness of the spring representing the leg of the SMM and l_0 is the uncompressed leg length.

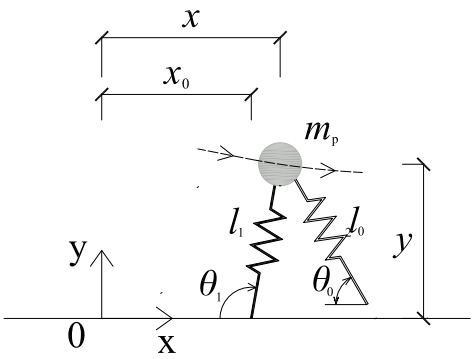

Figure A.6: Single support phase of spring mass model.

Derivatives of the Lagrangian with respect to $\dot{\theta_1}$, θ_1, $\dot{l_1}$, and l_1 are:

$$\frac{\mathrm{d}}{\mathrm{d}t}\left(\frac{\partial \mathcal{L}}{\partial \dot{\theta_1}}\right) = m_\mathrm{p}(2l_1\dot{l}_1\dot{\theta}_1 + l_1^2\ddot{\theta}_1) \tag{A.28}$$

$$\frac{\partial \mathcal{L}}{\partial \theta_1} = m_\mathrm{p} g l_1 \cos\theta_1 \tag{A.29}$$

$$\frac{\mathrm{d}}{\mathrm{d}t}\left(\frac{\partial \mathcal{L}}{\partial \dot{l}_1}\right) = m_\mathrm{p}\ddot{l}_1 \tag{A.30}$$

$$\frac{\partial \mathcal{L}}{\partial l_1} = m_\mathrm{p}\left[l_1\dot{\theta}_1^2 + g\sin\theta_1 + \frac{k}{m_\mathrm{p}}(l_0 - l_1)\right] \tag{A.31}$$

The equations of motion of the SMM for the single support phase can be derived as:

$$\ddot{\theta}_1 = \frac{1}{l_1}(g\cos\theta_1 - 2\dot{l}\dot{\theta}_1) \tag{A.32}$$

$$\ddot{l}_1 = l_1\dot{\theta}_1^2 + g\sin\theta_1 + \frac{k}{m_\mathrm{p}}(l_0 - l_1) \tag{A.33}$$

The GRF produced by the first leg is shown in Figure A.7 and calculated as:

$$F_{\mathrm{p},1} = k(l_0 - l_1)\cos\left(\theta_1 - \frac{\pi}{2}\right) \tag{A.34}$$

In the second single support phase (starting from Figure A.5c and ending at Figure A.5d), the equations of motion are similar to Equations A.32 and A.33. The only difference is the substitution of subscript from "1" to "2".

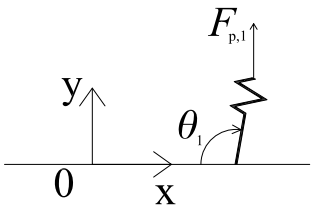

Figure A.7: Ground reaction force in single support phase of spring mass model.

A.3.2 Double support phase

The double support phase of the SMM is shown in Figure A.8. The coordinates of pedestrian mass m_p are the same as in Equations A.24 and A.25.

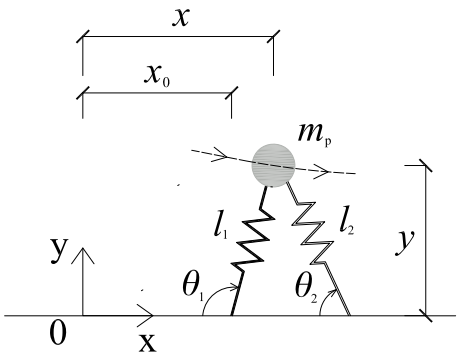

Figure A.8: Double support phase of spring mass model.

Kinetic energy in the double support phase is the same as in Equation A.26 while the potential energy contains the spring energy of the second leg:

$$V = -m_\mathrm{p} g l_1 \sin\theta_1 + \frac{1}{2}k(l_0 - l_1)^2 + \frac{1}{2}k(l_0 - l_2)^2 \tag{A.35}$$

Because of geometry constraints, θ_2 and l_2 are related to θ_1 and l_1 as:

$$\dot{\theta}_2 = \frac{1}{l_2}\left[\dot{l}_1 \sin(\theta_1 - \theta_2) + l_1\dot{\theta}_1 \cos(\theta_1 - \theta_2)\right] \tag{A.36}$$

$$\dot{l}_2 = \dot{l}_1 \cos(\theta_1 - \theta_2) - l_1\dot{\theta}_1 \sin(\theta_1 - \theta_2) \tag{A.37}$$

Then partial derivatives of l_2 with respect to θ_1 and l_1 are:

$$\frac{\partial l_2}{\partial \theta_1} = -l_1 \sin(\theta_1 - \theta_2) \tag{A.38}$$

$$\frac{\partial l_2}{\partial l_1} = \cos(\theta_1 - \theta_2) \tag{A.39}$$

Derivatives of the Lagrangian with respect to $\dot{\theta_1}$, θ_1, $\dot{l_1}$, and l_1 are the same as in Equations A.28–A.31.

The Lagrangian equations of motion applied for the SMM are:

$$\frac{\mathrm{d}}{\mathrm{d}t}\left(\frac{\partial \mathcal{L}}{\partial \dot{\theta}_1}\right) = \frac{\partial \mathcal{L}}{\partial \theta_1} + \frac{\partial \mathcal{L}}{\partial l_2}\left(\frac{\partial l_2}{\partial \theta_1}\right) \tag{A.40}$$

$$\frac{\mathrm{d}}{\mathrm{d}t}\left(\frac{\partial \mathcal{L}}{\partial \dot{l}_1}\right) = \frac{\partial \mathcal{L}}{\partial l_1} + \frac{\partial \mathcal{L}}{\partial l_2}\left(\frac{\partial l_2}{\partial l_1}\right) \tag{A.41}$$

The equations of motion of the first leg are:

$$\ddot{\theta}_1 = \frac{1}{l_1}\left[g\cos\theta_1 - 2\dot{l}\dot{\theta}_1 - \frac{k}{m}(l_0 - l_2)\cos(\theta_1 - \theta_2)\right] \tag{A.42}$$

$$\ddot{l}_1 = l_1\dot{\theta}_1^2 + g\sin\theta_1 + \frac{k}{m_\mathrm{p}}(l_0 - l_1) + \frac{k}{m}(l_0 - l_2)\cos(\theta_1 - \theta_2) \tag{A.43}$$

Equations A.36, A.37, A.42 and A.43 form the system of equations for the SMM in the double support phase.

GRF generated by each leg is calculated as in Equation A.34.

Appendix B

Consent and questionnaire forms

University of Warwick

School of Engineering
Civil Research Group

Project title: **Pedestrian interaction with lively low-frequency structures**

Investigators: Dr Stana Zivanovic and Mr Hiep Vu Dang

CONSENT & APPLICATION FORM

1. I, the undersigned, voluntarily agree to take part in the study above.
2. I have read and understood the *Project Information Sheet* dated 21/05/2012. I have been given a full explanation by the investigators of the nature, purpose, location, and likely duration of the study, and of what I will be expected to do. I have been given the opportunity to ask questions on all aspects of the study and have understood the advice and information provided. I am aware that I can take rest at any time during the study.
3. I have completed the *Physical Activity Readiness Questionnaire* and have been able to answer "NO" to all questions.
4. I agree to comply with any instructions given to me during the study and to co-operate fully with the investigators.
5. I understand that all personal data relating to volunteers are held and processed in the strictest confidence, and in accordance with the Data Protection Act (1998). I agree that I will not seek to restrict the use of the result of the study on the understanding that my anonymity is preserved.
6. I agree that photographs and video records in which I feature can be taken during experiments. I am aware that they will be used for the quality assurance and data analysis purposes only.
7. I do/do not (*delete as appropriate*) give permission for video records and photographs in which I feature to be used in seminars, publications, for conference presentations and in other forms of publicity of this research.
8. I understand that I am free to withdraw from the study at any time without needing to justify my decision. I agree that in case of withdrawal the data that have already been collected can be used in the research.
9. I understand that the University of Warwick holds insurance that cover claims for injury or deterioration in health, which arise directly from participation in clinical trials, but that it applies only in those situations where the University can be shown to be legally liable.
10. I confirm that I have read and understood the information above and freely consent to participating in this study. I have been given adequate time to consider my participation and agree to comply with the instructions and restrictions of the study.

Details to be completed by applicant:

Please **PRINT** clearly

Full name:			
Email address:		Contact number:	

Signature: ..... Date: .....

For admin use only:	TS#

University of Warwick

School of Engineering
Civil Research Group

Project title: **Pedestrian interaction with lively low-frequency structures**

Investigators: Dr Stana Zivanovic and Mr Hiep Vu Dang

PHYSICAL ACTIVITY READINESS QUESTIONNAIRE

We are asking you to complete this questionnaire to check whether you are suited for the kind of physical activity you will be asked to engage in. The activity will not be physically strenuous and the levels of fitness we are looking for are normal levels. However, before you participate in any experiment we would like to identify a small number of people for whom even this level of activity might be inappropriate. To enable us to do this, we need you to answer the questions below.

Please read the following questions carefully and answer them to the best of your knowledge by ticking the appropriate boxes.

	YES	NO
1. Has your doctor ever said you have a heart condition and recommended only medically supervised physical activity?	☐	☐
2. Do you have chest pain brought on by physical activity?	☐	☐
3. Have you developed chest pain within the last month?	☐	☐
4. Do you lose consciousness or fall over as a result of dizziness?	☐	☐
5. Do you have a difficulty in balancing your body while walking?	☐	☐
6. Has a doctor ever recommended medication for your blood pressure or a heart condition?	☐	☐
7. Are you currently on any medication that could affect your health when exposed to physical activity?	☐	☐
8. Are you aware, through your own experience or a doctor's advice, of any reason why you should not exercise without medical supervision?	☐	☐
9. Have you consumed excessive amount of alcohol or any other substance in the last 24h that could compromise your balance and alertness?	☐	☐
10. Have you recently participated in a similar research study involving exposure to vibration and physical activity?	☐	☐

This form will be kept securely by the investigators who will respect its confidentiality. The form will be shred no later than six months after completing the experiments.

I have completed this questionnaire truthfully to the best of my knowledge.

Signature: ..... Date: .....

For admin use only:	TS#

Appendix C

Risk assessments

C.1 Moving supports of Warwick Bridge

C.1.1 Procedure

The Warwick Bridge in Strong Floor lab, University of Warwick, is 20 metre long. Dynamic properties of the bridge can be altered through moving position of support(s), i.e. creating different bridge's span. Prior to the operation of changing span length, a new support with the same configuration with the existing two supports is built at a designated position. The procedure for moving support is described as follows:

- Gradually lift the bridge at one end using hydraulic jacks.
- Check that the bridge is not in contact with the plywood packing sheets.
- Lift the bridge using the jacks. The bridge is lifting for 20 mm, then elevations at jack locations and other critical points are checked. This lifting process repeats three times until the clear gap between the bridge and horizontal beams of the main support is at least 100 mm. At this stage, the bridge will be sitting on the supports at one end and the jacks on the other.

- Pack plywood sheets on the new support to minimise the gap between the new support and the bottom flange of the steel beam of the bridge.
- Lower the bridge elevation by releasing the hydraulic valves of the jacks. After this process, the bridge is situated on the new support and the operation finishes.

C.1.2 Risks and control measures

The risks involve in this operation and the control measures are detailed in Table C.1.

Table C.1: Risk assessments and control measures of moving support operation.

Risk	Control measures
Trapping the finger while inserting plywood sheets	Making sure that operations are performed so that no body part is under danger of being trapped
Injuring head by bumping into the bridge when underneath	Wearing protective equipment
During pumping operation, unexpected loss of pressure or similar can occur	No person should be close to the bridge during pumping
Bridge failure due to twisting during lifting or due to compromised strength	During lifting, no person should be beneath the bridge under any circumstances. The bridge failure would not be dramatic due to presence of props and "reserve supports". Once bridge has been lifted into the position, then the danger of it breaking would cease to exist.
Bridge slipping over the jacks in the longitudinal direction	Some slipping has to occur so that the bridge adjusts itself on the supports. The excessive slippage will be prevented by the limiters made of meccano pieces, built at each end of the bridge. In addition, no person should be standing on the short sides of the bridge under any circumstances.
Falling from the bridge	For general safety, no person will be allowed to be on the bridge at any time during the process and access to the lab will be restricted.

C.2 Experiments on Warwick Bridge

C.2.1 Procedure

The experimental programme is detailed in Section 5.3.3.

C.2.2 Risks and control measures

The risks involve in this operation and the control measures are detailed in Table C.2.

Table C.2: Risk assessments and control measures of experiments on Warwick Bridge.

Risk	Control measures
Test subject (TS) falls off the bridge	A safety hand-rail is positioned next to the bridge. Also, the experiment is closely monitored to reduced the speed if neccessary.
TS is surprised by the vibration level	The highest level of shaker-induced vibration is not introduced first so that the TS can get used to walking on a lively surface.
The bridge can be broken during the experiments	This risk unlikely happens due to the controlled stress level monitored for steel beams and estimated for concrete. TS is warned that only walking is allowed during experiments. More energetic activities, e.g. jumping, bouncing and running, are not allowed.

Appendix D

Interactive model

With the introduction of the structural length, the shape of a relevant vibration mode can be taken into account. The structural displacement at the location of m_p is $y_\mathrm{b}\phi_x$, where y_b is the modal displacement and ϕ_x is the corresponding mode shape coordinate at the position of the pedestrian (Figure D.1). Using notations from Appendix B, the coordinates of m_p are:

$$x = l\cos\theta_0 - l\cos\theta + x_0 \tag{D.1}$$

$$y = l\sin\theta + y_\mathrm{b}\phi_x \tag{D.2}$$

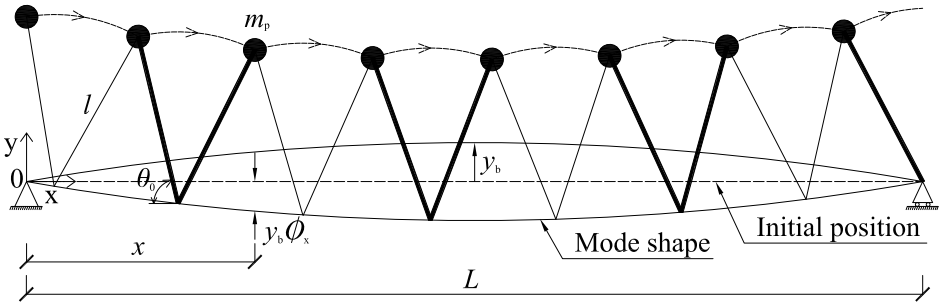

Figure D.1: Interactive pedestrian-structure model.

The velocities of m_p are:

$$\dot{x} = l\dot{\theta}\sin\theta \tag{D.3}$$

$$\dot{y} = l\dot{\theta}\cos\theta + \dot{y}_\mathrm{b}\phi_x \tag{D.4}$$

Kinetic energy (T) and potential energy (V) of the system are:

$$\begin{aligned} T &= \frac{1}{2}m_\mathrm{p}(\dot{x}_\mathrm{rel}^2 + \dot{y}^2) + \frac{1}{2}m_\mathrm{b}\dot{y}_\mathrm{b}^2 \\ &= \frac{1}{2}m_\mathrm{p}(l^2\dot{\theta}^2 + 2l\phi_x\dot{y}_\mathrm{b}\dot{\theta}\cos\theta + \phi_x^2\dot{y}_\mathrm{b}^2) + \frac{1}{2}m_\mathrm{b}\dot{y}_\mathrm{b}^2 \end{aligned} \tag{D.5}$$

$$V = -m_\mathrm{p}g(l\sin\theta + y_\mathrm{b}\phi_x) + \frac{1}{2}k_\mathrm{b}y_\mathrm{b}^2 \tag{D.6}$$

where m_b, k_b and $\dot{y}_\mathrm{b}$ are the modal mass, stiffness and velocity of the structure, respectively.

The dissipation energy in the bridge is defined as Rayleigh dissipation function F_R (Goldstein, 1980):

$$F_\mathrm{R} = \frac{1}{2}c_\mathrm{b}\dot{y}_\mathrm{b}^2 \tag{D.7}$$

where c_b is the modal damping of the structure.

Derivatives of the Lagrangian with respect to θ, $\dot{\theta}$, y_b, and $\dot{y}_\mathrm{b}$ are calculated as:

$$\begin{aligned} \frac{\mathrm{d}}{\mathrm{d}t}\left(\frac{\partial\mathcal{L}}{\partial\dot{\theta}}\right) &= \frac{\mathrm{d}}{\mathrm{d}t}\left(m_\mathrm{p}l^2\dot{\theta} + m_\mathrm{p}l\phi_x\dot{y}_\mathrm{b}\cos\theta\right) \\ &= m_\mathrm{p}l(l\ddot{\theta} + \phi_x\ddot{y}_\mathrm{b}\cos\theta + \dot{y}_\mathrm{b}\dot{\phi}_x\cos\theta - \phi_x\dot{y}_\mathrm{b}\dot{\theta}\sin\theta) \end{aligned} \tag{D.8}$$

$$\frac{\partial\mathcal{L}}{\partial\theta} = -m_\mathrm{p}l(\phi_x\dot{y}_\mathrm{b}\dot{\theta}\sin\theta - g\cos\theta) \tag{D.9}$$

$$\begin{aligned} \frac{\mathrm{d}}{\mathrm{d}t}\left(\frac{\partial\mathcal{L}}{\partial\dot{y}_\mathrm{b}}\right) &= \frac{\mathrm{d}}{\mathrm{d}t}\left(m_\mathrm{p}l\phi_x\dot{\theta}\cos\theta + m_\mathrm{p}\phi_x^2\dot{y}_\mathrm{b} + m_\mathrm{b}\dot{y}_\mathrm{b}\right) \\ &= m_\mathrm{p}l\phi_x\ddot{\theta}\cos\theta - m_\mathrm{p}l\phi_x\dot{\theta}^2\sin\theta + m_\mathrm{p}\phi_x^2\ddot{y}_\mathrm{b} + m_\mathrm{b}\ddot{y}_\mathrm{b} \end{aligned} \tag{D.10}$$

$$\frac{\partial\mathcal{L}}{\partial y_\mathrm{b}} = m_\mathrm{p}g\phi_x - k_\mathrm{b}y_\mathrm{b} \tag{D.11}$$

Lagrange equation for the IPM is:

$$\frac{\mathrm{d}}{\mathrm{d}t}\left(\frac{\partial \mathcal{L}}{\partial \dot{\theta}}\right) - \frac{\partial \mathcal{L}}{\partial \theta} + \frac{\partial F_{\mathrm{R}}}{\partial \dot{\theta}} = 0 \tag{D.12}$$

The equation of motion for the IPM can be derived as:

$$\ddot{\theta} = \frac{\cos\theta}{l}(g - \phi_x \ddot{y}_{\mathrm{b}}) \tag{D.13}$$

GRF generated by the IPM is calculated as:

$$F_{\mathrm{v}} = -m_{\mathrm{p}}(g - \ddot{y}) = -m_{\mathrm{p}}(g - l\ddot{\theta}\cos\theta + l\dot{\theta}^2\sin\theta - \phi_x \ddot{y}_{\mathrm{b}}) \tag{D.14}$$

Lagrange equation for the bridge is:

$$\frac{\mathrm{d}}{\mathrm{d}t}\left(\frac{\partial \mathcal{L}}{\partial \dot{y}_{\mathrm{b}}}\right) - \frac{\partial \mathcal{L}}{\partial y_{\mathrm{b}}} + \frac{\partial F_{\mathrm{R}}}{\partial \dot{y}_{\mathrm{b}}} = 0 \tag{D.15}$$

The equation of motion of the bridge is derived as:

$$m_{\mathrm{b}}\ddot{y}_{\mathrm{b}} + c_{\mathrm{b}}\dot{y}_{\mathrm{b}} + k_{\mathrm{b}}y_{\mathrm{b}} - \phi_x m_{\mathrm{p}}(g - l\ddot{\theta}\cos\theta + l\dot{\theta}^2\sin\theta - \phi_x\ddot{y}_{\mathrm{b}}) = 0 \tag{D.16}$$

For simulation, Equation D.16 is rewritten in the following form:

$$\begin{aligned}(m_{\mathrm{b}} + m_{\mathrm{p}}\phi_x^2\sin^2\theta)\ddot{y}_{\mathrm{b}} + 2\zeta m_{\mathrm{b}}(2\pi f_{\mathrm{n}})\dot{y}_{\mathrm{b}} + \\ m_{\mathrm{b}}(2\pi f_{\mathrm{n}})^2 y_{\mathrm{b}} - \phi_x m_{\mathrm{p}}(g\sin^2\theta + l\dot{\theta}^2\sin\theta) = 0\end{aligned} \tag{D.17}$$

where $f_{\mathrm{n}} = \frac{1}{2\pi}\sqrt{\frac{k_{\mathrm{b}}}{m_{\mathrm{b}}}}$ is the natural frequency and $\zeta = \frac{c_{\mathrm{b}}}{2\sqrt{k_{\mathrm{b}}m_{\mathrm{b}}}}$ is the damping ratio.

Equations D.13 and D.17 form the system of equations of the combined pedestrian-structure model.